

University of Southampton Research Repository
ePrints Soton

Copyright © and Moral Rights for this thesis are retained by the author and/or other copyright owners. A copy can be downloaded for personal non-commercial research or study, without prior permission or charge. This thesis cannot be reproduced or quoted extensively from without first obtaining permission in writing from the copyright holder/s. The content must not be changed in any way or sold commercially in any format or medium without the formal permission of the copyright holders.

When referring to this work, full bibliographic details including the author, title, awarding institution and date of the thesis must be given e.g.

AUTHOR (year of submission) "Full thesis title", University of Southampton, name of the University School or Department, PhD Thesis, pagination

UNIVERSITY OF SOUTHAMPTON

FACULTY OF ENGINEERING AND THE ENVIRONMENT

School of Engineering Sciences

Bioengineering Science Research Group

**Formation of Nanostructured Biomaterials in Lab-on-a-Chip
Microsystems**

by

Lorenzo Capretto

Thesis for the degree of Doctor of Philosophy

September 2011

UNIVERSITY OF SOUTHAMPTON

ABSTRACT

FACULTY OF ENGINEERING AND THE ENVIRONMENT
SCHOOL OF ENGINEERING SCIENCES

Doctor of Philosophy

FORMATION OF NANOSTRUCTURED BIOMATERIALS IN
LAB-ON-A-CHIP MICROSYSTEMS

By Lorenzo Capretto

The development of a microfluidic-based process is presented for the production of nanomaterials in continuous-flow microreactors. A flow focusing configuration was used enabling a controllable mixing process to assist the formation of the nanomaterials through precipitation, which was triggered by a solvent exchange process. Initially, Pluronic® tri-block copolymers were used as model polymeric biomaterials, relating to drug delivery applications, to investigate the production of empty polymeric micelles (PMs). Following the production of empty PMs, the production of copolymer stabilized organic β-carotene nanopartilces (NPs) was also investigated. The formation of both PMs and NPs, within microfluidic reactors, was further analysed by computational fluid dynamics (CFD) models in order to gain more insight into the nanoprecipitation process.

It has been shown that, besides the important role played by the width of the focused stream, the combined effect of reactor dimension, fluid properties, and flow condition significantly influenced the mixing condition and therefore the nucleation and growth process. When low water soluble molecules were co-precipitated together with polymeric stabilizer, competitive reactions resulted in the formation of two types of NPs, i.e., either with or without loading drug. The obtained results were interpreted by taking into consideration a new parameter representing the mismatching between the aggregations of the two precipitant species (polymer and drug), which played a decisive role in determining the size and polydispersity of the obtained NPs.

Finally, the established microfluidic production procedure was examined from a drug delivery point of view, by encapsulating a clinically relevant drug in PMs. PMs containing mithramycin were prepared and tested *in vitro* as a therapeutic protocol for beta-thalassemia.

In conclusion, the results of this study had demonstrated that microfluidics could facilitate the production of nanostructures for drug delivery purposes, and offer a novel method to control their properties including particle size, size distribution and pharmaceutical efficacy.

Table of Contents

<i>Abstract</i>	i
<i>Table of Contents</i>	iii
<i>List of Figures</i>	vii
<i>List of Tables</i>	xiii
<i>List of Symbols and Abbreviations</i>	xv
<i>Declaration of authorship</i>	xvii
<i>Acknowledgements</i>	xix
1 Introduction	1
1.1 Background	1
1.2 Objectives and scope	4
1.3 Novelty	5
1.4 Layout of the Thesis	7
2 Literature review	9
2.1 The microfluidic environment and mixing principles	9
2.1.1 Reynolds number and diffusion	9
2.1.2 Mixing in microfluidic devices	11
2.2 Microfluidic synthesis of nanomaterials	12
2.2.1 Materials and fabrication	13
2.2.1.1 Materials	13
2.2.1.2 Fabrication procedures	14
2.2.2 Advantages of microfluidic synthesis of nanomaterials	16
2.2.2.1 Micromixing and reactor design	18
2.2.2.2 Temperature control and heat transfer	23
2.2.2.3 Kinetic control and investigation	24
2.2.2.4 On-chip analysis	26
2.2.2.5 High throughput production	27

2.2.3 Nanostructured biomaterials produced by microfluidic approaches	28
2.3 Polymeric micelles for drug delivery	33
2.3.1 Composition and structure	33
2.3.2 Micelle preparation and stability	35
2.3.3 Aggregation kinetics	36
2.3.4 Drug solubilisation and release	38
2.3.5 Drug targeting	40
2.3.5.1 Passive targeting via EPR effect	40
2.3.5.2 Active targeting	41
2.3.5.3 Stimuli-responsive polymeric micelles	42
Summary of the literature review	43
3 Production of PMs in microreactors	47
3.1 Introduction and general considerations	47
3.1.1 Polymers	47
3.1.2 Microfluidic mixing	49
3.1.3 Polymeric micelles production strategy	51
3.2 Materials and methods	51
3.2.1 CMC determination: pyrene probe method	51
3.2.2 Critical water concentration (CWC) determination	52
3.2.3 Microfluidic reactor design and fabrication	52
3.2.4 Estimation of the focused stream width	54
3.2.5 Preparation of polymeric micelles	55
3.2.5.1 Preparation of PMs in batch reactors	55
3.2.5.2 Preparation of PMs in microfluidic reactors	55
3.2.6 PM size characterization	57
3.3 Results and discussion	57
3.3.1 CMC determination	57
3.3.2 Microfluidic reactors fabrication	58
3.3.3 Analytical estimation of mixing time	60
3.3.4 Preparation of PMs in microfluidic reactors	62
3.3.4.1 Effects of varying flow rate ratio (R) on PM characteristics	63
3.3.4.2 Effects of varying microreactor dimensions on PM characteristics	64
3.3.4.3 Matching between mixing and precipitation processes	69
3.3.4.4 Effects of solvent exchanges	72

3.3.4.5 Comparison between batch and microfluidic reactors	73
3.4 Summary	73
4 Computational study	75
4.1 Introduction	75
4.2 Materials	76
4.3 Methods	77
4.3.1 3D model generation	77
4.3.2 Mesh generation	80
4.3.3 Assumption, boundary conditions and model parameters	82
4.4 Flow and species transport analysis	83
4.5 Computational procedure	84
4.6 Results and discussion	86
4.6.1 Width of the focused stream	87
4.6.2 Velocity field	89
4.6.3 Diffusive mixing	93
4.6.3.1 Effect of viscosity on nanoprecipitation process	95
4.6.3.2 Focused stream shape	99
4.6.3.3 Mass fraction time evolution	101
4.7 Limitations of the model	103
4.8 Summary	104
5 Co-precipitation of drugs and block copolymers within microfluidic reactors	105
5.1 Introduction	106
5.2 Materials and methods	108
5.2.1 Materials	108
5.2.2 Fabrication of microfluidic reactor	108
5.2.3 Preparation of NPs in microfluidic reactor and by bulk mixing	108
5.2.4 Nanoparticle sizing and ζ -potential measurements	109
5.2.5 Transmission electron microscopy (TEM)	109
5.2.6 Critical water concentration (CWC) measurements	110
5.2.7 Computational fluid dynamics (CFD) study	110
5.3 Results and Discussion	112
5.3.1 General observation of NP formation within microreactors	112
5.3.2 Effects of varying β -carotene/polymer concentration on NP characteristics	115

5.3.3 Effects of varying β-carotene/polymer molecular ratios on NP characteristics	118
5.3.4 Effects of varying flow rate ratio and mixing time	122
5.3.5 Effects of laminar conditions and rapid mixing	124
5.4 Summary	133
6 Mithramycin encapsulated in polymeric micelles as novel therapeutic protocol for beta-thalassemia	135
6.1 Introduction	136
6.1.1 Beta-thalassemia	136
6.1.2 Mithramycin A (MTH)	137
6.1.3 MTH encapsulation in polymeric micelles	138
6.2 Materials and methods	140
6.2.1 Fabrication of microfluidic reactors	140
6.2.2 Preparation of PMs in microfluidic reactor and by bulk mixing	140
6.2.3 PM-MTH Characterization	141
6.2.4 Experimental design and statistical data	142
6.2.5 K562 cell cultures	142
6.2.6 Erythroid precursor cell cultures	142
6.2.7 RNA extraction and Real-Time quantitative PCR (RT-PCR)	143
6.2.8 HPLC analysis of haemoglobins	143
6.2.9 Statistical data analysis	144
6.3 Results and discussion	144
6.3.1 Effects of MTH encapsulation on PM characteristics	144
6.3.2 Optimization of PM-MTH production by DoE approach	146
6.3.3 Effect of PM-MTH on proliferation and differentiation of K562	151
6.3.4 Effect of PM-MTH on erythroid precursor cells	153
6.4 Summary	157
7 Conclusions	159
8 Future perspectives	163
<i>Appendix 1 List of publications</i>	165
<i>References</i>	167

List of Figures

1.1 Schematic representations of major class of nanoscale drug delivery systems: (a) Polymeric micelles; (b) polymer-drug conjugates; (c) liposomes; (d) Transmission electron micrograph of nanoparticles entering the cell through endocytosis; (e) comparison between the pharmacokinetics of Camptothecin (CPT) as a free drug molecules or encapsulated in nanoparticles. Readapted from [6].	3
2.1 Schematic of the pattern transfer process from a photomask to a photoresist layer. (a) Exposure of the photoresist through a mask (negative or positive). (b) Development of the pattern in the photoresist layer.	15
2.2 Schematic representation of the concentration relationship with the nanoprecipitation process [79].	16
2.3 Schematics of microfluidic devices LFR (a) and SFR (b). L1 and L2 represent the liquid inlets, G is the gas inlet and O is the outlet. Readapted from [104].	22
2.4 Production of CdS quantum dots by microfluidic two steps segmented flow reactor. Schematic diagram of the microfluidic network (a) and micrograph of the microfluidic device (b). Aqueous reagents R1, R2, and a separating stream S form droplets of the initial reaction mixture. Winding channels induce rapid mixing in droplets and initiate reaction 1. Reaction 1 is quenched when the stream of aqueous reagent R3 adds to aqueous droplets of the initial reaction mixture. readadapted from [103].	26
2.5 PMs as drug delivery systems. Schematic of the structure and salient features. Data readadapted from [136].	34
2.6 Mechanism of self-assembly of block copolymer PMs. Nucleation of block copolymer unimers (I), Fusion of existing particles and growth (II) and formation of overlapping brush corona that result in kinetically frozen nanoparticles (III). Readapted from [131].	37
2.7 Dependence of nanoparticle mean diameter on polymer concentration and mixing time. Data readadapted from [131].	38
2.8 Scheme of permeability and retention (EPR) effect and the implication in tumour passive targeting thought the vascular abnormalities of tumour vessels. readadapted from [10].	40
3.1 General chemical structure of Pluronic® block copolymers.	48
3.2 Focused enhanced mixing: the polymer stream is focused into a thin layer between the two sheath streams. Rapid mixing of the solvent takes place at the interface between the polymer solution and non-solvent streams.	50
3.3 Schematic representation of the channel pattern onto the photomask used for the fabrication of the microreactors. All the other quotes are reported in mm.	52
3.4 Schematic representation of the production procedure for glass microfluidic chips by isotropic wet etching.	53
3.5 Fluorescence intensity of pyrene vs. logarithm concentration of the Pluronic® F127 block copolymers in water.	57
3.6 A microfluidic reactor with three inlets creating a hydrodynamic flow focusing where the central stream is polymer Pluronic® solution in DMSO. The width of the focusing central stream, w_f , is controlled by varying the volumetric flow rates of the three inlets. Scale bar 30 μm (c) CAD-based design showing the cross section of the reactor channel. Values of w_0 , h and w_b are reported in Table 3.3.	58

3.7 Width of the focused stream at different hydrodynamic flow focusing conditions ("Reactor": Microreactor; "R": flow rate ratio; "PC": polymer solution concentration). Scale bar 100 mm.	60
3.8 Effects of flow rate ratio (<i>R</i>) on (a) PMs size at different polymer concentrations, and (b) size distribution at a polymer concentration of $7.5 \cdot 10^{-3}$ M using hydrodynamic flow focusing in Microreactor 2.	62
3.9 Effects of <i>R</i> and microreactor dimensions on PM size at polymer concentrations of (a) $1.5 \cdot 10^{-2}$ M and (b) $7.5 \cdot 10^{-3}$ M, and on (c) PM size distribution at a polymer concentration of $7.5 \cdot 10^{-3}$ M.	64
3.10 PM size distribution for Microreactors "2" (solid markers) and "1" (open markers) with <i>R</i> equal to 0.13 and 0.05, respectively. Pluronic F127 solution concentration: $7.5 \cdot 10^{-3}$ M.	65
3.11 Effect of width of focused stream on PM size in Microreactors 2 and 3 with an initial polymer concentration of $7.5 \cdot 10^{-3}$ M.	65
3.12 PM size distribution for Microreactors "2" (open markers) and "3" (solid markers) with <i>R</i> equal to 0.05 and 0.1, respectively. Pluronic F127 solution concentration: $7.5 \cdot 10^{-3}$ M.	66
4.1 Orthographic projection (a, b and c) and aerial view (d) of Microreactor 2 as designed in Gambit 2.4.6. (a) lateral, (b) top and (c) front views.	76
4.2 Microreactors dimensions comparison. Aerial views (a-c) and front view (d-e) of Microreactor 1 (a and d), Microreactor 2 (b and e) and Microreactor 3 (c and f).	77
4.3 Particular of the mesh near the junction section for Microreactors 1 (a), 2 (b) and 3 (c).	79
4.4 Simulated polymer solution concentration contours (a-d) corresponding photomicrograph (e-h) at a different polymer concentration (PC) (a, b) and different flow rate ratio (<i>R</i>) (c, d) in Microreactor 1 (a, b) and Microreactor 3 (c, d).	86
4.5 Relative focused stream width as a function of flow rate ratio (<i>R</i>) for Microreactor 2 (Solid squares: numerical simulation data; Open squares: experimental data). Inset reports the computed concentration profile for <i>R</i> = 0.03 (solid line) and the corresponding second derivate (dashed line) showing the relative position of the local maxima. Data referred to a polymer initial concentration of $7.5 \cdot 10^{-3}$.	87
4.6 CFD simulated velocity filed contours for PC= $1.5 \cdot 10^{-2}$, R=0.08 within Microreactor 2. Contours are showed for (a) three longitudinal sections at junction, middle and end of the main mixing channel at a distance from bottom and upper wall of 14.5 μm , and (b) corresponding cross section views.	88
4.7 CFD simulated velocity profile plots along the mixing channel at different distance from the channel junction and for different process set up. (a) PC= $1.5 \cdot 10^{-2}$, R=0.03 in Microreactor 2; (b) PC= $1.5 \cdot 10^{-2}$, R=0.08 in Microreactor 2; (c) PC= $1.5 \cdot 10^{-2}$, R=0.13 in Microreactor 2; (d) PC= $1.5 \cdot 10^{-2}$, R=0.08 in Microreactor 1; (e) PC= $7.5 \cdot 10^{-3}$, R=0.08 in Microreactor 2; (f) PC= $1.5 \cdot 10^{-2}$, R=0.08 in Microreactor 3.	90
4.8 CFD simulation of diffusive mixing along the main mixing channel in Microreactor 2. R = 0.06, Pluronic F127 solution concentration = $7.5 \cdot 10^{-3}$ M. (a) Simulated mass fraction contours showing three longitudinal sections at junction, middle and end of the main mixing channel. (b) Mass fraction profiles of DMSO at different distances along the channel. The profiles are on the middle plane between the bottom and top of the channel (at a channel depth of 14.5 μm).	92
4.9 CFD simulated (a) mass fraction profiles and (b) diffusion coefficient profiles of DMSO along the main channel of Microreactors 2 (open markers) and 3 (solid markers) with <i>R</i> equal to 0.05 and 0.1, respectively. Pluronic F127 solution concentration: $7.5 \cdot 10^{-3}$ M.	94

4.10 CFD simulated (a) mass fraction profiles and (b) diffusion coefficient profiles of DMSO along the main channel of Microreactor 3 at Pluronic F127 solution concentrations of $7.5 \cdot 10^{-3}$ M (open markers) and $1.5 \cdot 10^{-2}$ M (solid markers). $R = 0.13$.	96
4.11 CFD simulated mass fraction contours DMSO polymeric solution along the main channel of Microreactor 2 at Pluronic F127 solution concentrations of $1.5 \cdot 10^{-2}$ M for $R=0.03$ (a) and $R=0.13$ (b). The contours refer to a cross section 5mm downstream the channel junction.	97
4.12 CFD simulated mass fraction evolution of DMSO polymeric solution along the main channel of Microreactor 2 at Pluronic F127 solution concentrations of $1.5 \cdot 10^{-2}$ M for $R=0.03$ (a) and $R=0.13$ (b).	98
4.13 CFD simulated mass fraction evolution of DMSO as function of the residence time. (a) Microreactor 2 at Pluronic F127 solution concentrations of $1.5 \cdot 10^{-2}$ M, $R=0.13$ (open markers) and $R=0.03$ (solid markers); (b) $R=0.05$ at Pluronic F127 solution concentrations of $1.5 \cdot 10^{-2}$ M, Microreactor 3 (solid markers) and Microreactor 2 (open markers); (c) Pluronic F127 solution concentration at $7.5 \cdot 10^{-3}$ M, Microreactors 2 (open markers) and 3 (solid markers) with R equal to 0.05 and 0.1, respectively; (d) $R = 0.13$ in Microreactor 3 at Pluronic F127 solution concentrations of $7.5 \cdot 10^{-3}$ M (open markers) and $1.5 \cdot 10^{-2}$ M (solid markers).	100
5.1 Nanoprecipitation of β -carotene/Pluronic F127 hybrid NPs. (a) Schematic representation of the microreactor and of the experimental setup used. (b) Characterization of β -carotene/Pluronic F127 hybrid NPs in terms of ζ -potential and mean diameter of NPs produced using different component in the central organic stream. (c) TEM image of β -carotene/Pluronic F127 hybrid NPs.	111
5.2 Effect of β -carotene /polymer concentrations on NP size distribution. Three solutions of β -carotene /polymer in THF were used with polymer concentrations of 7.5 mM (solid, black squares), 10.0 mM (solid, grey squares), and 12.5 mM (open, black circles) while β -carotene /polymer MR was kept constant at 2.35. (b) Schematic representation of the mechanism of formation of additional empty PMs. At low concentration smaller NPs, which exhibits higher surface volume ratio, are formed, consuming all the polymer unimers. At high concentration, larger NPs with smaller surface to volume ratio are formed. In this condition, there is an excess of polymer unimers that is consumed with the formation of empty PMs.	114
5.3 Size and size distribution of NPs produced at different β -carotene/Pluronic molecular ratio (MR).	116
5.4 Effects of β -carotene/polymer MR on hybrid NPs nanoprecipitation. (a) Size distribution of NPs obtained at different β -carotene/polymer MRs. All the experiments were performed at a constant polymer concentration of 10.0 mM. (b) ζ -potential distribution curve for NPs obtained at corresponding β -carotene/polymer MRs. (c) Calculated size distribution of hybrid NPs (dashed line, solid circles) and empty PMs (dashed line, open circles) at MR of 1.41. The grey solid-line curve represents the sum of the values of the calculated hybrid NPs and unfilled PMs, while the open squares are the experimental data. (d) Peak area as a function of β -carotene/polymer MR for hybrid NPs (filled circles) and unloaded PMs (open circles).	118
5.5 Size distribution of NPs obtained at different flow rate ratio (R). Polymer concentration was 10 mM and MR=2.35.	121
5.6 (a) Relationship of CWC with concentration of β -carotene or Pluronic F127. (b) ζ -potential of different β -carotene and/or Pluronic F127 solutions in THF at different water concentrations, showing the two-step nanoprecipitation kinetics. Schematic representation of the precipitated species (inset).	122
5.7 (a) Normalized mass fraction profile by CFD for Pluronic F127 (open symbols), β -carotene (solid symbols) and water (grey line, no symbols) at different distances downstream the channel junction, where organic solution (Pluronic F127, β -carotene in THF) and antisolvent (water) first met. The mass fraction profile is computed for half-channel cross section due to the symmetric characteristics of the mixing	124

channel. (b) Mass fraction evolution of non solvent (water) along the mixing channel, computed at the centre of the focused stream, which represents the symmetry plane between the two halves of the mixing channel. The data are computed for MR = 2.35 with a Pluronic F127 concentration of 10 mM. No significant differences were found for the same set of data computed for different MRs and polymer concentrations. Arrows schematically represent the time mismatching (τ^*) to reach the CWC concentration for both, colloidal stabilizer (Pluronic F127) and active encapsulated species (β -carotene) for different β -carotene-Pluronic F127 MR; insets report MRs and associated τ^* .	
5.8 NPs made under bulk mixing conditions, with Pluronic F127 at 10.0 mM, MR = 2.35 and R = 0.04. (a) Size distribution and (b) TEM image of the produced hybrid NPs, scale bar 1 μ m.	128
5.9 (a) Normalized mass fraction profiles by CFD for Pluronic F127 (open symbols), β -carotene (solid symbols) and water (grey line, no symbols) at different distances downstream the channel junction. The mass fraction profile is computed for half-channel cross section due to the symmetric characteristics of the mixing channel. (b) Mass fraction evolution of non-solvent (water) along the mixing channel, computed at the centre of the focused stream for R = 0.04 (solid line), R = 0.1 (dotted line), R = 0.2 (dash-dotted line) and R = 0.3 (dashed line). Inset reports τ^* values.	129
6.1 Chemical structures of mithramycin.	135
6.2 Schematic representation of the preparation procedure for PMs by microfluidics.	138
6.3 Effect of preparation procedure on mean size (a) and size distribution (b-d) of PM-MTH produced at different MTH concentrations. PMs were prepared by bulk mixing in round bottom flask (open bars) and by microfluidics (filled bars). Data represent the average of three independent experiments (run in triplicate) \pm SD. Panels b-d respectively report the size distribution of PMs produced with 10.0 (b), 32.5 (c) and 55.0 (d) μ M mithramycin solution, by bulk mixing (open circles) and by microfluidics (filled circles).	143
6.4 DoE analysis for the preparation of PM-MTH. Response surface plots for PMs obtained by bulk mixing (green surfaces) or microfluidics (red surfaces). The following factors and responses were respectively investigated: "conc" and " R " vs. "size" (a), "conc" and " R " vs. "SD" (b) and "conc" and " R " vs. "drug ₂₀₀ " (b). The meanings of the factor are reported in Table 6.1. Experimental data points are reported in Table 6.2.	147
6.5 Effect of MTH on growth of K562 cells. Microphotographs showing the K562 cell density after 3 days of culture in the presence of the indicated nM MTH concentrations. Bottom left side: photomicrographs showing the control, cultured in absence of MTH, after 0 (bottom) and 3 (upper) days of culture. Corresponding graph: free MTH (squares), PM-MTHs prepared by microfluidics (circles) or bulk mixing (triangles). Data represent the average of three independent experiments (run in triplicate) \pm SD. Bar corresponds to 100 μ m.	150
6.6 Effect of MTH on erythroid differentiation of K562 cells (a-b). Cells were cultured for 7 days, in the presence of the indicated nM MTH concentrations added to the culture medium in form of free drug or encapsulated into PMs prepared by microfluidics or bulk mixing. Microphotographs of panel A were taken after staining with benzidine cells treated with PM-MTH (microfluidics), thereafter cells were counted and the per cent of benzidine-positive cells was determined and plotted. Scale bar 25 μ m. (b). Data represent the average of three independent experiments (run in triplicate) \pm SD (microfluidics Vs free MTH, p < 0.05). c. Effects of MTH on expression of globin genes. Cells were cultured for 4 days, in the presence of the 50 nM of MTH added to the culture medium in form of free drug or encapsulated into PMs prepared by microfluidics or bulk mixing, as indicated. RT-PCR was performed as indicated in methods for quantification of α -globin (open bars) and γ -globin (filled bars) mRNA sequences. Data represent fold content in respect to control uninduced cells (average \pm SD of three independent experiments); α -globin: microfluidics Vs bulk, p < 0.001, microfluidics Vs free MTH p < 0.05; γ -globin: microfluidics Vs bulk, p < 0.05,	152

microfluidics Vs free MTH p< 0.05.

- 6.7 Effect of MTH encapsulated into PMs prepared by microfluidics on HbF production by erythroid precursor cells (ErPC) from a β -thalassemia patient. ErPC were cultured in phase II with only EPO, or EPO plus free MTH or PM-MTH prepared by microfluidics. a: HPLC profile of uninduced ErPC (left), ErPC induced by PM-MTH (center) and free MTH (right). Panel b reports the quantitative effects on HbF and the production of α -aggregates in ErPC induced by PM-MTH (filled bars) and free MTH (grey bars). For comparison data referred to uninduced ErPC (open bars), are also reported (HbF: uninduced Vs microfluidics, p < 0.05, uninduced Vs free MTH p< 0.05; α -aggregates: uninduced Vs microfluidics, p < 0.001, uninduced Vs free MTH p < 0.001, microfluidics Vs free MTH p < 0.05). Panel C reports the RT-PCR analysis of ErPC, expressed as fold induction of α -globin, β -globin and γ -globin mRNA production. Cells were treated with PM-MTH (black bar) or free drug (grey bars). Data represent the average of three independent determinations \pm SD. 154

List of Tables

2.1	List of recent studies about the use of microfluidic technology for organic nanoparticle formation.	29
3.1	Physicochemical characteristics of Pluronic® block copolymers. Table readapted from Reference [144].	48
3.2	Characteristics of Pluronic® F127.	49
3.3	Microfluidic reactor dimensions.	58
3.4	Effect of reactor type, polymeric solution concentration (PC) on validation factor, a.	61
4.1	Material properties of the fluid used for the CFD simulation.	75
4.2	Mesh size of Microreactors 1, 2 and 3	78
4.3	Fluent setup: solver	83
4.4	Fluent setup: solver under relaxation factors values	84
5.1	Fluent setup: solver under relaxation factors values	110
6.1	DoE study of the influence of experimental parameters on the PM-MTH characteristics: investigated factors and responses.	145
6.2	Experimental design matrix and results of the DoE (design of experiments) approach for the preparation of PM-MTH.	146
6.3	Analysis of variance of the model (ANOVA).	149

List of Symbols and Abbreviations

Symbols

A	Cross sectional area (m^2)
D	Diffusion Coefficient ($\text{m}^2 \cdot \text{s}^{-1}$)
D_h	Hydraulic diameter (m)
h	Height of the channels (m)
I	Unit tensor
j	Diffusion flux ($\text{mol} \cdot \text{m}^{-2} \cdot \text{s}^{-1}$)
k	Boltzmann's constant ($k=1.381 \cdot 10^{-23} \text{J} \cdot \text{K}^{-1}$)
P_{wet}	Wetted perimeter (m)
Q	Total volumetric flow rates ($\text{m}^3 \cdot \text{s}^{-1}$)
Q_c	Volumetric flow rates for the central stream ($\text{m}^3 \cdot \text{s}^{-1}$)
Q_e	Total volumetric flow rates of the sheath streams ($\text{m}^3 \cdot \text{s}^{-1}$)
r	Radius of the particles (or molecules) (m)
R	Volumetric flow ratio
Re	Reynolds number
t	Time (s)
T	Absolute temperature (K)
U	Average velocity of fluid ($\text{m} \cdot \text{s}^{-1}$)
u	Velocity of fluid ($\text{m} \cdot \text{s}^{-1}$)
w_f	Width of the focused stream (m)
w_o	Width of the mixing channel (m)
w_b	Bottom width of the mixing channel (m)
x	Position of the species (m)
Y_i	Mass fraction

Greek Symbols

λ_{ex}	Excitation wavelength (nm)
λ_{em}	Emission wavelength (nm)
μ	Fluid dynamic viscosity ($\text{Pa} \cdot \text{s}$)
ν	Fluid kinematic viscosity ($\text{m}^2 \cdot \text{s}^{-1}$)
ρ	Fluid density ($\text{kg} \cdot \text{m}^{-3}$)
τ_{agg}	Aggregation time (s)
τ_{mix}	Mixing time (s)

τ^* Time mismatching to reach the CWC (s)

φ Species concentration (Kg·m⁻³)

Abbreviations

CFD	Computational fluid dynamics
CMC	Critical micellization concentration
CMT	Critical micellization temperature
CWC	Critical water concentration
<i>Da</i>	Damkohler number
DLS	Dynamic light scattering
DMSO	Dimethyl sulfoxide
EO	Ethylene oxide
EPR	Enhanced permeation retention
ErPC	Human erythroid precursor cells
FDA	Food and drug administration
Hb	Haemoglobin
HbF	Fetal Haemoglobin
HFF	Hydrodynamic flow focusing
MTH	Mithramycin
NP	Nanoparticle
NTA	Nanoparticle tracking analysis
PC	Polymer concentration
PCR	Polymerase chain reaction
PDMS	Polydimethylsiloxane
PEG	Polyethylene glycol
PM	Polymeric micelle
PM-MTH	Mithramycin containing polymeric micelles
PO	Propylene oxide
RTD	Residence time distribution
SLN	Solid lipid Nanoparticles
THF	Tetrahydrofuran

DECLARATION OF AUTHORSHIP

I, Lorenzo Capretto, declare that the thesis entitled FORMATION OF NANOSTRUCTURED BIOMATERIALS IN LAB-ON-A-CHIP MICROSYSTEMS and the work presented in the thesis are both my own, and have been generated by me as the result of my own original research. I confirm that:

- This work was done wholly or mainly while in candidature for a research degree at this University;
- Where any part of this thesis has previously been submitted for a degree or any other qualification at this University or any other institution, this has been clearly stated;
- Where I have consulted the published work of others, this is always clearly attributed;
- Where I have quoted from the work of others, the source is always given. With the exception of such quotations, this thesis is entirely my own work;
- I have acknowledged all main sources of help;
- Where the thesis is based on work done by myself jointly with others, I have made clear exactly what was done by others and what I have contributed myself;
- Part of this work has been published before submission, and a list of these publications is included in Appendices 1.

Signed:

Date:.....

Acknowledgements

"Before enlightenment; chop wood, carry water. After enlightenment; chop wood, carry water."

- Zen Proverbs -

First and foremost, I would like to thank my two supervisors Doctor Xunli Zhang and Professor Martyn Hill who have contributed with their advice, experience and patience to the work in this thesis, proving support and shove in the right direction whenever it was needed. My heartfelt thank Professor Claudio Nastruzzi and Stefania Mazzitelli for their priceless and continuous support and helpful discussions. I would like also to thank the group of Professor Roberto Gambari at University of Ferrara, which helped with the *in vitro* test of K562 and ErPC cells, and Dr. Lefteris Danos at University of Southampton for assistance in fluorescence experiments.

My gratitude to UK Engineering and Physical Sciences Research Council (EPSRC) for supporting this study financially and to BASF Chem Trade GmbH is for providing the polymer Pluronic® F127.

Many thanks to my past and present fellows postgraduates within the School of Engineering Science at Southampton University, friends and housemates, who have guided and supported me, proving coffee, laughs, beers and foods over the last three years. My thanks to Jonathan, Francis, Federico, Orestis, Orestis Jr., Maria, Amir, Tom, Stefano, Marco, Michele, Eduardo, Iole, Eleonora, Luca, Alan, Nick and everyone I missed.

I would like to especially thank Dario Carugo for his scientific support and friendship over the years and for being perhaps the best collaborator that everyone could ever want.

Lastly but not mean least, my warmest thanks also to those people overseas who have been there to support and encourage me in these three years. In particular, my love to my family who have always been supportive, and I know they always will, through the good times and bad; I am very lucky and profoundly grateful. Finally, I must thank my friends, Leonardo, Cristiano, Matteo, Marco, Luca, Lucia and Elena who constantly helped me to remember what is really important in life – and for that, I am deeply grateful.

Chapter 1

Introduction

1.1 Background

A drug carrier is a pharmaceutical formulation that serves as mechanism to improve the effectiveness of a drug by (i) enhancing the delivery of the drug to the target sites of pharmacological actions and (ii) prolonging the *in vivo* drug action. Drug carriers are used in drug delivery systems to alter the distribution of the drug within the organism. In fact, by controlling the distribution of drug in the body (i.e. targeted drug delivery), side effects are reduced and lower doses are often needed, with the clear benefit of improving product efficacy and safety, as well as patient compliance. Moreover, by using appropriate drug carrier even drugs with scarce water solubility can be formulated and used in therapy. This last point is particular appealing for pharmaceutical industries, where new drugs that demonstrate potent biological activity but poor water solubility, or a short circulating time, will likely deemed undevelopable due to the high development challenge. However, with the emerging trends in drug delivery, it has become increasingly possible to address some of the shortcoming associated with the development of new drugs. A number of drug carriers have been proposed and studied to this aim, including drug loaded biodegradable microspheres, drug polymer conjugates and drug loaded nanoparticles and colloidal systems.

Currently, a big part of the effort in developing new drug delivery systems is devoted to “nanomedicine”[1]. Over the past decade, nanomedicine has emerged as a new field of medicine where nanoscale materials are used to deliver a wide range of pharmaceutically active organic compounds including drugs, genes and imaging agents [2]. In this respect, the high versatility of nanoscale materials has stimulated their application in different fields including, but not limited to, drug delivery, *in vitro* diagnostic, *in vivo* imaging, biomaterials and tissue engineering [3]. As recognition of the importance of this research filed it is expected that the global market of nanomedicine could grow to \$70-160 billion by 2015 [4, 5]. In this perspective, the

current thesis project have addressed topic related to the production and application of nanoscale material in the medical field with specific focus on drug delivery.

Due to their small dimension, nanoscale drug delivery systems can be directly injected in the bloodstream in which they can provide a way for the drug to target a specific tissue. By the use of specific moiety for the active targeting, stimuli-responsive release capacity, or by lever the peculiar biodistribution of nanoparticles in the body¹, these delivery systems can preferentially release the drug in specific tissue without damaging healthy tissues [6]. Among a variety of nanoscale drug delivery systems such as liposomes, dendrimers, polymer/drug conjugates and polymer-DNA complexes, polymeric micelles (PMs) (see Figure 1.1) have increasingly attracted much attention. This mainly owing to their physicochemical properties and unique core-shell architecture, which allow to overcome solubility or bioavailability issues and eventually deliver poorly water-soluble drugs to the target site in the human body [7-9].

During the drug delivery process, size characteristics (i.e., mean size and polydispersity) of the nanoparticles play an important role relating to the rate of drug release, the accumulation site and the kinetics of elimination from the body [10]. Therefore, in the production of PMs, superior control of process parameters is crucial in order to produce such nanomaterials with desired features [11-13], whilst there remain challenges in the most commonly used macro-scale stirring batch systems.

In recent years, the development in the field of microfluidic and lab-on-a-chip technologies [14] has demonstrated that microfluidic-based reactors offer a series of advantages over conventional batch reactors in terms of speed, controllability, integration and automation [12]. This provides opportunities for the development of nanoparticle production processes as the small length scale used in microreactors restricts fluidics to laminar flow regime, thereby allowing spatial and temporal control and manipulation of fluids and fluidic interfaces for diffusive mixing [15]. In addition, the small dimension, and the resulting large surface area to volume ratio, enable a rapid and more uniform heat and mass transfer that, in turn, can significantly improve the process controllability [16]. Along with the wide application of microreactors in analytical and synthetic chemistry, microfluidic approaches have also been applied for the production of nanomaterials initially focusing only on inorganic based nanostructures, e.g., metal nanoparticles, semiconductor nanoparticles and quantum dots [17-22]. In addition, other groups including that of Barrow at Cardiff University [23] and Weitz at Harvard University [24] have used microreactors to produce micro-sized particles or droplets with a potential application in drug delivery. However,

¹ via the so called enhanced permeation retention effect (see below)

studies on the formation of organic nanoparticles are in the early stages in terms of synthesis vs. functionality and there is so far little significant experimental evidence available on the early stage of organic nanoparticle formation, especially during or immediately after the mixing of reactants.

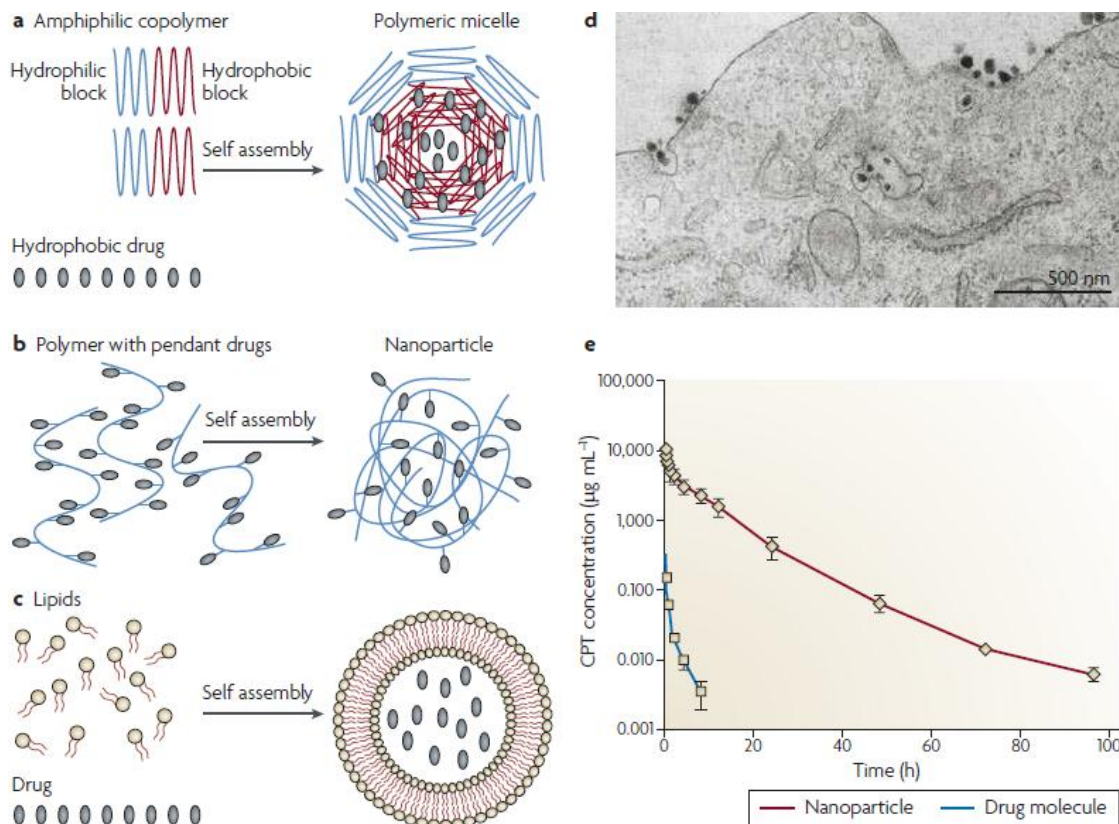


Figure 1.1 Schematic representations of major class of nanoscale drug delivery systems: (a) Polymeric micelles; (b) polymer-drug conjugates; (c) liposomes; (d) Transmission electron micrograph of nanoparticles entering the cell through endocytosis; (e) comparison between the pharmacokinetics of Camptothecin (CPT) as a free drug molecules or encapsulated in nanoparticles. Redadapted from [6]. Reprinted by permission from Macmillan Publishers Ltd: [Nature Reviews Drug Discovery](#) 2008. 7(9): p. 771-782, copyright 2008.

More recently, the fabrication of organic nanostructures, which are relatively less stable, has been investigated in microfluidic systems. For example, Ali *et al.* [25] prepared an aqueous hydrocortisone nanosuspension using microfluidic reactors, and examined the effect of microfluidic parameters together with the reactor design. Zhang *et al.* [26] and Jasch *et al.* [27] fabricated solid lipid nanoparticles (SLNs) in a microchannel system where the effects of liquid flow velocity and lipid concentration on the properties of SLNs were investigated experimentally. Attempts have also been made for the production of polymeric nanoparticles using microfluidic reactors [28,

29]. These studies further demonstrated the importance of both fluidic conditions and polymer compositions for the control of nanoparticle size. In addition, the integration of microreactors with nanoparticle sizing based on dynamic light scattering, by Chastek *et al.* [28] suggested a useful approach for nanoparticle measurements *in situ*.

1.2 Objectives and scope

The ultimate goal of this project was to develop a process based on microfluidic and lab-on-a-chip technology enabling the discovery and development of high performance PMs for applications in drug delivery, and create a knowledge base or platform for the generation of a variety of new functional materials and an increased scientific understanding of complex system. The specific objectives included:

- To design and construct a microfluidic based system to control and monitor the production of polymeric micelles and polymer stabilized organic nanoparticles in a continuous flow format.
- To investigate the role of microfluidic environment in controlling and directing the formation of organic nanostructure.
- To develop numerical microfluidic models incorporating mass transfer and the precipitation process within the microfluidic system in order to investigate the microfluidic-based nanoprecipitation process
- To develop numerical simulations to predict and optimise both system designs and operation conditions.
- Study the *in vitro* application of drug loaded polymeric micelles.

In this thesis, experimental, computational and biological data gathered are presented. Specifically, the production of empty PMs (without loading any drug) has been investigated using Pluronic® tri-block copolymer, as model block copolymer, in a series of microfluidic-based reactors, where a hydrodynamic flow focusing configuration was used. The effects on the PM size and size distribution have been examined systematically by varying polymer concentration, flow rate ratio of solvent to non-solvent water, and the microchannel geometry where three microreactors were employed with different reaction channel dimensions. The nanoprecipitation process

under microfluidic conditions has been analyzed further for the control of PM size and size distribution.

The mixing process enhanced by focusing flow within the microfluidic reactors has been further analyzed by means of a computational fluid dynamics (CFD) model in order to understand the hydrodynamics present during the PM formation process, and its effect on focusing flow and diffusion processes.

Following the production of empty Pluronic® PMs, the co-precipitation process of an active (β -carotene) together with a block copolymer stabilizer (Pluronic®) has been investigated. The effects on nanoprecipitation process of varying polymer and active concentrations, as well as fluidic conditions have been investigated both experimentally and computationally.

The use of microfluidic-based nanoprecipitation to assemble mithramycin drug-encapsulated PMs was then investigated. Mithramycin (MTH) has gained increasing attention as a potential therapeutic agent for haematological disorders, including β -thalassemia and sickle cell anemia. MTH's therapeutic effect stems from its capability to induce the *in vitro* erythroid cell differentiation that is associated with an increased expression of embryo-fetal globin genes [30]. The encapsulation process of mithramycin within the PM core has been investigated in a statistical fashion in order to understand the effect of different production parameters, such as drug concentration and flow rate ratio, on the encapsulation efficiency and dimension of the produced PMs. Finally, the produced micelles were analyzed *in vitro* for antiproliferative and differentiation activity.

1.3 Novelty

Different elements of novelty can be recognized in the presented work:

- The microfluidic reactor presented represents one of the first devices implemented for the production of PMs by microfluidic nanoprecipitation.
- The systematic study of the effect of a number of process parameters (i.e., flow rate ratio, polymer concentration and microreactor architecture) revealed that device architecture, fluidic conditions and fluids properties acted in concert to determine the nanoprecipitation process (see Sections 3.3.4.3 and 3.3.4.4).
- It has been demonstrated that the amount of solvent introduced in the microfluidic reactor (as result of the variation of the flow rate ratio) affects the size characteristic of the produced polymeric micelles. This effect has been

correlated with a lowering of the n barrier for unimers insertion (see Section 3.3.4.3).

- The mixing process within the microfluidic reactors has been analysed by computational modelling in order to analyse the implication of the hydrodynamic factor on the PM production process. The model also accounts for the effect of viscosity on the diffusion coefficient and diffusive mixing.
- This study had revealed that interfacial phenomena and fluid properties (i.e., polymer concentration, diffusivity and fluid viscosity) also significantly affect the nanoprecipitation alongside the effect of reactor geometry and fluidic conditions (see Section 4.6.3).
- The shape and the surface to volume ratio of the focused stream, together with different mixing rate in different location along the focused stream, have been recognized as possible sources of polydispersity (see Section 4.6.3).
- The production of polymer stabilized nanoparticles demonstrated the presence of a competitive reactions resulted in the formation of two types of nanoparticles (i.e., either with or without loading organic carotene in the core-shell structure). The corresponding peak area of the size distribution profiles quantitatively represented the amount of each type of nanoparticles as a function of carotene/polymer molecular ratio (see Section 5.3.3).
- In an effort to unveil the effect of the complex interplay between molecular and fluid dynamic properties of nanoprecipitating species, CFD models were integrated with an *in-house* code that simulated the effect of NP formation on their diffusion and advection² kinetics.
- The results had provided new insight on the role of the fluidic condition in controlling the competitive reaction that takes place during the polymer/drug co-precipitation process. The results were explained by taking into consideration a new parameter representing the mismatching between the aggregations of the two precipitant species (see Section 5.3.5).
- A microfluidic-based protocol for the production of a polymeric micelle based delivery system for mithramycin was developed and examined in comparison to micelles produced with conventional methods. The effects of different process

² Advection is a transport mechanism of a substance by a fluid due to the fluid's bulk motion in a particular direction [31].

operational parameters were investigated and their effect on the size and size distribution were evaluated (see Sections 6.3.1 and 6.3.2).

- PMs containing mithramycin were *in vitro* tested on K562 cells and human erythroid precursor cells. Mithramycin delivered as micellar formulation has been found to more active than free mithramycin (see sections 6.3.3 and 6.3.4).
- PMs containing mithramycin, as shown to be an effective fetal haemoglobin (HbF) inducers, which does not stimulate α -goblin gene expression, being instead able to induce β -globin and even more efficiently γ -globin gene expression (see Section 6.3.4).

1.4 Layout of the Thesis

This Thesis is organized as follows:

Following a general Introduction in Chapter 1, Chapter 2 presents a review of the literature relevant to the microfluidic based production of nanomaterials. This chapter is intended to guide the reader within the framework of microfluidic reactors and their applications in nanomedicine. However, detailed information, relevant to the obtained experimental findings, will be given together with the relevant results. This chapter is divided into three main sections focusing on: physics and mixing in microfluidic devices, production of nanomaterials by microfluidic approaches and PMs for drug delivery application, respectively.

Chapter 3 describes the technique used for the production of PMs by a microfluidic approach. Specifically, the characterization of the used polymer, the design and production of the microfluidic reactors, the characterization of hydrodynamic focusing to achieve mixing, and the effect of different experimental parameter on the size characteristics of PMs are covered. Results and discussion on the experimental data obtained are also presented at the end of this chapter.

Chapter 4 describes the materials used and the methodology employed for the computational study. It presents the process used to assess the hydrodynamic involved in PM formation in microfluidic reactors. Results and discussion on the numerical data obtained follow at the end of this chapter.

Chapter 5 presents a study on the co-precipitation of Pluronic ® F127 and β -carotene. The effects of operational fluidic conditions and feed concentration of polymers and actives were examined systematically on the size characteristics of the produce nanoparticles. The fluid dynamics within the microreactor was also analyzed by a CFD

model. The results were correlated to the characteristics of the produced nanoparticle and mixing conditions.

Chapter 6 presents the development of a formulation for mithramycin, based on PMs produced by microfluidic technology, and the *in vitro* analysis of the formulation as new therapeutic protocol for beta-thalassemia.

Chapter 7 summarizes the findings and outlines the conclusions of the presented investigations.

Chapter 8 outlines the future perspective of the work.

Chapter 2

Literature review

2.1 The microfluidic environment and mixing principles

In this section, the basic theory of fluid flow and the implication of using microfluidic devices for mixing are first discussed. Generally, the same laws that describe the flow at a macroscale govern fluid flow in the microenvironment. However, miniaturization confers additional characteristics that can be leveraged to perform processes not possible at a macroscale. Microfluidic devices, indeed, are not merely a miniature version of their macroscale counterparts because many physical characteristics, such as surface area-to-volume ratio and diffusion, do not simply scale linearly from large to small devices. Another important feature is the omnipresence of laminar flow conditions because in the microfluidic channel viscous forces dominate. These factors become significant at a microscale level, and their effects should be taken into account during the design and implementation of lab-on-a-chip devices.

In other words, it must be noted that, a microfluidic mixer is not just a scaled-down copy of a macroscale mixing device; it should be designed in ways that leverages the physical characteristics of the mixing in a confined space.

2.1.1 Reynolds number and diffusion

Fluid flow is generally categorized into two flow regimes: laminar and turbulent. Laminar flow is characterized by smooth and constant fluid motion, whereas turbulent flow is characterized by vortices and flow fluctuations. Physically, the two regimes differ in terms of the relative importance of viscous, the friction imparted by the channel walls and inertial forces and fluid momentum. The relative importance of these

two types of forces for a given flow condition, or to what extent the fluid is laminar, is measured by the Reynolds number (Re) [32]:

$$Re = \frac{\rho u D_h}{\mu} = \frac{u D_h}{\nu}, \quad (2.1)$$

where ρ and μ are the fluid density and dynamic viscosity, respectively; ν is the kinematic viscosity; u is the velocity of fluid and D_h is the hydraulic diameter of the channel. The hydraulic diameter of the channel is a characteristic number that depends on the cross-sectional geometry of the channel, and is given by [32]:

$$D_h = \frac{4A}{P_{wet}}, \quad (2.2)$$

where A and P_{wet} are the cross-sectional area and the wetted perimeter of the channel, respectively.

At low Re , the viscous effects dominate inertial effects and a completely laminar flow occurs. In the laminar flow system, fluid streams flow parallel to each other and the velocity at any location within the fluid stream is invariant with time when boundary conditions are constant. This implies that advective mass transfer occurs only in the direction of the fluid flow, and mixing can be achieved only by molecular diffusion [33]. By contrast, at high Re the opposite is true. The flow is dominated by inertial forces and characterised by a turbulent flow. In a turbulent flow, the fluid exhibits motion that is random in both space and time, and there are advective mass transports in all directions [34].

Between the definite regimes of laminar and turbulent flow, there is a transitional Re range. The exact values of this number range are a function of many parameters, such as channel shape, surface roughness, and aspect ratio. The transition Re is generally expected to be in the range of 1500 and 2500 for most situations [35]. For microfluidic systems, Re are typically smaller than 100 and the flow is considered essentially laminar. This characteristic has a direct consequence on mixing within microfluidic devices.

In an environment where the fluid flow is laminar, mixing is largely dominated by passive molecular diffusion and advection. Diffusion is defined as the process of spreading molecules from a region of higher concentration to one of lower concentration by Brownian motion, which results in a gradual mixing of material. Molecular diffusion is typically described mathematically using Fick's laws of diffusion [36]:

$$j = -D \frac{d\varphi}{dx}, \quad (2.3)$$

where j is the diffusion flux, φ is the species concentration (expressed in kilograms per cubic meter), x is the position of the species, and D is the diffusion coefficient (expressed in dimensions of m^2s^{-1}). For simple spherical particles, D can be derived by the Einstein-Stokes equation mass transport phenomena [37]:

$$D = \frac{kT}{6\pi\mu r}, \quad (2.4)$$

where k is Boltzmann's constant; T is the absolute temperature; r is the radius of the particles (or molecules) and μ is the viscosity of the medium. The diffusion coefficient is expressed in m^2s^{-1} (sometimes even in cm^2s^{-1}) and for a small molecule in water at room temperature has the typical value of $10^{-9} \text{ m}^2\text{s}^{-1}$ [38].

Diffusion is a non-linear process in which the time t required a species to diffuse scales quadratically with the distance x covered. A simple case of diffusion can be modelled in one dimension by the equation [39]:

$$x^2 = 2D \times t, \quad (2.5)$$

where t is the average time for particles to diffuse over the distance x . Regarding the microfluidic channel, x represents the stream width of the fluid to be mixed along the microfluidic channel. On a microfluidic length scale, the diffusion distance can be extremely small, particularly if the fluid streams are hydrodynamically focused. Because x varies with the square power, a decrease in distance dramatically reduces the time required for complete mixing. Therefore, diffusion becomes a viable method to move particles and mix fluid in microfluidic devices.

2.1.2 Mixing in microfluidic devices

At a macroscale level, mixing is conventionally achieved by a turbulent flow, which makes possible the segregation of the fluid in small domains, thereby leading to an increase in the contact surface and decrease in the mixing path. As discussed in the previous section, the Re is small in microfluidic systems, implying that hydrodynamic instability does not develop; therefore, the flows cannot be turbulent. Owing to this limitation, mixing in microfluidic devices is generally achieved by taking advantage of the relevant small length, which dramatically increases the effect of diffusion and advection, realizing efficient and fast mixing [40].

Micromixers are generally designed with channel geometries that decrease the mixing path and increase the contact surface area. According to the two different basic principles exploited to induce mixing at the microscale, micromixers are generally classified as being passive or active.

Active micromixers use external energy inputs, as well as fluid pumping energy, to introduced time-dependent perturbations that stir and perturb the fluid for accelerating the mixing process [41]. The type of external force employed by active micromixers can be further categorised as pressure field-driven [42], acoustic (ultrasonic)-driven [43], temperature-induced [44] or magneto-hydrodynamic [45]. Generally, active micromixers have higher mixer efficiency [46]. However, the requirement to integrate peripheral devices such as the actuators for the external power source into the microdevice, and the complex and expensive fabrication process, limit the implementation of such devices in practical applications. In addition, in active mixing mechanisms such as ultrasonic waves, high temperature gradients can damage biological fluids. Therefore, active mixers are not a popular choice when applying microfluidics to chemical and biological applications [47].

Passive mixing devices rely entirely on fluid pumping energy and use special channel designs to restructure the flow in a way that reduces the diffusion length and maximizes the contact surface area. Passive mixers were the first microfluidic device reported since they often entail less expense and more convenient fabrication than active micromixers, and can be easily integrated into more complex lab-on-a-chip devices. The reduction of mixing time is generally achieved by splitting the fluid stream using serial or parallel lamination [48, 49], hydrodynamically focusing mixing streams [50], introducing bubbles of gas (slug) or liquid (droplet) into the flow [51, 52] or enhancing chaotic advection using ribs and grooves designed on the channel walls [53, 54].

2.2 Microfluidic synthesis of nanomaterials

Size, shape and crystal-structure characteristics strongly affect nanoparticles' physical and chemical properties. Therefore, it is not surprising that in the production of nanoparticles a superior control of the process parameters, in order to produce material of required features, is desirable [12, 13, 55, 56]. In this respect, microfluidic reactors offer a series of potential advantages for the production of nanoparticles since they enable fine control and manipulation of the fluid and fluid interface. In microfluidic devices, the reactions are carried out in small reaction channels with diameter between a few and hundreds of microns. The small dimension, and the resulting large area to volume ratio, enables a rapid and uniform heat and mass transfer that can dramatically improve nanoparticles yield and size distribution while reducing undesirable by-product formation. In addition, the possibility of solvent

recycling, and integrated separation techniques, are likely to provide cost effective and environment friendly technology for the production of nanoparticles [57].

2.2.1 Materials and fabrication

This section outlines the most common microfabrication techniques used for the manufacturing of microfluidic reactors.

2.2.1.1 Materials

The fabrication techniques of microfluidic reactors are derived from microelectronic technology, where silicon is extensively used [58-60]. The use of monocrystalline silicon is justified because of its ready availability, the possible integration with electronic circuits and its physicochemical characteristics that are compatible with a large number of applications.

Besides silicon, glass has found also application in microreactors fabrication. Glass is a particularly favourable substrate material for microfluidic reactors because it has good optical properties, efficient heat dissipation and a high resistance to mechanical and chemical stress [61]. The most commonly used glass types in microfluidics are borosilicate, quartz and crown white glass because of their excellent optical properties and soda-lime glass. In addition, their low cost meets the economic requirement of disposable devices.

However, the main disadvantage in using glass as a substrate is its amorphous structure. This can generate non-parallel walls when it is processed using an isotropic HF wet etching technique. Because the etching process occurs on the exposed glass surface, as the channel etches deeper the walls are also etched leading to low aspect ratio channel geometries. To obtain a very deep channel, a dry etching technique such as deep reactive ion etching (DRIE) is used, but this requires expensive instrumentation [58].

The long cycle times and sophisticated equipment associated with silicon and glass microfabrication require more laborious and less accessible fabrication methods. Polymers have assumed the leading role as substrate materials for microfluidic devices in recent years [62], of which poly(dimethylsiloxane) (PDMS) has become the preferred material for the construction of microfluidic devices because it can be easily moulded and patterned into channels, can reproduce micrometer-sized features with high fidelity, is optically transparent and has low permeability to water. However, the major disadvantage of PDMS in organic nanoparticles synthesis is its organic solvent resistance; it can swell in contact with organic solvents, such as aliphatic and aromatic hydrocarbons, and even dissolve in amine and strong acids (e.g. sulphuric and

trifluoroacetic acid) [63]. Alternative polymer materials (i.e., modified PDMS, Acrylates, PEEK and COC) have recently been considered in a rapid prototyping technique to fabricate more solvent-resistant microfluidic reactors [64-66].

2.2.1.2 Fabrication procedures

Depending on the microfabrication requirements, including, type of materials and channel architecture different microfabrication techniques can be used.

Photolithography is the most accurate method to transfer a pattern to a substrate [67]. Fabrication starts by coating the substrate, usually a silicon or glass wafer, with a light-sensitive polymer film termed a photoresist. The substrate is subsequently illuminated through a lithographic mask (also called photomask) containing the desired pattern, which is generally designed using CAD software. The polymer layer is either cured (negative resist) or dissolved (positive resist) in the illuminated areas. UV light is typically used in the exposure step because one limitation of the resolution for lithographic techniques is the wavelength of the illuminating light. This physical limitation makes it advantageous to employ radiation with an even shorter wavelength, such as X-ray, or electrons as in electron beam lithography. The latter technique is a direct write method, and does not rely on a mask to define the pattern. Alternatively, a focused electron beam can be utilised with the desired pattern achieved by scanning the beam over the substrate [68]. However, photolithography is the cheapest and fastest technique.

After exposure, the uncured or decomposed photoresist is dissolved with an appropriate solvent to develop the pattern. This resist pattern can be used as a mask for further etching or employed to transfer the pattern to subsequent oxide or metal masks. The topological structure of the resist can also be used directly for replication.

After development, the resist constitutes a 2D representation of the pattern, whereas the desired structures such as flow channels are 3D. In silicon substrate microfabrication, this is usually achieved by transferring the resist pattern to the underlying silicon oxide layer using a silicon oxide etchant, such as HF (Figure 2.1). The oxide mask can subsequently be used for deep silicon etching using dry etching techniques such as reactive ion etching (RIE) or wet etching, which includes KOH or HNO_3 .

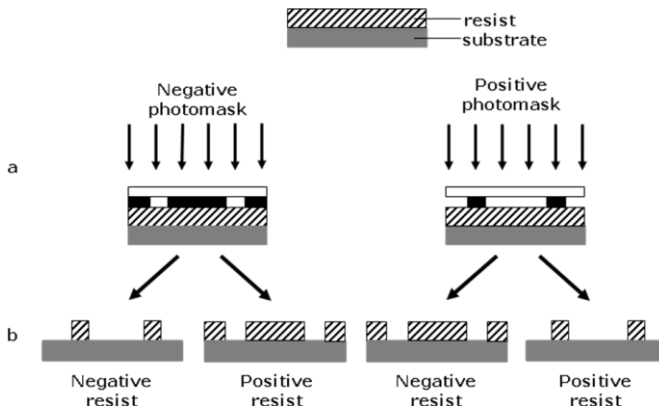


Figure 2.1 Schematic of the pattern transfer process from a photomask to a photoresist layer. (a) Exposure of the photoresist through a mask (negative or positive). (b) Development of the pattern in the photoresist layer.

RIE is a directional etching technique that is independent of the crystal planes in silicon. A series of alternating RIE etches and protective polymer depositions are used to make it possible to maintain a low undercut, resulting in almost vertical side walls [69]. Anisotropic etching can also be achieved by KOH, which is restricted by the silicon crystal planes, whereas HNO_3 results in isotropic etch profiles. In addition to silicon, early work on microfluidics often employed glass substrates, which typically are etched by isotropic wet etching, thereby restricting the obtainable etch profile.

Polymer microreplication techniques have been also frequently employed. In this case, after development of the pattern in the photoresist layer, the latter is directly used as a mold. PDMS can then be poured onto the mold and subsequently cured to obtain the final channel structure [70].

Open structures are generated from these methods, whereas most microfluidic applications demand closed channels. Open structures are sealed by bonding a lid to the surface. A thermal-based process can be used for sealing the thermoplastic material. This process simply requires heating the two parts to seal above their glass transition temperatures and then applying a force to bond them together [71-73]. However, care has to be taken not to damage the structure during the process. Another bonding method uses a dissolution process at the interface of the two slides to seal the microfluidic device. A solvent is sprayed onto the contact surfaces to locally dissolve the material. After the solvent has evaporated, the formation of chemical bonds by the interpenetration of the polymeric chains between the two parts confirms the seal [74-76].

Following a casting procedure of PDMS structures, the sealing process can be achieved in both reversible and irreversible ways. The reversible bond produces a conformal contact between the PDMS substrate and another flat surface, which involves in the formation of Van der Waals bonds. Irreversible bonding occurs after the exposure of both surfaces to air plasma. The plasma causes the oxidation of the surface of the PDMS and transforms methyl groups ($\text{Si}-\text{CH}_3$) into silanol groups ($\text{Si}-\text{OH}$), which can react with other groups on the other surface when the two come into contact. Glass, silicon and PDMS itself can all form an irreversible sealing with PDMS that can withstand pressure of the order of 35 to 50 psi (compared with 5 psi for the reversible bond) [70, 77].

2.2.2 Advantages of microfluidic synthesis of nanomaterials

The framework of classical nucleation and crystallization theory provides a useful model to describe the formation of colloidal system via wet method and for understanding the role of microfluidic environment in controlling the characteristics of the produced nanoparticles [78, 79]. Figure 2.2 showed a schematic representation of the nanoprecipitation process.

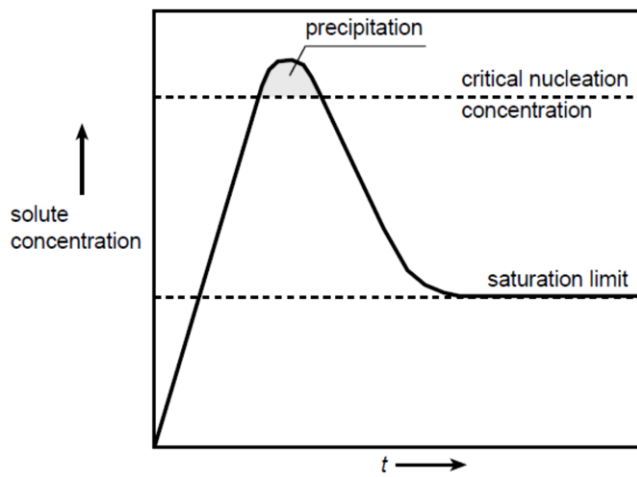


Figure 2.2 Schematic representation of the concentration relationship with the nanoprecipitation process [79].

Nanoprecipitation relies on the creation of a supersaturated solution, by means of a solvent shifting or by reaction-release guided process, that ultimately leads to the formation of a precipitate [80]. Nanoparticles formation model involves an initial nucleation phase in which seed particles, called nuclei, precipitate spontaneously and a subsequent growth phase in which the initial seeds capture the remaining dissolved

solute. The nucleation phase occurs when the concentration of the solute reaches a critical nucleation concentration in which a shower of nuclei is formed. The nucleation proceeds until the concentration of the solute falls below the critical nucleation threshold, where new nuclei cannot be formed. However, the concentration is still sufficient to allow the growth of the nuclei already formed. The growth phase proceeds until the concentration of the still-dissolved material has fallen to the equilibrium concentration (i.e., saturation limit).

In the nucleation phases, nucleation and growth occur concurrently, therefore, the earlier the nuclei are formed the larger the result nanoparticles will grow. To obtain nanoparticles batches with narrow size distribution it is important to tune the process in order to ensure that the nucleation occurs in a short period compared to the time required for the growth phase. In addition, since nucleation and growth rates depend on the supersaturation level, in order to obtain a monodisperse batch, an homogenous environment is required in terms of temperature and concentration during both nucleation and growth phases (i.e., temperature variation affect the solubility of the species, therefore the supersaturation level) [81].

Batch synthesis of nanoparticles is typically carried out in stirred flasks, where stirring is conventionally used to rapidly mix reactants and keep growing particles in suspension. Generally, during the synthesis process, the controlled addition of secondary reactants is required. In such cases, the addition rate and mixing speed often determines the presence or absence of secondary particle nucleation, homogeneity and state of aggregation of the final mixture. The homogeneity of concentration and temperature are also crucial for monodisperse particle size distributions because of the sensitivity of colloidal nucleation and morphology to local temperature and composition [79]. However, such batch-scale syntheses often involve the heterogeneous spatial and temporal distributions of concentration and temperature, as well as uncontrollable additions and mixing rates. These two factors lead to non-homogenous rate of nucleation and growth, resulting in polydisperse nanoparticles output.

Furthermore, batch synthesis tends to suffer from irreproducibility of size and quality of the nanoparticles from batch to batch. In addition, the relatively large amount of material used and the time consuming processes, further complicate screening and optimization of the synthesis condition and therefore the scale-up to batch-scale stirred flask synthesis for larger production [82].

In contrast, a series of features make microfluidic reactors particularly appealing in the production and investigation of nanoparticles as compared with conventional macroscale reactors. Most of these features derive from the unique characteristics of

the flow in microchannel and in general of the microfluidic environment, such as the omnipresence of the highly predictable laminar flow and a large surface to volume ratio. The implications and advantages, relevant to nanoparticles production, of such characteristics, are given in the following sections. Briefly, the characteristics include:

- Efficient and controllable mixing under continuous flow conditions resulting in a homogeneous reaction environment.
- Better and efficient temperature control and heat transfer.
- *In situ* monitoring of progress of nanoparticles formation through residence time based resolution.
- Temporal control of reactions by adding reagent at precise time interval during the reaction progress.
- Control of characteristics of nanoparticles by controlling the kinetics of the process.
- High-throughput screening of various formulations by on-line varying the process parameters.
- Opportunity to integrate post synthesis processes and measurement systems on a single technology platform.
- Possible scale up of the process by increasing the number of the microreactors.

The aforementioned set of characteristics reveals the significant potential of microfluidic to transform current classical batch technology for the production of nanoparticles into continuous microfluidic process. Different research groups have shown them, but clearly, this science is still in its infancy and much remains to be done in order to demonstrate the superiority of microfluidic process over the conventional batch process.

2.2.2.1 Micromixing and reactor design

The traditional batch methods lack precise control over the mixing and supersaturation level, leading to uncontrolled nucleation and growth process resulting in lack of control over final particles characteristics [83]. A rapid heat/mass transfer can greatly improve the controllability of these characteristics that in turn control the physicochemical properties of nanoparticles. In this respect, microscale reactors can provide homogeneous, fast (in the order of fraction to hundreds of ms) and

reproducible mixing condition, having the potential to represent a method to obtain nanoparticles with excellent dimensional characteristics.

Microscale mixers/reactors are characterized by a larger area-to-surface ratio offering the possibility to enhanced mass and heat transfer as compared to conventional bulk mixing systems [40, 84]. This leads to massively reduced mixing time (in the order of ms) that become comparable with the nucleation and growth kinetics, opening the possibility to exert a control on them [85].

With respect to the mixing approach and device characteristics, microreactors for nanomaterial production can be grouped in two categories: continuous flow microreactors and segmented flow microreactors.

Continuous flow microreactors

Continuous flow microreactors, compared to segmented flow reactor, are generally characterized by higher productivity and the possibility to continuously varying the reactant composition along the reactor channel [57]. The latter allows to realize multi-step process by connecting in series different reactions [86, 87]. Additionally, due to the simplicity of the flow pattern, process scale-up can be achieved by simply increasing flow rate [88]. Continuous flow microreactors can be further categorized in three main groups depending on the architecture of the microchannel network: capillary tube, coaxial flow and micromixer.

Capillary tube microreactors represent the simplest devices. They are constituted of a silica [89], steel [90] or polymer [91] capillary tubes with channel dimension in the order of microns. They have been generally applied for the production of metal nanomaterials, where an improved nanoparticles output was realized through a fast and accurate temperature control (see section 2.2.2.2 Temperature control and heat transfer). Their ease of manufacture, operation and the possibility to use robust materials, which can withstand the high temperature requirements, have attracted the attention on capillary device for the production of metal and semiconductor nanocrystals. However, capillary device suffer of problem of blockage, adhesion to channel surface, and relatively high product polydispersity [92].

In order to solve these issues, coaxial flow microreactors have been proposed [87, 92-94]. The ensheathing flow avoids the direct contact of the reaction mixture with the channel walls thus minimizing clogging and adhesion to channel walls. In addition, the ensheathing also provide a way to minimize the polydispersity by constraining the flow containing the precipitating species at the centre of the channel, where a more homogeneous velocity profile can be found. This results in more homogeneous residence time distribution (RTD) of the growing nanoparticles within the microreactor,

hence, different growing nanoparticles experience a similar growth process in term of time, with beneficial effect on nanoparticle polydispersity. The implication of RTD on microreactor-based nanoparticle synthesis is discussed later in this section (see *Segmented flow microreactors*)

A broad RTD also characterizes laminar flow micromixers. However, the possibility to integrate on chip characterization systems (see section 2.2.2.4 On-chip Integration), and realize tailored channel architectures, and the possibility to tune mixing performances, have attracted attention on the use of micromixer for nanoparticle production. Different types of micromixers, have been conveniently applied.

A basic “Y-shaped” channel configuration was used to produce nanoparticle of hydrocortisone, a poorly water soluble drug [25]. The author demonstrated the production of nano-sized dispersions, and possibility to control the mean particle size in the range of 80–450 nm by modifying the experimental parameters and design of microreactors. Using a similar set up, in a subsequent research [95], they employed artificial neural networks to identify relationships between variables affecting drug nanoprecipitation, demonstrating the critical role of antisolvent flow rate. A “T” type micromixer has been employed to prepare nanocrystals of barium sulfate and boehmite [88]. The authors, leveraging the impingement of the two streams, enhanced the mixing of the reactants, and exerted a control over nanoprecipitation output modifying the velocity of the impinging streams. The simple “T” and “Y” configurations have also been integrated with on line measurement systems to investigate the fundamental reaction processes [21] (see section, 2.2.2.3 Kinetic control and investigation), and to provide information for an in-line algorithm-based control of the process parameter, which can drive the system towards a desired goal [19] (see section, 2.2.2.4 On-chip analysis).

Wilde *et al.* [96] introduced a radial interdigitate microreactor based on the principle of parallel lamination for the production of thiol functionalized gold nanoparticles. The design was constituted of a 16 input radial interdigitate mixer, which represented a modification of the classical straight design for parallel lamination micromixer. The size standard deviations of the nanoparticles produced with micromixer ranged between 0.6 and 0.9 nm, in comparison with a range between 1.3 and 2.1 nm for the bulk syntheses. Results also indicated a control over the final mean size diameter by controlling the flow rate and, in turn, the residence time and the growth phase. Notably, the mixer was able to mix the reactants with high volumetric throughput up to $4500 \mu\text{L} \cdot \text{min}^{-1}$. Parallel lamination micromixers were also used for the production of CdS nanoparticles [18, 97]. Based on the measurement of the adsorption spectra, it was observed that the nanoparticles produced in the microfluidic device were more

homogeneous in terms of size, than those produced with conventional bulk methods. Moreover, a tendency toward the uniformity with the increase of the flow rate ratio was reported. Increasing the flow rate lessens the likelihood of nanoparticle coalescence since the nanoparticles are extracted from the reaction volume more quickly.

The use of a split and recombine (SAR) micromixers has been presented for the synthesis of metal nanoparticles [22, 98, 99], demonstrating that the mixing condition depend strongly on flow rate and local geometry. However, due to the complicate 3D architecture, the fabrication of this type of mixers might represent an issue.

In contrast, a simple planar flow focusing architecture does not require long fabrication process, and provide the possibility to control the dimension of the produced nanoparticles by simply varying the volumetric flow rates of the three inlet streams. The control over the dimensional characteristics is particularly important in the case of nanoparticles for drug delivery application since the dimension strongly influence the spatial and temporal release of the drug. Therefore, planar flow focusing architecture has been extensively applied for the production of different drug delivery carrier such as liposomes [100], solid lipid nanoparticles (SLN) [26] and polymeric micelles [29]. The use of microfluidic reactors for the production of nanoparticles for drug delivery application will be discussed more in detail in the next section (see section 2.2.3).

When high molecular weight hydrophobic species (i.e., > 45 kDa), such as poly-lactic-glycolic acid polymer (PLGA) are nanoprecipitated using planar focusing device fabricated in PDMS, they tend to aggregate on the channel walls, resulting in clogging of the device. The aggregation is caused by the adsorption of the hydrophobic species on the hydrophobic walls of the device, resulting in substantially reduces robustness of operation and, eventually, the device to irreversibly fail. A 3D focusing, in both the horizontal and the vertical dimensions, has been proposed to solve this issue [101]. The 3D focusing device did not require complicated fabrication process since it was composed of a monolithic single layer with three sequential inlets for vertical focusing, followed by a conventional cross-junction. However, since the vertical focusing was achieved through two additional streams of solvent, it caused a dilution of the initial polymeric stream resulting in a decrease of the attained supersaturation level.

A complete reactor system has been fabricated by integrating different units, around the mixing device [102]. It integrated pumps, mixer, valves, micro-heaters and temperature control. The authors reported a significant reduction of the reaction time for the formation of hexagonal gold nanoparticle that passed from 30 min to 5 min for traditional bulk and microfluidic synthesis, respectively.

Segmented flow microreactors

Alongside the laminar flow microfluidic reactors, different authors presented alternative approaches to the chemical synthesis based on segmented flow microreactors. These microreactors can be further categorized as slug flow (gas-liquid) or multiphase flow (liquid-liquid) microfluidic reactors [103, 104].

In chemical synthesis of nanoparticles, an important parameter, which strongly affects the monodispersity of the produced samples, is the residence time distribution (RTD), which reflects the mean time that each particle spends inside the reactor. In laminar flow microfluidic reactors the parabolic flow profile (fluid moving slower near the channel wall than in the centre) and the associated axial dispersion cause a variation in residence times, which in turn lead to a wider size distribution of the produced nanoparticles [105]. This problem with laminar flow reactors can be avoided with segmented flow microreactors, which lead to a better control of nanoparticle size distribution. This is because the droplets (liquid-liquid) or slugs (gas-liquid) can work as a micro-sized reactor that flows along the channel with a time that is determined only by the flow rate. Mixing in these micromixers is achieved leveraging the microstreaming created within the slug or droplet while is flowing along the straight and winding channels (see section A.1.6 Multiphase microfluidic and microdroplets based mixer).

It has been experimentally demonstrated that segmentation is beneficial in controlling the size distribution of the synthesized nanoparticles. Kahn *et al.* [105] studied the effect of the reactor design on the synthesis of silica nanoparticles. Two reactor designs were compared: (i) single phase laminar flow reactor (LFR) and segmented (gas-liquid) flow reactor (SFR) (see Figure 2.3).

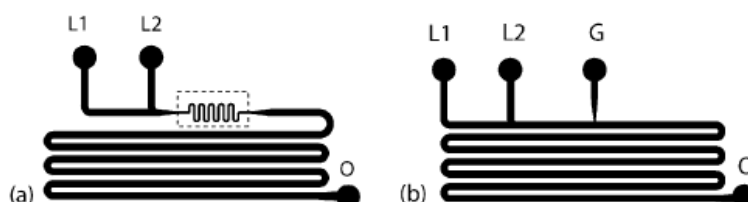


Figure 2.3 Schematics of microfluidic devices LFR (a) and SFR (b). L1 and L2 represent the liquid inlets, G is the gas inlet and O is the outlet. Readapted from [105]. Adapted with permission from Microfluidic synthesis of colloidal silica. Langmuir, 2004. 20(20): p. 8604-8611. Copyright (2004) American Chemical Society.

The size of the particles produced with LFR was found to be correlated with the residence time. Mean particle sizes increased with residence time in the reactor, as expected, because of the larger growth time available to the particles. Notably, the LFR

produced wider particle size distribution at higher linear velocity due to the steeper velocity profile, which caused higher axial dispersion of the growing colloidal particles as they flowed through the reactor. In agreement with the theory stated above, they found that the use of a SFR could minimize the axial dispersion effect, and led to a narrower size distribution of the produced nanoparticles.

Additional advantage of slug-flow reactors is the simple separation of the gas from the final reaction mixture. Therefore, they not require post processing purification step. However, careful operation and low throughput are usually required to achieve the stability of the multiphase gas-flow pattern [88].

Shestopalov *et al.* [104] reported the use of a droplet-flow (liquid-liquid) reactor, where the multiphase flow was generated from two immiscible fluids rather than from a gas liquid flow. They further demonstrated the utility of this droplet-based microfluidic method to perform a multi-step synthesis of CdS/CdSe core-shell particles. Slug-flow reactors present the problem of the physical contact of the particle with the wall of the microchannel that could result in the cross contamination and channel clogging. In contrast, microfluidic droplet based reactors represent a possible solution to this problem, since the reaction droplets are not in physical contact with the wall, but flow as droplets surrounded by the carrier fluid. An example of droplet-based microreactor was presented for the synthesis of CdSe nanocrystals in droplets flowing in a perfluorinated carrier fluid. The droplets were formed utilizing a flow-focusing nanojet structure with a steep increase in channel height [103].

The possibility to create stable droplet-flow not only provided a way to control the residence time but also allowed the opportunities for running multiphase process. Wang *et al.* [106] developed a method for the formation of TiO₂ nanoparticles using a microreactor that created a stable interface between two insoluble liquids. Two insoluble liquid systems were used in this study: 1-hexanol/formamide and cyclohexane/water. The interface between the two phases represented the site of the hydrolysis reaction between titanium tetraisopropoxide (TTIP) and water that led to the production of the titania nanoparticles. Droplet-based microreactors can also be used to implement multi-step synthesis [52] by adding additional reagent to droplets thought a droplets fusion process (see section 2.2.2.3 Kinetic control and investigation). However, the velocity of the flows must be carefully adjusted to permit the fusion of the droplets limiting the process versatility [104].

2.2.2.2 Temperature control and heat transfer

Temperature plays a critical role in controlling solubility, supersaturation and process kinetics during nanoparticles precipitation; therefore, efficient temperature control can improve nanoparticles synthesis. Typically, microfluidic devices have channels with

dimensions between 10 and 400 μm . This small dimension compared to conventional mixing systems results in an increase in the surface-to-volume ratio, to 10,000–50,000 $\text{m}^2 \cdot \text{m}^{-3}$ compared with 100–2,000 $\text{m}^2 \cdot \text{m}^{-3}$ of their macroscale counterparts [107].

Typical microfluidic devices exhibit high thermal transfer efficiencies because of their high surface-to-volume ratios, and this allows exothermic and/or high temperature reactions to be performed in an efficient and controllable (isothermal) manner [60, 108]. Microfluidic environments have been shown to provide an efficient temperature, and thereby reaction control, in continuous flow reactors chemical synthesis [107, 109].

The large surface-to-volume ratio of microreactors also offers the possibility of an accelerated heat exchange and accurate temperature control for nanoparticle synthesis. In this respect, it has been shown that only 0.4 s was needed for a 200 μm diameter channel to heat a liquid from 20 to 300 °C [110]. Nakamura *et al.* reported the use of capillary tubing in hot oil bath for the production of quantum dots. Efficient and fine temperature control of the micro-reactor was beneficial for controlling particle diameter and reproducible preparation of CdSe nanocrystals [110, 111]. By varying the temperature and the flow rate ratio, nanoparticles with different sizes were produced. In addition, the author reported a high reproducibility of particle size distribution that was considered to be caused by increased accuracy in temperature control. A method has also been reported that utilizes a three steps process in order to form CdSe-ZnS composite nanoparticles. The method involves in capillaries in heated in different oil bathes combined with a microfluidic mixer intermediate step [112].

2.2.2.3 Kinetic control and investigation

In addition to providing efficient control of the dimensional characteristics of the nanomaterials produced, microreactors also offer the possibility to investigate and control the fundamental reaction processes of the nanoparticles formation. Microfluidic devices provide a platform for the *in situ* monitoring of progress of nanoparticles formation through the ability to spatially resolve nucleation and growth phases in the reactor during synthesis [113]. Investigation of fundamental nanocrystal nucleation and growth is critical to understand how to control nanostructure synthesis on a production scale. Different techniques such as spatially resolved photoluminescence imaging and spectroscopy [21], and small angle X-ray scattering (SAXS) [114] were used to investigate kinetic and mechanistic of nanoparticle nucleation and growth during synthesis in a microfluidic reaction channel, demonstrating the capability of microreactors as investigation tools on fundamental of nanoprecipitation.

Nanomaterials synthesis in microfluidic devices takes also advantage of the unique ability of microfluidic channel to operate within continuous flow regimes that allow spatial and temporal control of reactions by adding reagent at precise time interval during the reaction progress. Such a feature endows microfluidic reactors with the ability to carrying out pre- and post- treatments and multi-step syntheses in the same reactor.

Shestopalov *et al.* [104] reported a droplet-based microfluidic method for performing multi-step synthesis of quantum dots with millisecond time-control. As can be seen from the Figure 2.4 the system is constituted of two separate and independent reaction zones that allow for the control of two different reactions or stages of the same reaction. For the production of CdS quantum dots, a mixture of CdCl₂ and mercaptopropionic acid (MPA), a solution of NaOH and a solution of Na₂S was infused through the left, centre and right inlets respectively. Droplets were formed when these aqueous streams were infused in the oil stream. The reaction was allowed to take place for 75 ms and then quenched with a stream containing MPA (from quench inlet R3). A comparison of the results obtained for the reactions with and without the quenching step indicates a decrease in monodispersity when the quenching step was eliminated. They were also able to produce CdS/CdSe core shell nanoparticles infusing Na₂Se instead MPA from the quench channel. System for growth of shell coatings with of tuneable thickness without complications of secondary nucleation has been also presented by Jensen *et al.* [115] for coating colloidal silica core particles with titania layers through controlled hydrolysis of titanium tetraethoxide (TEOT).

By controlling flow rates, reaction times and quenching procedure Kumar *et al.* [13] were able to prepare Co nanoparticles with three different crystal structures. The obtained results seem to indicate that the difference in flow rates ratio and residence time influences the nucleation phase in a critical way, leading to the production of nanoparticles with different crystalline structure. This study suggests the possible application of microfluidic device to obtain nanoparticles with different structure by controlling the process parameters, hence the kinetics of reaction. It is well known that synthesis of nanoparticles via metal salt reduction is often kinetically rather than thermodynamically controlled, leading to the possibility to generate particle in metastable phases. Control of the crystal structure is one of the key issues in nanoparticle synthesis since physical and chemical characteristics also depend directly on crystal structure [116].

The figure cannot be reproduced due to copyright issues. The figure can be find in:

Shestopalov I., Tice J., and Ismagilov R., Multi-step synthesis of nanoparticles performed on millisecond time scale in a microfluidic droplet-based system. Lab on a Chip, 2004. 4(4): p. 316-321. Figure 1.

Figure 2.4 Production of CdS quantum dots by microfluidic two steps segmented flow reactor. Schematic diagram of the microfluidic network (a) and micrograph of the microfluidic device (b).

Aqueous reagents R1, R2, and a separating stream S form droplets of the initial reaction mixture. Winding channels induce rapid mixing in droplets and initiate reaction 1. Reaction 1 is quenched when the stream of aqueous reagent R3 adds to aqueous droplets of the initial reaction mixture. readapted from [104].

2.2.2.4 On-chip analysis

Miniaturized and integrated on-chip analysis of nanoparticles can play an important role in high throughput characterization of various drug delivery formulations, accelerating the understanding of the effect and the optimization of the process parameter. On-chip detection devices are situated further downstream the nanoprecipitation zone to allow *in situ* measurements. Positioning the detection at different points along the channel also enables the collection of spatial and temporal reaction information. Unfortunately, few methods exist for the online size characterization of the particles in the channel. In traditional nanoparticle sizing, Dynamic Light Scattering (DLS) is a powerful tool for the *in situ* size analysis of nanometer structure. In addition, DLS is ideally suited to incorporate into microfluidic devices because it can be adapted to measure very small fluid samples.

Chastek and colleagues reported a microfluidic chip coupled with a DLS apparatus through fibre optic probes that delivered a quantitative measurement of micelles as small as 10 nm in diameter [28, 117]. Kuiper *et al.* [118, 119] described the use of an apparatus in which confocal correlation spectroscopy (CCS) was used for on-chip sizing of both fluorescent and non-fluorescent nanoparticles. CCS compared to other sizing techniques, such as light scattering, has the ability to measure dilute samples in small volumes. With such a device, they accurately measured particles ranging in diameter from 11 to 300 nm.

The potential of on-line characterization to offer a fast and effective way to optimize reactions based on real-time readout of particle dimensions is obvious, however, very little research has been conducted on on-chip characterization of nanoparticles, and the available information does not demonstrate a comparable result with traditional off-chip methods. In particular, both on-chip DLS and CCS provide the opportunity to on line measurement of nanoparticle size as small as 10 nm; however, this limits their application when nanoparticles with size comparable with the lower detectability limit are produced. In this respect, 100 nm limit is considered as the larger optimal size for NPs intended for cancer therapeutics applications [6].

Notably, DeMello's group proposed an improved system constituted by a microfluidic reactor to carry out the synthesis and an in-line spectrometer to monitor the emission spectra of the emergent particles [19]. The data collected were fed into a control algorithm that automatically updated, without any human intervention, the reaction conditions (flow rates and temperature) driving the system to the desired goal.

2.2.2.5 High throughput production

The use of microreactors for industrial-scale production of nanoparticles requires a large number of reactors in parallel, since each reactor provides only a small volume dedicated to reaction. Scale up microfluidic device fundamentally involves increasing the volumetric flow rate of the liquid that is processed through the microfluidic device according to the following equation [57],

$$Q = U \cdot A \quad (2.6)$$

where Q is the volumetric flow rate, U is the average velocity through the microchannel and A is the cumulative flow cross section of the microchannels. Since the practical limitation in increasing the average velocity in the microchannel, due to the increase in the pressure drop across the microchannel, generally, a scale up strategy involves increasing the cumulative flow through the cross-section of microchannels by increasing the number of microreactors. Generally, there are three level of scale-up:

- Increasing the number of channels arraying identical channels in the same lamina.
- Increasing the number of layers adding multi-layers with a channel arrays.
- Increasing the number of devices using identical device connected in parallel.

In order to achieve an efficient scale up of nanoparticles production in microfluidic channel the same flow rate must be ensured in all the arrayed microchannels. In fact, as explained in the previous section, the flow rate across the channel is important in controlling the reaction condition such as, heat and mass transfer and residence time [120]. The use of pumps for each channel can meet the requirement of uniform distribution of the flow but is not practical from the standpoint of the cost. A more reasonable strategy involved in distributing the flow from a common reservoir through the microchannels to a common product reservoir. However, the distribution of flow rate uniformly in each channel is not an easy task, and so far, only few authors have conducted investigation in this direction.

Amador *et al.* [120] studied, using a method based on electrical resistance networks, the flow distribution in arrayed microchannel for two different manifold structures called “consecutive” and “bifurcation”. They found that in the absence of channel dimensional variations the bifurcation structure always produced flow equipartition as long as the length of the straight channel after each channel bend was sufficient for a symmetrical velocity profile to develop. Commenge *et al.* [121] analyzed the influence of the geometrical dimensions of the reactor microstructure on the velocity distribution between channels, and optimize the flow distribution in a multichannel with a consecutive distribution. The results obtained were used to design a geometries resulting in uniform velocity distributions between the channels for single-phase flow.

2.2.3 Nanostructured biomaterials produced by microfluidic approaches

In the past decade, there has been a tremendous interest in the development of microfluidic methods for chemical synthesis of inorganic nanoparticles for the production of nanocrystalline semiconductors with tuneable size and uniform distribution of size [12]. However, there has been much less study on microfluidic methods for organic nanoparticles and colloidal system production.

The reason for the investigation of such type of materials mainly stems from their possible use as innovative pharmaceutical formulations able to increase, in different

ways, the efficacy of poorly soluble drugs. Table 2.1 lists the recent studies about production of organic nanoparticles by microfluidic approaches.

Table 2.1 List of recent studies about the use of microfluidic technology for organic nanoparticle formation.

Materials of reactor	Mixing strategy	Produced nanomaterial	Year of publication	Ref.
Teflon	T-junction multiphase	DPA nanoparticle	2007	[122]
PDMS/glass	HFF	PLGA-PEG PMs	2008	[29]
Teflon	Y-shaped mixer	Hydrocortisone nanoparticles	2009	[25]
Silicon	HFF	liposomes	2007	[123]
Silicon	HFF	liposomes	2004	[100]
Steel plate	HFF	SLN	2009	[26]
Steel plate	HFF	SLN	2008	[124]
PDMS	HFF	Alginate nanoparticles	2008	[125]
Silicon	HFF	liposomes	2010	[126]
PDMS	HFF	polymerosome	2010	[127]
Silicon	HFF	niosome	2010	[128]
PDMS/glass	HFF/Tesla mixer	Lipid-polymeric nanoparticles	2010	[129]
PDMS/glass	HFF	PLGA-PEG PMs	2010	[130]
PDMS/glass	3D HFF	PLGA-PEG PMs	2010	[101]

DPA: 2,2'-dipyridylamin

PLGA-PEG PMs: poly(lactide-co-glycolide)-b-polyethyleneglycol (PLGA-PEG) block polymeric micelles.

HFF: hydrodynamic flow focusing

SLN: solid lipid nanoparticles

The group of Yao reported a novel method of generation of solid lipid nanoparticles (SLN) using a flow focusing strategy [26, 124]. Solid lipid nanoparticles are a drug delivery system constituted of biodegradable physiological lipids or lipid substance and represent an alternative drug delivery system of the above cited liposomes and polymeric nanoparticles [131]. The microfluidic method presented involves in the precipitation of nanoparticles from a solution of lipid in water miscible solvent when it is brought in contact with two lateral aqueous streams. Using this strategy, the authors were able to produce SLN, with an almost spherical shape, in a range of mean diameters between 100 and 200 nm by simply varying the flow rate ratio of the two phases.

Ali and colleagues [25], recently reported a microfluidic strategy, based on and Y-shaped micromixer for the preparation of hydrocortisone nanosuspension through a nanoprecipitation technique. A relatively stable aqueous hydrocortisone nanosuspension was obtained, with nanoparticle dimension being controlled by flow rate and design of microfluidic reactor.

The production of drug carriers, such as liposome [123], niosomes [128] and polymeric micelles (PMs) [29], produced through the self-assembly of amphiphilic molecules (phospholipids, non-ionic surfactants and block-copolymer, respectively) were also investigated. As can be seen from Table 2.1, for the production of nanoparticles from the self-assembly of amphiphilic molecules, hydrodynamic flow focusing (HFF) represents the preferred approach since it provides an easy way to control the mixing time, hence the aggregation kinetics of the produced nanoparticles. Generally, a solvent exchange process triggers nanoprecipitation of such type of nanoparticles, where organic solutions of the amphiphilic molecules is mixed with a non-solvent (i.e., generally water).

The aggregation of amphiphilic molecules to form nanoparticles slightly differs from traditional nucleation and crystal growth that guide the nanoprecipitation of non-amphiphilic molecules (such as inorganic material and hydrocortisone) [132]. In the nanoprecipitation process of non-amphiphilic molecules, the size of the obtained nanoparticles is mainly controlled by the level of supersaturation of the solute to be precipitated, and on the time associated with the precipitation process. These two parameters can be controlled in microfluidic devices varying the relative flow rate ratio of the solvent and non-solvent stream and the residence time distribution (RTD) respectively, as demonstrated by other researchers [25, 104, 115]. In contrast, the size for nanoparticles from amphiphilic molecules is dictated by the magnitude of the steric and electrostatic interaction between the amphiphilic molecules that is controlled by the polarity of the surrounding solvent environment (i.e., solvent vs. non-solvent ratio) [8, 126, 132, 133]. As the mixing between solvent and non-solvent proceeds, the

polarity of the environment surrounding the amphiphilic molecules increases (i.e., increase in water content), and forces the closure of the growing nanoparticles to minimize the exposure hydrophobic portion with water. As a result, an insertion barrier is created that prevents new amphiphilic molecules from entering inside the closed nanoparticles, resulting in kinetically quenching of the growth phase [8, 132, 133].

HFF based reactors provide the possibility to varying the mixing time by varying the width of the focused stream. This gives opportunity to control the rate of solvent shift, and exert a control over the length of the aggregation time before the formation of kinetically quench nanoparticles. This ultimately results in a control on the nanoprecipitation process, resulting in controlled and tuneable characteristics of the produced nanoparticles. More details on the aggregation mechanism of polymeric micelles and its relation with mixing time are given in section 2.3.3. It is important to note that when drug and amphiphilic molecules are co-precipitated the two mechanisms of aggregation, for amphiphilic and non- amphiphilic molecules, act in concert to determine the nanoparticle characteristics (see Chapter 5)

The group of Locascio first reported the synthesis of liposomes by microfluidic approach [100, 123]. Liposomes are composed of a lipid bilayer usually made of phospholipids, which are extensively used as a drug and DNA delivery system. The bulk hydration of lipids in aqueous buffer generally yields large, polydisperse and multilamellar liposomes (i.e., constituted of more than one lipid bi-layers concentrically organized as an onion-like structure). This method and other traditional liposome production bulk methods, such as freeze-thaw cycling, film hydration and reversed phase evaporation, often lead to heterogeneous and uncontrolled chemical and mechanical conditions during liposome formation, and result in non-uniform liposomes in both in size and lamellarity.

Liposomes can be formed by microfluidic methods by spontaneous self-assembly from a solution of dissolved phospholipids triggered by a diffusion driven process [126]. The liposomes are formed by a diffusively driven process when a stream of lipids dissolved in an organic solvent such as isopropyl alcohol (IPA) is hydrodynamically sheathed between two oblique buffer streams in a microfluidic channel. The laminar flow conditions facilitate diffusive mixing at the two miscible liquid interfaces, predictably diluting the alcohol concentration below the solubility limit of lipids and initiating lipid self-assembly into small unilamellar vesicles (SUV).

The authors reported the production of liposomes with a mean size diameter varying from 50 to 150 nm by adjusting the ratio of the solvent to buffer volumetric flow rate. In other recent publications [123, 126], they examined the mechanisms that controlled

liposome size and homogeneity by modifying their microfluidic design. The deep channels of higher aspect ratio with a rectangular cross-sectional area led to a more homogeneous velocity profile across the channel height and reduced the impact of surface effects at the bottom and top of the channel. Using microfluidic techniques to produce liposome formulations of monodisperse distributions, whose size can be controlled by adjusting the fluid flow rates in the microfluidic network, was further demonstrated [126]. These studies clearly showed that nanometer-sized liposomes with a very narrow size distribution could be produced using microfluidics and potentially open applications for on-demand liposome-mediated delivery of point-of-care personalised therapeutics.

Recently the same group also presented a similar strategy for the production of niosome, or synthetic membrane vesicles formed by self-assembly of non-ionic surfactant in a mixture with cholesterol and dicetyl phosphate [128]. Notably, the author reported an effect of the microreactor dimension in controlling the niosome dimension. Specifically, wider microchannel geometry led to larger niosome as consequence of an increase in the diffusive mixing time. Thiele and colleagues [127] reported a microfluidic strategy being able to produce polymersomes over a wide range of sizes from 40 nm to 2 μm .

Similar focusing enhanced diffusion process was employed by Karnik and Gu for the production of PLGA-PEG block copolymer nanoparticles (or PMs) [29]. According to the mechanism of self-assembly of block copolymer nanoparticles [132, 134] (see section 2.3.3, aggregation kinetics), the results showed a decrease in nanoparticles size and increase in homogeneity with a decrease in mixing time. Notably, the nanoparticles showed a decrease in size as the relative flow rate of the polymer stream decreased and no break point was detected, even when the mixing time was considerably lower than the aggregation time to produce kinetically frozen polymeric micelles. The author hypothesized that the results might be related to the time scale of self-assembly of the nanoparticles. The role of microfluidic mixing in controlling the size of polymeric micelles will be discussed in the results section (see chapter 3-5).

An alternative method, based on the formation of droplets of polymeric solution, was developed for the production of alginate nanoparticles. The method differed from the others in that the diffusion process was not used to create a supersaturation state that normally triggers the particle aggregation and precipitation; instead it used the diffusion to shrink the drops and condensate of the polymer phase [125].

2.3 Polymeric micelles for drug delivery

Synthetic polymers are ideal tools for drug delivery because they are highly versatile in terms of composition and architecture, thereby, allow for the production of tailor made drug delivery systems. During the past decades, polymeric drug carriers, such as polymeric drug conjugate and PMs have proven to be useful in drug delivery, and several formulation have been studied in clinical trials [135, 136]. PMs are a class of polymeric nanoparticles with a core-shell structure that are usually spontaneously formed by self-assembly of block copolymers in a liquid, generally as a result of hydrophobic or electrostatic interactions between polymer segments. As drug carriers, PMs present a number of appealing features that make them one of the most promising drug and gene delivery systems [137, 138].

- Efficient solubilising capacity for hydrophobic and poorly water-soluble molecules that stems from their unique core-shell structure.
- The small size (generally up to 150 nm) endows PM with the ability to freely circulate in the blood stream after injection.
- Long circulating properties, which stems from the steric hindrance afforded by the presence of hydrophilic shell and the small dimension.
- Passive targeting in solid tumour and inflammation sites by the so-called enhanced permeability retention effect (EPR).
- Targeting and controlled release of drugs by functionalization of the outer surface.

2.3.1 Composition and structure

PMs are created by spontaneous self-assembly of individual polymeric chains, called unimers, which are synthetic amphiphilic di-block or tri-block copolymers. PMs are usually spherical shaped nanoparticles, with a core-shell structure and dimension typically ranges between 10 and 300 nm (see Figure 2.5) [137].

The inner compartment, represented by a hydrophobic core (micelle core), acts as a reservoir in which the biological active molecule can be retained by means of chemical (micelle forming polymer-drug conjugates), physical or electrostatic interactions (polymeric micelle nanocontainers). The external compartment (shell), represented by a hydrophilic corona, provides interactions with the solvent or biological media and makes the nanoparticles stable in the aqueous environment [139, 140].

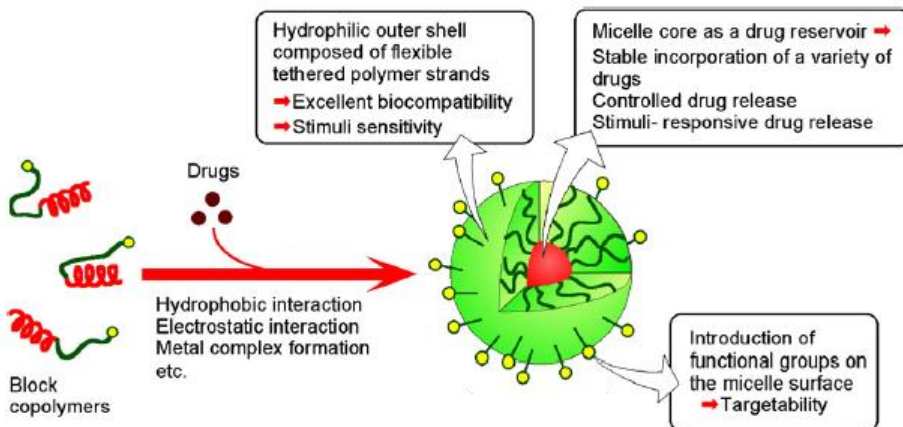


Figure 2.5 PMs as drug delivery systems. Schematic of the structure and salient features. Data readapted from [137]. Reprinted from Pharmacology & Therapeutics , Nobuhiro Nishiyama,Kazunori Kataoka, Current state, achievements, and future prospects of polymeric micelles as nanocarriers for drug and gene delivery, Pages No 630-648, Copyright (2006), with permission from Elsevier.

The process of self-assembly of amphiphilic block copolymer in water is based on hydrophobic interaction between the lipophilic core-forming blocks. The process is concomitantly driven by the so-called hydrophobic effect, which leads to a gain in entropy of the solvent molecules as the hydrophobic polymer segments segregate in the core and withdraw from the aqueous environment. The gain in entropy of the system can be theoretically explained since it is more entropically favourable for the hydrophobic parts to pack together than for water to order itself around each one separately in solution [141-143].

In order to avoid polymer accumulation in the body, micelles should be composed of either biodegradable components (poly-ester) or unimers that undergo renal excretion and therefore with a molecular mass up to 40 kDa. So far, the most commonly used hydrophilic forming blocks are represented by poly (ethylene oxide) (PEO) – also known as poly (ethylene glycol) (PEG) - chains with a block length typically between 1 and 15 KDa [10]. PEG is one of the most used because of its physicochemical characteristics, including high water solubility and significant chain mobility as well as its low toxicity. The PEG blocks prevent micelle opsonisation thus reducing micelle recognition by the reticulo-endothelial system (RES) cells (stealth properties), which enhances plasma residence time and provides, in this way, a passive targeting toward tumours via the enhanced permeability and retention (EPR) effect [144].

The core forming blocks polymer employed for drug delivery purposes are generally constituted of polyesters, polyether a poly (amino acid) derivatives [137, 139, 141, 145-148]. Polyester, such as Poly (lactic acid) (PLA) and poly (ϵ -caprolactone) (PCL), are biocompatible and biodegradable polyesters approved by the FDA for biomedical applications in humans. Poly (L-aminoacid) (PAA) based blocks, such as poly (aspartic acid) (PAsp), poly (glutamic acid) (PGlu), are particularly attractive because of their biodegradability, biocompatibility and structural versatility. By varying the chemical structure of PAA, it is possible to tailor their enzymatic degradability and degree of immunogenicity [149]. In addition, non-degradable polymer, such as polyethers, can be conveniently used for the production of PMs. Most of the polyethers of pharmaceutical interest belong to the Poloxamer family, also known as Pluronic®, that are constituted of tri-block copolymers in which the central hydrophobic block is poly(propylene oxide) (PPO) (see section 3.1.1) [145].

2.3.2 Micelle preparation and stability

The self-assembly of amphiphilic block copolymers is a thermodynamically driven, and reversible process, that starts when copolymer concentration reaches some specific value called the critical micelle concentration (CMC). At concentrations below the CMC, copolymer molecules exist in aqueous solutions as individual molecules (unimers). The CMC is primarily influenced by the length of the hydrophobic block; the longer it is, the lower the CMC. However, other parameters such as chemical nature and length ratio of hydrophilic and hydrophobic block also influence the CMC even though to a less extent. At room temperature for PEG-polyester and PEG-PAA copolymers the CMCs values range between 10^{-7} and 10^{-6} M, while for Pluronic copolymer the values range between 10^{-5} and 10^{-3} M [10].

The CMC value defines the thermodynamic stability of PMs. A micelle, in fact, is thermodynamically stable relative to disassembly to single chains in pure water if the total copolymer concentration is above the critical micelle concentration (CMC)[150]. The latter is a parameter of dramatic importance in drug delivery applications in which, during intravenous injection, PM dispersion undergo a dilution by circulating blood (usually about 25-fold dilution at bolus injection). However, even if a micelle system is below its CMC, it may still be kinetically stable and survive at least for some period of time after injection, if the core forming block has a T_g (glass transition temperature) above physiological temperature [150, 151]. Usually the latter are said to be PMs with “frozen core” referring to the scarce fluidity of the core. In addition, even the size of the hydrophobic block, and mass ratio of hydrophilic to hydrophobic blocks, have an effect on the kinetic stability of micelles. In general the bigger the core forming block,

the greater is the stability of PMs [150]. In order to stabilize PMs against premature dissociation, some author have proposed a strategy based on the induction of hydrogen bonds in the micelle core [152] or by cross linking either the core or the corona forming block [153, 154].

PM production and encapsulation of the drug in the micelle core nanocontainers is usually accomplished through one of the following methods of encapsulation:

- In dialysis methods the encapsulation is carried out through the dissolution of block copolymer and drug in a water-miscible organic solvent (such as THF, DMSO, DMF) followed by the dialysis of this solution against water. The gradual replacement of the organic solvent with water triggers the self-association of block copolymers and the entrapment of drug in the assembled structures [155].
- Oil in water emulsion method. This method is carried out by dissolving the drug in a volatile water immiscible organic solvent. The polymer can be dissolved in either organic or aqueous phases. Eventually the organic phase is added to the aqueous phase and the organic solvent is removed by evaporation [156].
- Solvent evaporation method is based on dissolving the drug and polymer in a volatile organic solvent and the complete evaporation of the organic solvent leading to the formation of polymer/drug film. This film is then reconstituted in an aqueous phase by vigorous shaking [149].
- Freeze-drying method involve in the use of a freeze-dryable organic solvent such as tert-butanol to dissolve the polymer and drug. This solution is then mixed with water, freeze dried and reconstituted with isotonic aqueous media [157].

2.3.3 Aggregation kinetics

Self-assembly of block copolymer nanoparticles during nanoprecipitation is currently believed to occur in three stages (see Figure 2.6) [132, 158].

In the first stage, the formation of a supersaturate solution above the CMC, caused by the solvent quality jump, leads to the initial nucleation of several unimers. In the second stage, the nascent nanoparticles grow in size, either by addition of more unimers and fuse of existing particle, through a diffusion-limited mechanism. This step ideally proceeds until a critical size, which corresponds to an overlapping brush corona, is reached, and either inter-particles fusion or addition of more unimers

becomes energetically unfavourable. Therefore, the end of the second stage results in kinetically frozen nanoparticles. The third step is characterized by small changes in the nanoparticles dimension due to exchange of unimers in order to reach the equilibrium [158]. In this last step, the remaining unimers must fuse to create new particle or find particle with low insertion barrier.

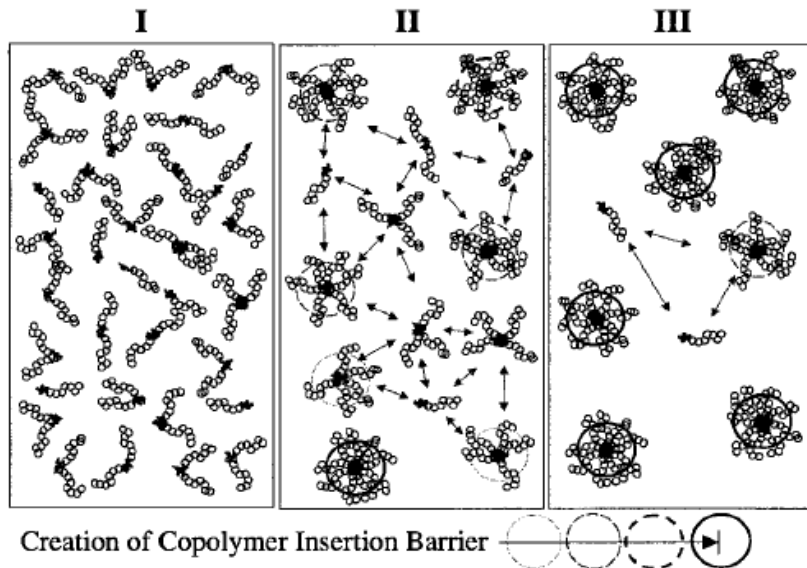


Figure 2.6 Mechanism of self-assembly of block copolymer PMs. Nucleation of block copolymer unimers (I), Fusion of existing particles and growth (II) and formation of overlapping brush corona that result in kinetically frozen nanoparticles (III). Readapted from [132]. [Reprinted figure with permission from: Brian K. Johnson and Robert K. Prud'homme, Physical Review Letters, 91, 118302, 2003. Copyright \(2003\) by the American Physical Society.](#)

The solvent quality affects the size of the particles by changing the critical aggregation size. Therefore, the nanoparticles size is expected to depend on the time scale associated with the jump of the solvent, τ_{mix} . The mixing time, τ_{mix} , gain importance if related to the time scale associated with block copolymer aggregation, τ_{agg} . The ratio between the two time scales is expressed as the Damkohler number (Da),

$$Da = \frac{\tau_{\text{mix}}}{\tau_{\text{agg}}} . \quad (2.7)$$

When $Da < 1$, the mixing occurs faster than the time scale associated with the nanoparticles aggregation. Therefore, the nanoparticles size is expected to become independent of the mixing time and polymer concentration. This results in nanoparticles with a characteristic dimension represented by the critical size, which corresponds to the creation of an overlapping brush corona. The nanoparticles are also expected to be more homogeneous than that produced with slower mixing.

Conversely, for $Da > 1$ the size of the produced nanoparticles increases with increase in either mixing time or polymer initial concentration as demonstrated by Johnson and colleagues [132]. Notably, the polymer concentration can affect the characteristic aggregation time since the concentration influences the length scale between the molecules and then the diffusion time as illustrated in Figure 2.7.

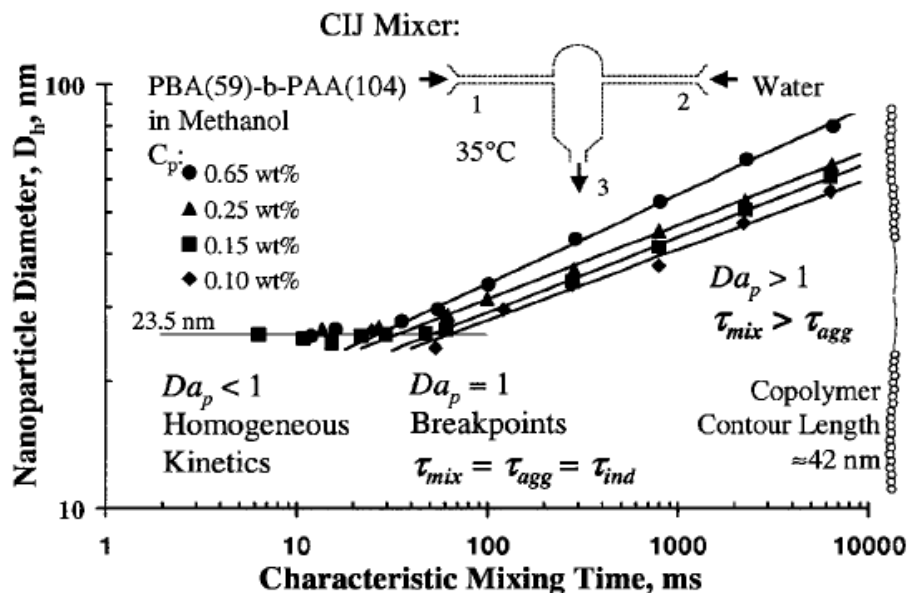


Figure 2.7 Dependence of nanoparticle mean diameter on polymer concentration and mixing time. Data readapted from [132]. [Reprinted figure with permission from: Brian K. Johnson and Robert K. Prud'homme, Physical Review Letters, 91, 118302, 2003. Copyright \(2003\) by the American Physical Society.](#)

The model described above for the aggregation of block copolymer nanoparticles is similar to the classical nucleation theory describe in the previous section. The main difference is the truncation of the growth process when an overlapping brush corona is formed that leads to a kinetically frozen nanoparticles. When $Da < 1$, The formation of the overlapping corona preclude the increase of the size of the formed nanoparticles, blocking the growth step and making the size independent from the initial concentration. The latter is fundamentally in contraposition with the classical nucleation theory in which the size of the produced nanoparticles depend on the initial concentration of the compound and on the length of the growth phase.

2.3.4 Drug solubilisation and release

Effective application of many existing drugs can be frustrated by their poor water solubility. Conventional solubilising agents, such as Cremophor® EL, usually exert toxic effect including hypersensitivity reactions [159]. In this regard, the development of efficient and safe solubilising agents is of great importance. The unique core-shell structure of amphiphilic block copolymers micelles can greatly affect the aqueous solubility of compounds by providing a hydrophobic reservoir where the drug can partition.

In recent years, PMs have been the focus of much interest as alternative vehicles for the solubilisation of poorly water-soluble molecules [160], especially anti-cancer drugs (e.g. paclitaxel [161-163] and doxorubicin [164, 165], rendering clear advantages over current solubilising agents in drug delivery [7]. The literature on PMs as solubilising agent underlines the importance of selecting an appropriate core forming block polymer in order to enhance the loading capacity of the system [166, 167]. The degree of compatibility and interaction between the core forming polymer and the drug in fact is the most important parameter in controlling the loading efficiency [150]. In this respect, Liu *et al.* [168] developed a theoretical approach, based on partial solubility parameters of polymers and drug (calculated by a group contribution theory) to predict the extent of polymer drug compatibility.

The mode of drug release from PMs mainly depends on the design used for the preparation of the PMs. Drug release, from sufficiently stable PMs, mostly depends upon the rate diffusion of drug from the micellar phase. Differently, in the case of PMs drug conjugates, also the rate of drug cleavage from the unimers has to be taken in consideration [169]. Beside the loading capacity, the strength of the interactions between the drug and the core-forming block also influences rate diffusion of the drug out from the PMs and in turn the kinetic of the release [170]. In general, the stronger the interaction between the drug and the core-forming block, the slower the release of the drug from the micelle. Other factors, such as the physical state of the micelle core and the localization of the drug within the micelle, can also influence the release rate. The movement of a drug in a glass-like core (the core forming block has a T_g above the physiological conditions) is slower in comparison to the movement of a drug in a more fluid core, therefore, even the diffusion rate is slower as demonstrated by Teng and colleagues [171]. Finally, the release rate of the drug is largely related of the localization of the drugs molecules within the micelle. Depending on its partition coefficient the incorporated drug may lie in the core, at the interface between the core and the corona or even within the corona. Drugs localized at the interface and within the corona are released in more rapid way while the drugs localized within the core are released with a slower kinetics [171].

2.3.5 Drug targeting

One of the main goals of nanomedicine is to provide a safe and effective drug carrier being able to selectively delivery their payload to tumour cell avoiding damage to the healthy tissue. Spatial control of the drug release (also referred as targeting) has been achieved with different strategy comprising: passive and active targeting, and stimuli responsive release. Passive targeting is exploited by the enhanced permeation retention (EPR) effect, while active targeting is provided by surface functionalization of the carrier with ligands that can specifically recognize tumour cells. Stimuli responsive release relies on a biological (i.e., pH) or external signal (i.e., ultrasound and temperature) to release the drug within the tumoral extracellular environment to facilitate drug uptake upon arrival at the target tumour site.

2.3.5.1 Passive targeting via EPR effect

PMs are considered to be one of the most promising delivery system for drug targeting in cancer therapy since their capability to passive accumulate in the tumour cell via the so called enhanced permeability and retention (EPR) effect [137, 142, 169, 171, 172]. Notably, the EPR effect has been also observed in inflammatory tissues providing a clue for the use of PMs even for treating inflammatory diseases.

Tumour tissue is characterized by the high rate of vessels growth with poorly aligned endothelial cells with wide fenestrations. Depending on the tumour type, the dimension of the gaps between the endothelial cells within the tumour tissues is between 380 nm and 1.2 μ m. This value is much higher than the gaps observed in the vessels of the normal tissues that are about 7 nm [173]. This impressive difference in the vessel fenestrations is the foundation of the enhanced accumulation of PMs in the tumour tissue (see Figure 2.8).

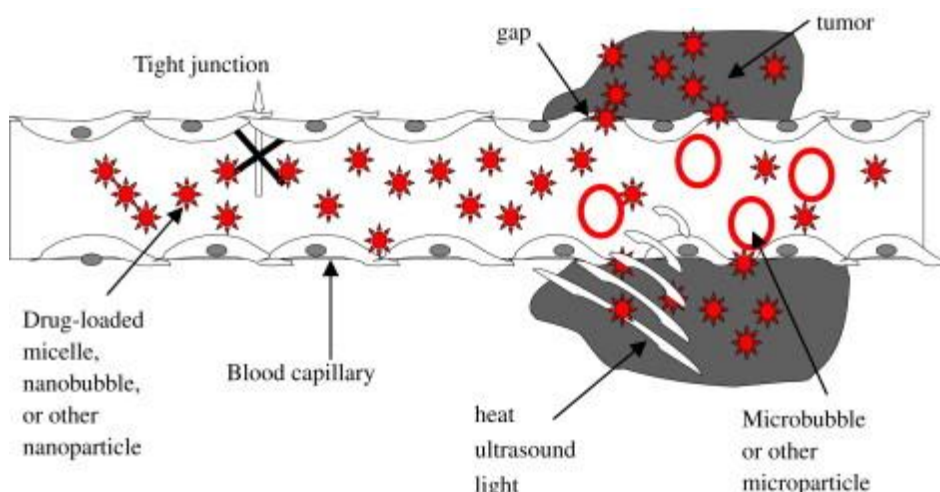


Figure 2.8 Scheme of permeability and retention (EPR) effect and the implication in tumour passive targeting thought the vascular abnormalities of tumour vessels. readapted from [10].

[Reprinted from Progress in Polymer Science, 32, Natalya Rapoport, Physical stimuli-responsive polymeric micelles for anti-cancer drug delivery, 962-990, Copyright 2007, with permission from Elsevier.](#)

The vascular abnormalities of tumour vessels is typically coupled with the low lymphatic drainage of tumour tissue, that prolongs the residence time of nanoparticles in the tumour volume, leading to an enhanced accumulation of nanoparticles in the solid tumour tissue [174].

In order to take advantage of the EPR effect and to lever the vascular abnormalities, drug carrier must be design in order to minimize the recognition of the immune system and have long blood circulating properties. Long circulation property (ideally over 6 h) is of primary importance since the extravasations is generally considered to be slow and passive process [138, 175].

In this respect, size characteristic of the drug carrier are of primary importance since has been demonstrated that tumours blood vessel can be permeable to particle up to 400 nm in diameter [176]. On the other hand, renal system is capable of filtering particle smaller than 10 nm [177] and a diameter of less than 150 nm is required to avoid spleen recognition[178]. These considerations restrict the ideal dimension for an efficient drug carrier between 10 and 150 nm [126, 176, 179, 180]. It is worth of notice that beside clearance rate, carrier size also affects the biodistribution in healthy organs [179], therefore PMs size must be considered when specific organ toxicity of the drug is demonstrated.

In addition to the size effect, physicochemical characteristics of the carrier also play a crucial role in prolonging the blood circulating properties. In this respect the presence of a PEG shell around the nanoparticle provides a method to hidden nanoparticles from reticulo-endothelial system (RES) which destroy any foreign material through opsonisation and phagocytosis [179, 181].

2.3.5.2 Active targeting

Modification of PMs with specific ligands to cancer cells results in selective binding and local retention of them in tumour tissues. In cellular specific targeting, a moiety (ligand) direct to a specific receptors over expressed on the surface of cancer cells, is conjugated at the end of the hydrophilic segment and extend outwards from the PMs shell ready to interact with their specific receptors [182-184]. The presence of ligands affects the biodistribution of the PMs and promote specific micelles uptake by the target cells through receptor-mediated endocytosis. Since ubiquitary expressions of

folate receptor on cancer cell, folate molecules has been conjugated with the corona forming block in order to provide molecular targetability. Result from the investigation of Bae *et al.* [182] demonstrated that the use of the folate-conjugated micelles may lower the effective doses over free doxorubicin, improving the safety of the clinical chemotherapy. In addition, micelles can also be conjugates with antibodies direct against tumour specific antigens [185, 186].

2.3.5.3 Stimuli-responsive polymeric micelles

Besides to the targetability to specific tissues, provided by the conjugation to specific moieties recognized by receptors expressed by cancer cell, “smart” PMs that release the drug as a response to a specific chemical or physical stimuli have been proposed to possibly enhance the therapeutic efficiency, and reduce the side effect of the drugs. Interstitial fluids in tumours are characterized to have a lower pH than that in normal tissues (6.75 against 7.25) [187]. In addition, cellular compartment such as endosomes and lysosomes, exhibits even a lower pH values (pH 5.0–5.5). These environmental characteristics can be lever creating pH responsive PMs that are capable of dissociating in response to decreased pH levels and in turn increase the release of the loaded drug [188, 189]. Beside the pH responsive PMs, other authors have proposed the use of different types of intracellular signals such as glutathione [190, 191] and specific enzymes [192] for designing environmental responsive PMs.

Other drug delivery systems are designed in order to release the drug in response to external stimuli. Different authors proposed the use of thermo-responsive PMs that react to a change of temperature of the environment with structural change that trigger the release of the drugs [153, 193, 194]. These types of drug delivery system required an external source for the local heating of the tumours that is generally achieved by the use of continuous wave ultrasound. Ultrasounds have been successfully applied also to trigger the release of ultrasounds responsive micelles [195, 196]. In addition, the mechanical action exerted by the ultrasounds perturbs the tumour cell membrane enhancing the intracellular drug uptake. Taken together the two effects result into an effective tumour targeted drug delivery and, therefore, to an effective suppression of the tumour growth.

Summary of the literature review

The recent development of microfluidic and lab-on-a-chip technologies has conclusively demonstrated that such miniaturised systems offer many advantages over conventional macroscale mixers/reactors in achieving controllable, informative-rich, high throughput and environmentally friendly processes [60]. This can be largely attributed to the key feature of microscale channel networks within such microdevices. When scaling down the operation space dimensions (compared with the conventional macroscale system) they not only reduce the sample volume, but also bring unique characteristics to the microscale fluidic environment, where the spatial and temporal control of reagents is achieved under a non-turbulent, diffusive mixing regime.

Compared with conventional macroscale batch systems, the microscale production of nanoparticles using microfluidic technology has unique operating characteristics and advantages. Firstly, it offers a laminar flow environment where diffusion dominates mass transfer. Laminar flow is the simplest flow structure and enables the flow to be modelled and controlled precisely. Secondly, a short and highly controlled mixing time can be easily achieved in the microscale synthesis system. In a microchannel with a width of a few tens of microns, where the mass transfer is dominated by diffusion, millisecond mixing times can be achieved based on a molecule's diffusion across the channel. This sub-second mixing time is believed to be important in the formation of nanoparticles, especially in the early stages. Through careful selection of flow rate and geometry, this mixing can be highly controlled. Thirdly, the microscale system provides a high surface-to-volume ratio. This feature, associated with small volumes, offers rapid heat transfer to achieve thermal homogeneity throughout the entire reaction volume, which is crucial to obtain monodisperse particles. Finally, the ability to manipulate reagent concentrations and reaction interfaces in both space and time within the channel network of a microreactor provides a high level of reaction control unattainable in conventional bulk reactors.

Owing to the possible theoretical advantage provided by the use of microfluidic reactors, over the past decade, there has been tremendous interest in the development of microfluidic methods for the production of inorganic nanoparticles such as nanocrystalline semiconductors with uniform and tuneable distributions of size [12]. The result obtained clearly demonstrated the superior control of microfluidic environment for the production inorganic nanoparticle respect to conventional bench

systems. However, there has been much less study on microfluidic methods for organic nanoparticle synthesis.

The development of new strategy for organic nanoparticle production stems from the extensively use of these nanosized products to deliver a wide range of pharmaceutically and diagnostic active compounds such as drugs, genes and imaging agents [1, 140, 169]. There is an increasing interest in nanomedicine since the bioavailability at the target site, and therefore efficacy, of many pharmacological active compounds can be significantly enhanced by their formulation as nanosized product relative to the conventional pharmaceutical formulation. This is achieved by increasing either the solubility of the bioactive compound [197] or the accessibility at the target site [198]. Furthermore, the possible targeting, either passive or active, of the bioactive compound to a specific site can greatly reduce side effects, with an undeniable improvement of both therapeutic activity and patient compliance [3].

From a drug delivery point of view, nanodispersed polymeric systems are attracting significant interest with regard to the control of the spatial and temporal kinetics of drug release at the site of action, which is key to achieving an optimal pharmacological effect [162]. However, the dimension, polydispersity and batch-to-batch size variation of PMs produced with conventional procedures produce undesirable variation in the rate of particle degradation and kinetics of drug release. In this regard, microfluidic technology can offer the potential to develop a method for precise and predictable and more industrially acceptable production of PMs (or colloidal system) [29, 126].

Thus, this study aims to develop a microfluidic-based strategy for the controlled production of PMs and address the effect of the various experimental parameters that control product output. A hydrodynamic mixing strategy has been applied and Pluronic® block copolymer and β -carotene have been utilized as a model polymer and active compound, respectively. In the first stage, PM production experiments were carried out to investigate the feasibility of the production method and to investigate the effect of flow rate ratio, polymer concentration and device dimension, on PM mean size and size distribution. Then a numerical simulation of the advective and diffusive transport within the microfluidic reactors was used to correlate our experimental findings with the hydrodynamic present during PM formation. Following the production of PMs, the use of microfluidic-based nanoprecipitation was investigated to encapsulate a therapeutically interesting drug, mithramycin, within PMs.

The assemble mithramycin drug-encapsulated PMs has been investigated in a statistical fashion in order to understand the effect of different production parameters, such as drug concentration and flow rate ratio, on the encapsulation efficiency and

dimension of the produced PMs. Finally, the produced micelles were *in vitro* analysed for antiproliferative and differentiation activity.

Chapter 3

Production of PMs in microreactors

The general production strategy applied for PM production is based on a nanoprecipitation process within the microfluidic environment. In this chapter, the production of empty (i.e., without drug loading) is first presented. It has been demonstrated that microfluidic environment improves control, reproducibility, and homogeneity of the size of the produced PMs. The relationship between polymer concentration, flow rate ratio and microreactor dimension and the size of PMs produced in continuous flow microreactors has been analyzed.

3.1 Introduction and general considerations

3.1.1 Polymers

Among different types of block copolymers that can be used for the production of PMs (see section 2.3.1 Composition and structure), the study focused on the use of Pluronic® block copolymers. Pluronic® block copolymers, also known as “Poloxamer”, are a well-studied class of commercially available (from BASF corp.) tri-blocks copolymers constituted of poly-propylene oxide (PO) block flanked by two poly-ethylene oxide (EO) blocks (Figure 3.1) [145]. This arrangement results in an amphiphilic copolymer, in which the number of hydrophilic EO (x) and hydrophobic PO (y) units can be varied with the aim to vary HLB (hydrophilic-lipophilic balance) of the unimers (Table 3.1).

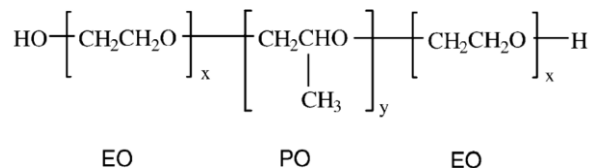


Figure 3.1 General chemical structure of Pluronic® block copolymers.

Table 3.1 Physicochemical characteristics of Pluronic® block copolymers. Table readapted from Reference [145]. [Reprinted from Journal of Controlled Release, 82, Alexander V Kabanov, Elena V Batrakova, Valery Yu Alakhov, Pluronic block copolymers as novel polymer therapeutics for drug and gene delivery, 189-212, Copyright 2002, with permission from Elsevier.](#)

Copolymer	MW ^a	Average no. of EO units (x) ^b	Average no. of PO units (y) ^b	HLB ^c
L35	1900	21.59	16.38	19
L43	1850	12.61	22.33	12
L44	2200	20.00	22.76	16
L61	2000	4.55	31.03	3
L62	2500	11.36	34.48	7
L64	2900	26.36	30.00	15
F68	8400	152.73	28.97	29
L81	2750	6.25	42.67	2
P84	4200	38.18	43.45	14
P85	4600	52.27	39.66	16
F87	7700	122.50	39.83	24
F88	11 400	207.27	39.31	28
L92	3650	16.59	50.34	6
F98	13 000	236.36	44.83	28
L101	3800	8.64	58.97	1
P103	4950	33.75	59.74	9
P104	5900	53.64	61.03	13
P105	6500	73.86	56.03	15
F108	14 600	265.45	50.34	27
L121	4400	10.00	68.28	1
P123	5750	39.20	69.40	8
F127	12 600	200.45	65.17	22

^a The average molecular weights provided by the manufacturer (BASF, Wyandotte, MI).

^b The average numbers of EO and PO units were calculated using the average molecular weights.

^c HLB values of the copolymers.

The Pluronics® posses an remarkable safety profile and is FDA approved for pharmaceutical and medical applications, including parenteral administration [199]. They exhibit a temperature dependent micellization implying that in order to form micelles in the unimers solution where the temperature must be above the critical

micelle temperature (CMT) and the concentration above the CMC. The CMC for aqueous solution of Pluronic® decreases with increasing temperature [200]. Typically, Pluronics used for drug delivery applications, at the physiological temperature (37 °C), have a CMC ranging from 1 µM to 1 mM [200, 201]. Notably, Pluronic® unimers also have an important role in drug delivery. Pluronic® block copolymers were shown to be potent biological response modifiers capable of sensitizing multidrug resistant (MDR) cancer cells with respect to various anticancer agents [202, 203]. Furthermore, Pluronic® unimers have been shown to inhibit drug efflux transporters and in turn enhancing drug transport across cellular barriers, such as polarized intestinal epithelial cells, Caco-2, and brain endothelium [204].

For the reasons stated above, Pluronic® block copolymers were chosen as polymers for the production of PMs in microfluidic systems. In particular, the selected polymer was Pluronic® F127 due to the easy availability in pharmaceutical grade as the commercial name of Lutrol® F127. The characteristics of the polymer are summarized in Table 3.2.

Table 3.2 Characteristics of Pluronic® F127.

Pluronic®	Mw (Da)	average number of EO units	average number of PO units	HLB
F127	~ 12600	~ 101	~ 65	> 21

3.1.2 Microfluidic mixing

Mixing strategy and design characteristics of the microfluidic platform are of primary importance for the control of nanoprecipitation process. As explained in Chapter 2, microfluidic based production of PMs relies on the use of microfluidic mixers that allow the rapid exchange of the solvents, and thus triggers the unimers aggregation. Based on a careful analysis of the literature, and considering the nanoprecipitation strategy to be applied, a flow focusing micromixers, fabricated in glass, was selected as the optimal microreactor for the production of PMs, and for the investigation of the nanoprecipitation process.

With regard to the reactor materials, the microfluidic reactors were fabricated in glass using an isotropic wet etching method. In brief, the microreactors consisted of a base plate, containing the etched microchannel network, which was thermally bonded to a top glass plate in which the inlet and outlet port were placed. Glass was selected as

substrate for the proposed microfluidic device since its chemical compatibility with organic solvent, required to solubilise the polymer, and its suitability to work with optical imaging and detection system. This provided an opportunity to observe the microfluidic environment and to compare it with numerical results (see Chapter 4). In addition, the hydrophilicity of the glass minimizes the adsorption of the polymer on the channel walls avoiding channel clogging [101]. This feature is important in order to avoid a reduction of the channel cross section, which might lead to a variation in the fluidic conditions during the nanoprecipitation process. Fluidic conditions are strictly related with the nanoprecipitation process conditions and their variation might lead to inter-batch and intra-batch variation of the obtained results.

A device based on hydrodynamic flow focusing mixing strategy (see Figure 3.2) was selected among other types of micromixers since it provides a number of features that can be leveraged for the production of PMs. In addition, extensive research has been carried out to characterize the mixing process within this type of device [50, 205], providing a background knowledge to interpret the nanoprecipitation results.

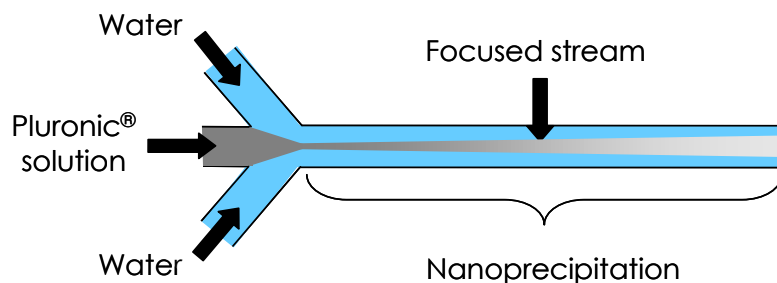


Figure 3.2 Focused enhanced mixing: the polymer stream is focused into a thin layer between the two sheath streams. Rapid mixing of the solvent takes place at the interface between the polymer solution and non-solvent streams.

In hydrodynamic flow focusing, the fluid stream to be mixed flows along the central channel meeting at the junction the two sheath streams. The central stream is then squeezed into a narrow stream between the two sheath streams. Since the mixing time is inversely proportional to the square of diffusion path length (see equation 2.5), represented in this case by the focused stream width, varying the stream width provides an easy way to control the mixing time. This feature provide the opportunity to exert a control on PMs dimension, not to mention the possibility to investigate the role of mixing time on the nanoprecipitation process.

Hydrodynamic flow focusing mixers are also characterized by extremely easy design and fabrication procedures. The flow focusing configuration represents a passive

micromixer and therefore does not require any external energy source, such as ultrasound actuator, in addition to fluid pumping energy to produce the mixing. It can be fabricated easily as a planar microfluidic chip by the classical wet etching procedure, unless “chaotic advection micromixers” and “sequential lamination micromixers”. Furthermore, a flow focusing configuration was preferred to a “segmented flow micromixer” since for PM preparation the crucial parameter is represented by the mixing time rather than the RTD (see section. 2.2.3 Nanostructured biomaterials produced by microfluidic approaches). In addition, the use of droplet mixer would imply the use of a second immiscible phase (i.e., oil or organic solvent) that would require an additional off-chip step to remove the immiscible transport phase.

3.1.3 Polymeric micelles production strategy

A schematic representation of the nanoprecipitation process is reported in Figure 3.2. The polymer was mixed in dimethyl sulfoxide (DMSO) to prepare the polymeric solution and then the latter was mixed with the non-solvent water within the microfluidic reactors.

The effects on the PM size and size distribution have been examined systematically by varying polymer concentration (PC), flow rate ratio of solvent to non-solvent (R), and the microchannel geometry where three microreactors were employed with different reaction channel dimensions. It has been demonstrated that microfluidic reactors provide a useful platform for the continuous-flow production of PMs with improved controllability, reproducibility, and homogeneity of the size characteristics.

3.2 Materials and methods

3.2.1 CMC determination: pyrene probe method

The value of the CMC for Pluronic® F127 was determined experimentally using the pyrene fluorescence method [155, 206-208]. From a stock solution of 1.25 mg/ml pyrene dissolved in chloroform, 80 μ L aliquots were transferred with a micropipette into a series of clean, dry test tubes and the solvent allowed to evaporate under vacuum by protecting from light to get 100 μ g of dry pyrene. A series of Pluronic® solutions ($1.95 \cdot 10^{-5}$ – $1.00 \cdot 10^{-2}$ M) in water were added to dry pyrene. Pyrene concentration in each tube was $1.236 \cdot 10^{-4}$ M. The mixtures were shaken in dark for 24 h at 25 °C and then filtered through a 0.45 μ m membrane filter for separation of undissolved pyrene crystals. The concentration of solubilised pyrene in micellar phase was determined

spectrofluorometrically at wavelengths of excitation (λ_{ex}) 339 nm and emission (λ_{em}) 390 nm using a fluorescence spectrometer (Bentham Instrument Ltd, UK). For CMC determination of copolymers, the fluorescence intensity of pyrene vs. logarithm of the copolymers concentration in water was plotted.

3.2.2 Critical water concentration (CWC) determination

The self-assembly of PMs was monitored using nanoparticle tracking analysis (NTA) system NanoSight LM10 (NanoSight Ltd. Amesbury, UK) as water was added stepwise (in steps of 5 μL) to 500 μL of either $1.5 \cdot 10^{-2}$ M or $7.5 \cdot 10^{-3}$ M solution of Pluronic F127® in DMSO. No nanoparticles were detected for $7.5 \cdot 10^{-3}$ M Pluronic F127 solution in DMSO until the concentration of water reached the value of 14.28% (V/V). For the second solution of Pluronic F127® in DMSO ($1.5 \cdot 10^{-2}$ M) the self-assembly of the PMs was detectable at a water concentration of 8.41 % (V/V).

3.2.3 Microfluidic reactor design and fabrication

The fabrication protocol used in this study is briefly outlined, as follow. The channel network was designed using AutoCAD drawing software first. A schematic representation of the channel architecture is reported in Figure 3.3. A commercial photo mask producer (J.D. Photo Tools, UK) printed channel pattern onto polyester base substrate as a negative photomask, with clear line in a black background. The width of the channel pattern onto the photomask (w) for the mixing channel was fixed at 10 μm . This value represents the minimum features width that can be printed with sufficient accuracy onto the polyester base substrate, according with the specification of the photomask producer. To keep the width of the channel pattern as low as possible, was required to obtain microchannel with the maximum available aspect ratio for the fabrication methodology applied.

For the microreactors fabrication, A photolithography/wet etching procedure was used (see Figure 3.4) [209].

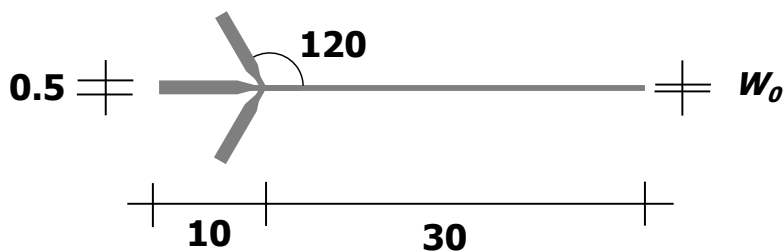


Figure 3.3 Schematic representation of the channel pattern onto the photomask used for the fabrication of the microreactors. All the other quotes are reported in mm.

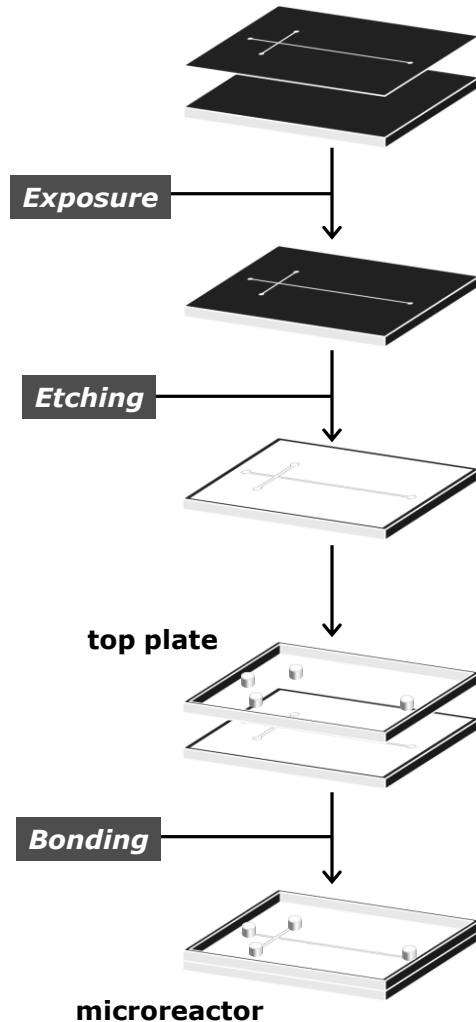


Figure 3.4 Schematic representation of the production procedure for glass microfluidic chips by isotropic wet etching.

Crown white glass (B270) plates (thickness of 1.5 mm) coated with a thin layer of chromium metal mask plus an upper layer of positive photoresist (AZ1500), supplied by Telic (Telic, USA), were used for channel network fabrication. The glass was cut by scoring the glass with a diamond in order to obtain a glass piece with desired dimension (depending on the dimension of the design to be etched).

With UV exposure, the pattern of interconnecting channels was transferred from the negative film to the photoresist layer onto the glass. The glass was then immersed in developer solution consisting of 50% Microposit developer (Chestech Ltd, UK) and 50% of deionised water. After the glass has been rinsed with water, it was immersed in MS8

Chrome etch solution (Chestech Ltd, UK), in order to remove chromium layer, until the pattern was clearly seen (60 s has been found to be suitable). Once the pattern to be etched was transferred onto the photoresist layer, glass plate was baked in at oven at 80°C overnight (~17 hrs) to dry and harden the mask on glass. The channel were then etched using 1% hydrofluoric acid (Sigma-Aldrich, UK) buffered with 5% ammonium fluoride (Sigma-Aldrich, UK) solution at 65 °C, under ultrasonic agitation (Ultrasonic Cleaner, VWR, UK). With the above mentioned setting, the etching rate has been found to be approximately 4.5 µm/min.

Once the chip was etched for the required time (that determined the depth of the etched pattern), it was removed and immersed in sodium bicarbonate (Sigma-Aldrich, UK) solution in water (9% w/v) to stop etching and finally washed with water and left to dry. The remained photoresist was removed using Microposit Remover 1165 (Chestech Ltd, UK) and the exposed chrome then removed using MS8 Chrome etch solution. The clean glass was then washed and left to dry. Finally, the etched glass was thermally bonded (595 °C for 3 hrs) with a top plate of the same material into which outlet and inlet holes had been previously drilled to link the channels. Before the bonding step the cross section profile of the etched microchannel was measure by a surface profiler (P-16+ stylus profiler, KLA Tencor, U.S.A.).

3.2.4 Estimation of the focused stream width

In order to estimate the focused stream width a hydrodynamic flow focusing configuration was created within the microreactors. Solution of polymer Pluronic F127® in DMSO ($7.5 \cdot 10^{-3}$ M or $1.5 \cdot 10^{-2}$ M) and deionised water were injected in the central and two lateral channels, respectively. TEFILON tubes (Upchurch Scientific, USA) with an inner diameter of 500 µm were used to connect the microreactor to gastight glass syringes (Hamilton, Reno, USA) where a KDS syringe pump (KD100, KD scientific Inc., USA) was used to control the flow rate. Syringes and tubing were rinsed with deionised water for the aqueous streams and with DMSO for the polymer stream before loading. Pulsing of the flow was minimized by introducing small air bubbles into the syringes. After starting the syringe pumps, enough volume (typically 200 µL) was allowed to flow through to ensure rinsing of the outlet tubing (dead volume c.a. 100 µL) and steady operation of the device.

Volumetric flow rate ratios, R , of polymer solution to water were varied by altering each stream's flow rate. The central and lateral streams flow rates were varied in order to obtain R ranging between 0.03 and 0.13. The total flow rates (Q) for the three microreactors were controlled at 2.00, 0.65 and 0.30 mL/h for Microreactors 1, 2 and 3, respectively.

To characterize the mixing process in terms of time needed for mixing by diffusion under hydrodynamic flow focusing conditions, the width of the central flow stream was determined using a digital imaging technique. An inverted microscope (Olympus IX51, Japan) was used to monitor the flow within the microchannel of the three microreactors. Dyes were not required since the different refractive index between water (1.333) and DMSO (1.479) provided enough contrast to determine the position of the interface between the two fluids. The dimension of the focused stream was determined by photomicrograph analyses (Image Pro Plus 6.2, Media Cybernetics Inc, USA).

3.2.5 Preparation of polymeric micelles

3.2.5.1 Preparation of PMs in batch reactors

DMSO was obtained by Sigma-Aldrich UK, and used as supplied. Polymer Pluronic® F127 was provided as a gift by BASF Chem Trade GmbH. PMs were prepared in batch systems using Pluronic F127® solutions in DMSO at a concentration of either $1.5 \cdot 10^{-2}$ M or $7.5 \cdot 10^{-3}$ M. PMs were formed by pipetting the polymeric solutions into deionised water (with a polymer solution to water volume ratio, R , ranging from 0.03 to 0.13) and stirred using the pipette. The preparation of PMs was performed at environmental temperature, typically ranging between 21-23 °C.

3.2.5.2 Preparation of PMs in microfluidic reactors

Solution of polymer Pluronic F127® in DMSO ($7.5 \cdot 10^{-3}$ M or $1.5 \cdot 10^{-2}$ M) and deionised water were injected in the central and two lateral channel, respectively. TEFLOU tubes (Upchurch Scientific, USA) with an inner diameter of 500 µm were used to connect the microreactor to gastight glass syringes (Hamilton, Reno, USA) where a KDS syringe pump (KD100, KD scientific Inc., USA) was used to control the flow rate. Syringes and tubing were rinsed with deionised water for the aqueous streams and with DMSO for the polymer stream before loading. Pulsing of the flow was minimized by introducing small air bubbles into the syringes. After starting the syringe pumps, enough volume (typically 200 µL) was allowed to flow through to ensure rinsing of the outlet tubing (dead volume c.a. 100 µL) and steady operation of the device.

Volumetric flow rate ratios, R , of polymer solution to water were varied by altering each stream's flow rate. The total flow rates for the three microreactors were controlled at 2.00, 0.65 and 0.30 mL/h for Microreactors 1, 2 and 3, respectively. An inverted microscope (Olympus IX51, Japan) was used to monitor the flow within the microchannel. The product sample was collected from the reactor outlet (typically, 2

mL), and used for further analysis and size characterization. The preparation of PMs was performed at environmental temperature, typically ranging between 21-23 °C.

3.2.6 PM size characterization

Following the preparation of PMs, water was added to the samples in order to have a comparable amount of solvent (3.2% v/v) in different samples. This prevented slight deviations of the measured size due to swelling of the PMs.

A nanoparticle tracking analysis (NTA) system NanoSight LM10 (NanoSight Ltd. Amesbury, UK) was used to measure the hydrodynamic particle diameter of the PMs. For each measurement, c.a. 300 µL of sample was loaded in the detection cell and five measurements were performed to give an average value using NanoSight NTA Analytical Software.

For comparison with NTA system, also the classical nanoparticle sizing equipment Dynamic Light Scattering (DLS) was used to obtain the hydrodynamic particle diameter. Particle sizing was performed using Zetasizer Nano ZS (Malvern Instruments Ltd., U.K.). For each measurement, c.a. 200 µL or more volume of the sample was loaded in a disposable low-volume cuvette. Three measurements were performed on each sample. The Z-average size and distribution fits were obtained using Dispersion Technology Software (Malvern Instruments Ltd. U.K.). Size distributions and Z-average sizes were obtained by averaging over three measurements. In addition, certified reference polystyrene latex nanoparticles (NanoSight Ltd. Amesbury, UK) with size of 100, 200 and 400 nm were used to assess the deviation of size measurements between the two instruments. Insignificant differences were observed between the measures performed with NTA and DLS systems.

3.3 Results and discussion

3.3.1 CMC determination

CMC can be determined from the plot reporting the pyrene fluorescence intensity vs. logarithm of the copolymers concentration in water (Figure 3.5).

At low polymer concentrations, low pyrene intensity was observed but beyond a specific polymer concentration pyrene intensity increased extremely. The sharp increase of the fluorescence intensity is closely related to the formation of micelles composed of a hydrophobic core into which pyrene is preferentially partitioned. A graph with two linear segments having different slopes was obtained. The intersection point of these two segments gave a CMC value (Figure 3.5).

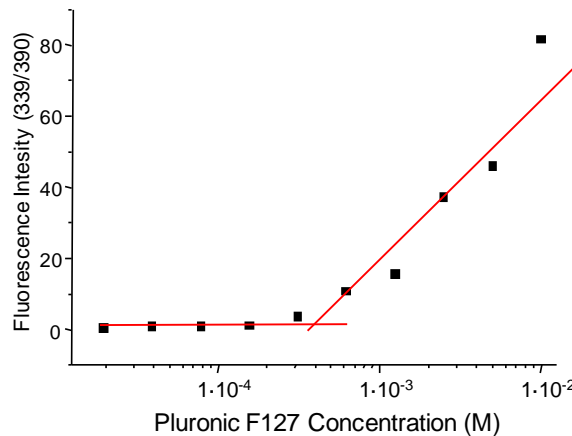


Figure 3.5 Fluorescence intensity of pyrene vs. logarithm concentration of the Pluronic® F127 block copolymers in water.

From the analysis of the fluorescence intensity vs. Pluronic® concentration plots reported in Figure 3.5 the CMC of the polymer was calculated to equal to $3.0 \cdot 10^{-4}$ M

It must be noted that, even if the CMC value represents a specific point in concentration, it is well known that a partial self-assembly of the unimers occurs also at smaller polymer concentration. In addition, unless purification processes are carried out, Pluronics, being synthetic polymers, are polydisperse both in overall size and in ratio of the block size [210-212].

3.3.2 Microfluidic reactors fabrication

In order to study the effect of the channel dimension on mixing time and on the characteristic of the produced PMs three microreactors with different dimensions were fabricated.

Microreactors were fabricated with the protocol reported in the previous section and named Microreactor 1, 2 and 3, respectively. Figure 3.6 shows the junction between the three inlets and the outlet channels for microfluidic Reactor 1.

The microreactors had an approximately semi-circular cross-section with the dimensions summarized in Table 3.3 for the three microreactors used.

A quasi-semicircular cross section is an unavoidable inconvenience when wet etching is used on glass substrate. The characteristic quasi semicircular cross section of the channel etched is due to the isotropicity of the etching procedure used in the fabrication step that cause the etching rate to be the same in all the three spatial directions [213]. This peculiar cross section makes difficult to predict mathematically the shape of the focused stream, which is closely related with the mixing time. To

solve this issue an experimental determination of the width of the focused stream was carried out (see following section). A computational fluid dynamic numerical model to estimate shape and dimension of the focused stream is also now under investigation.

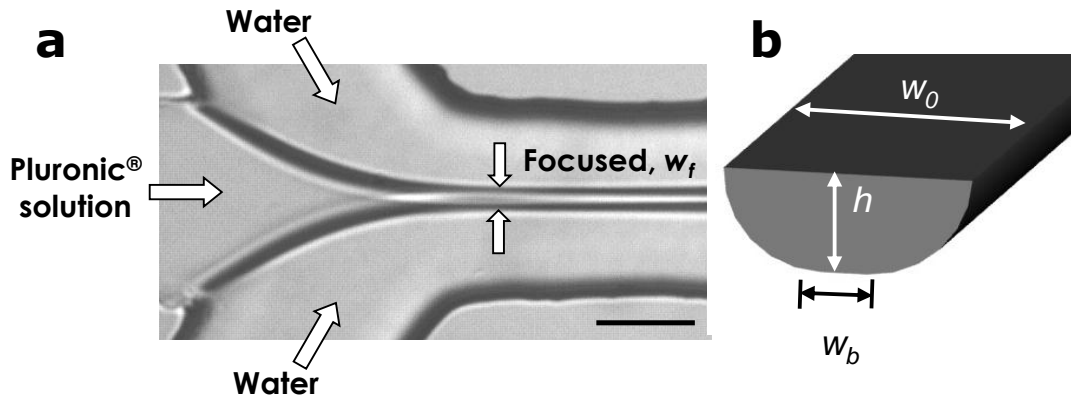


Figure 3.6 A microfluidic reactor with three inlets creating a hydrodynamic flow focusing where the central stream is polymer Pluronic® solution in DMSO. The width of the focusing central stream, w_f , is controlled by varying the volumetric flow rates of the three inlets. Scale bar 30 μm (c) CAD-based design showing the cross section of the reactor channel. Values of w_o , h and w_b are reported in Table 3.3. [Reprinted from Journal of Colloid and Interface Science, 357, Lorenzo Capretto,Dario Carugo,Wei Cheng,Martyn Hill,Xunli Zhang, Continuous-flow production of polymeric micelles in microreactors: Experimental and computational analysis, 243-25, Copyright 2011, with permission from Elsevier.](#)

Table 3.3 Microfluidic reactor dimensions.

Microreactors	1	2	3
h (μm)	53	29	17
w_o (μm)	130	80	57
w_b (μm)	24	22	23

Notably, the different width of the channel on the bottom and top wall of the channel is likely to cause the mixing to occur at different rate at the bottom and the top of the channel. This could be a cause of variation of the characteristic of the PMs that are created within the two extremes of the channel that could affect the homogeneity of the produced PMs (see section 4.6.3.2 Focused stream shape).

Furthermore, the isotropicity of the glass wet etching procedure prevents also the fabrication of channel with high aspect ratio. Having channel with high aspect ratio

gives the possibility to have a short mixing time and a large channel's cross section area that is required to have a large polymeric micelles production rate.

All the issues presented above could be solved using a fabrication technique that allows the creation of straight channel with rectangular section and high aspect ratio, such as thick resist lithography. However, the latest technique permits to fabricate microreactors based on poly-dimethylsiloxane (PDMS) that is known to have swelling problem when brought in contact with organic solvent [63]. Furthermore, PDMS is a compliant polymer. High pressures, from high volumetric flow rates, can cause deformation of the PDMS microchannel. As the deformation becomes substantial, it can affect the flow profile inside the microchannel and subsequently the ability to maintain a consistent focusing [128].

3.3.3 Analytical estimation of mixing time

Mixing is a key step in the nanoprecipitation process that can strongly affect the size characteristics of the produced PMs [132]. In the laminar flow regime at low Reynolds numbers mixing generally occurs through passive diffusion. Under hydrodynamic flow focusing conditions in the microchannels (Figure 3.6a), it is the diffusive process of molecules (water and DMSO) travelling into and out the polymer solution region that determines the mixing extent and therefore the precipitation outcome.

To predict the width of the focused stream, an analytical model that was based on the principle of mass conservation [214] was used. The focused stream width was computed under the simplified assumptions that:

- The flow in the microchannels was steady and laminar.
- The fluids were Newtonian.
- The fluids had the same density and viscosity in the four channels (three inlet channels and one outlet channel).
- The four channels had the same cross-section area.
- The focused stream had a rectangular cross- section.
- The velocity filed was assumed to be homogeneous across the channel width.

It was found that, by taking into account the shape the curved-edge of the microchannel cross-section, the width of the focused stream, w_f , can be represented by

$$w_f = \frac{Q_I}{Q_E + Q_I} \cdot \left(w_b + \frac{\pi}{2} \right) \cdot a \quad (3.1)$$

where Q_I and Q_E are the volumetric flow rates of the central stream (polymeric solution) and the total sheath stream (non-solvent), respectively; w_b and h are the bottom width and height, respectively, of the main channel (Figure 3.6 and Table 3.3). It should be noted that during the isotropic wet etching process, the channel width is associated with the channel depth produced (Figure 3.6); the width of channel top (w_f) was found to be typically equal to $w_b + 2h$ [15, 209].

Figure 3.7 shows bright field micrographs of at different hydrodynamic flow condition showing the dependence of w_f on R , polymer solution concentration (PC) and microreactor dimension. Micrographs also demonstrate that steady-state microfluidic condition without visible instability along the contact interface.

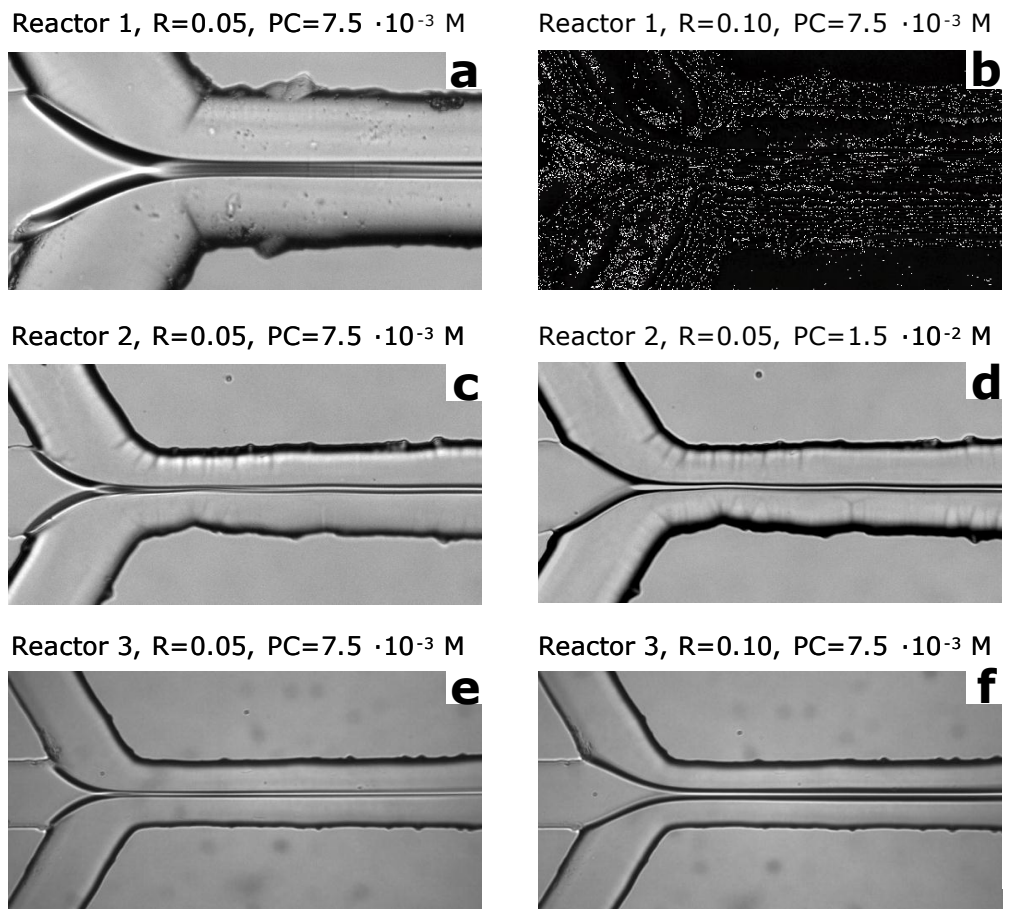


Figure 3.7 Width of the focused stream at different hydrodynamic flow focusing conditions (“Reactor”: Microreactor; “ R ”: flow rate ratio; “ PC ”: polymer solution concentration). Scale bar 100 μm .

Based on the experimental measurements of the focused stream width (w_f) within the microreactor, the theoretical model (Equation (3.1)) was validated by introducing a validation factor, a , which was found to be dependent on channel geometries and the viscosity of the Pluronic® organic solutions. Table 3.4 summarises the values of the validation factor, a , for the different Pluronic® organic solutions and microreactors used in the study.

Table 3.4 Effect of reactor type, polymeric solution concentration (PC) on validation factor, a .

PC	Reactor		
	1	2	3
$7.5 \cdot 10^{-3}$ M	2.57	2.10	1.94
$1.5 \cdot 10^{-2}$ M	2.55	1.97	1.80

Once the focused stream width (w_f) was determined, the mixing time, τ_{mix} , was then estimated in the diffusion dominated mixing process. The timescale for mixing by hydrodynamic flow focusing was estimated using a simplified two-dimensional model [29] that neglected the diffusion in the flow direction (see section 2.1.1).

$$\tau_{mix} \approx \frac{w_f^2}{4D} \approx \frac{\left(w_b + \frac{\pi}{2}\right)^2 \cdot a^2}{4D \left(1 + \frac{1}{R}\right)^2} \quad (3.2)$$

where D is the diffusion coefficient of the solvent, and R is the ratio of the focused stream to the total flow rate, Q/Q . Considering the diffusion coefficient of the solvent in water $D = 10^{-9}$ m²/s and flow rate ratios controlled between 0.03-0.13, the mixing time was estimated to be in the range of 35-250 ms, 10-40 ms and 4-18 ms, for Microreactors 1, 2 and 3, respectively. However, the mixing time estimated by equation 3.2 was an average since it might be possible that the different width of the top and bottom walls caused a difference in the effective mixing time within the top and bottom walls.

3.3.4 Preparation of PMs in microfluidic reactors

3.3.4.1 Effects of varying flow rate ratio (R) on PM characteristics

According to equation 3.2, the mixing time for solvent exchange can be controlled by varying the flow rate ratio (R) within a given microchannel geometry. In order to examine the effect of this experimental parameter on the size characteristics of the PMs produced, the polymeric solution and water flow rates were varied with R being controlled in the range of 0.03 to 0.13 in Microreactor 2. The initial concentration of the polymer solution was also varied at two levels ($1.5 \cdot 10^{-2}$ or $7.5 \cdot 10^{-3}$ M). The results are depicted in Figure 3.8.

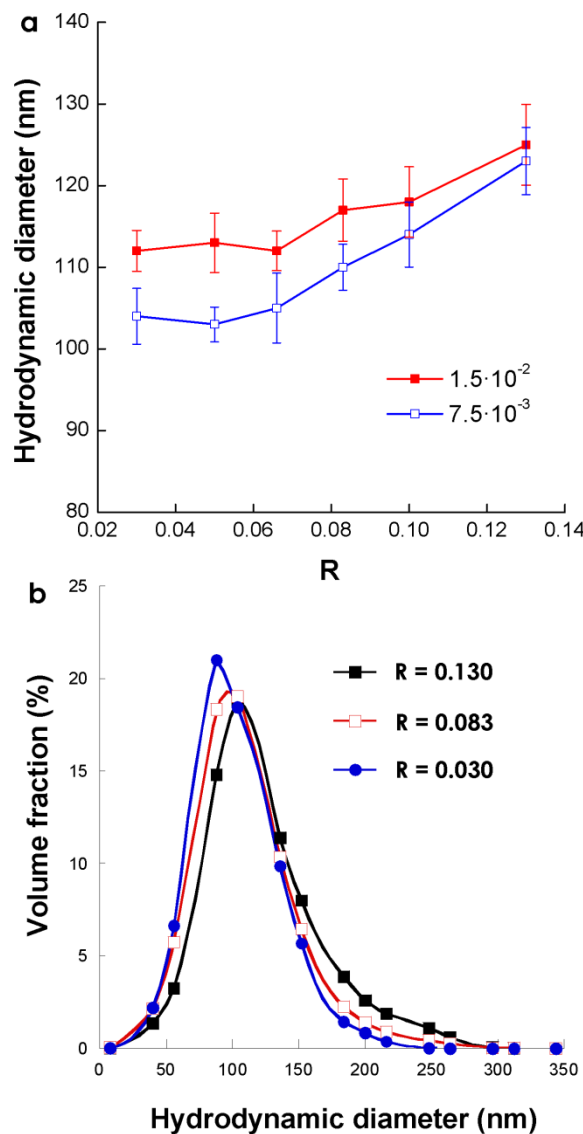


Figure 3.8. Effects of flow rate ratio (R) on (a) PMs size at different polymer concentrations, and (b) size distribution at a polymer concentration of $7.5 \cdot 10^{-3}$ M using hydrodynamic flow focusing in Microreactor 2. [Reprinted from Journal of Colloid and Interface Science, 357, Lorenzo Capretto, Dario Carugo, Wei Cheng, Martyn Hill, Xunli Zhang, Continuous-flow production of polymeric micelles in microreactors: Experimental and computational analysis, 243-25, Copyright 2011, with permission from Elsevier.](#)

As can be seen from Figure 3.8a, when R increased, the PM size increased from about 100 nm to 125 nm at a polymer concentration of $7.5 \cdot 10^{-3}$ M, and from 110 nm to 125 nm at a higher polymer concentration of $1.5 \cdot 10^{-2}$ M. It was also observed that, for the same polymer concentration when R decreased, the particle size distribution became narrower (Figure 3.8b), indicating an increase in the uniformity of the PMs produced. This was attributed to the narrower central stream width created at lower R , which provided a shorter mixing time. This will be further analyzed in later sections.

It should be noted that the PMs obtained had relatively larger diameters than the previously reported data for Pluronic F127 PMs [31]. This was mainly due to the presence of DMSO (3.2% V/V in all the samples) causing a considerable swelling of PMs. When the solvent (DMSO) was removed through dialysis against water, the PM diameter was found to reduce to between 5 and 20 nm which is in agreement with previous reports [215].

3.3.4.2 Effects of varying microreactor dimensions on PM characteristics

Three different microreactors were used to characterize the combined effect of device geometry and R on PM output. The three devices had different channel dimension and geometrical scaling (see Table 3.3). Neglecting the effect of the parabolic flow profile and of the viscosity gradient between water and polymer solutions, the focused stream width will scale linearly with the mixing channel width, so that the focused stream width in reactor 3 will be roughly 3 and 2 times smaller than in Microreactor 1 and 2 respectively. According to Equation 3.2, an alteration of the microchannel dimension, in particular the channel width, will result in variation in the width of the focused stream thereby in the calculated diffusive mixing time, τ_{mix} , which, in turn, can affect the characteristics of PMs produced. These effects were examined by using three microreactors with different channel dimensions (Table 3.3) where Q were adjusted to give a comparable residence time (i.e., ~ 300 ms).

The measurement results of both PM size and size distribution under different conditions are shown in Figure 3.9. The results from a batch reactor are also included for comparison using identical chemical compositions.

As shown in Figure 3.9, at a given R value, the PM mean diameter decreased when the microchannel dimension was reduced. For example, when $R = 0.03$ the PMs size decreased from 134 to 110 nm as the channel dimension was reduced in Microreactors 2 and 3 compared to Microreactor 1, at a polymer concentration of $1.5 \cdot 10^{-2}$ M (Figure 3.9a). Similar changes were observed at a polymer concentration of $7.5 \cdot 10^{-3}$ M (Figure 3.9b). It should be noted that for the smaller polymer concentration PM batches with similar mean size could be produced within the two different microfluidic devices just

tuning R (Figure 3.9b). However, with a given PM mean diameter, PMs that are more homogeneous can be produced using smaller device (Figure 3.10). Although the PM mean diameters showed no significant difference between Microreactors 2 and 3, the size distribution measurements (Figure 3.9c) confirmed the increased uniformity of the PMs when smaller microreactor dimensions were selected.

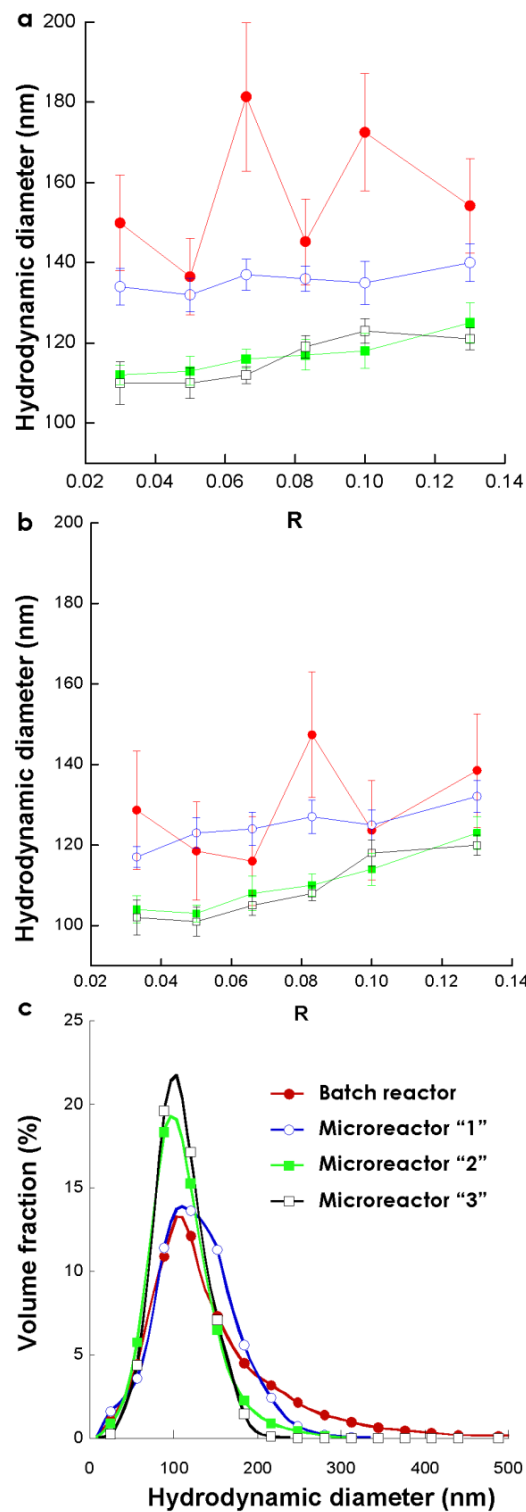


Figure 3.9 Effects of R and microreactor dimensions on PM size at polymer concentrations of (a) $1.5 \cdot 10^{-2}$ M and (b) $7.5 \cdot 10^{-3}$ M, and on (c) PM size distribution at a polymer concentration of $7.5 \cdot 10^{-3}$ M. [Reprinted from Journal of Colloid and Interface Science, 357, Lorenzo Capretto,Dario Carugo,Wei Cheng,Martyn Hill,Xunli Zhang, Continuous-flow production of polymeric micelles in microreactors: Experimental and computational analysis, 243-25, Copyright 2011, with permission from Elsevier.](#)

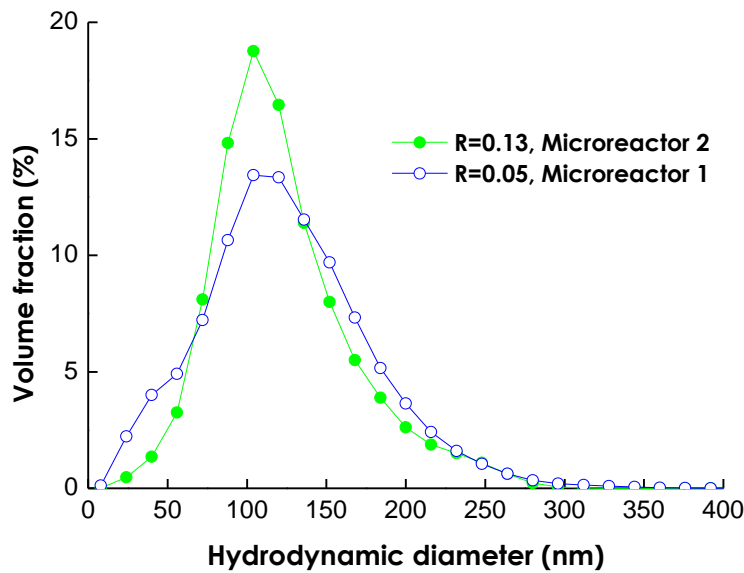


Figure 3.10 PM size distribution for Microreactors “2” (solid markers) and “1” (open markers) with R equal to 0.13 and 0.05, respectively. Pluronic F127 solution concentration: $7.5 \cdot 10^{-3}$ M.

Figure 3.11 shows the variation of the mean size of PMs as a function of width of the focused stream within Microreactors 2 and 3, respectively. In this experiment, in order to obtain the same mixing time between the two microreactors, R was chosen to be greater in Microreactor 3 than that in Microreactor 2.

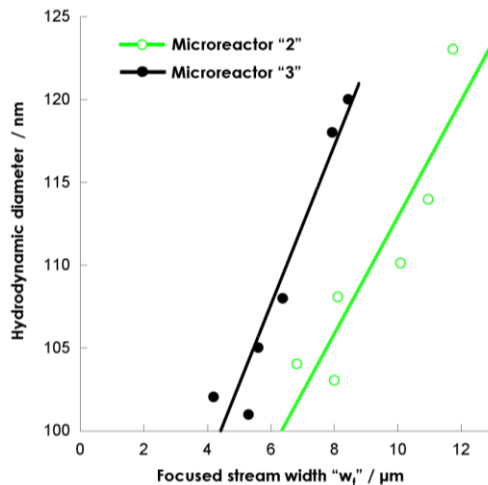


Figure 3.11. Effect of width of focused stream on PM size in Microreactors 2 and 3 with an initial polymer concentration of $7.5 \cdot 10^{-3}$ M. [Reprinted from Journal of Colloid and Interface Science, 357, Lorenzo Capretto, Dario Carugo, Wei Cheng, Martyn Hill, Xunli Zhang, Continuous-flow production of polymeric micelles in microreactors: Experimental and computational analysis, 243-25, Copyright 2011, with permission from Elsevier.](#)

A good linear relationship between PM mean size and width of the focused stream was found for both microreactors. However, the difference between the two straight lines from the two microreactors was indicative that the width of the focused stream was likely only one of the key parameters that affected the PM size. Specifically, with a given width of the focused stream the PMs produced in the smaller microchannel (Microreactor 3) were larger and more disperse (Figure 3.12) than those obtained in a wider microchannel (Microreactor 2).

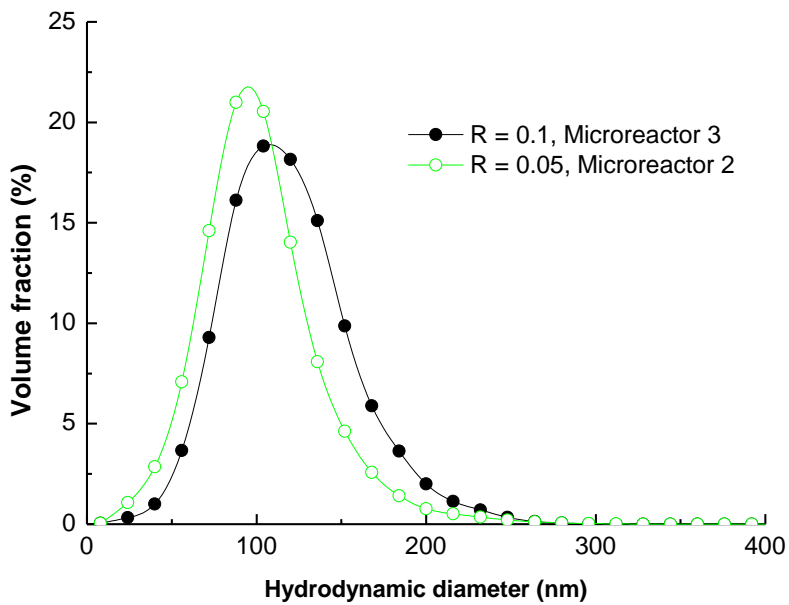


Figure 3.12 PM size distribution for Microreactors “2” (open markers) and “3” (solid markers) with R equal to 0.05 and 0.1, respectively. Pluronic F127 solution concentration: $7.5 \cdot 10^{-3}$ M.

These results demonstrated that microreactor dimension had a significant effect on the production output in term of size and homogeneity of the PMs produced even at similar w_f . As implemented, PM microfluidic production was solely dependent neither on R (Figure 3.10) nor on the focused stream width (Figure 3.11). The interplay between these two factors must be considered from the perspective of the solvent/non-solvent (i.e., DMSO/water) interface and the resulting diffusive mixing and nanoprecipitation processes.

As shown in Figure 3.9b, PM batches with similar mean size were produced within the two different microfluidic devices just tuning R . This shows that microfluidic device dimension was not fundamental for the production of a wide range of PM size batches; nevertheless, this has important technological consequence. Firstly, microfluidic device width larger channels are easier to fabricate and operate, and produce larger volumetric throughput. However, in order to produce smaller PMs, R must be lowered

leading to a smaller PM concentration in the final mixture. From a pharmaceutical point of view, this has various implications that must be considered when a production strategy for PMs is implemented. For instance, the final drug concentration, thus the concentration of the drug that can be loaded in a finite volume of PM dispersion, decrease with the concentration of PMs in the mixture, hence less concentrated dispersion must be injected in larger volume in order to have similar dose of drug. In addition, during intravenous injection, PM dispersion undergo to a dilution by circulating blood, and the use of low concentration mixture of PMs (close to the CMC value) can increase the possibility of a premature disassembly and release of the drug. Conversely, small microfluidic devices are more complicated to fabricate and operate, due to the increase of pressure drop and clogging issues, and produce a smaller volume throughput but with higher concentration. In addition, reducing the dimension also increased the PM homogeneity for similar mean diameter (Figure 3.10).

3.3.4.3 Matching between mixing and precipitation processes

In conventional nanoscale production technique, micelle formation is primarily determined by macroscopic experimental parameter such as reagent adding rate and stirring rate [216]. The ability to precisely control and predict mixing conditions and its impact on PM formation is limited by the chaotic nature of the mixing under turbulent condition that characterized batch method. In contrast to batch procedures, microfluidics enabled precise steady-state control of the mixing process under laminar flow condition, which resulted in predictable and reproducible continuous flow mixing. In this respect, the improvement in achieving a predictable and reproducible process for the formation of PMs within the microfluidic reactor, can be attributed to the tuneable match between the mixing process and the precipitation process of PMs. Specifically, the diffusive mixing within the microreactors controls the polarity of the block copolymer surrounding fluidic environment and directs the self-assembly of amphiphilic polymer chain into PMs.

Fundamentally, the core-shell structured nanoparticles, PMs, are formed spontaneously by self-assembly of block copolymer unimers in fluids [137], where block copolymers are constituted of homopolymer segments covalently bonded together, and the self-assembly occurs to minimize free energy by minimizing the number of enthalpically unfavourable contacts between the constituting blocks and the water [217]. This aggregation of amphiphilic block copolymer unimers to form PMs is different from traditional nucleation and crystal growth that guide the nanoprecipitation of non-amphiphilic molecules (such as inorganic material and hydrocortisone) [132]. In the nanoprecipitation process of non-amphiphilic molecules, the size of the obtained PMs is mainly controlled by the level of supersaturation of the solute to be precipitated and

on the time associated with the precipitation process. These two parameters can be controlled in microfluidic devices varying the relative flow rate ratio of the solvent and non-solvent stream, and the residence time distribution respectively, as demonstrated by other researchers [25, 104, 105]. In contrast, the size for block copolymer micelles (PMs) is dictated by the magnitude of the steric and electrostatic interaction between the polymer chains, that leads to the formation of an insertion barriers when a critical size is reached that kinetically quench the PMs growth [132, 133, 218].

Furthermore, differences are also present with regard to the aggregation kinetics of low molecular weight non-ionic surfactants. One key difference that has been consistently reported is that aggregation of Pluronics® occurs over a range of concentrations, rather than at a unique CMC [211].

During the generation of amphiphilic PMs, the self-assembly of block copolymer unimers is generally believed to take place in three stages: (i) nucleation of block copolymer unimers, (ii) fusion of existing particles and, (iii) formation of an overlapping brush corona that results in kinetically frozen PMs [132]. The solvent quality affects the size of the particles by changing the brush corona repulsion characteristics, and in turn, the critical aggregation size. Therefore, the PM size is dependent on the time scale associated with mixing in the solvent, τ_{mix} . The relationship between the mixing time, τ_{mix} , and the time scale associated with block copolymer aggregation, τ_{agg} is also significant. The ratio between the two time scales is expressed as the Damkohler number (Da) [134],

$$Da = \frac{\tau_{\text{mix}}}{\tau_{\text{agg}}} \quad (3.3)$$

When $Da < 1$, the mixing time is shorter than the time scale associated with the PM nucleation, therefore, the PM size is expected to be independent of the mixing time and polymer concentration. As a result, PMs have a characteristic dimension represented by the critical size, which corresponds to the creation of an overlapping brush corona, and the PMs are expected to be more homogeneous than those produced with slower mixing. In contrast, when $Da > 1$, the slow change in solvent quality permits fusion and unimer exchange to take place for a longer time, therefore, larger PMs can be formed with an increase in mixing time, polymer initial concentration or magnitude of the solvent jump. The results reported in section 3.3.4 demonstrated the effects of these parameters on the size of PMs suggesting that the applied conditions led to greater τ_{mix} than τ_{agg} , i.e., $Da > 1$.

By use of an impinging jet mixer, τ_{agg} was found to be in the range of 26–60 ms for polybutylacrylate-b-poly(acrylic acid) (PBA(59)-PAA(104)) copolymers [132]. It is

understood that Pluronic F127, being a different polymer, is characterized by a different τ_{agg} , however, the previous result can provide a reference time scale to interpret the results presented so far. The analytical estimation of τ_{mix} (see equation 3.2) for the used microfluidic devices, with R ranging between 0.13 and 0.03, gave an estimated τ_{mix} of 35-250, 10-40 and 4-18 ms for Microreactor 1, 2 and 3, respectively. The calculated τ_{mix} falls therefore, within the time frame posed by τ_{agg} , especially for Microreactors 2 and 3, therefore a PM size independent from the τ_{mix} (i.e., R) would be expected. However, results in Figure 3.9 showed a consistent decrease of PM size as R and polymer concentration were decreased. This implies that the microfluidic environment affects the nanoprecipitation, and in turn PMs size, even a relative fast mixing (i.e., $Da < 1$). Similar, results were also presented by Karnik *et al.* [29], and was putatively associated with rearrangement of block copolymer during the growth process; as results, a faster mixing may results in a slower self-assembly that favour nucleation over growth phase, leading to the formation of smaller PMs.

It can also be argued, that τ_{mix} might be underestimated because equation 3.2 does not take into account the role of viscosity in controlling the diffusivity of the species. In this respect, the role of the viscosity and fluidic conditions on the mixing process will be discussed in Chapter 4.

In addition, it must be considered that R value also affects the amount of solvent introduced in the microreactor. A larger amount of solvent might lower the brush corona repulsion characteristics, decreasing the insertion barrier energy for a unimer within a growing, not yet kinetically locked, PMs. As results, a larger amount of DMSO (i.e., larger R) may result in an increase of the critical aggregation size and to the formation of larger PMs independently from the τ_{mix} . In other word, for τ_{mix} smaller than the τ_{agg} (i.e., $Da < 1$) the PMs size is still independent from τ_{mix} , as previously reported [132], but can still be affected by the amount of solvent present during the aggregation process (i.e., R). This view is agreement with the results reported in Figure 3.9, and by Karnik *et al.* [29] where a decrease in R is associated with a consistent decrease in size. However, it proposed a different mechanism to explain the effect of R on PMs size obtained at $Da < 1$. It is also further supported by the similar PM mean size obtained for microfluidic reactors 2 and 3 when employed at same R . In this respect, it should be noted that, decreasing the channel dimension, a short τ_{mix} can be achieved, however, due to the comparable value of τ_{mix} and τ_{agg} (i.e., $Da < 1$) achieved within Microreactor 3 and 2, a decrease in τ_{mix} does not significantly affect the PMs mean size (see Figure 3.9).

3.3.4.4 Effects of solvent exchanges

Under the laminar flow conditions in the microfluidic channel the mixing between the flow streams is dominated by molecular diffusion in a direction normal to the liquid flow streamlines. As a result, the solvent exchange between DMSO and water alters the solvent composition. When the water amount in the mixture reaches a critical water concentration (CWC), it triggers the polymer unimers in the solvent to self-assemble into closed spherical structures, PMs. In the focusing flow configuration, the width of the focused organic solvent stream (w_f) determines the mixing time for the centre of the focused stream to reach the CWC. The effect of w_f on the time required to reach the CWC in the entire domain of the focused stream will be discussed in Chapters 4 and 5. In addition, w_f also determines how fast the solvent displacement process between solvent (i.e., DMSO) and non-solvent (i.e., water) proceeds. Consequently, the increase in the width of the focused stream gives an increase in the mean size of PMs whilst the size distribution of the produced PMs becomes wider. This was confirmed by the experimental results (Figure 3.9).

The self-assemble of the unimers to form the primary nuclei and the subsequent PM growth, result in a decrease of the diffusion coefficient and an increase in tendency of the newly formed species to advect along the streamline. Because of that, they tend to remain in the centre of the channel within the streamline of the focused stream and are exposed to the change of polarity of the environment due to the movement of DMSO and water that have significantly higher diffusivity [123]. Specifically, the solvent exchange between DMSO and water continues in the direction normal to the streamlines, at the interface between polymer and water streams, causing the concentration of DMSO to remain high inside the focused stream domain. This will create an environment where the insertion barrier for unimers exchange is lowered causing the aggregation of larger PMs. With a wider focused stream it generally needs longer time for the diffusive mixing to occur, therefore, DMSO concentration will remain high for a longer time and larger and more disperse PMs will be formed. An increase in R also provides a relatively wider focused stream, thus has the similar effect (see Figures 3.8 and 3.9).

Whilst the R value reflects the physical dimension of each flow stream within the microchannel, its variation also causes changes in the chemical composition within the microenvironment in which the aggregation takes place. The difference in PMs size and size distribution observed in the two microreactors at a given focused stream width (Figure 3.11) was likely due to the solvent composition change that might influenced the mixing extent by an effect on diffusivity of the species (see section 4.6.3 Diffusive mixing). It has also been suggested that the size of the particles could be influenced by the solvent quality via the changing of the brush corona repulsion characteristics

[132]. In that case, an increase in R provides a larger amount of solvent (DMSO) present which can potentially lower the insertion barrier during the aggregation step, therefore resulting in an increase in PM dimension and polydispersity.

3.3.4.5 Comparison between batch and microfluidic reactors

Comparing microfluidic reactors with batch systems, it was found that the mean size of the PMs obtained using microreactors was generally smaller than that using a batch reactor (Figures 3.9a and 3.9b). This effect on mean diameter of the PMs was also accompanied by a significant increase in the uniformity of the PMs (Figure 3.9c) within microreactors. The increased polydispersity of PMs produced by batch reactor was also accompanied with the formation of a small number of large aggregate of block copolymer with dimension greater than 500 nm. Conversely, the formation of such big aggregate was not observed for on-chip production. This represents an additional advantage of microfluidic production that does not require post processing procedure to remove larger aggregate or precipitate before the injection [155, 178].

In addition, notable fluctuation in the mean size of PMs was observed when R was varied in the batch reactor (Figure 3.9a and 3.9b). In addition, for the same batch of PMs produced by microfluidic approach the hydrodynamic diameter was typically reproducible to within ± 5 nm between different experiments, demonstrating the robustness of on-chip production. The same degree of reproducibility was not observed for PMs produced with conventional approach

From the results showed is evident the effectiveness of the microfluidic environment in controlling the mixing process and thereby the nanoprecipitation process. The focused enhanced mixing can be leveraged to exert a more efficient fast and controllable mixing that leads to a better control of PMs produced in term of dimension and polydispersity. Furthermore, the notable fluctuation of the hydrodynamic diameter in batch reactor when R was varied indicated a less predictable and reproducible (higher inter batch standard deviation) process within batch reactors in comparison with microfluidic reactors where a turbulence-based mixing takes place.

3.4 Summary

To summarise, the strong safety profile, commercial availability, well-studied physical properties and the capacity of sensitizing multidrug resistant (MDR) cancer cells, make Pluronic® block copolymers particularly appealing for drug delivery purposes. Among the different type of Pluronic, type F127 was selected, due to its easy availability in pharmaceutical grade required for the ongoing studies. In order to estimate the

concentration of the polymeric solution to be used for the microfluidic based formation of polymeric micelles, CMC was determined by pyrene probe method.

Focusing enhanced micromixers were designed and fabricated. Such type of mixer was preferred to other type since it provided an efficient way to control and vary the mixing time and was easier to fabricate and use. The microreactors were fabricated in glass by a photolithography/wet etching procedure. Glass was selected as substrate for the microreactor since it provided a good optical property, excellent compatibility with the solvent used for the production of PMs, and avoids adsorption of the polymer on channel walls.

Stable hydrodynamic flow focusing was successfully achieved in all three microreactors with the polymer solution in the central focused stream and water in the adjacent streams. Desired width of the focused stream, relating to diffusive mixing time, was obtained and controlled by altering three inlet flow rates. An analytical estimation of the focused stream width was derived and validated with the experimental data. Finally, the mixing time by diffusion for hydrodynamic flow focusing was estimated using a two-dimensional model.

Microfluidic-based reactors were used for the production of PMs in a continuous-flow format. The effects of process operational parameters, polymer concentration and microchannel geometries were examined on the controllability of PM size and size distribution produced. It was found that, within a given microreactor channel dimension, PM size decreased when the flow rate ratio of polymer solution to water was decreased, and a narrower size distribution was observed. That was attributed to the short mixing time needed for a complete mixing by diffusion. Under similar operational conditions, the PM mean diameter decreased when the microchannel dimension was reduced while the PM size homogeneity was improved, showing the contribution of the mixing efficiency on PM characteristics. The analysis of the experimental data also revealed that microfluidic reactor design and fluid flow parameters act in concert to determine the nanoprecipitation process output by controlling the chemical environment in which the aggregation took place.

It was demonstrated that, compared to conventional batch systems, microfluidic reactors provided a more controllable and reproducible process for the production of PMs in terms of both size and size distribution. This represents an important benefit from the point of view of the demand of personalized controlled drug delivery formulation that requires reproducible size distribution and batch-to-batch consistency. For all these reasons, the microfluidic approach developed can provide a simple and effective platform for the production of PMs related to drug delivery applications in the field of nanomedicine.

Chapter 4

Computational study

As described above, microreactor dimension, polymer concentration and flow rate ratio (R) all are important parameters relating to mixing process for solvent exchange. However, it is difficult to experimentally or analytically quantify their effects on mixing process mainly due to the change of solvent composition during diffusive mixing; this change is further associated with fluid viscosity, diffusion coefficient and the fluid velocity profile within the channel geometry. For example, the analytical models (equations 3.1 and 3.2) developed above are largely based on mass flow balance and two-dimensional diffusion without taking account the contribution of viscosity gradient and velocity profile. Using a finite volume method (FVM) based CFD tool, Ansys Fluent 12.1.4, the mixing process was simulated and analyzed in order to quantify the effects of these key parameters.

4.1 Introduction

A simple analytical model based on mass flow balance and on a simplified two-dimensional diffusion was established in the previous chapter (see section 3.3.3) to estimate width of focused stream and mixing time, respectively. However, this analytical model neglects the contribution of viscosity gradient and velocity profile, thus cannot accurately describe the hydrodynamic and the diffusive/advective processes occurred in the microreactors under study.

Since the mixing process represents a crucial step in nanoprecipitation, a more accurate prediction of temporal and spatial distribution of species is desirable for better understanding the microfluidic based production of PMs. In this respect, computational fluid dynamics (CFD) method allows modelling of 3D flow phenomena with high degree of accuracy and providing insight into the flow behaviour within microfluidic mixers/reactors [47, 205, 219-221]. This is because CFD solutions are

based on a full three dimensional calculation which avoids making simplifying assumptions on velocity profiles and shapes of the microfluidic devices. This opens up the possibility to study complex fluid dynamic problems by taking into account the effect of many parameters not easily addressable with a simplified analytical model.

Firstly, the effect of a slightly complicated geometry of both channel and channel junction derived by the isotropic wet etching procedure, which produced approximately a hemispherical cross section; the microchannel geometry, in turn, affects flow profile and shape of the focused stream.

Secondly, the effect of viscosity difference between central and sheath streams, that has been shown to have an effect on the width of the focused stream, as demonstrated previously for channel with rectangular cross section [205, 222].

Thirdly, the effect of non-uniform velocity profile produced by both pressure driven flow [223] and viscosity gradient [205] on diffusive flux within micro environment. Specifically, a non uniform velocity profile across the channel section produces position-dependent secondary effects on diffusive flux [224], which result from the dependence of local residence time from the location within the channel cross section [48]. Vice versa, diffusive mixing has also an effect on velocity profile demonstrating a high extent of coupling between velocities field and concentration field [205]. When miscible streams with different viscosity are used, as the mixing proceeds, the local viscosity across the channel will change as the different species diffuse. As a consequence the velocity profile also changes as function of the mixing extent [224] making more complicated an analytical estimation of the mixing extent.

Lastly, by means of an in-house build code, the effect of the local viscosity change on the diffusivity (D) of the species, and its implication on mixing process could be addressed.

For all the reasons stated above, a numerical model describing the hydrodynamic focusing mixing process used for PM production has been established. Method and results of the simulations are reported in the following section.

4.2 Materials

The study was carried out using three different fluids, namely two Pluronic® solutions in DMSO, $7.5 \cdot 10^{-3}$ and $1.5 \cdot 10^{-2}$ M, and deionised water. Dynamic viscosity and density of the two Pluronic solutions were determined experimentally, while water properties were found in the material database of Fluent 12.1 software.

Kinematic Viscosity measurements were carried out using Cannon-Fenske viscometer (Sigma-Aldrich, UK). Viscometers with different capillary size, namely 50 and 150, were used to match the viscosity ranges of the solutions. All the measurements were performed at constant temperature of 25 °C. The values represent the average of five different measures for each sample.

For density measurements, the following procedure was applied. The liquid was left to equilibrate at 25 °C in a thermostatic bath. Once the equilibrium was reached, the liquid was poured into a calibrated volumetric flask previously equilibrated at the same temperature. The volume of fluid was then weighted using an analytical scale (PS-100, Fisher Scientific, UK). The density was then calculated by dividing the obtained mass by the volume of the fluid. The value was an average value of five different measures for each sample. Material properties for the three fluids used are reported in Table 4.1.

Table 4.1 Material properties of the fluid used for the CFD simulation.

Material	μ (Pa·s)	ρ (Kg·m ⁻³)
Pluronic® 7.5·10 ⁻³ M*	9.108·10 ⁻³	1095.0
Pluronic® 1.5·10 ⁻² M*	28.190·10 ⁻³	1091.9
Water (liq.)	0.894·10 ⁻³	997.1

*: Pluronic® solution in DMSO

μ : Dynamic viscosity measure at 25°C

ρ : density at 25°C

4.3 Methods

The modelling started with the creation of three-dimensional models of the three used microreactors. Microreactors volumes were then meshed. Finally, fluids flow and species transport analyses were run to assess the hydrodynamics present during the PM formation process.

4.3.1 3D model generation

The three-dimensional geometries of the three microreactors were created with a CAD software Gambit 2.4.6 (Simmetrix Inc., U.S.A.). The channel measures were obtained using a surface profiler (P-16+ stylus profiler, KLA Tencor, U.S.A.) and were the same as reported in Table 3.3.

Since the unavoidable imperfection coming from the microreactor fabrication procedure, such as variation of the channel width and height and walls roughness, the cross section of the real channels might differ from the ideal geometry designed by the CAD software in some section of the microreactors. Nevertheless, it is believed that these minor differences from the real microreactors will not have a significant effect on the outcome of the finite element analysis.

Moreover, connection tubes between the microreactors and syringes, and the initial wider parts of the inlet channels (see Figure 3.7) were not included in the 3D model. It was calculated that the effect of these parts on the pressure was negligible compared to the pressure drop along the reactor. Furthermore, it was also calculated that the 300 μm long inlet channels included in the 3D model were sufficiently long to have a completely developed flow at the channel junction. Therefore, keeping these parts would have given more elements and nodes that would have increased unnecessarily the computational cost.

Figure 4.1 shows the orthographic projections and aerial views of Microreactor 2 CAD design, while Figure 4.2 shows a comparison between the dimensions of the three microreactors.

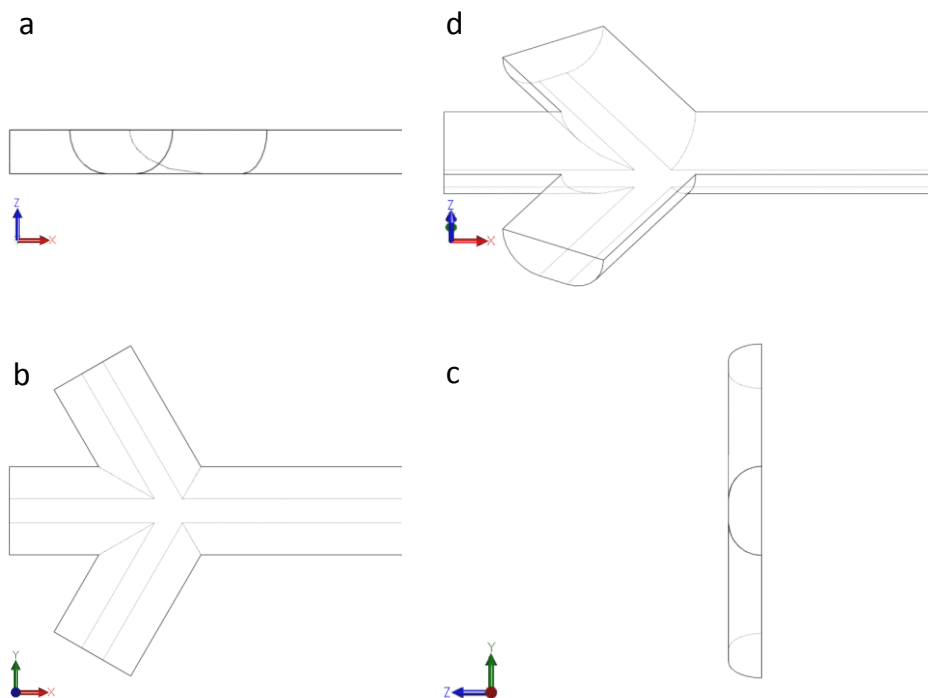


Figure 4.1. Orthographic projection (a, b and c) and aerial view (d) of Microreactor 2 as designed in Gambit 2.4.6. (a) lateral, (b) top and (c) front views.

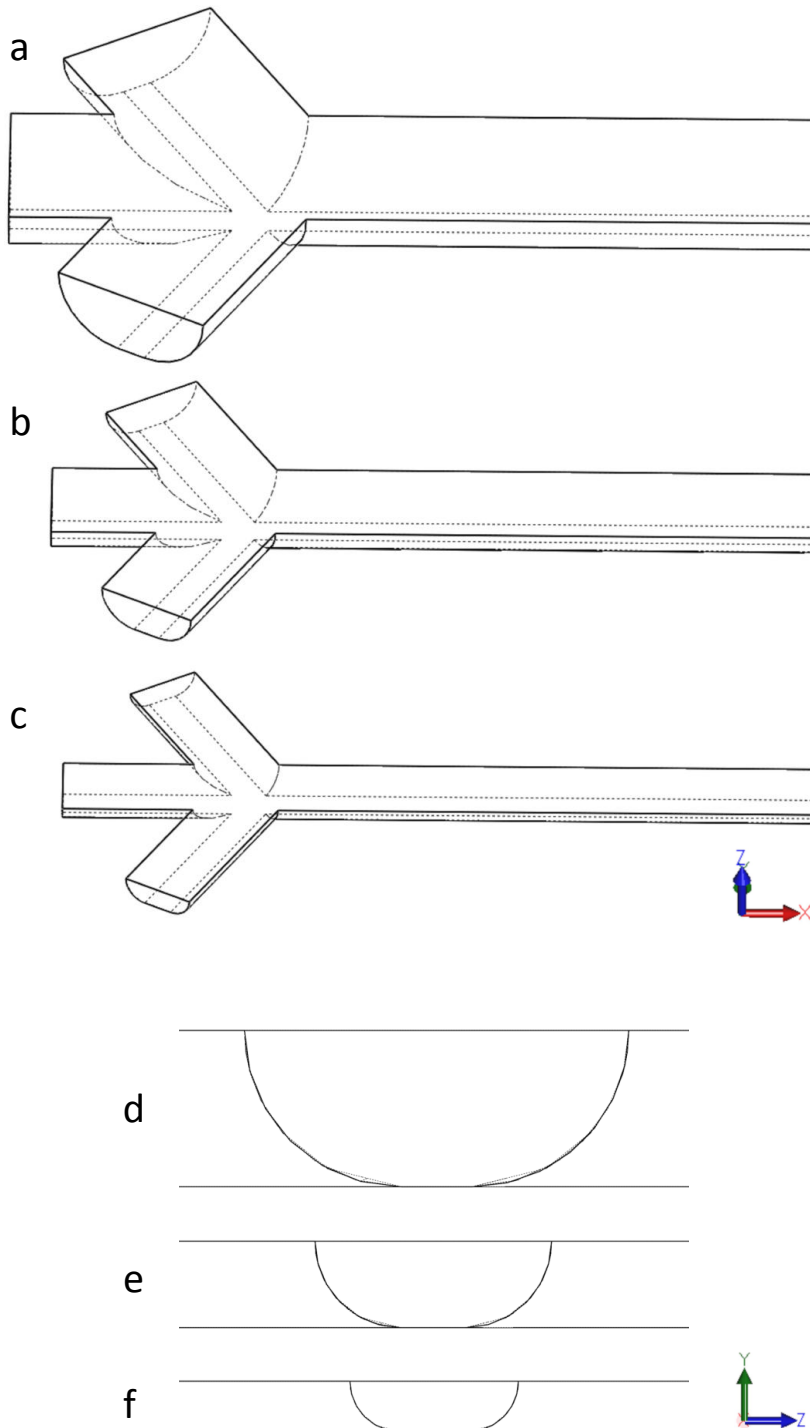


Figure 4.2. Microreactors dimensions comparison. Aerial views (a-c) and front view (d-e) of Microreactor 1 (a and d), Microreactor 2 (b and e) and Microreactor 3 (c and f).

It must be noted that decreasing the channel height, the channel aspect ratio tend to increased. This unavoidable trend is related to the fabrication technique that is characterized by an under-etching effect. Because of this effect, the channel dimension at the glass bonding surface (top wall) is typically equal to $w_b + 2h$, where w_b is the width

of the bottom wall (typically comparable with the width of the photoresist pattern) and h is the channel depth. Experimental measure of channel cross section by surface profiler agreed well with the expected geometry.

4.3.2 Mesh generation

The computational domain was discretized with software Gambit 2.4.6 using a stair-step meshing scheme. The stair-step meshing scheme creates and meshes a faceted volume with a shape that approximates the volume to be meshed. All the mesh elements in the faceted volume are cubic hexahedra of uniform size.

Stair-step scheme was selected since it provided the possibility to have a high number of elements avoiding creation of highly skewed or inverted elements that would had been affected the simulations. Furthermore, the stair-step scheme resulted in a more uniform mesh density within the channel volume than a classical body-fitted mesh scheme. The number of elements in the meshed volumes was chosen to be as large as possible in order to provide improved accuracy and satisfactory resolution of the numerical analysis. A high number of mesh elements was also selected in order to reduce the stair-step-like shape of the channel walls.

The maximum number that could be produced with the used hardware/software set-up dictated the maximum number of the elements. A cell size of $2 \mu\text{m}$ was chosen for Microreactor 2 and 3, which leads to a total number of 9,670,768 and 4,393,130 cells, respectively. Due to the difficulties of decreasing the cell size below $2.5 \mu\text{m}$, a cell size of $2.5 \mu\text{m}$ was chosen for Microreactor 1, which leads to a total number of 3,403,439 cells. Table 4.2 summarizes the number of elements and nodes of the three microreactors used. Figure 4.3 shows the meshed volume in the region of the channel junction for the three used microreactors.

Table 4.2 Mesh size of Microreactors 1, 2 and 3

	Microreactor 1	Microreactor 2	Microreactor 3
Number of elements	3403439	9670768	4393130
Number of nodes	3825416	10678615	5071187

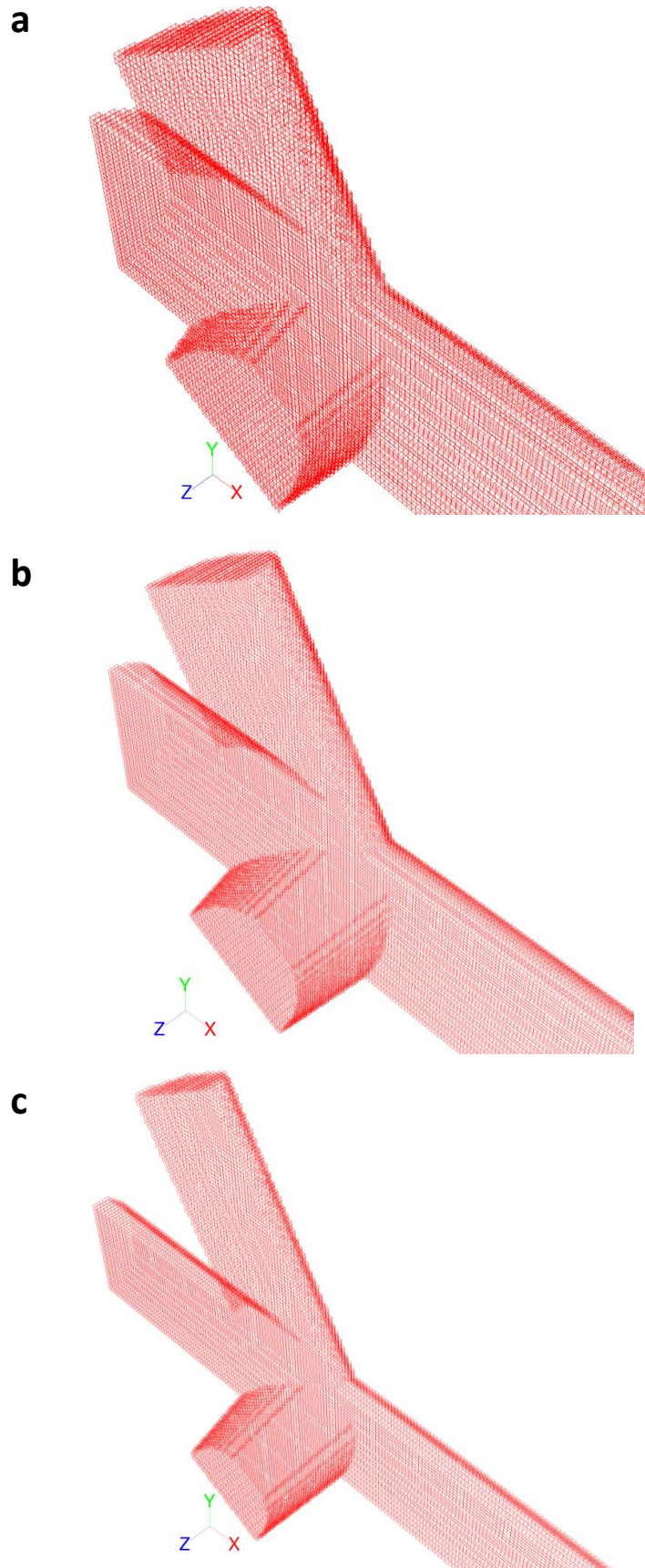


Figure 4.3 Particular of the mesh near the junction section for Microreactors 1 (a), 2 (b) and 3 (c).

4.3.3 Assumption, boundary conditions and model parameters

In computational works, it is often necessary to make some assumptions as not all parameters can be considered. This is generally due to a lack of computational resources. For the present analysis, the following assumptions were applied:

- The size of the mesh was subjected to a compromise between a fine mesh density and the computational cost.
- Contact angle and interfacial force between the two liquid (Pluronic® solutions and water) and channels walls were not included.
- Fluids were considered incompressible.
- Fluids (Pluronic® solutions) and their water mixtures were considered Newtonian (the viscosity does not depend on the shear stress applied).
- Velocity at flow inlet boundary was assumed to have a uniform profile.
- Constant pressure (equal to 101,325 Pa) was imposed at downstream outlet boundary.
- No-slip boundary condition at channel walls.
- Zero-species concentration flux was applied at the solid walls of the microreactors.
- Constant temperature analysis ($T=25$ °C)
- Approximation of material properties (i.e., diffusion coefficient).

In addition, in this study the fluid mixture density and viscosity were assumed to vary according with a volume-weighted mixing law and mass-weighted mixing law, respectively. The density was computed as,

$$\rho = \frac{1}{\sum_i \frac{Y_i}{\rho_i}}, \quad (4.1)$$

where Y_i is the mass fraction and ρ_i is the density of the fluid i . Viscosity was computed as mass fraction average of the pure fluid viscosities,

$$\mu = \sum_i Y_i \mu_i , \quad (4.2)$$

where μ_i is the dynamic viscosity of the fluid i . To investigate the effect of viscosity variation on the microfluidic mixing process, a user defined function was implemented in order to describe the effect of the variation of μ on the diffusion coefficient (D) of the species (DMSO and water). To this aim, the species were approximated as spheres, so that their diffusion coefficient were given by the Einstein-Stokes relation,

$$D = \frac{kT}{6\pi\mu r} \quad (4.3)$$

where K_B is the Boltzmann's constant, and r the radius of the species. From the assumption that temperature and density were constant, an approximate dependence of the diffusion coefficient on viscosity of the medium could be written as [224],

$$\frac{D_{\mu_1}}{D_{\mu_2}} = \frac{\mu_2}{\mu_1} , \quad (4.4)$$

then, knowing the value of diffusion coefficient (D_{μ_1}) at a certain viscosity μ_1 , equation 4.4 could be used to estimate D_{μ_2} at any other viscosity. The binary diffusion coefficient for DMSO/water was assumed to be $10^{-9} \text{ m}^2 \cdot \text{s}^{-1}$ at viscosity μ_1 equal to $0.894 \cdot 10^{-3} \text{ Pa} \cdot \text{s}$ (viscosity of water at 25°C).

It should be noted that in the current numerical models Pluronic® solutions in DMSO were considered as single substance fluid and not comprising two independent species (i.e., DMSO and Pluronic®). Fluid mass flow rates were selected according to the experimental setting (see section 3.4).

4.4 Flow and species transport analysis

Ansys Fluent 12.0 computational fluid dynamics package, which utilizes the finite volume method for spatial discretization, was used to solve three dimensional conservation equations for mass, momentum (Navier-Stokes) and chemical species. Mass continuity equation in an inertial reference frame can be written as follow:

$$\frac{\partial \rho}{\partial t} + \nabla \cdot (\rho \vec{v}) = 0 \quad (4.5)$$

where ρ is the density of the fluids and v is their velocity. The term $\partial \rho / \partial t$ represents the variation of the fluid density over the time, however as stated in section 4.3.3, in

In the current analysis the fluids were considered incompressible laminar flow with negligible temperature dependence therefore, this term was neglected since always equal to 0. With respect to temperature, it must be noted that density and viscosity value of the fluids were experimentally determined at the temperature of 25 °C. Obtained values were used as boundary condition in the computational analysis.

Momentum conservation equation in an inertial reference frame is described as follow,

$$\frac{\partial}{\partial t}(\rho \vec{v}) + \nabla \cdot (\rho \vec{v} \vec{v}) = -\nabla p + \nabla \cdot \vec{\tau} + \rho \vec{g}$$

(4.6)

where p is the static pressure and the term $\rho \vec{g}$ is the gravitational body force. $\vec{\tau}$ is the stress tensor expressed as,

$$\vec{\tau} = M \left[\left(\nabla \vec{v} + \nabla^T \vec{v} \right) - \frac{2}{3} \nabla \cdot \vec{v} I \right] \quad (4.7)$$

where M is the molecular viscosity and I is the unit tensor. Mass conservation for chemical species (i^{th}) transport equation was computed as,

$$\frac{\partial}{\partial t}(\rho Y_i) + \nabla \cdot (\rho \vec{v} Y_i) = -\nabla \cdot \vec{J}_i, \quad (4.8)$$

where Y_i and \vec{J}_i represents the mass fraction and the diffusion flux due to concentration gradient of the species i^{th} respectively. Diffusion flux was computed using Fick's law given by,

$$\vec{J}_i = -\rho D_{i,m} \nabla Y_i, \quad (4.9)$$

where $D_{i,m}$ is the mass diffusion coefficient for the specie i in the mixture as computed by the used defined function reported in equation 4.4.

4.5 Computational procedure

In the solution procedure, a finite volume differencing scheme was adopted to solve the algebraic equations and their boundary conditions formed by discretizing the closed set of governing equations (see previous sections). Fluent 12.0 setup used for the computational analysis is reported in Table 4.3.

Table 4.3 Fluent setup: solver

Discretization of the momentum, mass and chemical species equations conservation and their solutions	Steady-state pressure-based solver
Governing equation	Linearized using an implicit formulation
Pressure velocity coupling method	Segregated, Semi-Implicit method for Pressure Linked Equation (SIMPLE) algorithm
Gradient spatial discretization	Least square based
Pressure spatial discretization	Second order
Momentum spatial discretization	QUICK
Species mass fraction spatial discretization	QUICK

With regard to species transport equation, it must be noted that the numerical simulation are subjected to numerical diffusion. Numerical diffusion represents a numerical error introduced by the spatial discretization of the convective terms in chemical species transport equations (see eq. 4.8) that introduce an additional unphysical diffusion mechanism [47]. In order to minimize the effect of numerical diffusion in the current numerical analysis a third-order QUICK spatial discretization scheme was used for species mass fraction [47, 221, 225]. Moreover, during the meshing step, care was taken in order to have a large number of cells in the grid, and to have cells edges parallel to flow direction [47, 226].

Under relaxation technique was adopted to avoid divergence during iterative solution procedure. Under relaxation factors associated with each solved equation with the pressure based solver are reported in Table 4.4.

A number of preliminary tests were necessary to establish the fluent set up and the corresponding values of relaxation factors that provided a sufficient stability and that increase the convergence of the computational method. Once the optimal setup parameters were selected, a steady state calculation was performed.

Table 4.4 Fluent setup: solver under relaxation factors values

Pressure	0.3
Density	1
Body force	1
Momentum	0.5
Species mass fraction	0.96

The velocity and species mass fraction component were obtained by solving the governing equations reported in section 4.4. At first, the velocity components, pressure and species mass fraction values were initialized in the entire domain with assumed realistic averaged values to speed up the convergence. Then, Fluent solved the governing equations to obtain the new accurate values of these variables. It was noted that, in order to increase the stability of the calculation, an initial 30 iterations for only flow equations (mass and momentum conservations) were necessary. After this initial step, the equations governing the species transport (equations 4.4 and 4.9) were also included. An average number of 3000 iterations were necessary to reach the solution convergence, where the values of the normalised residuals of the variables reached constant small values (typically less than 10^{-6}). At solution convergence, the calculation was stopped and the results obtained stored for further post processing analysis.

Velocity field, mass fraction and effective diffusion coefficient of both DMSO and water were selected as outputs in order to assess the hydrodynamic inside the microreactor. The values of the different output parameters were calculated at each node. Data post-processing was carried out with MATLAB 10R 2010a (The Matworks Inc., USA) and ORIGIN 8 SR4 (Origin Lab Corp., USA) software.

4.6 Results and discussion

The computational procedure described in the previous section was applied for 36 different CFD models, which represent all the possible combinations of the following experimental matrix:

- 3 different microreactors: Microreactors 1, 2 and 3 (see Table 3.3)
- 2 different initial polymer concentrations (PC): $1.5 \cdot 10^{-2}$ and $7.5 \cdot 10^{-3}$ M

- 6 different flow rate ratios (R): 0.13, 0.10, 0.083, 0.066, 0.05 and 0.03

The accuracy and reliability of the code were verified using the experimental results of the width of the focused stream [227]. The numerical results have been found to be concurred with the experimental results (see below). Typical results of the output parameters are presented in the following sections.

4.6.1 Width of the focused stream

The focused stream width (w_f) represents a crucial parameter which controls the mixing time since it reflects the diffusion distance. Therefore, to verify the reliability of the code, a comparison between the numerical and experimental results of focused stream width was carried out [227]. Figures 4.4 shows the simulated concentration polymer solution counters at different focusing conditions (a-d). Adjacent microphotographs (e-h) qualitatively validate the numerical results. In particular, the effect of polymer solution concentration (a, b), microreactor dimension (b, c) and flow arte ratio (R) (c, d) variation are reported. It must be noted the different values of DMSO/water mass fraction obtained for different focusing condition are related to the effect on the diffusive mixing time and will be discussed in the next section.

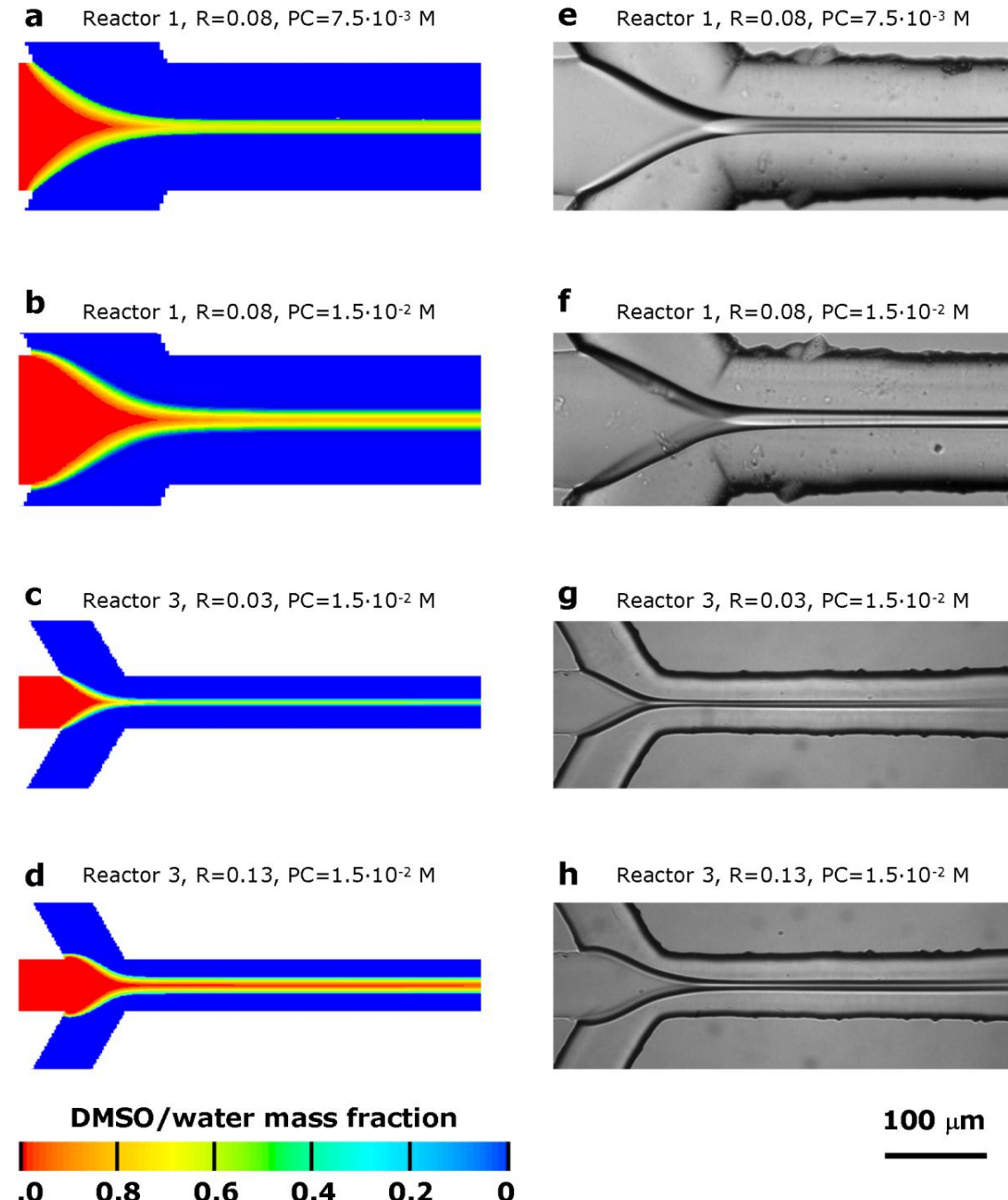


Figure 4.4 Simulated polymer solution concentration contours (a-d) corresponding photomicrograph (e-h) at a different polymer concentration (PC) (a, b) and different flow rate ratio (R) (c, d) in Microreactor 1 (a, b) and Microreactor 3 (c, d).

The analysis of the data in Figure 4.4 shows that a high degree of accuracy was achieved with the implemented numerical method. To further demonstrate the reliability of the code, a comparison between experimental and numerical values of width of focuses stream is reported in Figure 4.5. In the numerical model, w_f was defined as the distance between the local maximum of the second derivate of the mass

fraction profile in the mixing channel [205]. Specifically, the mass concentration profile was extrapolated from a horizontal plane in the mixing channel at a distance of 100 μm downstream the centre of the channel junction, and vertically at the middle level between from the channel bottom and top. The chosen position corresponds to the point where experimental measurements were taken.

The difference between experimental and numerical data for the relative width of the focused stream was less than 6% (error bars) indicating a good agreement. The difference between the numerical and experimental values was likely due to the effect of numerical diffusion as well as uncertainty in the experimental measurement.

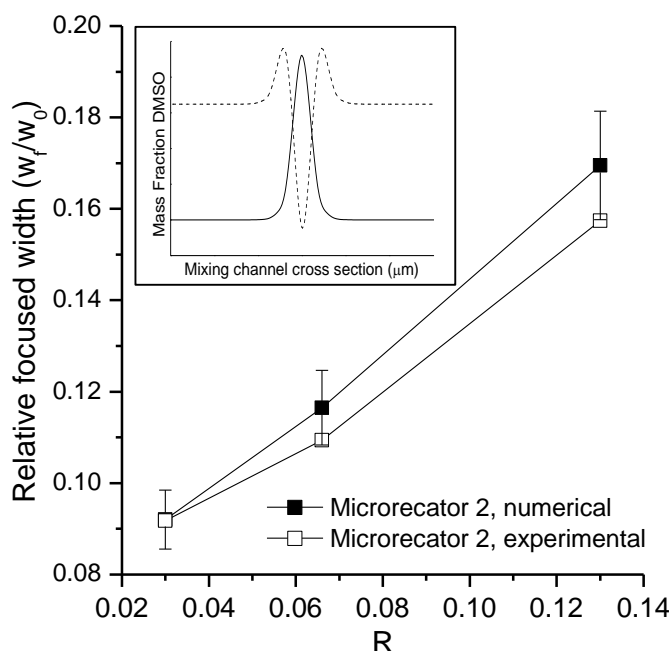


Figure 4.5 Relative focused stream width as a function of flow rate ratio (R) for Microreactor 2 (Solid squares: numerical simulation data; Open squares: experimental data). Inset reports the computed concentration profile for $R = 0.03$ (solid line) and the corresponding second derivative (dashed line) showing the relative position of the local maxima. Data referred to a polymer initial concentration of $7.5 \cdot 10^{-3}$.

4.6.2 Velocity field

Velocity field within the microfluidic channel is strictly related to width of focused stream and diffusive-advection transport phenomena as previously demonstrated [205, 228]. Based on that, the velocity field within the microreactors was studied to better understand the interplay between hydrodynamic, diffusive mixing phenomena and nanoprecipitation process.

Figure 4.6 shows a typical CFD simulated velocity field contours obtained by Ansys Fluent 12.0.

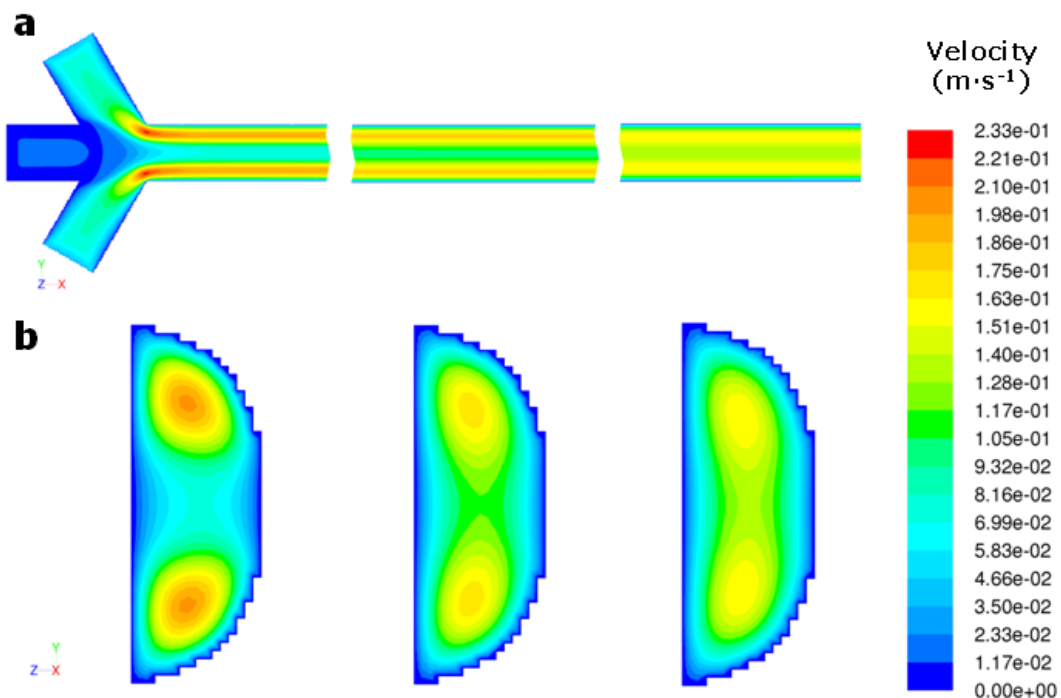


Figure 4.6 CFD simulated velocity field contours for $\text{PC}=1.5\cdot10^{-2}$, $R=0.08$ within Microreactor 2. Contours are showed for (a) three longitudinal sections at junction, middle and end of the main mixing channel at a distance from bottom and upper wall of $14.5 \mu\text{m}$, and (b) corresponding cross section views.

The presence of the central focused stream caused velocity to be slower in the central region of the channel occupied by the more viscous stream (i.e., polymeric solution). This effect was more pronounced at the mixing channel entrance, while tended to disappear as the fluid flow downstream the channel. This effect is due to the species transport that occurs at the interface between water and polymer solution, which mixes the two phases creating a mixture of them. Specifically, mixing between the two phases leads to a change in viscosities, which in turn affects the velocity field. The latter is therefore strictly correlated with the extent of mixing.

The relative difference in velocity between central and lateral stream was found to be dependent on different parameters such as, R , PC and mixing channel dimension (e.g. microreactor dimension). The effect of the different parameters could be appreciated from the velocity profile in Figure 4.7. Velocity profiles were computed for a horizontal plane in the mixing channel at different distance downstream the centre of the channel junction and vertically equidistant from bottom and upper channel walls.

The results clearly indicated the influence of diffusive mixing on the velocity profile along the mixing channel. For small R (Figure 4.7a) and low PC (Figure 4.7b), the velocity profile at the end of the mixing channel (i.e., 30 mm downstream the channel junction) assumed the typical parabolic velocity profile of a single fluid flow in microchannel. Conversely, when, R (Figure 4.7a-c), PC (Figure 4.7b,e) and reactor dimension (b, d, and f) were increased, at the end of the mixing channel, the velocity profile was characterized by a higher velocity magnitude where the less viscous liquid (i.e., water) was flowing, suggesting a smaller mixing extent. Nevertheless, a flattening of the velocity profile along the channel could still be appreciated.

To conclude, the peculiar shape of the velocity profile and its evolution demonstrated that the assumption of a uniform average velocity used in the analytical model described in the experimental section cannot be used to accurately describe the mixing process within microfluidic reactors. Conversely, a numerical model considering the different velocities can describe well the influence of the hydrodynamic on the nanoprecipitation process.

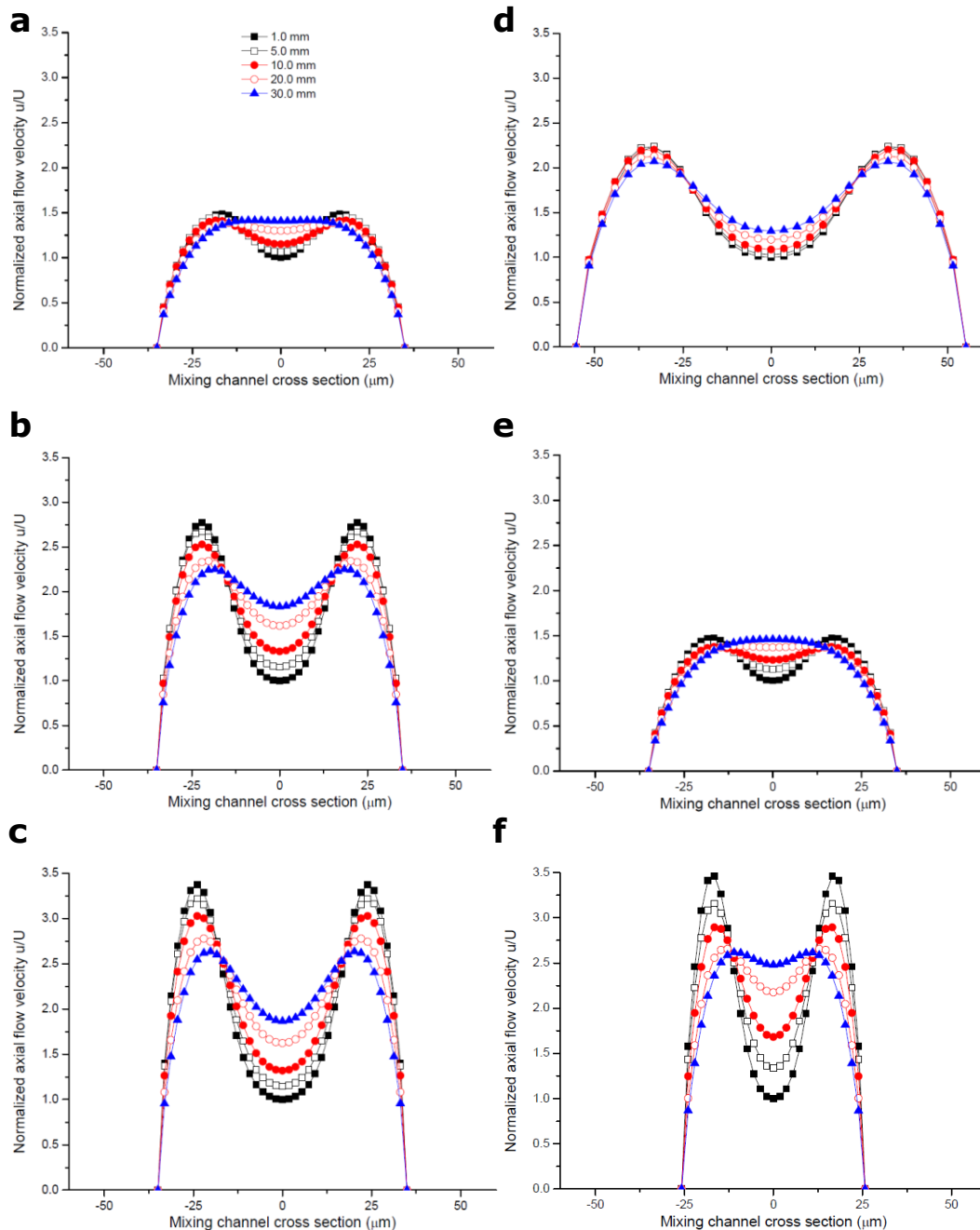


Figure 4.7 CFD simulated velocity profile plots along the mixing channel at different distance from the channel junction and for different process set up. (a) $\text{PC} = 1.5 \cdot 10^{-2}$, $R = 0.03$ in Microreactor 2; (b) $\text{PC} = 1.5 \cdot 10^{-2}$, $R = 0.08$ in Microreactor 2; (c) $\text{PC} = 1.5 \cdot 10^{-2}$, $R = 0.13$ in Microreactor 2; (d) $\text{PC} = 1.5 \cdot 10^{-2}$, $R = 0.08$ in Microreactor 1; (e) $\text{PC} = 7.5 \cdot 10^{-3}$, $R = 0.08$ in Microreactor 2; (f) $\text{PC} = 1.5 \cdot 10^{-2}$, $R = 0.08$ in Microreactor 3.

4.6.3 Diffusive mixing

Experimental results and CFD models [126, 228] have shown that two different regions, characterized by different mechanisms of mixing, can be identified within a focused stream. The first region, characterized by a rapid convective-diffusive transport is located in the arrowhead-shaped focusing region at the channel junction. The second, in which the mixing is limited by molecular diffusion in the direction normal to streamlines, is located in the focused stream region, downstream the channel junction. Within the focused stream, mixing is limited by the exchange of solvent through the interface boundary in the span-wise direction normal to streamline. The surface-to-volume ratio of the focused stream, therefore, assumes a crucial role in controlling the rate of exchange between the two fluids, DMSO and water.

Figure 4.4 shows the polymeric solution concentration contours in Microreactor 1 (a, b) and 3 (b, c) and at two different polymer initial concentration (PC) namely, $7.5 \cdot 10^{-3}$ (a) and $1.5 \cdot 10^{-2}$ M (b-d). The solution composition is expressed as mass fraction of DMSO in the mixture of DMSO and water resulting from the solvent exchange process.

Higher polymer solution concentration (Figure 4.4a) and high R (Figure 4.4d) resulted in a slightly wider focused stream width and a relatively shallow concentration gradient. A wider focused stream is characterized by a relatively low surface to volume ratio (of the focused stream) which led to a slow and gradual solvent shifting process along the interface between the two phases. Consequently, polymer solution mass fraction remained relatively high in the centre of the focused stream past the arrowhead-shaped focusing region. This is likely to have an effect on the PM output as demonstrated in the experimental section (see section 3.3.4). With these mixing conditions, only a small fraction of the unimers started to self-assemble in the convective-diffusive focusing region while, a large fraction of unimers remained solubilised in the solvent (DMSO) and eventually self-assembled within the mixing channel downstream focusing region. Within the mixing channel, a relatively slow diffusion process resulted in a gradual spatial and temporal variation of the polarity of the environment around the polymer. This slow mixing maintained the DMSO mass fraction high within the focused region and leads to longer growth phase and lowering of the insertion barrier resulting in relatively larger PMs.

Conversely, smaller PC (Figure 4.4a), R (Figure 4.4c) and channel dimension resulted in relatively narrow focused stream width in which, as demonstrated previously, mixing process is dominated by the diffusive transport within the initial focusing region [228]. This can be appreciated from the lower DMSO mass fraction value in the inner part of the focused stream. In this focusing condition, advection within the focusing region,

abruptly reduce the focused stream width reducing the diffusion length and resulting in an abrupt spatial and temporal concentration gradient. As R decreases the flow velocity of the central stream decreases, therefore, diffusion in the arrowhead-shaped focusing region becomes significant.

In addition, the relatively higher surface-to-volume ratio leads to a rapid depletion of the focused stream content by diffusive transport in the mixing channel. These constrain the assembly of PMs in a shorter time, and a large fraction of unimer self-assembly in PMs within the initial focusing region resulting in smaller and uniform PMs (see section 3.3.4). Figure 4.8 shows example mass fraction profiles of DMSO on the middle plane between the channel top and bottom (i.e., at a depth of 14.5 μm) at different distances along the channel in Microreactor 2 where R equals to 0.06 and initial Pluronic F127 concentration in DMSO is $7.5 \cdot 10^{-3} \text{ M}$.

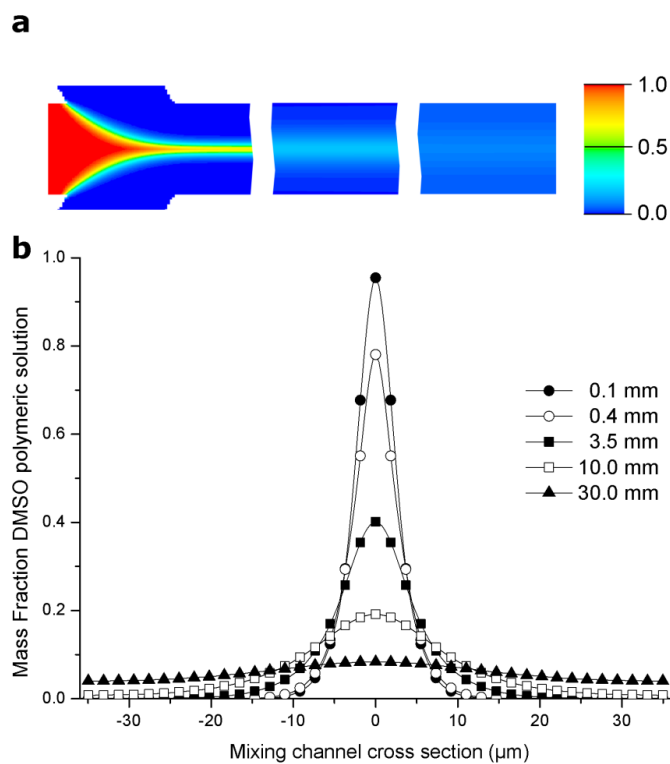


Figure 4.8 CFD simulation of diffusive mixing along the main mixing channel in Microreactor 2.

$R = 0.06$, Pluronic F127 solution concentration = $7.5 \cdot 10^{-3} \text{ M}$. (a) Simulated mass fraction contours showing three longitudinal sections at junction, middle and end of the main mixing channel. (b) Mass fraction profiles of DMSO at different distances along the channel. The profiles are on the middle plane between the bottom and top of the channel (at a channel depth of 14.5 μm). [Reprinted from Journal of Colloid and Interface Science, 357, Lorenzo Capretto,Dario Carugo,Wei Cheng,Martyn Hill,Xunli Zhang, Continuous-flow production of polymeric micelles in microreactors: Experimental and computational analysis, 243-25, Copyright 2011, with permission from Elsevier.](#)

It is observed (Figure 4.8a) that, while the three streams flow along the main channel diffusive mixing takes place across the channel as indicated by the broadening of the middle DMSO stream. This is further quantified by the mass fraction profiles of DMSO at different distances along the main channel (Figure 4.8b). It can be seen from the profiles that DMSO mass fraction peak decreases along the channel, and there is a significant drop immediately after the three flows meet at the channel junction due to the convective-diffusive transport in the arrowhead-shaped focusing region. For example, at a distance of 0.4 mm DMSO mass fraction drops down to 0.78. It has been found that the critical water concentration (CWC) for the formation of PMs is 14.28% (V/V) which corresponds to a DMSO mass fraction of 0.852. This suggests that solvent composition in the main domain of the focused flow stream reaches the CWC enabling PM formation. At a distance of about 30 mm the mass fraction of DMSO is around 0.07 across the channel section indicating the approximately complete mixing.

Further insight regarding the mixing process can be obtained considering the advection of unimers nuclei and growing PMs along the different streamlines, and the kinetics of the DMSO polymeric solution mass fraction evolution along the mixing channel for a give hydrodynamic focusing condition. As follows from the analysis of velocity and mass fraction profiles reported in Figure 4.7 Figure 4.8 respectively, a nanoprecipitation intermediate (nuclei or growing PMs), flowing along a streamline closer to the centre of the focused stream, is exposed to a slower solvent change that results in a longer τ_{mix} . This leads to larger and more polydisperse PMs. Vice versa, an intermediate advecting along a streamline close to the water/polymeric solution interface, undergo a fast environment polarity change resulting in shorter τ_{mix} and smaller and more uniform PMs. The two different rates at which the solvent shifting proceeds represents therefore a possible source of polydispersity. Increasing R , an increasing portion of unimers self-assembly within the diffusive region, resulting in larger PMs as compared to those produced in the convective-diffusive region.

4.6.3.1 Effect of viscosity on nanoprecipitation process

To further examine the mixing process within different channel geometries at different R levels, CFD simulations were carried out under the identical conditions used for obtaining the results shown in Figure 3.11. The simulated mass fraction profiles of DMSO are displayed in Figure 4.9a for Microreactors 2 and 3 where R was set at 0.05 and 0.1, respectively. It should be noted that a greater R was selected for Microreactor 3 in order to obtain a comparable focused stream width (8 μm) in the two microreactors which have different channel widths. As can be seen from the profiles (Figure 4.9a) mass fractions of DMSO decreased along the channel for both microreactors but to different extent; the profiles for Microreactor 2 were generally

lower than that for Microreactor 3, especially in the first section of the mixing channel (up to a distance of 0.4 mm from the junction centre). When the mixing proceeds further along the channel, the difference became insignificant where the DMSO mass fraction is lower than the critical point (i.e., CWC) in both reactors.

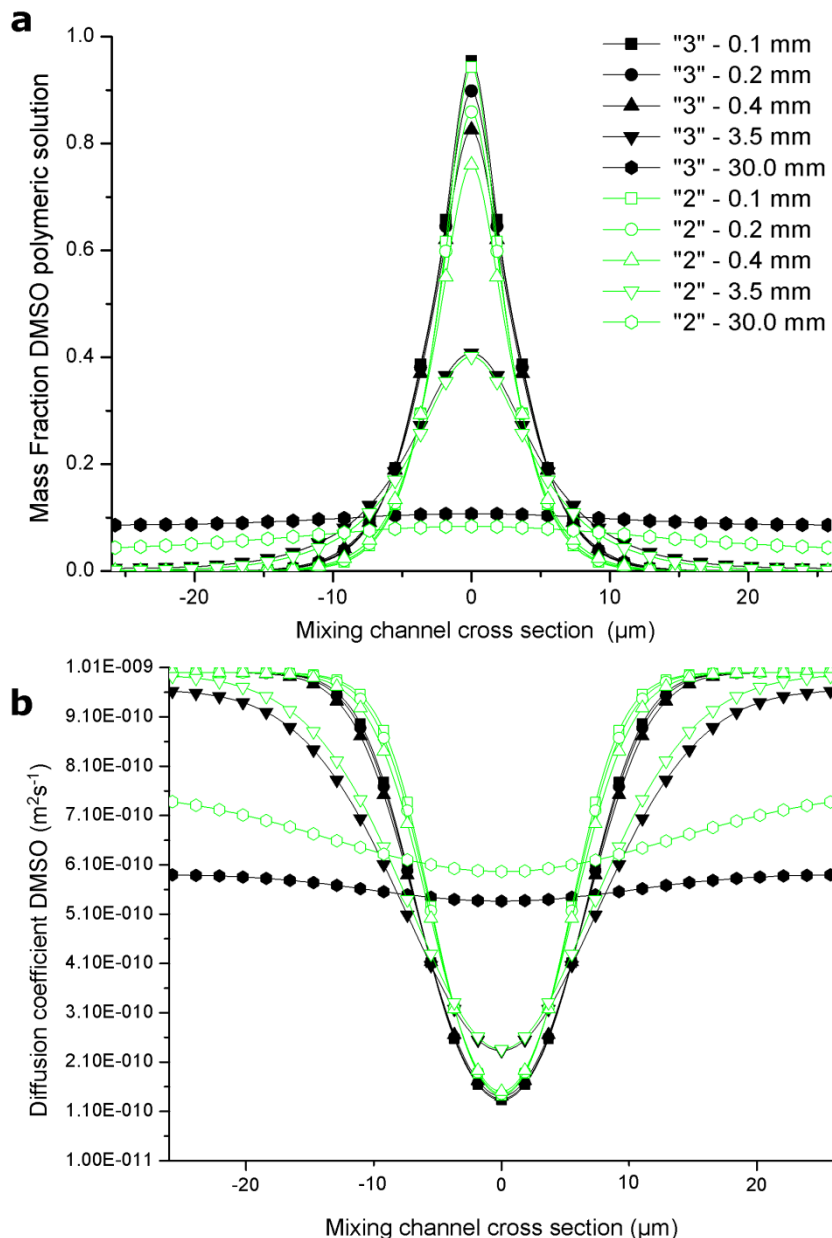


Figure 4.9 CFD simulated (a) mass fraction profiles and (b) diffusion coefficient profiles of DMSO along the main channel of Microreactors 2 (open markers) and 3 (solid markers) with R equal to 0.05 and 0.1, respectively. Pluronic F127 solution concentration: $7.5 \cdot 10^{-3}$ M. [Reprinted from Journal of Colloid and Interface Science, 357, Lorenzo Capretto,Dario Carugo,Wei Cheng,Martyn Hill,Xunli Zhang, Continuous-flow production of polymeric micelles in microreactors: Experimental and computational analysis, 243-25, Copyright 2011, with permission from Elsevier.](#)

The simulated results (Figure 4.9a) showed clearly that the mixing in Microreactor 2 proceeded faster than that in Microreactor 3 while a comparable width of the focused stream was set. This is because, during the solvent exchange between DMSO and water streams the solvent composition changes can result in variation in solvent diffusivity. This was further evidenced by the diffusivity difference between the two microreactors (Figure 4.9b), where the increased R with a larger amount of polymeric solution caused a locally increase in the viscosity, which in turn decreased the diffusivity of the species and the mixing process. Figure 4.9b shows the CFD simulated DMSO diffusivity profiles across the channel at given distances along the channel for both microreactors. It can be seen that the diffusivity variation is in line with the change in DMSO mass fractions; lower diffusivities corresponds to slower mixing. In general, diffusivity in Microreactor 2 is greater than that in Microreactor 3. A shorter mixing time throughout the domain of focused stream resulted in more homogeneous environment in which the self-assembly takes place. It is well known, that in nanoprecipitation process homogeneous conditions are associated with more homogeneous PMs [79, 132, 229, 230]. In addition, a shorter mixing time permits to reach the CWC throughout the entire domain of focused stream in shorter time. This results in a rapid depletion of unimers through nucleation and, in turn, more homogeneous and smaller PMs [79, 229]. This was further confirmed by the result reported in Figure 3.12 and 3.13.

Figure 4.10 illustrates the effect of polymer concentration on the mixing process in Microreactor 3 where R equal to 0.13. From the profiles reported it can be seen (Figure 4.10a) that the mass fraction of $1.5 \cdot 10^{-2}$ M Pluronic F127 solution is generally higher than that of $7.5 \cdot 10^{-3}$ M solution at a comparable position. It is also observed that at higher polymer concentrations with higher viscosities (the viscosities of the two solutions are 0.02819 and 0.009108 Pa· s, respectively) the mass fraction decreases along the channel at a lower rate indicating a slower mixing process. This difference was further pronounced by the diffusivity profiles associated with viscosity (Figure 4.10b). As can be seen from the diffusivity profiles, the diffusivity of the higher concentration solution is generally lower than that of the lower concentration solution. The largest difference was found around the centre of the focused stream where the diffusivity was about one order of magnitude smaller for the higher concentration polymer solution. As a result, the decrease in the diffusivity causes a slower solvent exchange between the focused and laterals streams that decreases the efficiency of the mixing.

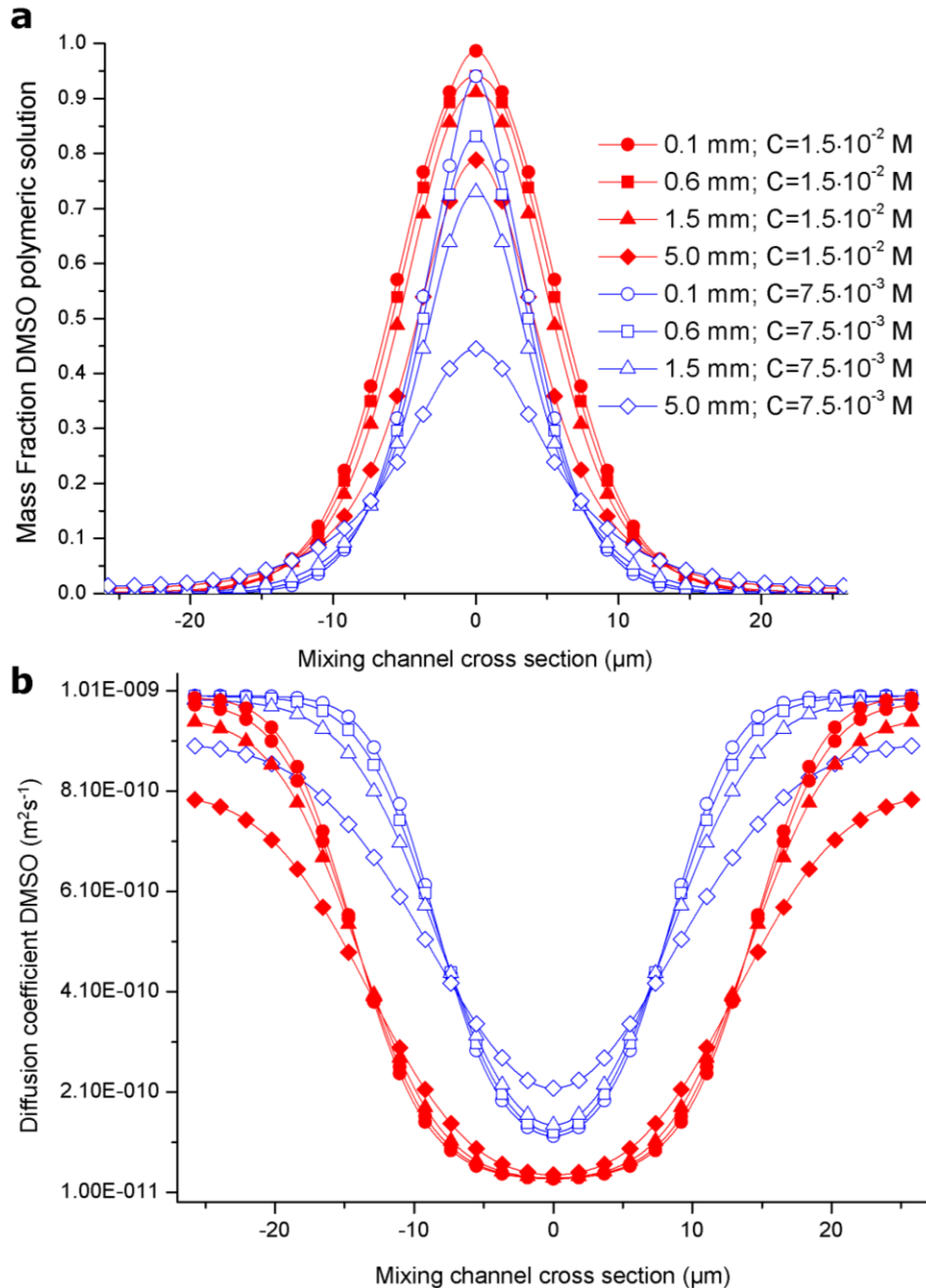


Figure 4.10 CFD simulated (a) mass fraction profiles and (b) diffusion coefficient profiles of DMSO along the main channel of Microreactor 3 at Pluronic F127 solution concentrations of $7.5 \cdot 10^{-3} \text{ M}$ (open markers) and $1.5 \cdot 10^{-2} \text{ M}$ (solid markers). $R = 0.13$. [Reprinted from Journal of Colloid and Interface Science, 357, Lorenzo Capretto, Dario Carugo, Wei Cheng, Martyn Hill, Xunli Zhang, Continuous-flow production of polymeric micelles in microreactors: Experimental and computational analysis, 243-25, Copyright 2011, with permission from Elsevier.](#)

The increase in PM dimension obtained with a higher initial polymer concentration (Figure 3.9) could be explained as an effect of viscosity increase and diffusivity decrease (Figure 4.10b). However, an effect could also be played by a decrease in the

distance between unimers, which in turn leads to a decrease in the aggregation time (τ_{agg}). The shortened τ_{agg} further enhanced the mismatching between τ_{agg} and τ_{mix} [132].

4.6.3.2 Focused stream shape

One important characteristic of the current multi-fluid flow fluidic condition is the high viscosity difference between the central focused stream and the two sheath fluids. These multi-fluid flows are characterized by the tendency for the lower viscous fluids to place themselves where the shear stress is greater (near the channel walls) and envelops the high viscosity fluid (polymeric solution) [222]. In addition, the diffusion between the two components induces complex viscosity gradients which affect velocity field and mixing [222].

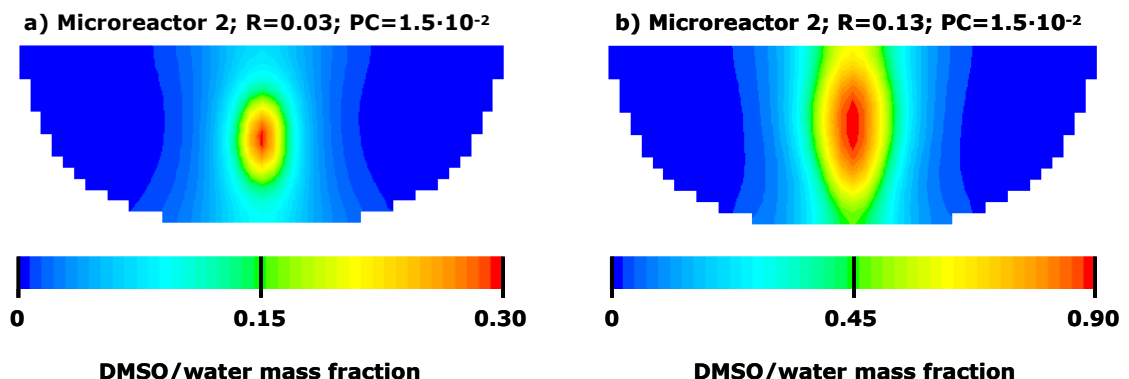


Figure 4.11 CFD simulated mass fraction contours DMSO polymeric solution along the main channel of Microreactor 2 at Pluronic F127 solution concentrations of $1.5 \cdot 10^{-2}$ M for $R=0.03$ (a) and $R=0.13$ (b). The contours refer to a cross section 5mm downstream the channel junction.

Figure 4.11 shows the numerical simulated mass fraction contours of polymeric DMSO solution at a distance from the channel junction of 5 mm for two different R , namely 0.03 (a) and 0.13 (b). It is shown that at small R (Figure 4.11a) the more viscous fluid is detached from the top and bottom walls and become ensheathed by the less viscous fluid leading to the formation of a viscous thread. This effect is also present for larger R (Figure 4.11b) but at significant less extent. This viscous ensheathing process is likely to have an effect on mixing extent; however, a quantitative study of the importance of this effect has not been yet addressed. Nevertheless, a qualitative analysis of this effect showed that decreasing R the focused stream become progressively more ensheathed by water streams. This results in a progressive increase of the volume-to-surface ratio of the contact interface between the two phases, which is likely to result in faster mixing and thus smaller and less polydisperse PMs.

In addition, from the analysis of the mass fraction contours reported in Figure 4.10b, can be appreciated the characteristics focused stream cross-sectional shape. Wider section located at the centre of the channel and narrower section near the upper and bottom walls characterize it. Furthermore, in Figure 4.11a can be appreciated a slightly higher polymeric solution mass fraction value in proximity of the bottom wall compared to the region near the upper wall that indicate a faster mixing in the upper region of the channel respect to the bottom region. This counterintuitive result is likely to be caused by the shape of the channel junction that exposes the polymeric stream fluid to the water streams in gradual temporal fashion. In particular, the polymeric stream flowing in the upper side of the channel meets the two water streams in advance respect to the fluid flowing in the lower section (see Figure 4.1). However, this effect seems not affecting the mass fraction contour for larger R .

To further demonstrate the correlation between focused stream shape and mixing process Figure 4.12 shows a typical computed polymeric solution mass fraction evolution along the mixing channel at two different R . The mass fraction profile was computed along three lines located in midsagittal plane of the mixing channel at three different distance from the bottom channel wall, namely 7.25 (*lower*), 14.5 (*centre*) and 21.75 μm (*upper*). The graph shows that the mass fraction of polymeric solution evolves with different kinetics in the three regions. Specifically the mass fraction tends to remain higher in the central region while decrease faster in upper and lower regions. Notably, mass fraction in the upper region decreases faster than in the lower region for smaller R ($R=0.03$), while it decreases slower than in lower section for higher R ($R=0.13$).

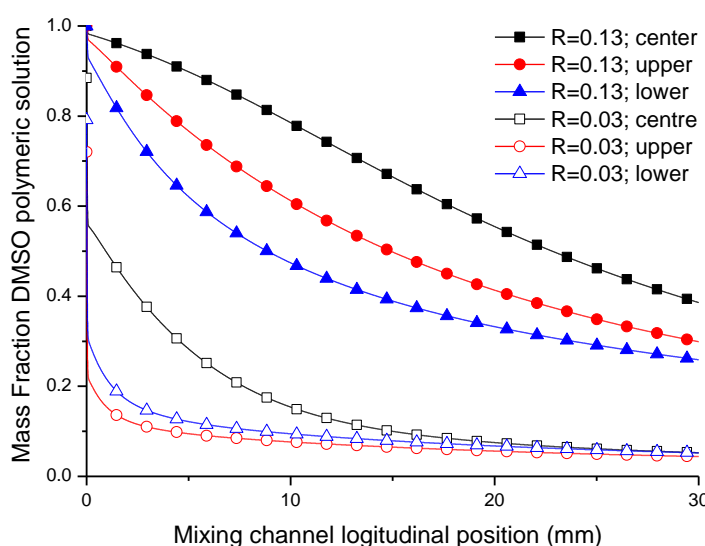


Figure 4.12 CFD simulated mass fraction evolution of DMSO polymeric solution along the main channel of Microreactor 2 at Pluronic F127 solution concentrations of $1.5 \cdot 10^{-2}$ M for $R=0.03$ (a) and $R=0.13$ (b).

In addition, for larger R , a larger difference in the value of the mass fraction in the three regions can be noted. The different kinetics of the evolution of DMSO mass fractions are likely to have an effect on the PM assembly resulting in the production of PMs with different size characteristics within the three different regions. In order to better characterize this effect a novel computational model to study the effect of viscous force and channel shape on the focused stream shape is under study.

4.6.3.3 Mass fraction time evolution

Figure 4.13 shows the computed DMSO mass fraction evolution along the mixing channel as function of the residence time for different flow focusing conditions. The mass fraction evolution was computed at the centre of the focused stream equidistant from the top and bottom walls. The mass fraction time evolution clearly depicts the kinetics of the mixing process in a fashion that is not convoluted with the role of velocity field. Is therefore possible to investigate the role of mixing process and residual solvent content during the self-assembly of PMs.

In section 4.6.2 has been shown that hydrodynamic and diffusive mixing in microchannels are highly coupled features, therefore, to investigate solely the effect of mixing process, computed mass fraction evolutions along the mixing channel have been processed through an *in-house* developed Matlab-based code. The code was used to transform the domain of space (i.e., mixing channel longitudinal position) into the domain of time (i.e., residence time). Specifically the residence time (t_{res}) was calculated using the following equations,

$$t_{\text{res}} = \sum_{i=0}^N \frac{x_{i+1} - x_i}{\bar{v}} \quad (4.10)$$

$$\bar{v} = \frac{v_{x_i} + v_{x_{i+1}}}{2} \quad (4.11)$$

where, x_i is the distance from the channel junction of the node (i) in which the mass fraction of DMSO was computed, N represents the maximum number of nodes within the line in which mass fraction of DMSO was computed, and v_{x_i} is the velocity of the fluid at the node (i).

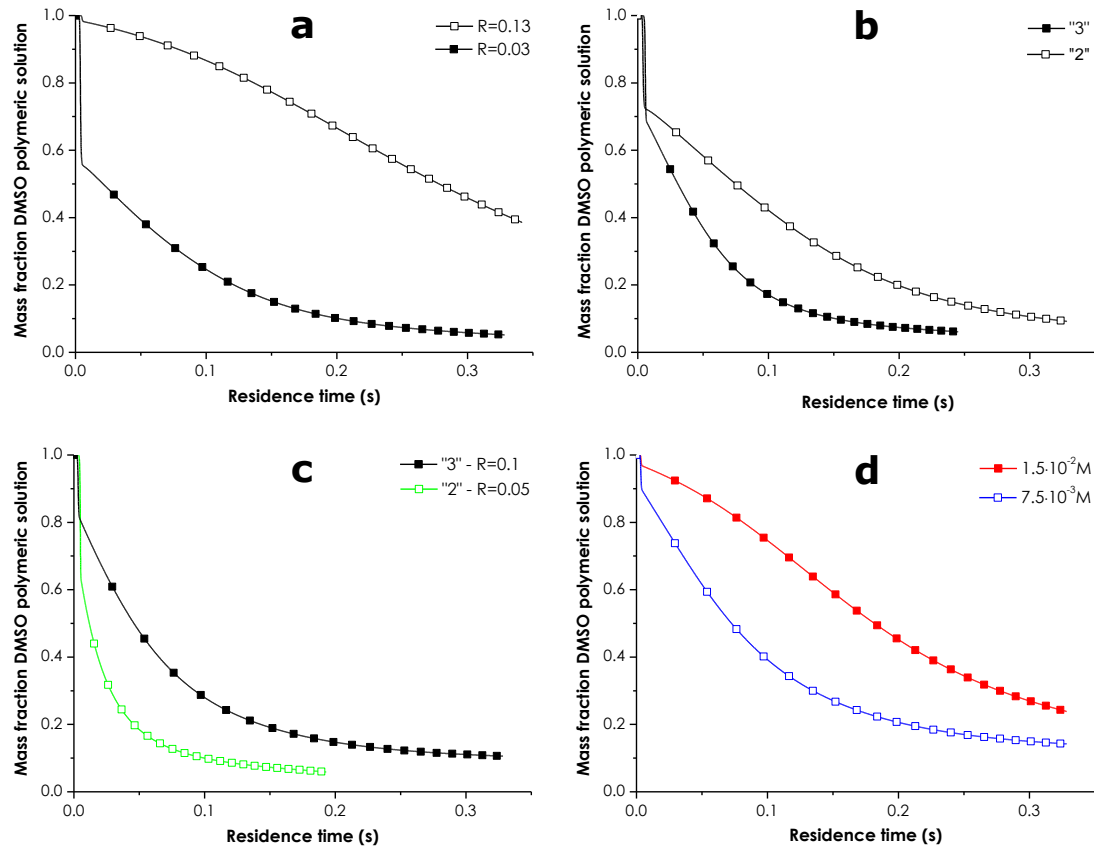


Figure 4.13 CFD simulated mass fraction evolution of DMSO as function of the residence time.

(a) Microreactor 2 at Pluronic F127 solution concentrations of $1.5 \cdot 10^{-2}$ M, $R=0.13$ (open markers) and $R=0.03$ (solid markers); (b) $R=0.05$ at Pluronic F127 solution concentrations of $1.5 \cdot 10^{-2}$ M, Microreactor 3 (solid markers) and Microreactor 2 (open markers); (c) Pluronic F127 solution concentration at $7.5 \cdot 10^{-3}$ M, Microreactors 2 (open markers) and 3 (solid markers) with R equal to 0.05 and 0.1, respectively; (d) $R = 0.13$ in Microreactor 3 at Pluronic F127 solution concentrations of $7.5 \cdot 10^{-3}$ M (open markers) and $1.5 \cdot 10^{-2}$ M (solid markers).

Figure 4.13a reports the mass fraction time evolution at two different flow rate ratio, 0.03 and 0.13, in Microreactor 2 at polymer concentration of $1.5 \cdot 10^{-2}$ M. It is shown that decreasing R a much faster mixing kinetics can be obtained as clear from the lower values of DMSO mass fraction obtained at $R=0.03$ as compared with $R=0.13$. In particular, for small residence time (i.e., $\lesssim 10$ ms), mixing at $R=0.03$ shown an abrupt reduction of the mass fraction due to the mixing in the arrowhead-shaped focusing region. In addition, a faster rate also characterized the mixing at residence time > 10 ms, as suggested by the higher slop of the curve at $R=0.03$. This is probably due to a series of factors including, higher diffusivity (see section 4.6.3.1 Effect of viscosity on nanoprecipitation process), narrower focused stream width and ensheathing (see section 4.6.3.2 Focused stream shape). For $R=0.03$, less than 4 ms are needed to drop the DMSO concentration below the CWC within the entire domain of the focused

stream causing a fast nucleation of the unimers. Conversely, for $R=0.13$, a longer time (~ 80 ms) to trigger the nucleation within the entire domain of the focused stream is required. As a result of a faster nucleation rate and a lower amount of DMSO during the self-assembly process, smaller and more homogeneous PMs can be produced with at smaller R (see Figure 3.9).

Figure 4.13b shows the effect of the channel dimension on the mixing process where R and polymer concentration were kept constant at $R=0.05$ and $1.5 \cdot 10^{-2}$ M, respectively. It is shown that, while the initial drop of mass fraction is similar within the two reactors, mixing proceeds faster when a smaller microreactor is used. This results in higher DMSO concentration during the PM growth process that is likely to lower the insertion barrier for unimers causing the formation of a slightly larger PMs (see section 3.3.4.3 Matching between mixing and precipitation processes, and Figure 3.9).

To further investigate the kinetics of the mixing process, CFD simulations were carried out under the identical conditions used for obtaining the results in Figures 3.11 and 4.9. Figure 4.13c shows that, despite the same w_p , mixing in Microreactor 2 proceeds faster than in 3 resulting in a smaller amount of solvent present during the self-assembly process and in turn smaller PMs (Figure 3.11). The more efficient mixing in Microreactor 2 is due to an abrupt reduction of the DMSO concentration at the beginning of the mixing process, and to a subsequently faster rate of mixing. These two characteristics result from an increased extent of mixing in the focusing region and to an increased focused stream ensheathing, respectively. Moreover, as demonstrated previously (see section 4.6.3.1 Effect of viscosity on nanoprecipitation process), a larger R results in a larger amount of polymer fed in the microreactor that, increasing the fluid viscosity, causes a slower diffusivity. The effect of viscosity on diffusivity is further demonstrated in Figure 4.13d where a larger polymer concentration results in slower mixing where R and microreactor dimension were kept constant (see also Figure 4.10).

4.7 Limitations of the model

Despite the qualitative agreement between our numerical results and the existing theory of PM formation, a more in-depth elucidation of nanoprecipitation process within microfluidic device is still confounded by the complex interplay between molecular and hydrodynamic phenomena. In this respect, some limitations can be identified in the current numerical model.

Firstly, the polymeric solution was simplified as a one-component fluid and did not take into account the relative difference in diffusion behaviour between unimers and

solvents. In addition, the various kinetic of advection and diffusion of unimers and intermediate PM structure (nuclei and growing PMs) had not been addressed (see Chapter 5 Production of drug loaded PMs).

Secondly, the mixing law used to describe the variation of viscosity of the fluid did not take into account the different effect of viscosity produced by the dissolution of the polymer within, solvent, non solvent and any mixtures of them. To address these limitations and propose a quantitative study of PM formation by computational model remains the subject of future work.

4.8 Summary

Computational fluid dynamics (CFD) method has been shown to allow modelling of 3D flow phenomena with high degree of accuracy, providing insight into the flow behaviour within microfluidic mixers/reactors. With the aid of a numerical model, the hydrodynamic inside the microreactor was characterized, and its effect on the mixing process was correlated with the nanoprecipitation process output. The numerical model was validated using experimental data of the width of the focused stream, revealing a good agreement between experimental and computational data and reliability of the code.

The study of the velocity flow profile inside the microreactor showed that hydrodynamic and diffusive mixing in microchannels are highly coupled features and this interplay should be considered carefully during the development process of micromixers.

From the compared analysis of experimental and computational results it is evident that different parameters (R , polymer concentration, channel dimension and shape, viscosity difference) act in concert to influence mixing process and microreactors output. It was demonstrated that varying R , channel dimension and polymer concentration, is possible to alter the relative amount of unimers self-assembly in the convective-diffusive hydrodynamic focusing region versus unimers assembly in the diffusive dominated mixing region. Mixing extent and velocity have been also correlated with the variation in viscosity and diffusivity during solvent exchange across the flow streams. Shape of the channel junction and viscosity difference between water and polymeric streams are likely to influence focused stream shape and relative mixing process. These results also indicate a possible source of polydispersity in PM size distribution. It is anticipated that the current code could be conveniently applied to study newly design of microreactor and possibly predict their effect on mixing and nanoprecipitation process.

Chapter 5

Co-precipitation of drugs and block copolymers within microfluidic reactors

Microfluidic reactors have shown to be a powerful tool for the production of organic nanoparticles (NPs). However, there is still a lack of understanding of the role that the microfluidic environment plays in directing the nanoprecipitation process. Here is reported the experimental investigation of the production of block copolymer stabilized organic NPs using a microfluidic-based reactor where the core-shell structured NPs contained the active β -carotene stabilized by block copolymer Pluronic F127. The results were interpreted in combination with computational fluid dynamics modelling of our microfluidic implementation, which also accounts for the complex interplay of molecular and hydrodynamic phenomena within the nanoprecipitation process, in order to understand the hydrodynamic process and its influence on the NP formation process. The effects of operational fluidic conditions and feed concentration of polymers and actives were examined systematically on the NP characteristics and on the kinetics of the co-nanoprecipitation process. It was demonstrated that competitive reactions resulted in the formation of two types of NPs, i.e., either with or without loading organic active. The obtained results were interpreted by taking in consideration a new parameter representing the mismatching between the aggregations of the two precipitant species (polymer and drug), which plays a decisive role in determining the size and polydispersity of the prepared hybrid NPs. These results expand the understanding of the co-nanoprecipitation mechanism of active and block copolymer stabilizer, and on the role exerted by microfluidic environment, proving information that could be translated to the emerging fields of microfluidic formation of organic NPs and nanomedicine.

This part of the work has been carried out in collaboration with Dr. Wei Cheng in the University of Southampton. In particular, Dr. Wei Cheng carried out the experiments for the production of NP at different β -carotene/Pluronic F127 molecular ratio.

5.1 Introduction

NPs have attracted much attention owing to their unique properties and numerous promising applications that result from a reduction in particle dimension. In particular, organic NPs have been investigated for potential applications such as drug delivery [231], targeted bioimaging [232], pigment dispersion in foodstuffs and paints, and plant protection, where a very diverse range of chemical products with a low water solubility are used [7, 9, 79, 128, 137].

Increased attention has been given to block polymeric based NPs as drug delivery vehicles, due to their ability to minimize systemic distribution of cytotoxic agent, localize drug by passive or active targeting, and increase drug bioavailability [231, 233]. It is understood that those unique properties are associated with NP size and polydispersity which have a primarily role in controlling their cellular interaction and biodistribution. Therefore, to improve the controllability over NPs preparation output is of critical importance for their success in potential clinical applications [134, 230, 234]. However, this still remains a challenge associated with the conventional bulk methods [231, 233].

Moving from conventional bulk systems, Johnson and Prud'homme [134, 230, 234], have successfully developed meso-scale continuous flow confined impinging jets (CIJ) and multiple inlet vortex (MIVM) mixers, and have demonstrated that a very fast mixing process is critical to obtain kinetically controlled nanoprecipitation, and consequently a control over NP size and polydispersity [235, 236]. Recent advances in the development of continuous flow microfluidic reactors have also provided powerful tools for the production of NPs, and the investigation of the associated nanoprecipitation process [83, 85]. Of particular relevance to NP production is the small length scale used in which fluidics is restricted to laminar flow and diffusive mixing. This allows a very fast mixing process and precise prediction and control of fluid flow in a continuous flow format, which can be leveraged to exert control over size, polydispersity and surface properties of NPs in a reproducible manner [100, 129]. Additionally, NP size control allows the elimination of post-synthesis purification procedures required for the removal of macroscopic aggregates, which are generally formed in bulk synthesis, resulting in no material loss and high productivity [129, 235].

Microfluidics also offers the possibility to solve some of the drawbacks associated with CIJ and MIVM, by allowing the study of the effect of different fluid flow ratios and fast preparation and screening of the small sample batches [230, 236]. The small internal volume provides an opportunity to decrease the amount of sample required for the

analysis/reaction, which is particularly useful when rare and valuable substances/samples are used, and during NP formulation optimization [129]. In addition, laminar flow microfluidic reactors operate under steady-state conditions, which results in predictable and reproducible mixing across fluid interfaces. This, together with the visual accessibility of the systems, has enabled real time monitoring to assist the investigation of the NP formation mechanism [19, 21, 114, 129].

Whilst microreactors have been largely employed for the preparation of a wide range of inorganic colloidal nanoparticles such as gold, silver and silica [20, 105], relatively little has been done for the fabrication of organic NPs [25, 29, 237]. Attempts have been made to produce polymeric stabilized NPs using microreactors [29, 101, 130]. These studies have further demonstrated the advantages of using microreactors for the control of NP size characteristics.

Despite the interest in organic NP production, there is still a general lack of fundamental understanding of the nucleation and growth process [21, 114, 126, 158]. This is particularly true for the production of NPs in microscale reactors, where, owing to their unique characteristics, the microfluidic environment and associated parameters (i.e., flow rate ratio, channel dimension and residence time) have been shown to considerably affects NP output in terms of dimension and stabilization [126, 129].

In Chapters 3 and 4, It has been demonstrated that polymeric micelle (PM) size characteristics are determined not solely by flow rate ratio, as largely understood, but also by microreactor dimensions, variation of viscosity and fluidic conditions, all of which act in concert to direct the mixing process and NP output. Similar findings were also demonstrated by Jahn *et al.* [126] for the production of lipid vesicles. They also examined the role of total flow rate ratio in fine tuning the vesicle dimensions under certain focusing regimes. Karnik *et al.* [29] have shown a consistent decrease in size as the mixing time decreased far below the estimated aggregation time for block copolymer NPs. This was in contrast with the previous results from Johnson *et al.* [132] with CIJ mixers, where a characteristic minimal critical size was associated with a breakpoint mixing time, and was putatively associated with rearrangement of block copolymer during the growth process (see section 2.3.3 Aggregation kinetics). Furthermore, they showed an effect of mixing time on controlling the surface properties of NPs, as results of a smaller portion of hydrophilic block buried in nascent NPs. These observations indicated that the mechanism of NP production in a microfluidic environment might differ from that postulated for CIJ and MVIM mixers, and more investigations are therefore required to open the way for industrial applications of microfluidic production of organic NPs.

In this respect, this section reports a detailed study on the formation of block copolymer stabilized NPs (hybrid NPs) by controlled microfluidic mixing. The effects of operational fluidic conditions and feed concentration of polymers and actives on the size characteristics and the polymer coverage of the organic actives were examined systematically. Pluronic F127 was used as a model block copolymer whilst highly hydrophobic β -carotene was used as a model drug. The reported results demonstrated the existence of competitive reactions resulting in the formation of two types of nanoparticles, i.e., either with or without loading β -carotene in the core-shell structure. The fluid dynamics within the microreactors was also analyzed by a CFD model and correlated to NP outputs and mixing conditions. With the aim of initially investigating the complex interplay of molecular and hydrodynamic phenomena, the CFD model also accounts for the effect on the diffusion process and advection of the formation of slow diffusive species (i.e., nuclei), when the critical water concentration (CWC) is reached. The results were interpreted on the basis of a mismatch between the aggregation starting points of the two precipitant species, and its implication on hybrid NPs formation mechanism is discussed.

5.2 Materials and methods

5.2.1 Materials

Amphiphilic block copolymer Pluronic F127 (average molecular weight 12600) was provided as a gift by BASF Chem Trade GmbH. β -Carotene (purum \geq 97.0%, molecular weight 536.9) and tetrahydrofuran (THF) were obtained from Sigma-Aldrich UK, and used as supplied. Unless otherwise stated all other chemicals were obtained from Sigma-Aldrich UK, and used without further purification.

5.2.2 Fabrication of microfluidic reactor

The glass-made microfluidic reactor employed for the preparation of NPs was fabricated by a photolithography/wet etching procedure, as previously reported (see sections 3.2.3 and 3.3.2).

5.2.3 Preparation of NPs in microfluidic reactor and by bulk mixing

NPs were prepared using microfluidic Reactor 2 (see Table 3.3) and with the method described in section 3.2.5 with minor adaptations. Pluronic F127 and β -carotene were

dissolved in THF at concentrations varying from 12.60 to 157.50 mg·mL⁻¹ and 0.63 to 15.70 mg·mL⁻¹, respectively, and subsequently filtered through 0.22 µm filters before use. ρ and μ measurements of various Pluronic F127 solutions in THF were performed as described in section 4.2. All the measurements were performed at a constant temperature of 25 °C. ρ was found to vary from 890.8 to 913.3 Kg· m⁻³ increasing the concentration of Pluronic F127 from 12.60 to 157.50 mg·mL⁻¹. The reduced viscosity was found to be 24.7 cm³·g⁻¹, resulting in η ranging from 0.60 to 2.24 Pa·s for the different Pluronic F127 THF solutions used.

The production of NPs was carried out in a continuous flow format within microreactors where nanoprecipitation was achieved in a hydrodynamic focusing flow configuration. The organic solution with β-carotene and co-polymer flowed in the central focused stream, and water, acting as a non-solvent, in the adjacent streams. The flow rate of each stream was controlled by the syringe pumps to achieve a desired volumetric flow rate (R) of organic solution to water. R was set at 0.04 for all the experiments unless stated otherwise. Total volumetric flow rate was set at 1 mL·h⁻¹. An inverted microscope (Olympus IX71, Japan) was used to monitor the flow within the microchannel during nanoprecipitation. To prepare NPs at bulk mixing conditions Pluronic F127 and β-carotene solutions were mixed with deionized water (with an organic solution to water volume ratio, R) using the pipette tips.

5.2.4 Nanoparticle sizing and ζ -potential measurements

Typically, 2 mL of the produced NPs were collected and used for analysis and size characterization. Immediately after the preparation of NPs, their size and size distribution were determined both by Dynamic Light Scattering (Zetasizer Nano ZS, Malvern Instruments Ltd., UK) and/or by nanoparticle tracking analysis (NanoSight LM10, NanoSight Ltd. Amesbury, UK). For each measurement, 300 µL of NP suspension was loaded in the detection cell and five measurements were performed to give an average value using Zetasizer software 6.12 (Malvern Instruments Ltd., UK) and NanoSight NTA Analytical Software (NanoSight Ltd. Amesbury, UK), respectively. The NP surface ζ -potential was measured by Zetasizer Nano ZS (Malvern Instruments Ltd., UK) and recorded as the average of three independent measurements.

5.2.5 Transmission electron microscopy (TEM)

TEM examination was carried out on an FEI Technai 12 instrument (FEI, USA) with a beam intensity of 120 KeV. The TEM samples were prepared by depositing 10 µL of NP suspension onto 400-mesh carbon film coated Copper grids (Agar Scientific, UK) and

then dried under reduced pressure. Observations were performed directly following grid preparation.

5.2.6 Critical water concentration (CWC) measurements

The self-assembly of NPs was monitored using dynamic light scattering and ζ -potential with Zetasizer Nano ZS as water was added stepwise (in steps of 20 μL) to 2.0 mL of Pluronic F127 and β -carotene solutions prepared as described in the previous section. The critical water concentration (CWC) represented the percentage of water in the mixture at which the formation of NPs was first detected. ζ -potential measurements were used to obtain an indication of the type of NPs formed at different water percentages.

5.2.7 Computational fluid dynamics (CFD) study

Computational fluid dynamic studies were carried out with similar method (see section 4.3 Methods) and procedures (see sections 4.4 Flow and species transport analysis, and 4.5 Computational procedure) reported in Chapter 4 with minor adaptations.

Mass fraction profiles of β -carotene, THF and Pluronic F127 within injected polymer stream sheathed by two adjacent water (non-solvent) streams were numerically simulated with a two-dimensional model using Ansys Fluent 12.1.4 (ANSYS Inc., Canonsburg, PA). Computational fluid dynamics simulations based on the finite element method (FEM) were performed on a geometry applying 2505650 quadrilateral (2D) mesh elements accounting for the fluid domain comprised between channel junctions and channel outlet. The device developed, as described in Chapter 3, shows some relevant three-dimensional characteristics, including non-uniform velocity and diffusion of the focused stream across the vertical midplane due to no-slip boundary conditions at the top and bottom walls. Nevertheless, the flow and the mass transfer were approximated at the vertical midplane (i.e., equidistant from the top and bottom walls of the channel) with 2D simulations to capture the most salient features of the diffusive process. A symmetry plane was set at the horizontal midplane of the mixing channel.

The flow field and mixing dynamics within the device were modelled using single phase two-dimensional continuity and full Navier-Stokes equations for incompressible flow coupled with the convection-diffusion equations for β -carotene, THF and Pluronic F127 mass transfers. The governing conservation equations of mass, momentum and species are reported in section 4.4.

Constant ρ and μ of $998 \text{ Kg} \cdot \text{m}^{-3}$ and $1 \times 10^{-3} \text{ Pa} \cdot \text{s}$, respectively, were set for water, while for THF solutions they were assumed according with the experimental measurements performed on the Pluronic F127 solutions. The effect of the dissolution of β -carotene on the viscosity was found to be negligible. Density (ρ) and viscosity (μ) of fluid mixture were assumed to vary according with a volume-weighted mixing law (equation 4.1) and mass-weighted mixing law (equation 4.2), respectively [238, 239]. Diffusion coefficients were set as 0.80×10^{-9} [240], 5.22×10^{-11} [241], $1.80 \times 10^{-9} \text{ m}^2 \cdot \text{s}^{-1}$ [242], for β -carotene, Pluronic F127 and THF respectively. The effect of the aggregation of β -carotene and Pluronic F127 on the mass fraction distribution of the two species within the mixing channel was also investigated within the computational model by means of an *in-house* developed user defined function (UDF). In particular, the diffusion coefficients of the species within a specific mesh element were decreased by one order of magnitude when the CWC was reached within the mesh element to account for the reduced diffusivity of the β -carotene and Pluronic F127 nuclei formation. As a result the diffusion coefficients were set at 8.00×10^{-11} and $5.00 \times 10^{-12} \text{ m}^2 \cdot \text{s}^{-1}$ for β -carotene and Pluronic F127, respectively. The two values were in agreement with the diffusion coefficient of small NPs in the range of 10 and 100 nm dimensions [243, 244], representing a good approximation of the formed initial nuclei of the two species. The CWC was set according to the experimentally measured CWC for β -carotene and Pluronic F127.

The velocity and the species concentration at the flow inlet boundary were assumed to have uniform profiles, while a constant pressure (101325 Pa) was imposed at the outlet boundary. Finally, no-slip conditions and zero species concentration flux were applied at the solid walls of the device.

The governing equations and their boundary conditions were solved iteratively until steady-state was reached using an implicit technique (see Table 4.3). In order to minimize the effect of numerical diffusion in the current numerical analysis, a third-order QUICK spatial discretization scheme was used for momentum and species mass fraction [47, 225, 226]. Moreover, during the meshing step, care was taken in order to have a large number of cells in the grid, and to have cells edges parallel to flow direction [47, 225, 226]. Note that under-relaxation technique was adopted to avoid divergence during the iterative solution procedure (see Table 5.1).

Table 5.1 Fluent setup: solver under relaxation factors values

Pressure	0.3
Density	1
Body force	1
Momentum	0.7
Species mass fraction	1

The accuracy and reliability of the code were validated by comparing the numerical outcome with experimental data of the width of the focused stream [227]. The focused/sheath stream interface calculated numerically was defined as the contours that have a Pluronic F127 mass fraction equal to 0.5.

5.3 Results and Discussion

5.3.1 General observation of NP formation within microreactors

Controlled nanoprecipitation of NPs relies on minimizing the mixing time to ensure a homogeneous environment during nucleation and growth of the NPs (see Chapter 3). This is realized by a fast solvent shifting, from organic to non-solvent, that provides a high level of supersaturation for all species, leading to nucleation and diffusion-limited aggregation of precipitates [80]. An effective way to obtain controllable, fast and predictable mixing is the use of a microreactor architecture that allows the creation of a hydrodynamic focusing flow pattern, as shown in previous Chapters.

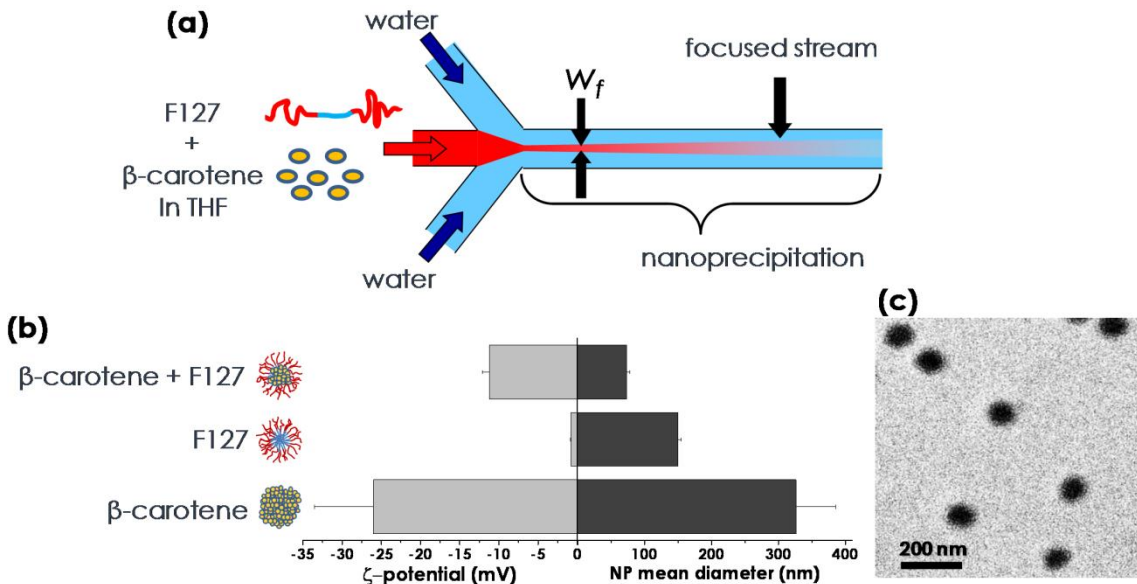


Figure 5.1 Nanoprecipitation of β -carotene/Pluronic F127 hybrid NPs. (a) Schematic representation of the microreactor and of the experimental setup used. (b) Characterization of β -carotene/Pluronic F127 hybrid NPs in terms of ζ -potential and mean diameter of NPs produced using different component in the central organic stream. (c) TEM image of β -carotene/Pluronic F127 hybrid NPs.

Figure 5.1a shows a schematic of the Microreactor 2 used to synthesize block copolymer stabilized β -carotene NPs. THF solution with dissolved amphiphilic block-copolymer Pluronic F127 and β -carotene flowing from the middle inlet, was mixed with water flowing from the two side inlets. A stable hydrodynamic focusing flow was achieved along the main channel with the organic solvent in the central focused stream and water in the adjacent streams. The mixing time (τ_{mix}) is a key parameter for the formation of NPs through precipitation, which directly affects the size characteristics of the NPs produced (see Chapters 3 and 4) [7, 245]. The control of the mixing process by adjusting w_f provided a direct means for the control of particle characteristics, as demonstrated previously [100, 246]. The theoretical mixing time (τ_{mix}) was calculated as,

$$\tau_{\text{mix}} \approx \frac{w_f^2}{4D} \quad (5.1)$$

where D represents the diffusion coefficient for THF.

In the microreactor used, w_f was $4.1 \mu\text{m}$ when $R = 0.04$, resulting in an average τ_{mix} of $\sim 4.4 \text{ ms}$, therefore the mixing was sufficiently fast to be comparable with the induction time (τ_{ind}) for β -carotene NPs and the aggregation time for PMs (τ_{agg}), being in

the order of 20-60 ms [132, 230]. This allowed the creation of homogeneous starting conditions for nanoprecipitation in which the role of mixing was not convoluted with the kinetics of aggregation.

To ensure that β -carotene/Pluronic F127 hybrid NPs were effectively produced, rather than a mixture of unprotected β -carotene NPs and empty PMs, the produced NPs were characterized by different techniques including size (mean diameter) and surface charge (ζ -potential) measurements, and microscopic imaging using a transmission electron microscope (TEM). By altering the compositions in the central organic stream with THF as solvent containing either polymer alone (10.0 mM), β -carotene alone (23.5 mM) or a combination of both, the characteristics of such produced NPs were investigated.

When only Pluronic F127 was used, PMs with a mean diameter of 130 nm were obtained (Figure 5.1b), which was typical for Pluronic F127 PMs produced by microfluidics as previously reported (see Chapter 3). PM ζ -potential was close to 0 mV, as expected due to the electro-neutral nature of the polymer [247]. When only β -carotene was used, it was found that β -carotene precipitated immediately when the flow streams of organic solution were brought in contact with water at the arrow-shape section of the focused stream. As a result, the microchannel was blocked by the precipitated within 2-3 minutes. This was not surprising as the precipitated particles of β -carotene tended to aggregate when they were not dispersed and stabilized by surfactant agents [248].

In order to have an indication of the physicochemical characteristics of the unprotected β -carotene NPs, their production was carried out with bulk mixing approach using the same solution composition and volumetric ratio (R). The produced NPs showed a much larger mean diameter and polydispersity, mainly due to the slow mixing condition applied. They also presented a negative ζ -potential of -26.4 mV (Figure 5.1b), likely resulting from impurities or oxidation as previously reported [249, 250]. Furthermore, the NP suspensions were unstable showing the formation of particle sediment within a few hours after preparation.

NPs prepared when both β -carotene and co-polymers were present showed a much smaller size of around 70 nm, and surface charge of -11.2 mV (Figure 5.1b). They were stable over a long period of time (up to 6 weeks of storage, at the time of the study), with no sedimentation visibly detected. The smaller dimension of the produced NPs, where both the components co-precipitate simultaneously, suggested that a polymer coating stabilized the β -carotene NPs formed. The coating provided multi functions to halt further NP growth thus resulting in reduced hybrid particle size, and to provide colloidal stability during storage. The reduction of the net surface charge further

confirmed the presence of polymer coverage that concealed the negative charge of the β -carotene core. As revealed from TEM images (Figure 5.1c), hybrid NPs exhibited a spherical shape and highly uniform particle size. In addition, the particle size measured from TEM imaging was in good agreement with that measured by the laser scattering and NTA techniques.

5.3.2 Effects of varying β -carotene/polymer concentration on NP characteristics

After confirming the core-shell structure of the hybrid NPs, a series of experiments was conducted aiming to elucidate the interplay between β -carotene and copolymer kinetics of nanoprecipitation, in order to understand the mechanism of self-assembly of hybrid NPs in laminar-flow microfluidic environment. To examine the effect of concentrations of both β -carotene and copolymer, formation of NPs in the microreactor was carried out with three solution compositions (Pluronic F127 concentrations of 7.5, 10.0 and 12.5 mM) at fixed β -carotene/polymer molar ratio (MR) of 2.35. Figure 5.2a illustrates the experimental results showing the effect on NP size at different conditions applied.

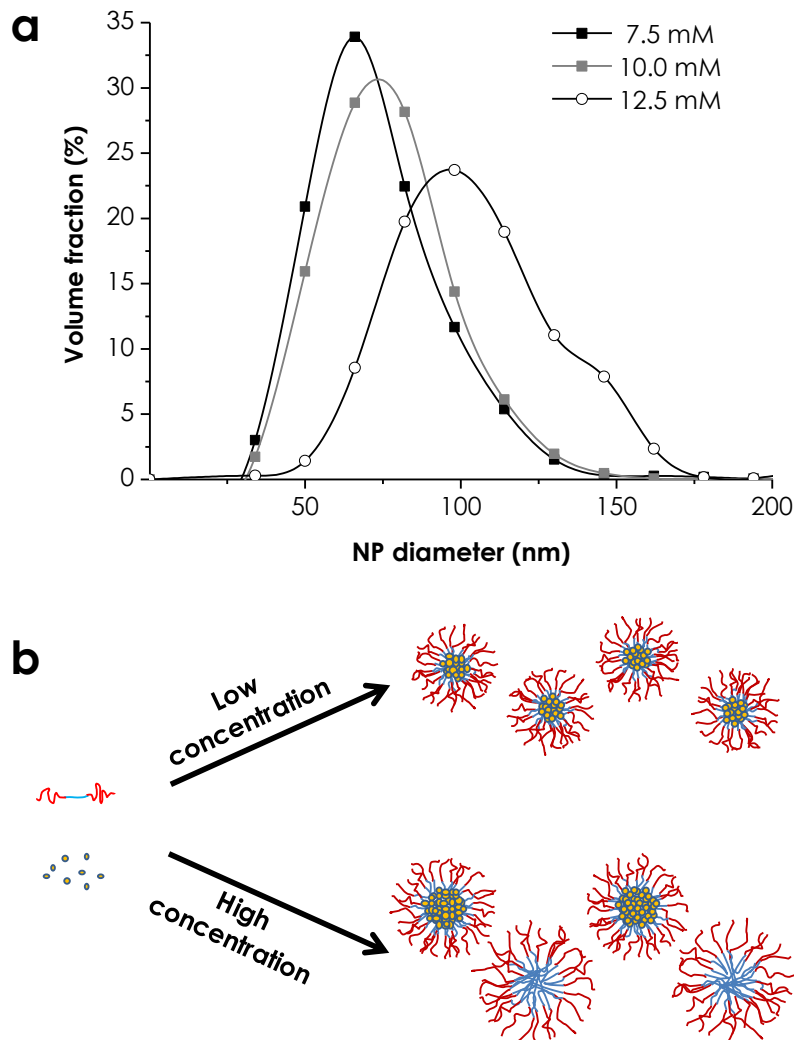


Figure 5.2 Effect of β -carotene /polymer concentrations on NP size distribution. Three solutions of β -carotene /polymer in THF were used with polymer concentrations of 7.5 mM (solid, black squares), 10.0 mM (solid, grey squares), and 12.5 mM (open, black circles) while β -carotene /polymer MR was kept constant at 2.35. (b) Schematic representation of the mechanism of formation of additional empty PMs. At low concentration smaller NPs, which exhibits higher surface volume ratio, are formed, consuming all the polymer unimers. At high concentration, larger NPs with smaller surface to volume ratio are formed. In this condition, there is an excess of polymer unimers that is consumed with the formation of empty PMs.

It can be seen from the figure that the particle size increased with increasing concentration of the nanoprecipitating species. Increasing the concentrations, from 7.5 mM polymer and 17.62 mM β -carotene, to 12.5 mM polymer and 29.4 mM β -carotene, the average particle diameter increased from 73 to 96 nm. This observation agreed with that found during the formation of polymeric micelles (without loading organic contents) in microreactors (see Chapter 3), and can be explained by taking into consideration various phenomena associated with the supersaturation level and fluidic

conditions. A higher concentration corresponds to a higher supersaturation level and faster nucleation and growth kinetics, therefore, stabilization occurs when growing NPs reach a larger size [134, 236]. In addition, the larger number of nuclei formed at higher concentrations could lead to particle aggregation before the stabilization took place, thus forming larger NPs [251]. Furthermore, it has also been suggested that the increased viscosity of the organic phase at higher species concentrations might hindered the diffusion between solvent and non-solvent requiring a longer mixing time and hence affecting the NP size and size distribution (see Chapters 3 and 4) [251].

Along with the variation in the average NP size, the effect on size distribution was also observed by varying the composition of organic solutions. As can be seen from Figure 5.2a, when the concentration of β -carotene and polymers increased the size distribution became wider indicating a decrease in the uniformity of the nanoparticles produced. The results also agreed with those obtained for the formation of polymeric micelles (without loading organic contents).

It is interesting to note the variation in the shape of the three particle size distribution curves. The particle size distribution curves for the two low concentration solutions (7.5 and 10.0 mM) appear approximately symmetric representing a bell-shape distribution, suggesting the formation of only hybrid NPs. However, the curve for the high concentration (12.5 mM) exhibits a peak shoulder at a particle size range of approximately 130 nm, corresponding to the size range observed for empty PMs in the previous studies (see Chapter 3). This suggests a concomitant formation of PMs (\sim 130 nm) whilst producing hybrid nanoparticles (\sim 70 nm) in the high concentration solution (i.e., 12.5 mM). It is interesting to note that, as shown in section 3.3.4.1, PMs considerably swell due to the presence of the solvent while hybrid NPs, even after complete removal of solvent maintain their size as shown from TEM image in Figure 5.1c.

In this study, the molecular ratio of organic material (β -carotene) to polymer (Pluronic F127) was kept at a constant of 2.35, and the particle size increased with increasing concentration. For spherical nanoparticles, the increase in particle size means a decrease in surface to volume ratio, which is inversely proportional to the particle diameter. It suggests that bigger particles have smaller specific surface area, thus required less polymer molecules to cover the surface allowing the formation of empty PMs without loading β -carotene (Figure 5.2b).

In addition, a higher polymer starting concentration decreased the length scale between precipitating unimers within the initial organic solution leading to a decrease in the aggregation time (τ_{agg}) [252] which could mismatch PMs aggregation and β -

carotene nucleation and growth resulting in the self-assembly of empty PMs (see section 5.3.5 Effects of laminar conditions and rapid mixing).

5.3.3 Effects of varying β -carotene/polymer molecular ratios on NP characteristics

In another set of experiments, higher molecular ratios above 2.35 were used in order to investigate the effect of stabilization and nanoprecipitation control provided by relatively lower molar concentrations of block co-polymer stabilizer. The β -carotene concentration was kept at a constant of 23.5 mM which was below the solubility limit in THF at 25 °C (~31.0 mM) [230] to avoid any premature precipitation at the channel junction, whilst sufficiently high to provide high level of supersaturation. Polymer concentration was varied between 3.2 and 1.0 mM. With regard to the polymer concentration, due to the high critical micellization concentration (CMC) value of Pluronic F127 (~300.0 μ M) (see 3.3.1 CMC determination), an $R=0.04$ resulted in a final unimer concentration in the range of 40 to 120 μ M which is below the CMC. This led to an assumption that no PM formation took place during the β -carotene nanoprecipitation, providing instead the possibility to stabilize β -carotene NPs by shell deposition [253, 254].

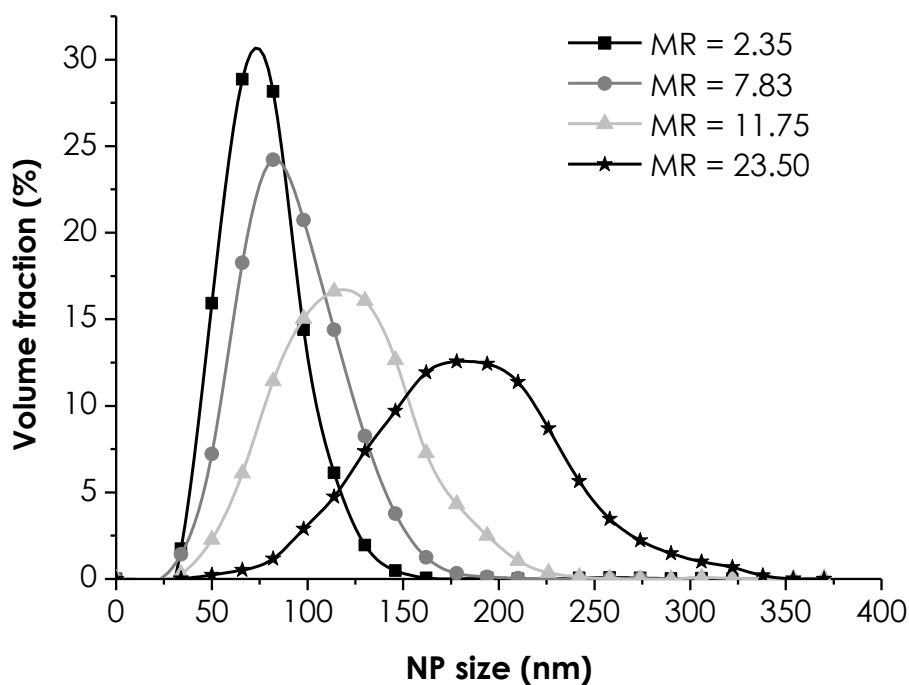


Figure 5.3 Size and size distribution of NPs produced at different β -carotene/Pluronic molecular ratio (MR).

Figure 5.3 compares the size and size distribution of hybrid NPs formed at four molecular ratios of 2.35, 7.83, 11.75 and 23.5. It can be seen that when the MR increased (i.e., less polymer stabilizer was added) the average NP diameter increased (from 73 to 182 nm for MR = 2.35 and 23.5, respectively) and the size distribution became wider. The bell-shape distribution shape without a secondary peak suggested that the particles were still in a mono-modal state with variation in the size uniformity, and no empty PMs were formed. The hybrid NPs were found to be stable with no sedimentation visibly detected for up to 6 weeks of storage.

A very high β -carotene/polymer MR of 47.0, corresponding to a weight ratio of 2:1, was also tested. In that case, significant precipitation was observed which took place along the mixing channel. Particle accumulation started from the channel wall, resulting in a thick precipitated film that grew and eventually occluded the channel completely, as similarly observed when β -carotene alone was used. These observations indicated that a molecular ratio below 47.0 was necessary to efficiently stabilize the growing β -carotene NPs and prevent their aggregation and deposition on the microchannel walls. The size increase in the produced hybrid β -carotene NPs, when β -carotene/polymer MR increased, was likely due to the inefficient stabilization provided by the small amount of polymer present. This allowed the growing nuclei to aggregate, and/or growth phase to take place for a longer time by addition of free bulk β -carotene.

The change responding to the concentration variation was in agreement with that observed during the formation of PMs (see Chapter 3) and other organic NPs [252]. The results also suggested that the increasing loading efficiency should be balanced with the loss of the desired NP characteristics depending on the application. It is worthwhile to notice that the diameter of the NPs produced at lower stabilizer polymer concentrations showed a larger mean size, beyond the 100 nm limit considered as the larger optimal size for NPs intended for cancer therapeutics applications [6].

To further examine the effect of varying β -carotene /polymer MR on NP characteristics and co-nanoprecipitation mechanism, the formation of NPs was carried out with smaller β -carotene/polymer MR ranging from 0 to 2.35 with a given polymer concentration of 10 mM. The results are presented in Figure 5.4a.

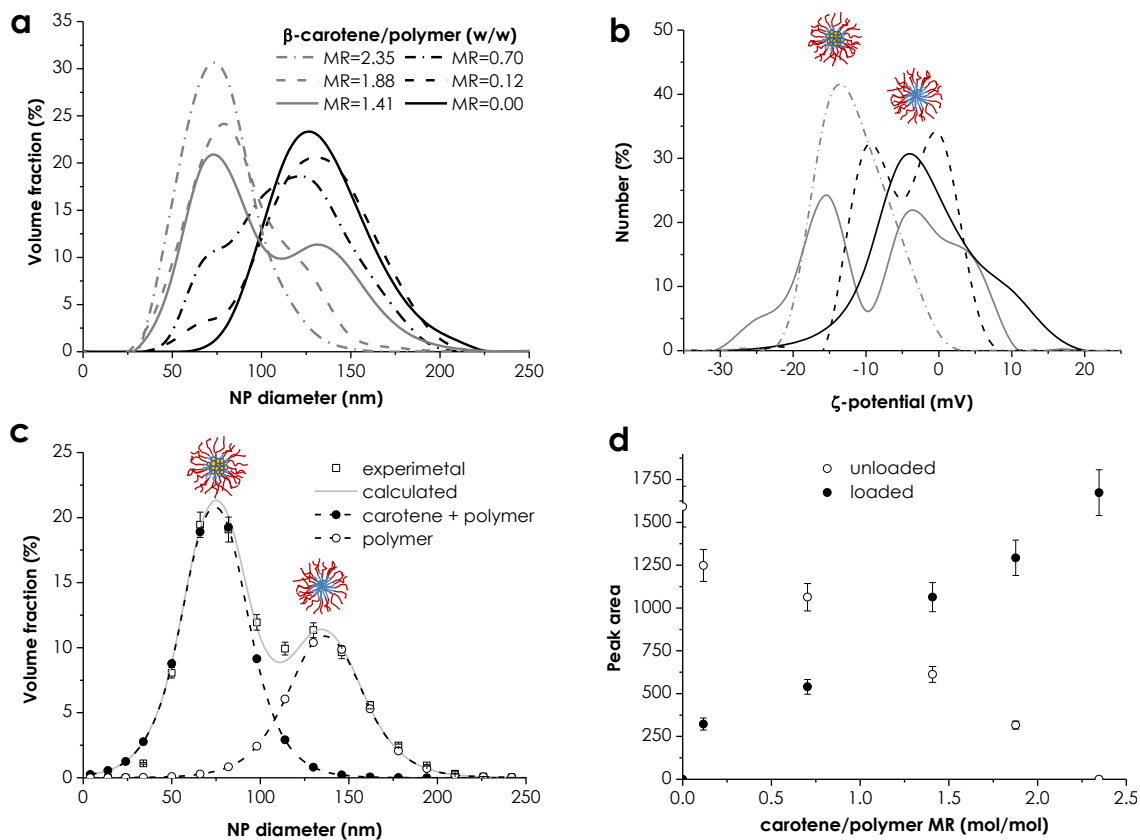


Figure 5.4 Effects of β -carotene/polymer MR on hybrid NPs nanoprecipitation. (a) Size distribution of NPs obtained at different β -carotene/polymer MRs. All the experiments were performed at a constant polymer concentration of 10.0 mM. (b) ζ -potential distribution curve for NPs obtained at corresponding β -carotene/polymer MRs. (c) Calculated size distribution of hybrid NPs (dashed line, solid circles) and empty PMs (dashed line, open circles) at MR of 1.41. The grey solid-line curve represents the sum of the values of the calculated hybrid NPs and unfilled PMs, while the open squares are the experimental data. (d) Peak area as a function of β -carotene/polymer MR for hybrid NPs (filled circles) and unloaded PMs (open circles).

Starting with the MR of 2.35 as described above, the narrow size distribution with an average diameter of 73 nm was indicative of the production of a single type of NP represented by stable β -carotene/polymer hybrid NPs. When the MR decreased to 1.88, a peak shoulder appeared around 130 nm, suggesting the formation of empty PMs. With further reduction of MRs to 1.41, 0.70 and 0.12, the formation of empty PMs with an average diameter of 130 nm was pronounced whilst the amount of hybrid NPs reduced accordingly. In the extreme, where Pluronic polymer only was present in the solution without the presence of β -carotene, PMs having a normal size distribution with an average diameter of 130 nm were produced. The increase in area of the volume fraction peak corresponding to empty PMs indicates that, at β -carotene/polymer MRs

smaller than 2.35, there was enough polymer to completely cover the β -carotene NPs, and the excess polymer present resulted in the formation of empty PMs.

This was further supported by the measurements of ζ -potential of NPs produced. As can be seen from Figure 5.4b, when MR was 2.35, only one peak with an average value of -11.2 mV was found in the ζ -potential distribution curve, indicating the formation of solely hybrid NPs. A single symmetric-shaped peak was also found when only polymer was used, but with an average of -0.8 mV. In contrast, when polymer and β -carotene at MRs were set to 0.12 and 1.41, two distinguishable peaks appeared. In both cases, the two peaks had approximately mean values similar to those detected for the formation of solely hybrid NPs and PMs, confirming the production of a mixture of the two types of NPs. It should also be noted that no unprotected β -carotene NPs were formed as no ζ -potential peaks were observed at around -26 mV (as indicated in Figure 5.1b for β -carotene NPs only).

It has been suggested from the previous studies that at lower β -carotene concentrations (in our case 20-fold decrease), lower supersaturation levels would be attained, resulting in longer induction time (τ_{ind}) for nucleation and growth of β -carotene NPs [230]. This in turn, would result in smaller hybrid NPs. This was based on the assumption that with smaller β -carotene concentrations the growth would be blocked at smaller NP size if the aggregation time (τ_{agg}) for Pluronic F127 PMs remained unvaried, as expected by having the same polymer concentration. However, in the present study this effect was not noticed. As displayed in Figure 5.4a, for the entire range of MRs applied the peak position at 73 nm, corresponding to hybrid NPs, showed only a little shift in size. This indicated that, independently of β -carotene concentration, the NP growth was arrested at the same stage, and the variation of τ_{ind} had insignificant effect on particle size. Similarly, the PM peak position appeared to be almost unvaried with the variation of MR. This suggested that the two processes of formation of PMs and hybrid NPs were distinct and occurred in parallel to concur in the final NP mixtures.

Based on the parallel process model, it was further hypothesized that the distribution curves with double peaks represented the sum of the two peaks for each type of particle, and both types of particles had a typical symmetric bell-shape size distribution, as described by the probability density function [255],

$$f(x; \mu_x, \sigma) = \frac{\exp\left(-\frac{x - \mu_x}{\sigma}\right)}{\sigma \left(1 + \exp\left(-\frac{x - \mu_x}{\sigma}\right)\right)^2} \quad (5.2)$$

where μ_x is a location parameter of the peak representing the average particle size, σ is a scale parameter of the peak width reflecting the particle size distribution. Using a best-fitting method for the experiment data, both μ_x and σ can be determined. Figure 5.4c shows the best-fitting results for the two types of NPs formed with a β -carotene/polymer ratio of 1.41 where the average particles size (μ_x) was estimated to be 74 nm and 136 nm for encapsulates and unloaded polymeric micelles, respectively. Once the two parameters in equation 5.2 were determined, the area (A) of the two overlapped peaks can be calculated from

$$A = \int_0^{\infty} f(x)dx \quad (5.3)$$

Using the best-fitting method, the parameters of Equation 5.2 for other MR were obtained, and the corresponding peak areas were calculated using Equation 5.3 for the two types of NPs formed. The results are plotted in Figure 5.4d.

It is interesting to note that both increase and decrease in area for hybrid and empty PMs are in a good linear relationship with increasing β -carotene/polymer MR. This demonstrates a quantitative approach for the control and evaluation of loading efficiency of hydrophobic organic molecules in polymer stabilized NPs. The latter represents an important parameter for drug delivery applications, and the relation found provides the possibility to predict the threshold amount of polymer to specifically produce only stable hybrid NPs, rather than a mixture of hybrid NPs and empty PMs.

5.3.4 Effects of varying flow rate ratio and mixing time

Under hydrodynamic flow focusing conditions, the diffusive process of molecules (water and THF) travelling into and out of the focused stream region determines the mixing extent, and therefore the nanoprecipitation output, by controlling nucleation and growth kinetics and environment [230]. In the flow focusing microfluidic channel, an increase in flow rate ratio, R , increased the width of the middle stream of organic solution, thus, requiring a longer time for the diffusive mixing to be completed across the side-by-side streams (see Chapters 3 and 4). From the measured w_f , τ_{mix} was estimated by equation 5.1 to be 27, 124 and 231 ms for R equal to 0.1, 0.2 and 0.3, respectively.

To investigate the effect of R on the co-nanoprecipitation process, the size distributions of the NPs produced at a constant β -carotene/Pluronic MR of 2.35 but at different R were compared. The results are depicted in Figure 5.5.

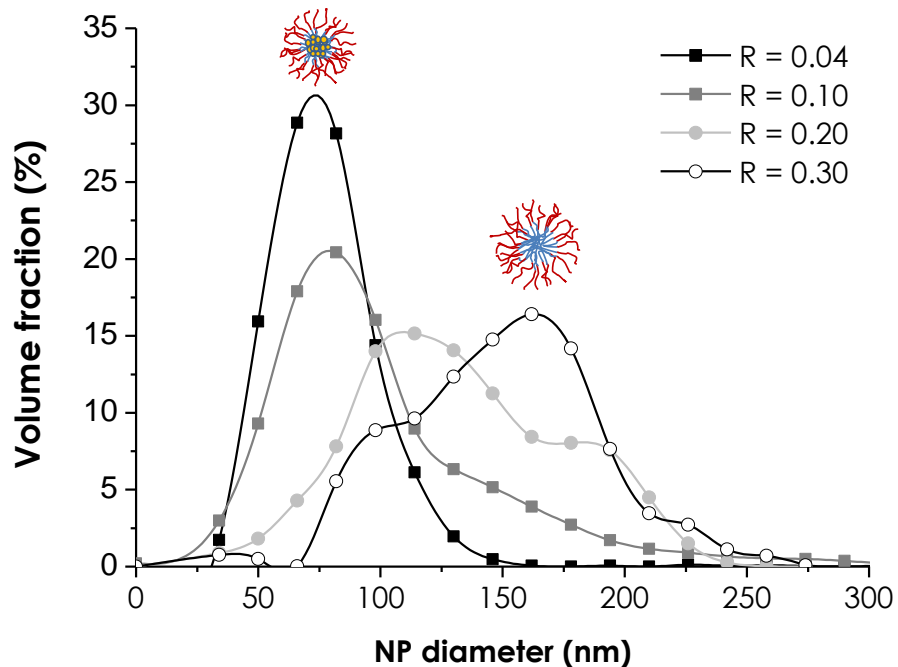


Figure 5.5 Size distribution of NPs obtained at different flow rate ratio (R). Polymer concentration was 10 mM and MR=2.35.

As can be seen from the figure, by increasing R , a shift of the size distribution curve towards larger and more polydisperse NPs can be noted. This was not surprising since, it is well known, that an increase in τ_{mix} leads to a longer growth phase and consequently to the formation of larger NPs [29, 134]. It should be noted that an increase in R also resulted in a larger amount of solvent in the final mixture causing the possible swelling of the produced NPs. However, the increase in mean size was accompanied with the loss of unimodal distribution, which indicated the formation of empty PMs. When $R = 0.1$, the volume fraction of the empty PMs was relatively low and it appeared only as a thick tail of the size distribution curve. When $R = 0.2$ and 0.3 the amount of empty PMs increased as suggested by the increased area of the right hand peak within the size distribution curves. For R higher than 0.3 it was not possible to obtain NPs due to clogging of the channel, possibly resulting from the large amount of polymer introduced within the device. These results revealed that, along with the β -carotene/Pluronic MR, the fluidic conditions also played an important role in affecting the relative amount of the produced empty PMs and hybrid NPs. The mechanism and implication of this control are further analyzed by CFD modelling in the following sections.

5.3.5 Effects of laminar conditions and rapid mixing

In order to gain more insights into the role of the microfluidic environment in controlling the formation of β -carotene/polymer hybrid NPs, a CFD model was implemented to analyze the microfluidic behaviour and mixing process within the microchannel during nanoprecipitation. The model also accounts for the interplay between molecular and hydrodynamic phenomena, on the diffusion and advection kinetics of growing NPs. In particular, the formation of slow diffusive species (i.e., nuclei) was simulated with an *in-house* code that introduces a drop in the diffusion coefficient when the critical water concentration (CWC) was reached. The CWC for each solution was experimentally determined and the results are reported in Figure 5.6a.

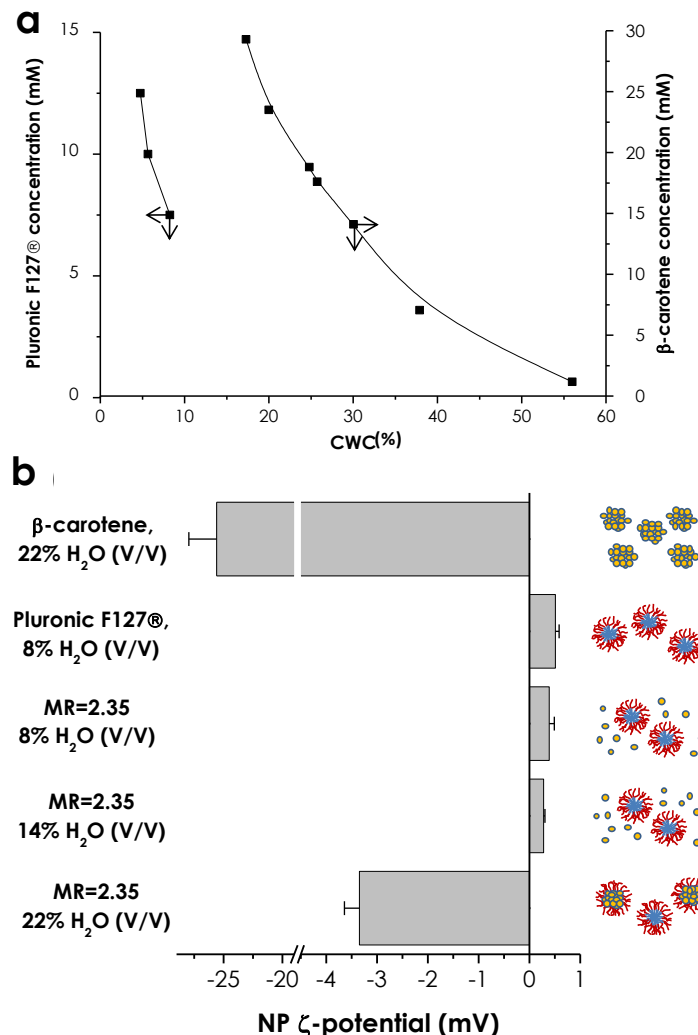


Figure 5.6. (a) Relationship of CWC with concentration of β -carotene or Pluronic F127. (b) ζ -potential of different β -carotene and/or Pluronic F127 solutions in THF at different water concentrations, showing the two-step nanoprecipitation kinetics. Schematic representation of the precipitated species (inset).

As expected, CWC was found to be dependent on the concentration of the species, with smaller CWC required to trigger the precipitation at higher species concentrations. In addition, the results showed that nanoprecipitation of Pluronic was triggered at lower water concentrations than that of β -carotene. When CWC was determined for Pluronic and β -carotene mixtures, it was found that the formation of NPs was first detected at the water concentration that represents the CWC for the polymer, suggesting that at lower water concentrations only empty PMs were formed. This result was also corroborated by the ζ -potential measurements (Figure 5.6b) carried out with the same mixture compositions. ζ -potential measurements clearly showed that for water concentrations smaller than the CWC for β -carotene (i.e., > 20.0 % V/V) only slightly positive charged NPs (~0.4 mV) were precipitated. These NPs had a similar surface charge to PMs precipitated from a solution of only Pluronic F127. When the water concentration was increased to the threshold where β -carotene precipitation was triggered, the average ζ -potential decreased to -3.4 mV, due to the presence of negatively charged β -carotene NPs. It should be noted that 78% of solvent is still composed by THF hence only a small portion of β -carotene can precipitate inside the core of growing PMs. This can results in a less negative ζ -potential of the produced hybrid NPs as shown in Figure 5.6b when compared with those in Figure 5.1b. Notably, the results from Figure 5.6b suggested that the two precipitation processes were triggered independently as results of reaching the CWC of the specific species (i.e Pluronic or β -carotene).

The experimentally measured values of CWC were then implemented in the computational model to account for the formation of NPs in the diffusion process. Figure 5.7a shows the computed mass fraction profiles along the mixing channel of the three species of interest namely, Pluronic F127, β -carotene and water. In the graph, the mass fraction profile for each species was normalized with the mass fraction of the specie itself at the inlet, in order to make the value of the mass fractions independent from the initial concentration of the species at the inlet, therefore solely dependent on the kinetics of diffusion of the species.

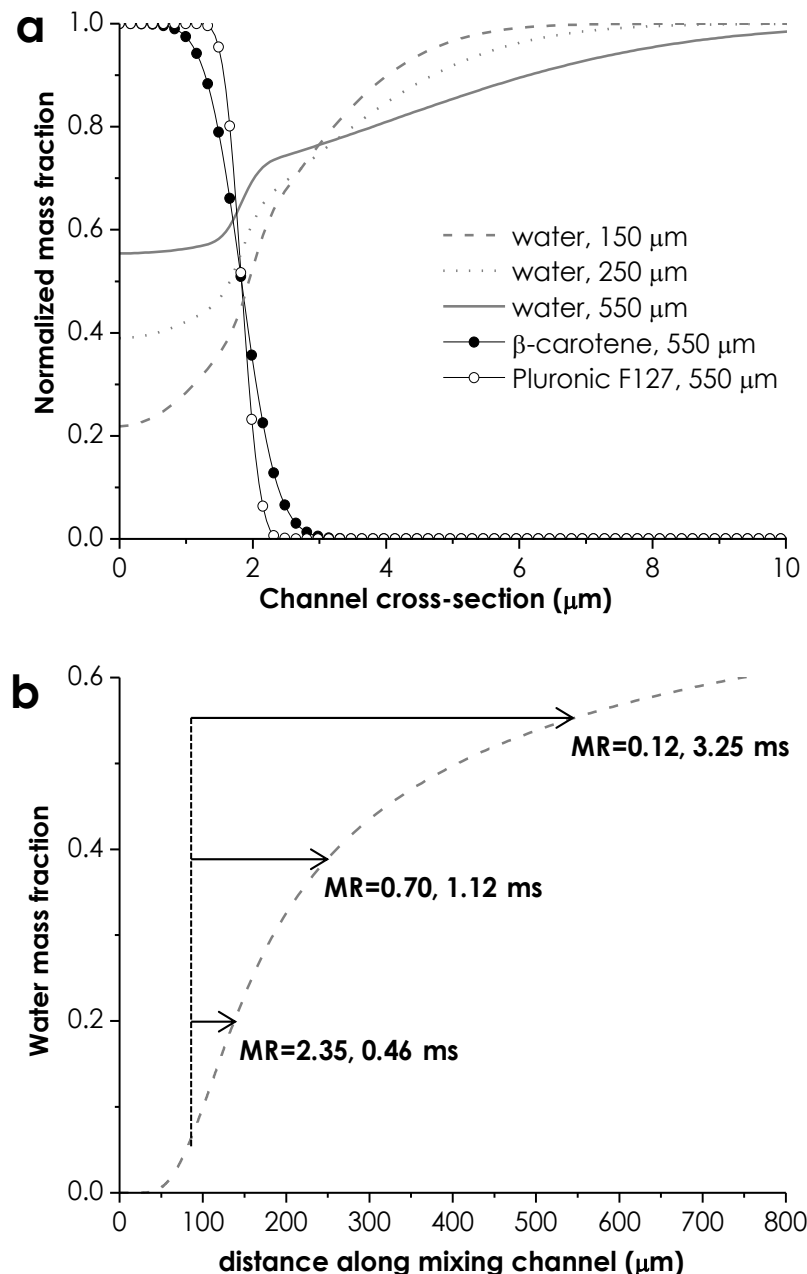


Figure 5.7. (a) Normalized mass fraction profile by CFD for Pluronic F127 (open symbols), β -carotene (solid symbols) and water (grey line, no symbols) at different distances downstream the channel junction, where organic solution (Pluronic F127, β -carotene in THF) and antisolvent (water) first met. The mass fraction profile is computed for half-channel cross section due to the symmetric characteristics of the mixing channel. (b) Mass fraction evolution of non-solvent (water) along the mixing channel, computed at the centre of the focused stream, which represents the symmetry plane between the two halves of the mixing channel. The data are computed for MR = 2.35 with a Pluronic F127 concentration of 10 mM. No significant differences were found for the same set of data computed for different MRs and polymer concentrations. Arrows schematically represent the time mismatching (τ^*) to reach the CWC concentration for both, colloidal stabilizer (Pluronic F127) and active encapsulated species (β -carotene) for different β -carotene-Pluronic F127 MR; insets report MRs and associated τ^* .

It can be noted that the concentration of Pluronic F127 decreases at a slower rate compared to that of β -carotene due to the lower diffusivity of the solubilised and precipitated species, which was two orders of magnitude smaller than those of β -carotene. It is also worth noting that the kinetics of diffusion for water was faster compared to the other species due to its higher diffusion coefficient, and the non-precipitation kinetics.

The mass fraction profile can provide a qualitative reference of the location, within the cross section of the mixing channel, in which the nucleation of either β -carotene and/or Pluronic took place. It also quantitatively showed the percentage of initial fraction of either Pluronic or β -carotene that was present within the domain in which the nucleation is triggered. The mass fraction profile reported in Figure 5.6a was computed at a distance of 550 μm from the channel junction, where a mass fraction of water above 55% (V/V) was found within the entire region of the focused stream. The value of 55% was chosen because it represents the CWC for the lower β -carotene concentration. At that distance, only a small fraction of β -carotene and Pluronic diffused out the focused stream (~5%) as inferred by the steep shape of the mass fraction profiles. This suggested that the nanoprecipitation process was confined within the focused stream domain, and when β -carotene started to nucleate, the growing NPs were in a region with high concentration of stabilizer.

Compared to slow bulk mixing, this type of fast mixing process represents a peculiar feature of the flow focusing configuration, which confines the aggregating molecules within a thin layer (i.e., focused stream) realizing an high supersaturation level and increasing the possibility to efficiently cover and stabilize the growing β -carotene nuclei [129].

From the water mass fraction profiles in Figure 5.7a, it can be also noted that the diffusion of water within the focused stream was a progressive process, hence at a certain distance from the channel junction (i.e., different residence times), different streamlines within the focused stream experienced different amount of water mass fraction.

This progressive mixing kinetics, together with the difference in CWC values for β -carotene and Pluronic, suggested that the nanoprecipitation of the two species was triggered at two different locations along the mixing channel hence, at two different stages during the mixing process. Therefore, the formation of hybrid NPs can be seen as a two-step process in which an initial precipitation of Pluronic polymer was followed by the β -carotene precipitation.

In order to estimate the mismatching between the two triggering times of the two processes, a new parameter, the nanoprecipitation mismatching (τ^*) was introduced. τ^*

was obtained through the computational model and was defined as the difference in residence time between the points in which the CWC for the polymer and β -carotene is reached. In other words, it represents the elapse time between the initial nucleation of PMs and β -carotene. It should be noted that τ^* is different from τ_{mix} , which instead represents the time required to attain the same mass fraction value within the entire width of the focused stream. Therefore, even if homogenous condition can be obtained throughout the focused stream within the time frame posed by τ_{ind} , the nanoprecipitation kinetics can still be mismatched. To investigate the role of τ^* on the co-nanoprecipitation process, the experimental data were studied in conjunction with the computational model.

Figure 5.7b displays the water mass fraction evolution along the mixing channel, computed at the centre of the focused stream. The insets represent the τ^* for different MRs. CFD simulations were carried out under the identical conditions used for obtaining the results shown in Figure 5.4a. It can be noted that with decreasing MR, τ^* increases from 0.46 to 3.25 ms, due to the higher CWC at lower concentrations of β -carotene. τ^* is therefore relatively small compared to τ_{agg} (26-30 ms). Thus, we can assume that when β -carotene nucleates, PMs are not yet formed. Hence, growing β -carotene cannot be locked out the already formed PMs.

The microfluidic-based fast kinetics of diffusion, which are not achievable in batch reactors (i.e., precipitation with slow dialysis), and the relative location in which the aggregation is triggered have important implications for the formation of Pluronic F127 and β -carotene hybrid NPs. The fast mixing rate obtained within a microfluidic device permits to create metastable PMs nuclei within the same time window where the metastable β -carotene nuclei are formed, so that homogeneous competitive kinetics dictate the resulting product [134]. After the nucleation intermediate Pluronic structures (nuclei and growing PMs) are formed. These intermediate structures have a smaller diffusivity and therefore tend to advect along the streamline where they are initially formed. Following that, the CWC for β -carotene will also be reached and the insoluble portion of the polymer acts as a nucleation point for β -carotene molecules and dictates the production of composite NPs [134].

Based on the ζ -potential measurements, it can be argued that the growing PMs act only as nucleation points but not as nucleation promoters, since no significant increase in NP surface charge was detected in the ζ -potential measurement in Figure 5.6b. In particular, in the case of precipitation from the mixture of β -carotene and polymer, at low water concentrations (8 and 14 %), if the growing PMs acted as nucleation promoters, it would have obtained a negative ζ -potential value, as expected by the precipitation of hybrid NPs.

In this case, once the β -carotene precipitates, the formed nuclei tend to aggregate near the hydrophobic region of the unimers, where their growth time will be finally dictated by the formation of completely enveloping polymer shell, which halts further growth. However, the growth step for β -carotene is small, because it happens within the τ_{agg} of PMs, therefore hindering the effect of a difference in growth kinetics at different concentration levels (see Figure 5.4). In addition, the polymer coating around the growing nuclei is likely to change their surface properties such that additional molecules will not be incorporated quickly, favouring nucleation over growth. It is also possible that more forming β -carotene nuclei would form one single hybrid NPs due to the process of fusion of growing PM nuclei (however, it has been recently proposed that growth might proceed as a single chain exchange [158]). As results, the confined microfluidic space is likely to play a role in favouring nucleation over growth, as the precipitation of both the species occurs in the focused stream, where the forming β -carotene nuclei are in intimate contact with growing PMs.

This view is in agreement with the invariance of the hybrid NP size with variation of β -carotene concentration (Figure 5.4a). It also explains the effect of MR on controlling the relative amount of hybrid NPs and empty PMs formed. At lower β -carotene concentrations, a relatively small number of molecules of β -carotene are present within the focused stream, causing the formation of a relatively small amount of composite nuclei. However, most of the Pluronic unimers that are confined within the focused stream region can aggregate by themselves and create larger PMs. In contrast, at higher β -carotene concentrations the number of composite nuclei formed is larger, and therefore, more Pluronic is sequestered to create stabilized particles, decreasing the amount of Pluronic that precipitates as empty micelles.

However, this mechanism model is only valid for the microfluidic environment, due to the fast mixing and the confinement of the species within a small region represented by the focused stream. Under bulk mixing conditions, and for a $\text{MR} = 2.35$, the τ^* value is expected to be higher, causing the formation of a larger number of empty PMs that can be formed prior to the precipitation of the β -carotene (see Figure 5.8). When τ^* becomes larger, only a small portion of β -carotene can precipitate inside the core of growing PMs. The growing β -carotene NPs will be not efficiently stabilized and hence can grow for longer time resulting then in larger NPs as shown in Figure 5.3.

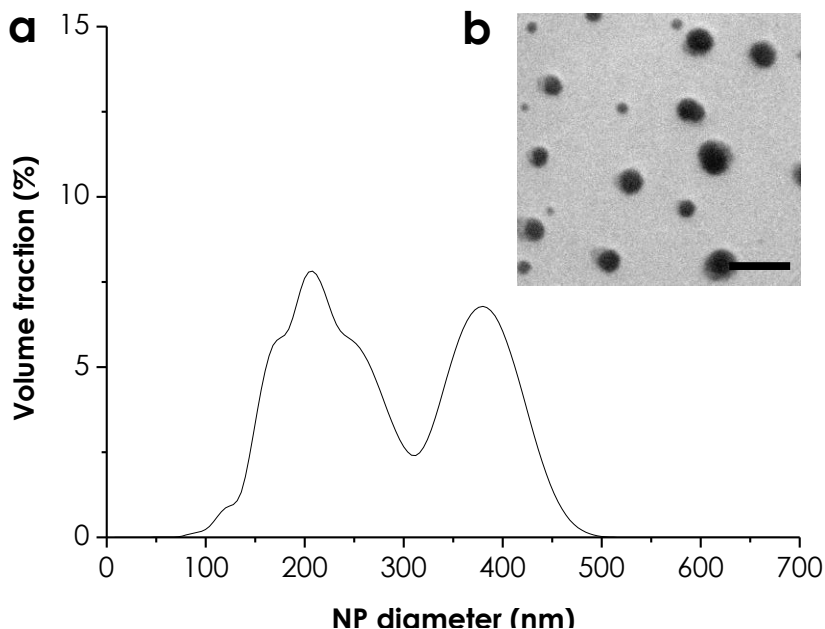


Figure 5.8 NPs made under bulk mixing conditions, with Pluronic F127 at 10.0 mM, MR = 2.35 and $R = 0.04$. (a) Size distribution and (b) TEM image of the produced hybrid NPs, scale bar 1 μm .

Figure 5.9a reports the computed mass fraction profiles along the mixing channel of the three species, at different distances from the channel junction. Specifically, when $R = 0.1$ the mass fraction profiles are computed at a distance of 0.55 mm, while when $R = 0.3$, they were computed at a distance of 4.30 mm.

The selected distances, as for Figure 5.7a, reflect the position where a mass fraction of water above 20% (V/V) can be found within the entire region of the focused stream. The value of 20% was chosen because it represents the CWC for the β -carotene at the used concentrations. In this respect, CFD simulations were carried out under the identical conditions used for obtaining the results shown in Figure 5.5. Similar to the case at $R = 0.04$, at the distance where β -carotene starts to precipitate, only a small fraction of the initial β -carotene and Pluronic diffuses out the focused stream confirming the confinement of the precipitant species within the focused stream region also for larger R values.

Besides the well-known effect of increasing the τ_{mix} , an R increment also prolongs the τ^* . This effect can be deduced from the water mass fraction evolution along the mixing channel for different R reported in Figure 5.9b. From the CFD model the τ^* was estimated to increase from 0.46 ms, for $R = 0.04$, to 17.47 ms, for $R = 0.3$. τ^* was calculated as the difference in time to reach water mass fractions of 5.6 % and 20%, as required for the precipitation of the two species at the used concentrations.

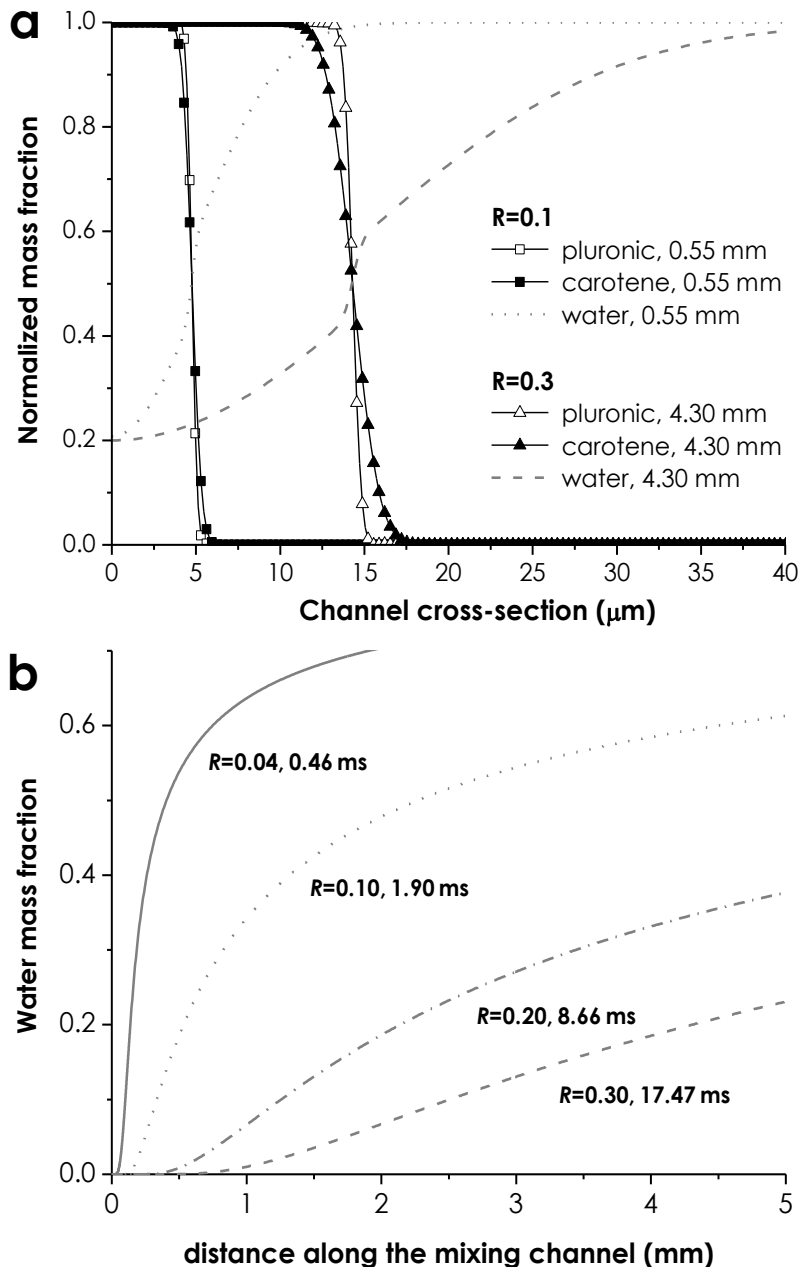


Figure 5.9 (a) Normalized mass fraction profiles by CFD for Pluronic F127 (open symbols), β -carotene (solid symbols) and water (grey line, no symbols) at different distances downstream the channel junction. The mass fraction profile is computed for half-channel cross section due to the symmetric characteristics of the mixing channel. (b) Mass fraction evolution of non-solvent (water) along the mixing channel, computed at the centre of the focused stream for $R = 0.04$ (solid line), $R = 0.1$ (dotted line), $R = 0.2$ (dash-dotted line) and $R = 0.3$ (dashed line). Inset reports τ^* values.

This effect could be explained by taking into consideration the kinetics of mixing with a hydrodynamic focusing configuration, in relation to the surface-to-volume ratio of the contact interface between organic stream and water (see section 4.6.3 Diffusive

mixing). Experimental results and CFD models [126, 228] have shown that two different regions, characterized by different mechanisms of mixing, can be identified within a focused stream. The first region, characterized by a rapid convective-diffusive mixing, is located at the hydrodynamic focusing region at the channel junction. The second, in which the mixing is limited by molecular diffusion in the direction normal to streamlines, is located in the focused stream region, downstream of the channel junction. An increase in R , resulting in a larger w_f , decreases the surface-to-volume ratio of the focused stream, increasing the portion of the central stream that is mixed in the low diffusive region downstream of the channel junction. In contrast, low R results in a high surface-to-volume ratio and the rapid depletion of the centre stream by convective-diffusive mixing in arrowed-shape region of the focused stream.

Specifically in this case case, at a low R , a fast increase in water mass fraction can be realized in the first 200 μm of the mixing channel, as can be notice from the abrupt increase of the water content in the centre of the focused stream (Figure 5.9b). Higher R , instead, results in shallower increase in the mass fraction of water, hence in longer τ^* , similar to the case of bulk mixing in Figure 5.8. This longer τ^* , which becomes comparable to the τ_{agg} of PMs, then causes the formation of a large fraction of empty PMs as shown from the experimental results in Figure 5.5. A longer τ^* results indeed in further mismatching between the two competitive processes of formation of hybrid NPs and empty PMs, increasing the possibility to produce locked PMs prior to the precipitation of β -carotene. In this respect, it must be noted that Pluronic F127, being a synthetic polymer is polydisperse, both in overall size and in ratio of the block size [210, 211], opening the possibility to the presence of a range of kinetics of aggregation rates. A portion of unimers can be then characterized by a faster τ_{agg} and be able to form closed PMs prior the precipitation of β -carotene. A longer τ^* can then increase the portion of unimers that can precipitate within the time frame posed by the mismatching.

The excess of β -carotene so created will precipitate forming larger hybrid NPs (see Figures 5.5 and Figure 5.8) since they are only partially stabilized by the remaining Pluronic F127 unimers. Nevertheless, this effect is consistent with the view of precipitation of hybrid NPs explained above that favours the nucleation over the growth. When β -carotene starts to precipitate, it will then nucleate at the hydrophobic block of the still free, or only partially aggregated, unimers. At the stage where most of the nucleation points are consumed, the newly forming nuclei will growth as naked (not stabilized) particles where growth is not inhibited. Eventually, a polymer shell provided by the unimers that remain in solution will cover these naked NPs, and their growth will be arrested. It must be noted that the polymer used has a quite high CMC, so a large number of unimers remain in free state after the formation of PMs. This

mechanism of stabilization is similar to that used to explain the results in Figures 5.3 and 5.8. Consistent with those results, a decrease of polymer available results in the formation of larger hybrid PMs.

In addition, a larger R also reflects a longer growth phase for PMs due to the higher content of solvent (see section 4.6.3.3 Mass fraction time evolution) that can lower the barrier for the unimer insertion in the growing nuclei [132]. There is a complex interplay between the different process kinetics that is confused by the longer τ_{mix} and further experiments are required to definitely corroborate the role that τ^* plays in controlling the nanoprecipitation of hybrid NPs. Nevertheless, the data here presented show the existence of such effects and the miss matching between the two aggregation points can explain the finding, expanding the knowledge on the not yet fully understood mechanism of block copolymer self-assembly [158] and, opening the possibility of further research and investigation.

5.4 Summary

A microfluidic-based reactor has been used for the production of organic NPs in a continuous-flow format where the core-shell structured hybrid NPs containing synthetic β -carotene are encapsulated by amphiphilic block copolymer Pluronic F127. This setup was used to investigate how the microfluidic environment determines the NPs size and stabilization in order to facilitate further application of this rapidly growing technique. The effects of process operational parameters, β -carotene and polymer concentrations, and β -carotene/polymer MR were examined on the controllability of NPs size and on the kinetics and mechanism of the co-nanoprecipitation process.

It was demonstrated that a competitive reactions resulted in the formation of two types of nanoparticles (i.e., either with or without loading hydrophobic β -carotene in the core-shell structure). The corresponding peak area of the size distribution profiles quantitatively represented the amount of each type of nanoparticle as a function of β -carotene/polymer MR. In addition, it has been shown that when the β -carotene/polymer MR increased, the average particle diameter increased and the size distribution became wider. The experimental results were interpreted with the aid of CFD simulations.

In an effort to unveil the effect of the complex interplay between molecular and fluid dynamic properties of nanoprecipitating species, CFD models were integrated with an *in-house* code that simulated the effect of NP formation on their diffusion and advection kinetics.

The results were explained by taking into consideration a new parameter representing the mismatching between the aggregations of the two precipitant species. It is understood, that the characteristic τ_{agg} time for the copolymer is the primary characteristic that controls the process of nanoprecipitation of hybrid NPs [134]. The importance of this parameter was highlighted by the presented data showing that the mechanism of precipitation hypothesized for a confined impinging jet (CIJ) still applies for a microfluidic environment. However, data presented shows that τ^* also plays an important role in controlling the co-nanoprecipitation process of drugs with a colloidal stabilizers. The comparison of NP formation under different experimental conditions, emphasizes the role of τ^* in the mechanism of precipitation and stabilization of growing NPs, which plays a decisive role in determining the size, polydispersity of the prepared hybrid NPs.

The knowledge of this parameter would aid the proper selection of a stabilizer type, concentration, and process parameters to obtain stable NP batches, characterized by a high percentage of loading while avoiding the formation of unwanted empty stabilizer aggregates. In this respect, it also provides a way to minimize the use of unreasonably high level of excipients in drug delivery formulations.

In addition, it is worth noticing that these results with β -carotene and Pluronic F127 as a model hydrophobic drug and stabilizing polymer, respectively, could be translated to a variety of similar drug/polymer combination, and be useful in the emerging fields of microfluidic formation of organic NPs and nanomedicine. Optimization of a particular NP formulation will depend on the specific properties and requirements of the systems under consideration.

Chapter 6

Mithramycin encapsulated in polymeric micelles as novel therapeutic protocol for beta-thalassemia

Following the investigation of nanoprecipitation process, the use of microfluidic based nanoprecipitation to assemble mithramycin drug-encapsulated PMs was investigated. This section reports that the DNA binding drug mithramycin (MTH) can be efficiently encapsulated in polymeric micelles (PM-MTH), based on Pluronic block-copolymers, by a microfluidic approach. The effect of different production parameters has been investigated for their effect on PM-MTH characteristics. The compared analysis of PM-MTH produced by microfluidic and conventional bulk mixing procedures, revealed that microfluidics provides a useful platform for the production of PM-MTH with improved controllability, reproducibility, smaller size and polydispersity. Finally, the compared investigation of the effect of PM-MTH, produced by microfluidic and conventional bulk mixing procedures, on the erythroid differentiation of both human erythroleukemia (K562) and human erythroid precursor cells (ErPC) is also reported. It is demonstrated that PM-MTH exhibited a slightly lower toxicity and more pronounced differentiate activity when compared to free drug. In addition, PM-MTH were able to up regulate preferentially gamma globin mRNA production and to increase fetal haemoglobin (HbF) accumulation, the percentage of HbF containing cells, and their HbF content, without stimulating α -globin gene expression that is responsible for the clinical symptoms of beta-thalassemia. These results are of potential clinical significance because an increase of HbF alleviates the symptoms underlying beta-thalassemia and sickle cell anemia. In conclusion, this report suggests that MTH-PM produced by microfluidic approach warrant further evaluation as potential therapeutic protocol for beta-thalassemia.

This part of the work has been carried out in collaboration with the groups of Professors Gambari and NatruZZI in the University of Ferrara, which helped with the *in vitro* test on K562 and ErPC cells.

6.1 Introduction

6.1.1 Beta-thalassemia

Haemoglobin (Hb) is an iron-containing metallo-protein that can be found in the red blood cells of all vertebrates. Hb is a tetramer of two α -like and two β -like globin chains. Globin synthesis is regulated during ontogeny and is characterized by two major switches [256]. The first switch from embryonic Hbs to fetal Hb (HbF) ($\alpha_2\gamma_2$) takes place in the first two months of gestation and subsequently, while the second switch, in which HbF is gradually replaced by adult Hb (HbA) ($\alpha_2\beta_2$), takes place immediately follows the birth. The second switch leads to a reduction of HbF, from 85-98% of the total Hb present immediately after birth down to 5%. This reduction is accompanied to a concomitant increase in HbA up to 90-95% of the total Hb in red blood cells (RBCs) in adult healthy patients [257, 258].

β -thalassemia is an inherited autosomal recessive blood disease. In β -thalassemia the genetic defect affects the β -globin gene or its regulatory region causing absence or reduced production of β -globin chains that make up haemoglobin [257]. This is associated with a corresponding excess of synthesis of α -globin chains that leads to the formation of abnormal haemoglobin molecules. The outcomes of this unbalanced globin production is the destruction of the erythroid precursor by apoptosis and short survival of RBCs within the blood. These result in anemia which is the characteristic presenting symptom of the β -thalassemia [259].

It is well established that an increase in HbF production ameliorates the clinical symptoms β -thalassemia patient by functionally compensate for the absence of β -globin genes [260-262]. Thus, pharmacological mediated regulation of the expression of γ -globin genes has been proposed as a potential therapeutic approach for β -thalassemia and sickle cell anemia [30, 263, 264]. In this respect, DNA-binding drugs such as tallimustine, chromomycin and mithramycin A (MTH), have been shown to control gene expression and induce the erythroid differentiation of erythroid precursor cells with an associated increased expression of embryo-fetal globin genes [30, 263].

6.1.2 Mithramycin A (MTH)

Among the different DNA-binding drugs, MTH presents the lowest cytotoxicity [259] and for this reason was selected in this study to produce drug-encapsulated PMs. MTH, also called plicamycin, is an aureolic acid-type polyketide, which is normally isolated from various strains of the bacterium *Streptomyces* (see Figure 5.1) [265].

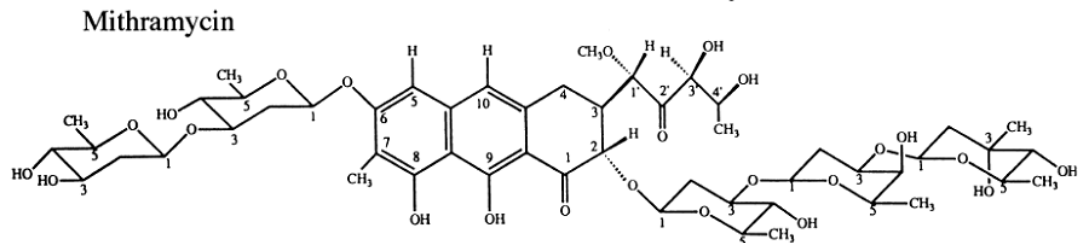


Figure 6.1 Chemical structures of mithramycin.

Mithramycin has been used clinically for many years to treat testicular carcinoma and several types of cancer including leukaemia, as well as hypercalcemia in patients with metastatic bone lesions and Paget's disease [266]. The ability of MTH to bind the DNA minor groove is of great interest, since pharmacologically mediated modulation of DNA/nuclear protein complex formation represents a promising approach to control gene expression. For instance, MTH was found to inhibit the binding of the transcription factor Sp1 to its promoter [267], leading to the gene transcription modulation of different genes, including VEGF [268], c-MYC and ha-RAS, as well as antiapoptotic genes [269]. It was also shown that MTH inhibited the p53-mediated transcriptional responses, the DNA methyltransferase and the multi-drug resistant gene (MDR)-1 [270], therefore putatively sensitizing tumour cells to chemotherapeutic agents.

With regard to the possible use as therapeutic protocol for beta-thalassemia, it has been demonstrated that MTH can induce erythroid differentiation of the human leukaemic K562 cell line through the induction of γ -globin mRNA accumulation [263]. This data is particularly important for clinic applications since even a moderate increase in the production of HbF could be associated with significant improvement in the clinical status of the patients [259]. The erythroid differentiation in K562 cell line was associated with a dose dependent decrease in the proliferation efficacy of K562. However, the concentration that was found to be effective to increase HbF production was lower (10-50nM) than the concentration used for *in vivo* cancer treatment with MTH (300-350 nm plasma level) [263]. On one hand, this shows that MTH can be relatively safely used to exert differentiative activity avoiding cytotoxic and

antiproliferative effects. On the other hand, this points out the need for and efficient control of its plasma level through and drug delivery strategy.

6.1.3 MTH encapsulation in polymeric micelles

In spite of the above mentioned therapeutic potential, the clinical use of MTH is still limited mainly due to its severe side effects including gastrointestinal, hepatic, kidney and bone marrow toxicity [271]. One of the possible strategies to enhance its safety and efficacy is to develop different formulations of delivery systems such as nano- or micro- particles, liposomes [272] and polymeric micelles (PMs) [273]. Among them, PMs loaded with MTH represent an appealing formulation since MTH has lipophilic moieties in its molecular structure that makes it possible to dissolve in a wide range of solvents including water and organic solvents. MTH is relatively soluble in water, lower alcohols, acetone, ethyl acetate and methyl isobutyl ketone; it is slightly soluble in diethyl ether and benzene and insoluble in petroleum ether, carbon tetrachloride and cyclohexane. In this respect, MTH shows a $\log p$ of 1.290 ± 1.454 [274], suggesting a slight lipophilic nature and the possibility to be incorporated into PMs which may contribute to improve drug transport and cellular uptake.

The use of PMs for the delivery of MTH, can provide a controlled and targeted delivery, alter the drug circulation time, change the cellular distribution and increase the amount of MTH delivered to the cells, possibly resulting in a higher drug efficacy and lower side effects. In particular, the drug circulation time is increased by the nanoscale size and the presence of the polyethylene glycol (PEG) shell. PEG chains create a highly water bound barrier on the particle surface which blocks the adhesion of opsonins and the subsequent recognition and phagocytosis by the reticulo-endothelial system (RES) [275]. The circulation time is additionally prolonged by a reduced renal excretion of PMs compared to free drug [276]. A prolonged circulation time is likely to be particularly beneficial when the target of drug action is represented by circulating and bone marrow cells [277], as in the case of erythroid differentiating drugs.

With respect to PM preparation, currently two main approaches are usually followed, depending on the physicochemical properties of block copolymer(s) and drug [142]. One method is based on the direct dissolution of the polymer together with the drug in an aqueous environment, usually involving moderately hydrophilic copolymers (e.g., poloxamers). By contrast, the second approach is more appropriate for copolymers that are sparingly soluble in water, thus a water miscible organic solvent is needed to dissolve both copolymer and drug. The commonly used solvents include dimethylsulfoxide, N,N-dimethylformamide, acetonitrile, THF, acetone and dimethylacetamide. In this method, the solvent-removal is particularly crucial since it

triggers the nanoprecipitation process and therefore the final PM dimensional and entrapment characteristics. The solvents are generally removed by “bulk” and slow procedures such as dialysis against water [155].

Microfluidic approach described in the previous chapters, allows the removal of organic solvent in a controlled fashion, through a fast and adjustable mixing process made possible by the peculiar microfluidic environment, resulting in highly controlled procedure for PM preparation [29]. By this method, the production of PMs is robust, reproducible and permits the precise control of PM physicochemical characteristics, essential for their biopharmaceutical applications. In this respect, Farokhazad *et al.* [130] reported the use of microfluidic produced PMs to co-deliver cisplatin and docetaxel to prostate cancer cells, demonstrating that PMs produced by microfluidic approach could be used for therapeutic applications. With respect to conventional bulk methods, PMs produced by microfluidic reactors show a number of advantages, including: smaller mean size, high homogeneity and increased drug loading efficiency [29]. Regarding the PM size and size distribution, previous studies demonstrated that small PMs are more effective at evading scavenging from macrophages, exhibiting prolonged circulation in the blood stream [6, 177, 278, 279]. It was also demonstrated that the reduction of the size was a critical factor to improve non-phagocytic nanoparticles translocation within blood cells [280]. In addition, microfluidics does not require post-processing steps, which are normally needed for “bulk” procedure to remove large particle or aggregates, before their *in vitro* or *in vivo* testing [126, 129].

To summarize, the current study presents the development of an advanced formulation for MTH, based on PMs (PM-MTH), produced by microfluidic technology and the *in vitro* analysis of the formulation as new therapeutic protocol for beta-thalassemia. For comparison, PMs produced with conventional bulk methods were also considered. The production parameters and their effects on PM characteristics were analyzed, and the effects of MTH association in PMs on the erythroid differentiation of both human erythroleukemia (K562) and human erythroid precursor cells (ErPC) were investigated. For the production of PM-MTH, Pluronic® F127 was employed, as a model block-copolymer, due its well studied characteristics and the impressive safety profile that makes it FDA approved for pharmaceutical and medical applications, including parenteral administration [199].

6.2 Materials and methods

6.2.1 Fabrication of microfluidic reactors

The glass-made microfluidic reactors employed for the preparation of PMs were fabricated by a photolithography/wet etching procedure, as previously reported (see sections 3.2.3 and 3.3.2).

6.2.2 Preparation of PMs in microfluidic reactor and by bulk mixing

PM-MTH were prepared using microfluidic Reactor 2 (see Table 3.3) and with the method described in section 3.2.5 with minor adaptations. A schematic representation of the used experimental setup is depicted in Figure 6.2.

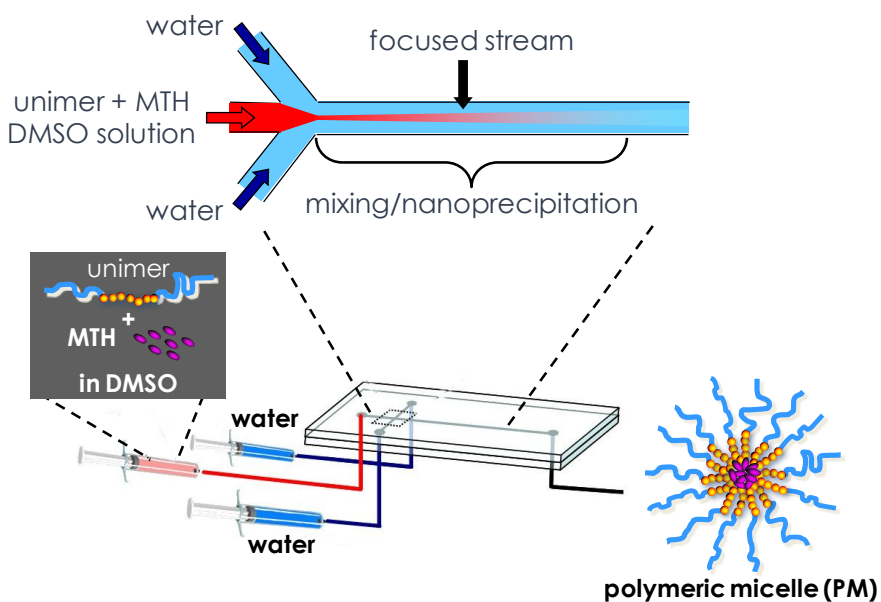


Figure 6.2 Schematic representation of the preparation procedure for PMs by microfluidics.

Briefly, MTH (Sigma-Aldrich, UK) was dissolved in DMSO (Sigma-Aldrich, UK) at concentrations of 4 mg/mL. MTH solution in DMSO was added to Pluronic® F127 (BASF Chem Trade GmbH) solution ($1.5 \cdot 10^{-2}$ M) to make up three different working mixtures in which the concentration of MTH were 55.0, 32.5 and 10.0 μ M. The flow focusing was generated where the central stream of polymer/drug/DMSO solution met the two lateral sheath streams of water side by side. The volumetric ratio of the organic solution over water (R) was varied by changing the relative flow rates. Total flow rate (Q) was set at 0.65 mL/h, accordingly with that used for the production of empty PMs

(see section 3.2.5 Preparation of polymeric micelles). An inverted microscope (Olympus IX51, Japan) monitored the flow within the microchannels.

PM-MTHs samples were also prepared by bulk mixing. A polymeric solution in DMSO, in the presence or the absence of MTH, was added to 2-10 mL of deionised water in a glass round-bottom flask and thoroughly mixed by vortexing for 5 min. Different volumetric ratios (R) of organic solution to water were selected varying between 0.03 and 0.13. For both, microfluidic and bulk mixing procedures, the preparation of PMs was performed at environmental temperature, typically ranging between 21-23 °C.

6.2.3 PM-MTH Characterization

Before characterization, the amount of water was adjusted in order to have the same DMSO/water ratio in all samples (i.e., 3.2 % DMSO, v/v), samples were then divided in three aliquots stored in dark and used for the analysis.

The size and size distribution of PMs were determined by Dynamic Light Scattering (Zetasizer Nano ZS, Malvern Instruments Ltd., U.K.) and/or by nanoparticle tracking analysis (NanoSight LM10, NanoSight Ltd. Amesbury, UK). For each measurement, 300 µL of PM suspension was loaded in the detection cell and five measurements were performed to give an average value using Zetasizer software 6.12 (Malvern Instruments Ltd., U.K.) and NanoSight NTA Analytical Software (NanoSight Ltd. Amesbury, UK), respectively. PMs sizing was performed at environmental temperature, typically ranging between 21-23 °C.

To have an estimation of the amount of drug associated in small (i.e., PM with a mean diameter ≤ 200 nm, $PMs_{\leq 200}$), and large PMs (i.e., ≥ 200 nm in diameter), after preparation PM suspension was passed through a 0.2 µm pore size filter as previously reported [230]. The MTH concentration in filtrates was estimated by measuring its fluorescence at $\lambda_{ex} = 440$ nm and $\lambda_{em} = 523$ nm using a fluorescence spectrometer (Bentham Instrument Ltd, UK). The percentage of drug associated in $PMs_{\leq 200}$ ($drug_{\leq 200}$) was calculated using the following equation,

$$drug_{\leq 200} = \frac{a}{b} \times 100 \quad (6.1)$$

where a is the weight amount of drug in $PMs_{\leq 200}$ (g) and b is the total amount of drug used for PM preparation (g).

To estimate the drug association, defined as the percentage of drug associated to PMs (PM-MTH), samples were filtrated through a semi-permeable membrane with 3,000 Da NMWL (Amicon Ultra-4 Centrifugal Filter Device, Millipore Ltd, Watford, UK) for 15 min at 1.25 g, to separate water phase from micelles. The amount of free MTH in the

filtrate was determined by spectrofluorimetric analysis at $\lambda_{\text{ex}} = 440$ nm and $\lambda_{\text{em}} = 523$ nm (Cary Eclipse, Agilent Technologies, Lakeside, UK).

6.2.4 Experimental design and statistical data

The influence of experimental parameters on the PM size and drug₂₀₀, was studied by Design of Experiments (DoE) approach consisting of 11 runs. The DoE approach used was a Full Factorial design plus two additional centre points for the estimation of reproducibility. The experimental design and the evaluation of the experiments were performed by the software MODDE 8.0 (Umetrics AB, Sweden), followed by multiple linear regression (MLR) algorithms as previously described [281].

6.2.5 K562 cell cultures

Human myeloid leukemia K562 cells were cultured in humidified atmosphere of 5% CO₂ in RPMI 1640 (Sigma-Aldrich, Italy) supplemented with 10% fetal bovine serum (Celbio, Milano, Italy), 50 U/mL penicillin and 50 µg/mL streptomycin [282]. Treatment of K562 cells with free (dissolved in DMSO at the appropriate concentrations) or PM associated MTH was carried out by adding the appropriate concentration of drug at the beginning of the cultures (cells were seeded at 30,000/mL). The medium was not changed during the entire induction study. Cell number/mL was determined with a ZF Coulter Counter (Counter Electronics, Hialeah, FL, USA) at different days 4 and 7 from the culture set-up. The proportion of benzidinepositive cells (which contain haemoglobin, an index of erythroid differentiation) was determined after 7 days in culture using a solution containing 0.2% benzidine in 5 M glacial acetic acid (10% H₂O₂), as previously described [30, 264].

6.2.6 Erythroid precursor cell cultures

Patients were from Day Hospital Talassemici, Azienda Ospedaliera Universitaria di Ferrara U.O. Pediatria dell’Ospedale S. Anna, Ferrara, Italy; written informed consent was obtained from each patient and the samples of peripheral blood were collected just before the transfusion treatment. Mononuclear cells were isolated by Ficoll-Hypaque density gradient centrifugation, and seeded in α -minimal essential medium supplemented with 10% FBS (Celbio, Milano, Italy), 1 µg/ml cyclosporine A (Sandoz, Basel, Switzerland) and 10% conditioned medium from the 5637 bladder carcinoma cell line. The cultures were incubated at 37°C, under an atmosphere of 5% CO₂ in air, with extra humidity. After 7 days incubation in this phase I culture, the non-adherent cells were harvested, washed, and then cultured in fresh medium composed of α -medium,

30% FBS, 1% deionised bovine serum albumin, 10^{-5} M β -mercaptoethanol, 1.5 mM L-glutamine, 10^{-6} M dexamethasone, and 1 U/ml human recombinant erythropoietin (EPO) (Tebu-bio, Magenta, Milano, Italy) and stem cell factor (SCF) (Inalco, Milano, Italy). This part of the culture is referred to as phase II. After phase II, the induction period with erythroid inducer MTH was usually of 4 days [30].

6.2.7 RNA extraction and Real-Time quantitative PCR (RT-PCR)

Cells were isolated by centrifugation at 1500 rpm for 10 min at 4°C, washed in PBS, lysed in Tri-reagentTM (Sigma Aldrich, St.Louis, Missouri, USA), according to the manufacturer instructions. The isolated RNA was washed once with cold 75% ethanol, dried and dissolved in diethylpyrocarbonate treated water before use. Reverse transcription-polymerase chain reaction (RT-PCR) was performed as follows. After production of cDNA, using 1 μ g total RNA, a control PCR for γ -globin gene expression was performed using the γ -globin mRNA-specific primers 5'-ACTCGCTTCTGGAACGTCTGA-3' and 5'-AGTGCCTGTCCTCCAGATAC-3'. Quantitative real-time PCR assay of γ -globin mRNA, β -globin, and α -globin transcripts were carried out using gene-specific double fluorescently labeled probes in a 7700 Sequence Detection System version 1.6.3 (Applied Biosystems, Warrington Cheshire, United Kingdom). The following primer and probe sequences were used for real-time (RT) PCR: γ -globin forward primer, 5'-TGGCAAGAAGGTGCTGACTTC-3'; γ -globin reverse primer, 5'-TCACTCAGCTGGCAAAGG-3'; γ -globin probe, 5'-FAM-TGGGAGATGCCATAAACGCACCTGG-TAMRA-3'; β -globin forward primer, 5'-CAAGAAAGTGCTCGGTGCCT-3'; β -globin reverse primer, 5'-GCAAAGGTGCCCTTGAGGT-3'; β -globin probe, 5'-FAM-TAGTGATGCCCTGGCTCACCTGGAC-TAMRA-3'; α -globin forward primer, 5'-TCCCCACCACCAAGACCTAC-3'; α -globin reverse primer, 5'-CCTTAACCTGGCAGAGCC-3'; α -globin probe, 5'-FAM-TCCCGCACTTCGACCTGAGCCA-TAMRA-3'. The fluorescent reporter and the quencher were 6-carboxyfluorescein (FAM) and 6-carboxy-N,N,N',N'-tetramethylrhodamine (TAMRA), respectively. For real-time PCR of the reference genes, the endogenous control human glyceraldehyde-3-phosphate dehydrogenase (GAPDH) and β -actin kits were used. The probes were fluorescently labeled with VIC (Applied Biosystems).

6.2.8 HPLC analysis of haemoglobins

ErPC were harvested, washed once with PBS and the pellets were lysed in lysis buffer (sodium dodecyl sulphate 0.01%). After incubation on ice for 15 min, and spinning for

5 min at 14,000 rpm in a microcentrifuge, the supernatant was collected and injected. Hemoglobins (Hb) present in the lysates were separated by cation-exchange HPLC [283], using a Beckman Coulter instrument System Gold 126 Solvent Module-166 Detector. Hb were separated using a Syncropak CCM 103/25 (250 mm x 4.6 mm) column, samples were eluted in a solvent gradient using aqueous sodium acetate-BisTris-KCN buffers and detection was performed at 415 nm. The standard controls were the purified HbA (SIGMA, St Louis, MO, USA) and HbF (Alpha Wassermann, Milano, Italy).

6.2.9 Statistical data analysis

All the data were normally distributed and presented as mean \pm SD. Statistical differences between groups were compared using 1-way ANOVA (ANalyses Of VAriance between groups) software. Statistical significance was assumed at a *p* values less than 0.05 (*) or 0.001 (**).

6.3 Results and discussion

6.3.1 Effects of MTH encapsulation on PM characteristics

Previous investigations for the production of empty PMs (see Chapter 3) have shown that using Microreactor 2 at polymer concentration of $1.5 \cdot 10^{-2}$ M it was possible to produce PMs in a robust and reproducible fashion. Compared to the other employed microreactors, Microreactor 2 also represents a good compromise between smaller mean size, high homogeneity of the produced PMs and high volumetric throughput. For these reasons, the production of PM-MTH was carried out using Microreactor 2 at a Pluronic F127 concentration of $1.5 \cdot 10^{-2}$ M, with identical experimental conditions (i.e., temperature, Q and solvent type) used for the production of their empty counterparts (see Figure 3.9).

Figure 6.3 reports the dimensions of PMs produced by microfluidics in comparison with bulk mixing results, in the presence of different concentrations of MTH at 10.0, 32.5 and 55.0 μ M, with *R* = 0.03. For comparison the results for empty PMs are also reported (i.e 0 μ M).

Both preparation procedures resulted in the formation of PMs larger in size with respect to their empty counterparts. This result could be explained by the intercalation of MTH molecules (possessing amphiphilic properties) within the polymer chains into the core/shell interfacial region of the micelles [284]. The presence of “guest” drug

molecules is likely to decrease on one side the interactions between unimers during the PM aggregation process [132] and on the other side to increase the interfacial surface area [285] resulting in larger PMs. However, how MTH and, in general, a non-precipitating amphiphilic molecule interferes with the PMs precipitation is still not clear and remains the subject of future research.

At a concentration of 55.0 μM , MTH caused an increase in PM mean diameter from 113 to 122 nm and from 150 to 196 nm for microfluidic and conventional procedures, respectively (Figure 6.3). As it is evident, MTH had a remarkable effect especially during the bulk mixing procedure, where it caused the formation of a thick tail of PMs with a characteristic diameter above 240 nm (see Figures 6.3b-c). In contrast, it caused only a small increase in the size of PM-MTH produced by microfluidics where for the three MTH concentrations employed more than 90% of the produced PMs had a characteristic diameter below 200 nm.

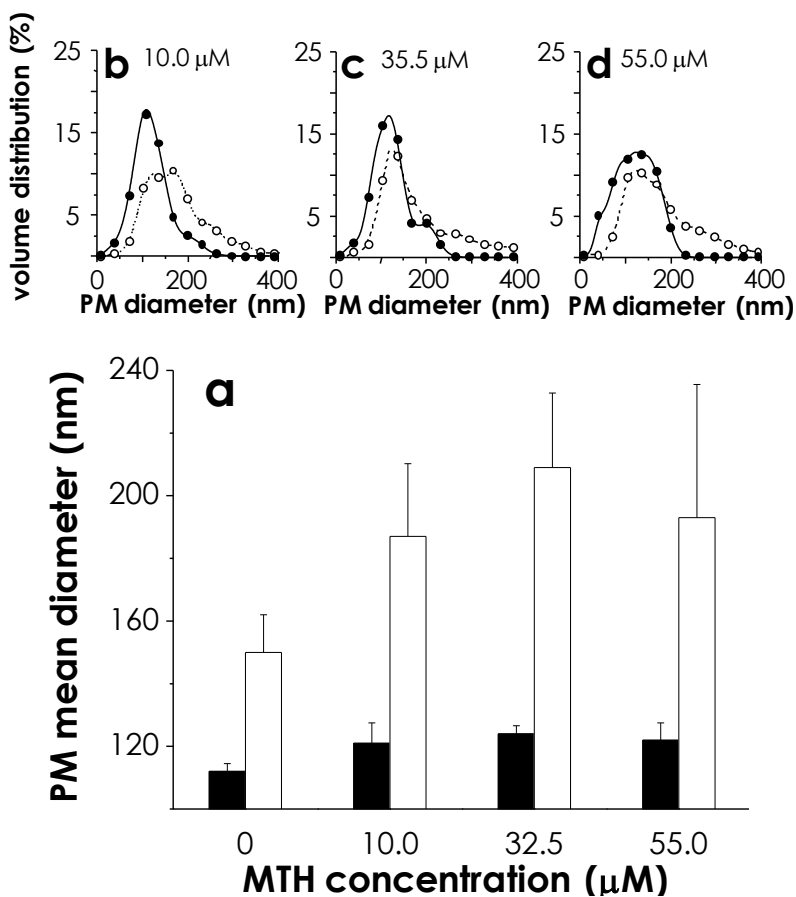


Figure 6.3 Effect of preparation procedure on mean size (a) and size distribution (b-d) of PM-MTH produced at different MTH concentrations. PMs were prepared by bulk mixing in round bottom flask (open bars) and by microfluidics (filled bars). Data represent the average of three independent experiments (run in triplicate) \pm SD. Panels b-d respectively report the size

distribution of PMs produced with 10.0 (b), 32.5 (c) and 55.0 (d) μM mithramycin solution, by bulk mixing (open circles) and by microfluidics (filled circles).

Furthermore, the lower inter-batch standard deviation found for microfluidic samples, indicated a higher reproducibility of the method. Specifically, inter batch S.D. increased from 11.9 to a maximum of 42.5 for batch reactor while had only a modest increases from 2.5 to a maximum of 6.5 for microreactor.

Due to the amphiphilic properties of MTH, it was important to determine the amount of MTH that was effectively associated with the PM structure with respect to the amount of free MTH. The determination of drug association showed that MTH is preferentially partitioned in the micellar phase. Specifically, the determinations demonstrated that about 85 and 83 % (w/w) of the total MTH is associated to the micellar phase, for microfluidics and bulk mixing preparation procedures, respectively. This result is supported by the drug logP (1.290 ± 1.454) that indicates the slight lipophilic nature of MTH molecule [274].

6.3.2 Optimization of PM-MTH production by DoE approach

In order to comparatively study the influence of experimental parameters on the PM-MTH characteristics, produced by microfluidic vs. conventional bulk mixing, a statistical data analysis, based on a design of experiment (DoE) was performed.

The response variables, and their target ranges, were selected taking into consideration that it is well-established that size and size distribution are major factors determining the pharmacokinetic and biodistribution of PMs *in vivo* [150, 286, 287]. Typically, PMs with mean diameter between 100 and 200 nm maximize stealth properties, reducing recognition by the immune system components with prolonged plasma circulation times, as compared to those with larger diameter [141, 275, 276, 288, 289]. In addition, PMs larger than 200 nm in diameter has been demonstrated to be removed from circulation by interendothelial cell slits spleen filtration [7, 141, 144, 290]. Taking into account the above reported consideration, the goal was to obtain PMs with a size comprised between 100 and 200 nm in diameter, a size distribution as narrow as possible and a high drug₂₀₀.

As reported in previous Chapters and depicted in Figure 6.3, *R* and MTH concentration represent the two main factors affecting PM-MTH size characteristics. Therefore, the experiments were designed to simultaneously investigate the effects of the factors: “*R*” and “conc” on the responses: “size”, “SD” and “drug₂₀₀” (see explanations in Table 6.1).

Table 6.1 DoE study of the influence of experimental parameters on the PM-MTH characteristics: investigated factors and responses.

Parameter	Abbreviation	Meaning	Range
<i>Factor</i>			
Volumetric ratio	R	the volumetric ratio between the polymeric solution in DMSO and water phase	0.03-0.13
mithramycin concentration	conc	the concentration of the mithramycin solution in DMSO, employed for the PM production	10.0-55.0 μM
<i>Responses</i>			
Polymeric micelle size	size	the mean diameter of polymeric micelle containing MTH as determined by Dynamic Light Scattering	
SD of polymeric micelle size	SD	the standard deviation of the size distribution curve of the polymeric micelle containing MTH	
MTH in polymeric micelles <200 nm	drug ₂₀₀	the percentage of drug encapsulated in polymeric micelles with a mean diameter ≤ 200 nm	

Each factor was tested at three levels, and two additional centre points were added, in order to get an estimation of the experimental error. In Table 6.2 and Figure 6.3 the complete list of experimental data and results are reported.

Table 6.2 reports the results (i.e. data points) for the experimental matrix of the DoE analysis, while the 3D graphs, reported in Figure 6.4 report the interpolated response surfaces. The graphs show the factors influence on “size” (a), “SD” (b) and “drug₂₀₀” (c) of PM-MTH, produced by microfluidics (red surfaces) Vs conventional bulk mixing (green surfaces). The reported results indicate the superior overall quality of PM-MTH produced by microfluidics. Indeed, the red surfaces show a better quality of the produced PMs in terms of “size”, “SD” and “drug₂₀₀”. Specifically, for the microfluidic protocol, clear trends of the factor effects on the size characteristics have been found. An increase in the factor “R”, from low to high level (0.03-0.13), resulted in a moderate increase in the response “size” that rises from about 120 to around 180 nm, while the response “SD” remains almost constant, with only a slightly increase as results of increased “R” and “conc”.

Table 6.2 Experimental design matrix and results of the DoE (design of experiments) approach for the preparation of PM-MTH.

Run	Factors		Responses		
	conc ^a	R ^b	size ^c	SD ^d	drug ₂₀₀ ^e
Microfluidics					
#1	10.0	0.30	120	42	77.0
#2	55.0	0.30	122	44	58.6
#3	10.0	0.13	162	46	92.3
#4	55.0	0.13	180	56	48.1
#5	10.0	0.08	138	42	89.8
#6	55.0	0.08	142	46	55.3
#7	32.5	0.03	124	44	84.7
#8	32.5	0.13	146	48	65.0
#9	32.5	0.08	152	50	86.8
#10	32.5	0.08	148	42	86.4
#11	32.5	0.08	150	52	87.0
Bulk mixing					
#1-b	10.0	0.30	188	94	72.3
#2-b	55.0	0.30	194	112	35.0
#3-b	10.0	0.13	184	72	79.7
#4-b	55.0	0.13	212	74	35.8
#5-b	10.0	0.08	218	134	76.1
#6-b	55.0	0.08	200	104	49.2
#7-b	32.5	0.03	110	140	59.1
#8-b	32.5	0.13	246	104	49.2
#9-b	32.5	0.08	240	146	38.7
#10-b	32.5	0.08	212	110	34.9
#11-b	32.5	0.08	220	98	37.5

^athe micromolar (μM) concentration of the mithramycin solution in DMSO, employed for the PM production.

^bthe volumetric ratio between the polymeric solution in DMSO and water phase.

^cthe mean diameter of the obtained PMs as determined by Dynamic Light Scattering, expressed in nanometers (nm).

^dthe standard deviation of the size distribution curve of the polymeric micelle containing MTH.

^ethe MTH drug₂₀₀, calculated as reported in the experimental section.

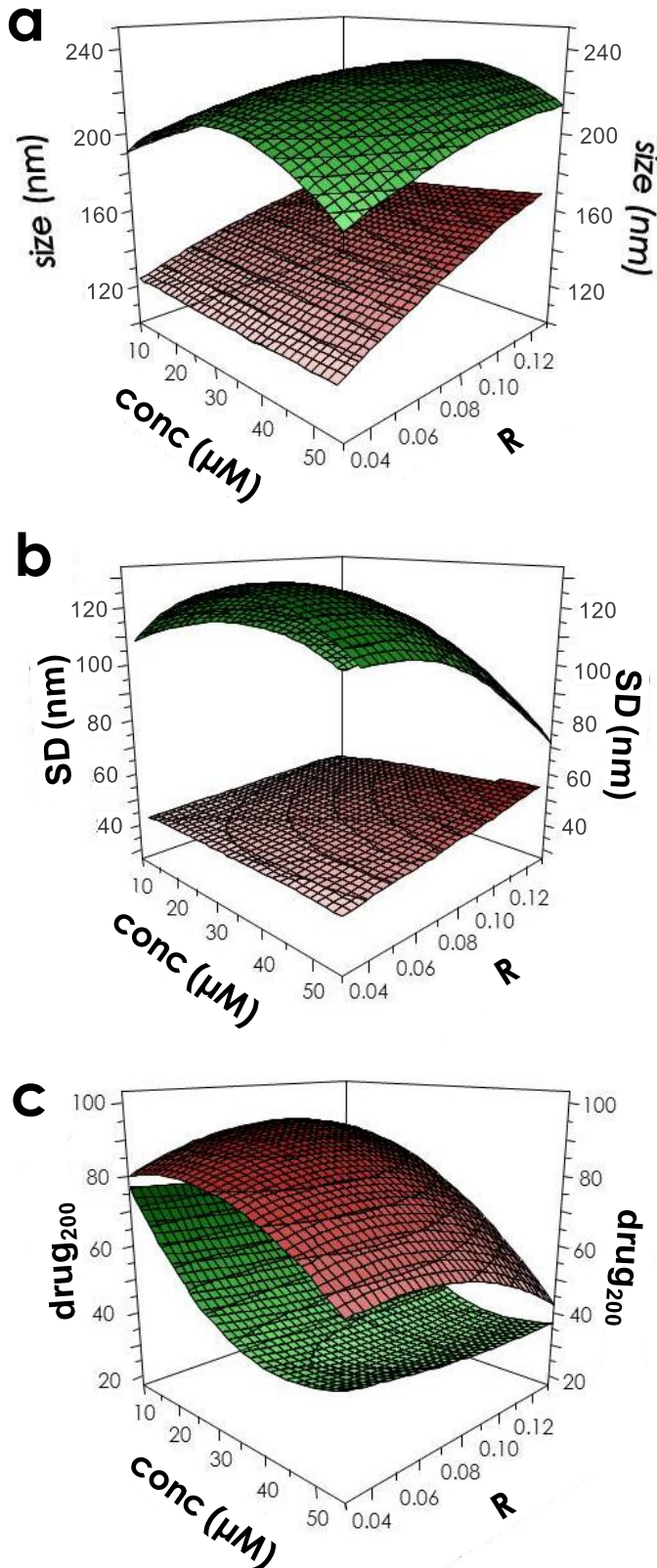


Figure 6.4 DoE analysis for the preparation of PM-MTH. Response surface plots for PMs obtained by bulk mixing (green surfaces) or microfluidics (red surfaces). The following factors and responses were respectively investigated: “conc” and “R” vs. “size” (a), “conc” and “R” vs. “SD” (b) and “conc” and “R” vs. “drug₂₀₀” (b). The meanings of the factor are reported in Table 6.1.

Experimental data points are reported in Table 6.2.

These results clearly demonstrated the precise control over the mixing under laminar flow conditions, resulting in predictable continuous flow preparation of PM-MTH of controlled size (Figure 6.4a-b). In contrast, the bulk mixing led to a lacking of a dimensional correlation between experimental parameters and PM size. It is indeed evident that the bulk mixing caused the formation of large and polydisperse PMs (see Figure 6.3). The limited size control is likely due to the chaotic nature of mixing under the turbulent conditions, associated with bulk mixing procedures.

The response factor “drug₂₀₀” was taken into consideration to estimate the amount of drug associated in PMs smaller than 200 nm in diameter. The analysis of this factor gives us a coarse indication of the percentage of drug that is associated into small PMs, which exhibit prolonged circulation properties and can be uptaken by the cells through non-phagocytic translocation. In this respect, it has been shown that a reduction of the size was a critical factor to improve such mechanism of translocation within blood cells [280]. The “conc” factor deeply influences this response; specifically, an increase of “conc” is accompanied by a decrease of the “drug₂₀₀” (Figure 6.4c and Table 6.2) for PM-MTH produced with bulk mixing. On the contrary, the microfluidic-based procedure is much less affected by the loss of drug during the filtration step, as evident by the higher value for “drug₂₀₀”. As general explanation of the “drug₂₀₀” trend, the progressive rise of MTH molecules probably causes the formation of an increasing number of large PM-MTH aggregates (Figure 6.2b-d). Interestingly, at the same “conc” level, the micelles produced by bulk mixing, at different “R”, show a similar “drug₂₀₀”, indicating that “R” has only a minor effect on “drug₂₀₀” for this preparation procedure.

Once again, the microfluidic procedure shows a superior control over the final PM-MTH characteristics; for instance, the highest “drug₂₀₀” is achieved at the intermediate “R” value (0.08). The authors believe that this effect could be related to the complex interactions between molecular and hydrodynamic phenomena occurring during the micelle self-assembly, even if, at this stage, there is no sufficient experimental evidence to corroborate this hypothesis.

The DoE analysis offers also indications for the development of a robust preparation procedure that is of primary importance for the therapeutic application of PMs, where an efficient control of the PMs’ characteristics is required to achieve an optimal and reproducible therapeutic efficacy [10, 130]. In this respect, the validity and the significance of the DoE model was assessed by the analysis of variance (ANOVA). Table 6.3 reports the ratio of the variation of the response explained by the model (R^2) and the model reproducibility, for both bulk and microfluidic mixing procedures.

Table 6.3 Analysis of variance of the model (ANOVA).

Responses	N	R ²	Reproducibility
Bulk mixing			
Size	11	0.632	0.445
SD	11	0.576	-0.445
drug ₂₀₀	11	0.845	0.987
Microfluidics			
Size	11	0.831	0.992
SD	11	0.646	0.098
drug ₂₀₀	11	0.916	0.999

N is the number of experiments

R² is the ratio of variation of the response explained by the model

The two mixing strategies applied resulted in different predictability and reproducibility of the results for the three studied responses. Specifically, slightly higher predictability and reproducibility were obtained for the microfluidic procedure when compared with bulk mixing as indicated by the higher R² and reproducibility of the obtained results, respectively. From the analysis of the experimental data points reported in Table 6.2, it is possible to identify that PM-MTH produced by microfluidic showed a better linear relationship between the variation of experimental factors and the obtained responses when compared to PM-MTH produced by bulk mixing procedure. This resulted in a better fitting of the data obtained with the MLR algorithm and consequently a higher R² values. Moreover, microfluidic procedure showed a smaller variation within the response values of the three centre points of the experimental matrix (i.e. conc= 32.5 µM and R=0.08, in Table 6.2) that resulted in the higher reproducibility of the microfluidic mixing procedure when compared with that of bulk mixing.

Taken together these results revealed that the laminar condition of microfluidic mixing procedure resulted in a more controllable and reproducible formation of PM-MTH when compared to the turbulent-based mixing that characterized the bulk mixing procedure.

6.3.3 Effect of PM-MTH on proliferation and differentiation of K562

After optimization, the produced PM-MTHs were *in vitro* tested to investigate their biological activity and effectiveness as potential treatment for beta-thalassemia. To this aim, micelle produced with “R” and “conc” equal to 0.03 and 32.5 µM, respectively, were selected, as the optimal formulation due to their small size and homogeneity. For

comparison, PM-MTH produced both by conventional bulk mixing and microfluidic procedures were considered.

K562 cells, derived from a patient who had chronic myeloid leukaemia in terminal blast cell crisis, posses certain erythroid characteristics, and can be induced to produce embryonic and fetal but not adult haemoglobin. Therefore such cell line can be conveniently employed as model for studying haemoglobin production upon differentiation [263].

Figure 6.5 reports the effect of PM-MTH on the proliferation of K562 cells, when employed at the concentrations exerting a differentiative activity.

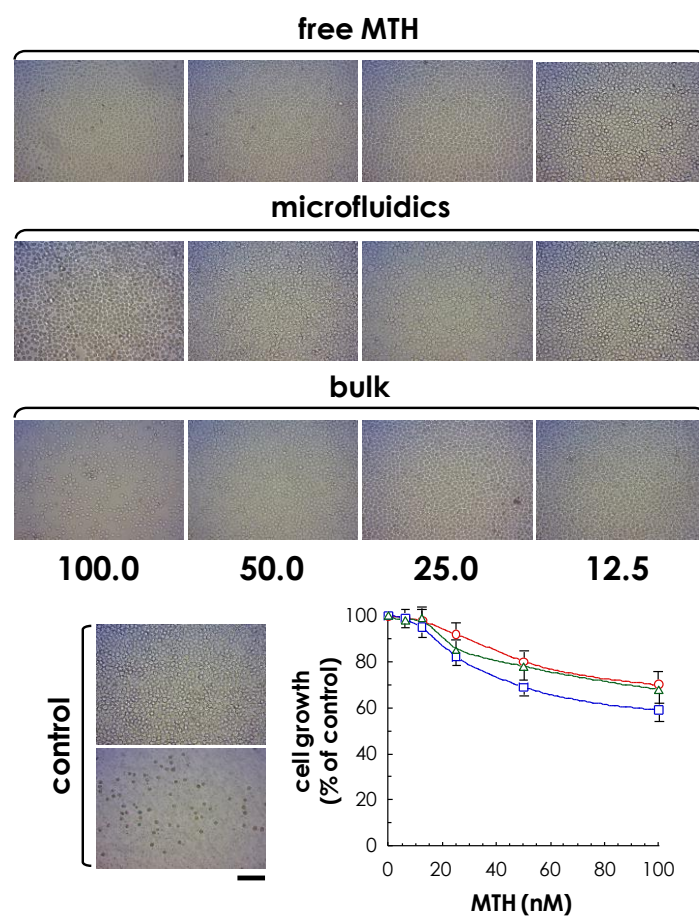


Figure 6.5 Effect of MTH on growth of K562 cells. Microphotographs showing the K562 cell density after 3 days of culture in the presence of the indicated nM MTH concentrations. Bottom left side: photomicrographs showing the control, cultured in absence of MTH, after 0 (bottom) and 3 (upper) days of culture. Corresponding graph: free MTH (squares), PM-MTHs prepared by microfluidics (circles) or bulk mixing (triangles). Data represent the average of three independent experiments (run in triplicate) \pm SD. Bar corresponds to 100 μ m.

For comparison, Figure 6.5 reports also the data obtained by the free drugs. The three untreated control cells showed a SD of the proliferation rate of 2.6%. Cells were cultured for 3 days, in the presence of the indicated concentrations of MTH, added to the culture medium in form of free drug or encapsulated into PMs, prepared by microfluidics or bulk mixing procedures. The results show that MTH cause a dose-dependent decrease in the proliferation efficacy of K562 cell. Specifically, when the drug is employed in the range of concentrations comprised between 6 and 50 nM, had only a limited effect on cell proliferation (< 35%). K562 cells cultured in the presence of Pluronic F127 empty PMs (i.e., without drug), prepared with the same chemical composition and using an identical experimental setup used for the production PM-MTH, displayed a viability and proliferation rate super-imposable to the untreated control cells. Notably, the delivery by PM-MTH appears to have a positive effect on the cytotoxic activity of the drug. In fact, PM-MTH for all the tested concentrations presented a slightly less pronounced effect on cell growth, with respect to the free drug.

After having demonstrated that free MTH and PM-MTH at concentrations below 50 nM presented no significant activity on cell growth, the ability of PM-MTH to induce the erythroid differentiation of K562 cells was tested. To determine the number of cell that underwent erythroid differentiation cells containing haem or Hb were detected by specific reaction with a benzidine/hydrogen peroxide solution. Figure 6.6 shows that the cell treatment at the indicated concentration of free MTH and PM-MTH, induced a clearly evident erythroid differentiation, as proved by the intense positive blue colour developed by the cells, after benzidine staining (Figures 6.6a-b).

Empty Pluronic F127 micelles, used as control, did not show any appreciable difference in cell differentiation when compared with untreated cells (data not shown). Notably, the delivery by micelles produced by microfluidics appears to have a positive effect on the differentiative activity of MTH. In fact, at 50.0 nM PM-MTH presented a slightly more pronounced differentiation, with respect to free drug (microfluidics Vs free MTH, $p<0.05$).

In order to obtain quantitative results and additional information at the molecular level, RT-PCR was performed, for the analysis of α - and γ -globin mRNA expression levels (Figure 6.5c). The quantification of β -globin mRNA was not performed, since it is well known that the β -globin gene is not efficiently transcribed in K562 cells [291]. The obtained results indicate that microfluidic prepared PM-MTH are more active in inducing α - and γ -globin mRNA accumulation when compared to free MTH or PM-MTH prepared by bulk mixing (α -globin: microfluidics Vs bulk, $p<0.001$, microfluidics Vs

free MTH p< 0.05; γ -globin: microfluidics Vs bulk, p< 0.05, microfluidics Vs free MTH p< 0.05).

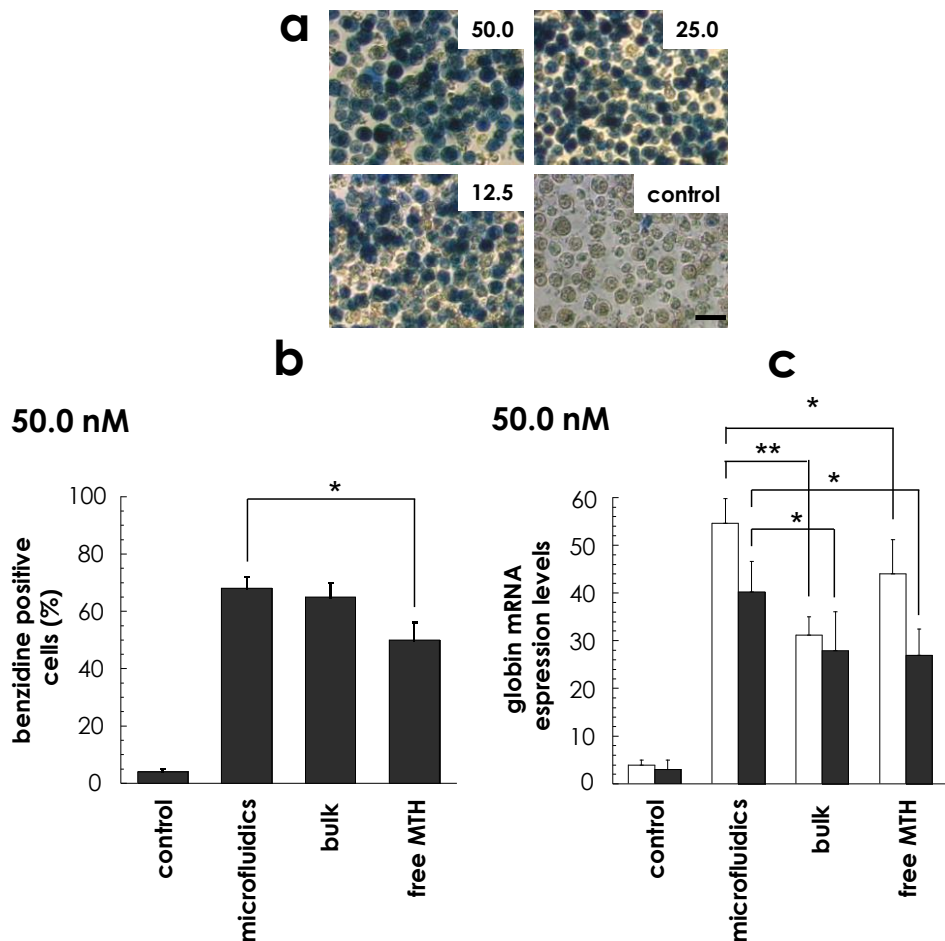


Figure 6.6 Effect of MTH on erythroid differentiation of K562 cells (a-b). Cells were cultured for 7 days, in the presence of the indicated nM MTH concentrations added to the culture medium in form of free drug or encapsulated into PMs prepared by microfluidics or bulk mixing.

Microphotographs of panel A were taken after staining with benzidine cells treated with PM-MTH (microfluidics), thereafter cells were counted and the per cent of benzidine-positive cells was determined and plotted. Scale bar 25 μ m. (b). Data represent the average of three independent experiments (run in triplicate) \pm SD (microfluidics Vs free MTH, p< 0.05). c. Effects of MTH on expression of globin genes. Cells were cultured for 4 days, in the presence of the 50 nM of MTH added to the culture medium in form of free drug or encapsulated into PMs prepared by microfluidics or bulk mixing, as indicated. RT-PCR was performed as indicated in methods for quantification of α -globin (open bars) and γ -globin (filled bars) mRNA sequences. Data represent fold content in respect to control uninduced cells (average \pm SD of three independent experiments); α -globin: microfluidics Vs bulk, p< 0.001, microfluidics Vs free MTH p< 0.05; γ -globin: microfluidics Vs bulk, p< 0.05, microfluidics Vs free MTH p< 0.05.

The smaller dimension of the microfluidic produced PM-MTH, as compared with those produced by bulk procedure (see Figure 6.4 and Table 6.2) might be the reason of more efficient cell internalization through non-phagocytic translocation mechanism, resulting in a higher intracellular MTH concentration and a relative higher differentiative activity. Further investigations on the mechanism of cells internalization are underway to elucidate the mechanism of this effect.

6.3.4 Effect of PM-MTH on erythroid precursor cells

As further investigation, the ability of MTH, delivered by microfluidic produced PM-MTH, to stimulate the HbF production in erythroid progenitor cells from β -thalassemia patients was analyzed. ErPC were stimulated with EPO in the absence of MTH (uninduced ErPC) or in the presence of MTH (either free drug or PM-MTH) and the lysates were analyzed by HPLC. As demonstrated by Figure 6.7a-b, an increase of HbF is observed from 17.23 (uninduced ErPC) to 22.71 % (ErPC treated with PM-MTH). As expected, also free MTH stimulates an HbF increase (20.35%), even if to a lower extent. Of interest is the parallel reduction of α -globin aggregates, which represent 24.39% of the total haemoglobin (for uninduced ErPC), both in ErPC treated with PM-MTH (6.71 %) or free MTH (11.30 %) (HbF: uninduced Vs microfluidics, $p<0.05$, uninduced Vs free MTH $p<0.05$; α -aggregates: uninduced Vs microfluidics, $p<0.001$, uninduced Vs free MTH $p<0.001$, microfluidics Vs free MTH $p<0.05$).

The decrease in α -globin aggregates following treatment with HbF inducers is of a great importance, since the excess of α -globin production by thalassemic patients is responsible for the clinical symptoms of this pathology. This finding is further sustained by the RT-PCR analyses on mRNA samples (see Figure 6.7c). No increase of α -globin mRNA is observed in both ErPC treated with PM-MTH or free MTH, while PM-MTH is able to induce γ -globin mRNA (2.87 fold) and β -globin mRNA (1.68 fold) more efficiently than free MTH (1.64 fold and 1.14 fold, respectively).

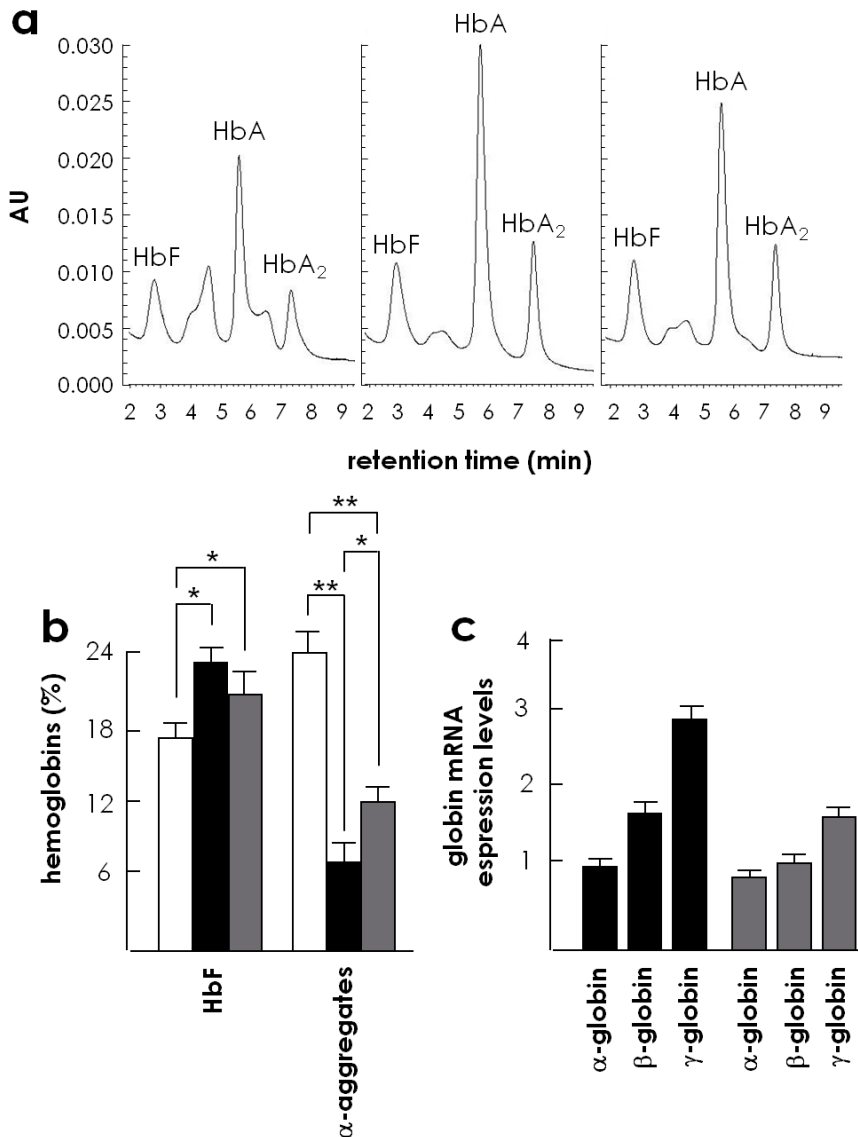


Figure 6.7 Effect of MTH encapsulated into PMs prepared by microfluidics on HbF production by erythroid precursor cells (ErPC) from a β -thalassemia patient. ErPC were cultured in phase II with only EPO, or EPO plus free MTH or PM-MTH prepared by microfluidics. a: HPLC profile of uninduced ErPC (left), ErPC induced by PM-MTH (center) and free MTH (right). Panel b reports the quantitative effects on HbF and the production of α -aggregates in ErPC induced by PM-MTH (filled bars) and free MTH (grey bars). For comparison data referred to uninduced ErPC (open bars), are also reported (HbF: uninduced Vs microfluidics, $p < 0.05$, uninduced Vs free MTH $p < 0.05$; α -aggregates: uninduced Vs microfluidics, $p < 0.001$, uninduced Vs free MTH $p < 0.001$, microfluidics Vs free MTH $p < 0.05$). Panel C reports the RT-PCR analysis of ErPC, expressed as fold induction of α -globin, β -globin and γ -globin mRNA production. Cells were treated with PM-MTH (black bar) or free drug (grey bars). Data represent the average of three independent determinations \pm SD.

6.4 Summary

A microfluidic-based protocol for the production of a micellar delivery system for MTH (PM-MTH) was developed and examined in comparison to PM-MTH produced with conventional methods. The effect of different production parameters was investigated and their effects on the size and size distribution of PM-MTH were statistically evaluated. The results indicate that MTH can be efficiently formulated as micellar nanoparticles, in a controlled and reproducible manner not achievable in conventional bulk method. After preparation and characterization, PM-MTH prepared both by microfluidic and bulk methods were *in vitro* tested to investigate their biological activity and effectiveness as potential treatment for beta-thalassemia. Interestingly, PM-MTH exhibited a slightly lower toxicity and more pronounced differentiative activity when compared to the free drug. Moreover, the presented data suggest that the delivery of MTH by PMs produced by microfluidic is able to induce, at high levels, globin mRNA accumulation in K562 cells. Noteworthy, the RT-PCR data, obtained using erythroid precursor cells, demonstrated that MTH encapsulated in polymeric micelles, as the most effective HbF inducers, is able to induce β -globin and even more efficiently γ -globin gene expression, without stimulating α -globin gene expression. This result is sustained by the HPLC analyses, showing an increase of HbF and a decrease of α -globin aggregates in ErPC treated with EPO, in the presence of PM-MTH produced by microfluidics.

In conclusion, it is suggested that PM-MTH might be of great interest in inducing HbF in thalassemic patients, offering exciting avenues for future development of micellar and more, in general, nanomedicine related therapeutic protocols for beta-thalassemia. Also considering the simplicity and reproducibility of the microfluidic technology, the presented production strategy might be suitable for personalized medicine applications, which require controllable PM characteristic and consistency from batch to batch.

Chapter 7

Conclusions

Advances in nanomedicine have dictated the need for development of more robust and controllable procedures for the production of nanoparticles [292, 293]. Classical methods for their production rely on bulk mixing and tend to suffer from irreproducibility from batch to batch and difficulties to implement fast screening and optimization of the nanomaterial properties. In this respect, continuous flow microfluidic reactors have shown the capability to produce micro- and nanoparticles in a controllable and reproducible manner offering a possible solution to the aforementioned issues [83].

Compared to the intense research at the intersection between inorganic nanoparticles and microfluidic, relatively little has been done for the production of organic nanoparticles. Considering the high potential of polymeric nanoparticles as drug delivery vehicles, in the previous chapters, the use of microfluidic-based reactors for the production of polymeric micelles has been analyzed under different aspects. Experimental and computational results were used to investigate the fundamental of nanoprecipitation in microfluidic environment, while biological data were used to assess whether, microfluidic produced polymeric micelles, are more effective in delivery their drug payload to cells.

The results showed that hydrodynamic flow focusing reactors provide a tool to control the nanoprecipitation process leading to smaller and more homogeneous polymeric micelles when compared with conventional bulk mixing procedure. This represents an important benefit from the point of view of controlled drug delivery formulations that require reproducible size distribution and batch-to-batch consistency. It has been shown that, besides the important role played by the width of the focused stream, many different aspects also affect the characteristics of the produced polymeric micelles. Specifically, reactor dimension and fluid flow parameters act in concert to determine the nanoprecipitation process by controlling the amount of solvent present within the environment in which the aggregation took place. In this respect, it has been

shown that a larger amount of solvent within the microreactor is likely to lower the barrier for unimer insertion leading to the self-assembly of larger PMs.

Numerical model showed that the combined effect of reactor dimension, fluid properties and flow condition affect mixing condition altering the mixing extents at different location along the focused stream (i.e., near the arrowed-shaped focusing region or further downstream), diffusivity of the species and shape of the focused stream. All these factors concur in controlling mixing time and amount of solvent in the focused stream hence affecting the nucleation and growth process. These results also indicate a possible source of polydispersity in PM size.

The investigation of the co-nanoprecipitation process of a low water soluble molecule, β -carotene, and polymeric stabilizer showed that a competitive reaction resulted in the formation of two types of nanoparticles (i.e., either with or without loading hydrophobic β -carotene in the core-shell structure). The relative amount of the two types of nanoparticles was found to be a function of β -carotene/polymer molecular ratio. Computational model, accounting also for molecular dynamic phenomena, showed the presence of a complex interplay between the two competitive reactions. The results were explained by taking into consideration a new parameter representing the mismatching between the aggregations of the two precipitant species, which plays a decisive role in determining the size, polydispersity of the prepared hybrid nanoparticles. Also in the case of co-nanoprecipitation process, the mixing was found to be critical, highlighting the role of microfluidic environment in controlling the nanoprecipitation output.

Finally, the established microfluidic production procedure was examined from a drug delivery point of view encapsulating a clinically relevant drug. To this aim polymeric micelles containing mithramycin were prepared and tested *in vitro* as a therapeutic protocols for beta-thalassemia. The results indicate that, despite its water solubility, mithramycin can be efficiently formulated as micellar nanoparticles, in a controlled and reproducible manner not achievable in conventional bulk method. Interestingly, comparing with the result obtained for their empty counterparts, the encapsulation of mithramycin caused an increase of the dimension of the produced polymeric micelles. This result is in contrast with that found for the encapsulation of β -carotene, where smaller nanoparticles were produced as results of the co-precipitation of drug and polymer. This finding suggest that the production of polymeric micelles containing amphiphilic drugs is likely to proceed with a different mechanism from that showed for the co-nanoprecipitation with hydrophobic drugs such as β -carotene. In this respect, it should be noted that mithramycin is soluble in water at the used concentrations unlike β -carotene, hence does not precipitate, but simply partition within the micellar phase due to a favourable partition coefficient. As result, mithramycin molecules are likely to

intercalate within the polymer chains into the core/shell interfacial region of the micelles [284], decreasing on one side the interactions between unimers during the PM aggregation process [132], and on the other side increasing the interfacial surface area [285] resulting in larger PMs.

In vitro tests showed that mithramycin encapsulated in polymeric micelles exhibited a slightly lower toxicity and more pronounced differentiative activity when compared to the free drug. Interestingly, microfluidic prepared polymeric micelles are more active in inducing α - and γ -globin mRNA accumulation when compared to free mithramycin or polymeric micelles prepared by bulk mixing. In addition, microfluidic produced polymeric micelles showed a parallel reduction of α -globin aggregates in erythroid precursor cells when compared to free drug. This result is of particular clinical interest since the excess of α -globin production by beta-thalassemic patients is responsible for the clinical symptoms of this pathology.

In conclusion, the results of this study had established that microfluidics could facilitate the production of nanoparticles for drug delivery purposes, offering a novel method and knowledge to improve and control their property including particle size, size distribution and pharmaceutical efficacy. Considering that rapid expansion of both the fields of nanomedicine and microfluidic, the expansion of the knowledge at their intersection, is likely to provide new exiting avenues in the future for tailoring the properties of nanomaterial through controlled microfluidic precipitation.

Chapter 8

Future perspectives

The results presented here are encouraging, but there are many areas that should be investigated in the future. Computation models have shown that hydrodynamic flow focusing brings an implicit cause of nanoparticle polydispersity due to the parabolic flow profile; therefore, novel microfluidic mixing strategy would be required to improve further the nanoparticle properties. In addition, hydrodynamic focusing suffers from channel clogging posing a limit to the amount of polymer and drug that can be introduced. A 3D focusing, in both the horizontal and the vertical dimensions, has been proposed to solve this issue [101]. However, since the vertical focusing was achieved through two additional streams of solvent, it caused the dilution of the initial polymeric stream resulting in a decrease of the attained supersaturation level. In this respect, a microfluidic reactor able to produce a 3D focusing configuration in which the non-solvent stream surrounds a central solvent stream would be required to solve this issue. Such microreactors are expected to speed up the mixing process and lead to smaller and more homogenous nanoparticles by increasing the surface-to-volume ratio of the focused stream, and avoiding focusing stream shape and parabolic flow related source of polydispersity.

However, focusing based mixers rely on the reduction of the central focused stream width to speed up the mixing process. This implies both the reductions of the channel width and of the flow rate ratio, causing a lowering of the nanoparticle production throughput. A possible strategy to solve this issue could be offered by the use of mixers that rely on parallel lamination, chaotic advection or active mixing. Further investigations in this field will also require to develop scale-up strategies to realize large scale production, making microfluidic nanoprecipitation practical for industrial applications.

In addition, it is important to note that for many therapeutic applications of nanoparticles, it is required to carry out post-processing steps on the produced nanomaterial, such as derivatization or cross-linking of the surface, and to remove

solvent residue from the final nanoparticle formulation. These steps are conventionally accomplished through batch and time-consuming procedures. Therefore, it is desirable to develop and implement on-chip post-processing techniques for nanoscale materials in the future. Another important advancement will be the development of reliable on-line detection systems. These will permit to both, investigate the nanoprecipitation process and characterize the produce nanoparticle in real time, thus shortening the time to optimize production conditions.

The investigation of the nanoprecipitation process with different drug and polymer combinations would be also required to corroborate the here presented findings. Particularly interesting would be the study of the nanoprecipitation process with no precipitating amphiphilic drugs, and of polymer and drug combination characterized with a negative mismatching time (drug precipitate prior the polymer).

New insights into the mechanism and kinetics of the nanoprecipitation process will also aid the development of new computational models that will address further the complex interplay between molecular and hydrodynamic phenomena. In particular, the implementation of a more complex relation between nanoparticle formation processes and hydrodynamics is required. A possible strategy could be offered following the path designed by the finite particle model developed for gas-phase processes [294]. This would give more authentic information on the nanoprecipitation process, likely providing suggestions for new and more efficient designs of microreactors.

Finally, despite the growing interest in microfluidics, there is still a limited knowledge on the effective biological role of microfluidically produced nanoparticles as compared with that produced with conventional methods. It is also worth of notice that many of the proposed advancements of nanoparticles produced with microfluidic approaches, such as long circulation and targeting properties, resulting from the small particle size and size homogeneity, could be addressed only *in vivo* setting. Considering the interesting results obtained with encapsulation of mithramycin, *in vivo* tests may prove the effectiveness of this micellar delivery system as therapeutic protocols for beta-thalassemia.

Appendix 1

List of publications

Conference abstracts

D. Carugo, D. N. Ankrett, P. Glynne-Jones, L. Capretto, R. J. Boltryk, P. A. Townsend, X. Zhang, M. Hill, Contrast agent-free cell sonoporation using a continuous-flow microfluidic device, *MicroTAS 2011*, 2-6 October, Seattle, Washington, United States, 2011.

D. Carugo, L. Capretto, S. Willis, A. Lewis, D. Grey, M. Hill, X. Zhang, A microfluidic device for the characterization of embolization with microspherical beads, *MicroTAS 2011*, 2-6 October, Seattle, Washington, United States, 2011.

Lorenzo Capretto, Stefania Mazzitelli, Xunli Zhang and Claudio Nastruzzi. Preparation of alginate microfiber for cell entrapment using a microfluidic device. *MicroTAS 2010* - 3-7 October 2010 - Groningen, NETHERLANDS.

Lorenzo Capretto, Stefania Mazzitelli, Xunli Zhang and Claudio Nastruzzi. Microfluidic production of polymeric micelles for mithramycin encapsulation. XVIII International Conference on Bioencapsulation, 1-2 October 2010, Porto, Portugal.

D. Carugo, L. Capretto, E. Nehru, M. Mansour, W. Cheng, N. Smyth, N. Bressloff, X. Zhang, Microfluidic-based quantification of blood fluid dynamic behaviour in the microcirculation, Virtual Physiological Human network, 30 September-1 October 2010, Brussels, Belgium.

X. Zhang, D. Carugo, L. Capretto, E. Nehru, M. Mansour, W. Cheng, N. Smyth, N. Bressloff, An on-chip model of human microcirculatory network: fluid dynamic analysis using micro-PIV, *Bioengineering* 10, 15-16 September 2010, Nottingham, UK.

Lorenzo Capretto, Wei Cheng, Dario Carugo, Martyn Hill, Xunli Zhang. Microfluidic reactors for controlled synthesis of polymeric micelles. *Journal of Controlled Release* 148 (2010) e25-e26. -11th European Symposium on Controlled Drug Delivery (11th ESCDD), 6-9 April 2010, Egmond aan Zee, The Netherlands.

Lorenzo Capretto, Stefano Focaroli, Xunli Zhang, Stefania Mazzitelli, Claudio Nastruzzi. Production of low cost microfluidic chips by a “shrinking” approach: Applications to emulsion and microparticle production. *Journal of Controlled Release* 148 (2010) e26-e28. -11th European Symposium on Controlled Drug Delivery (11th ESCDD), 6-9 April 2010, Egmond aan Zee, The Netherlands.

Stefania Mazzitelli, Lorenzo Capretto, Xunli Zhang, Letizia Penolazzi, Elisabetta Lambertini, Roberta Piva, Claudio Nastruzzi. Process optimization for the production of alginate microparticles containing wjmscs by a design of experiments (doe) approach. *Journal of Controlled Release* 148 (2010) e76-e27. -11th European Symposium on Controlled Drug Delivery (11th ESCDD), 6-9 April 2010, Egmond aan Zee, The Netherlands.

Journal articles

L. Capretto, W. Cheng, D. Carugo, M. Hill, X. Zhang, Nanoprecipitation of organic actives and block co-polymers within microfluidic reactors, *ACS nano*. (submitted).

D. Carugo, D. N. Ankrett, P. Glynne-Jones, L. Capretto, R. J. Boltryk, P. A. Townsend, X. Zhang, M. Hill, CA-free sonoporation: an efficient ultrasonic standing wave system for the delivery of pharmaceutical agents, *Ultrasound in medicine and biology*, 2011 (submitted).

D. Carugo, L. Capretto, E. Nehru, M. Mansour, N. Smyth, N. Bressloff, X. Zhang, A microfluidic-based model of human arteriolar system for bioanalytical and biophysical investigations, *Current Analytical Chemistry*, 2011 (submitted).

X. Han, C. Van Berkel, J. Gwyer, L. Capretto, H Morgan. Microfluidic lysis of human blood for leukocyte analysis using single cell impedance cytometry. *Analytical Chemistry*. (submitted).

L. Capretto, S. Mazzitelli, E. Brognara, I. Lampronti, D. Carugo, M. Hill, X. Zhang, R. Gambari, C. Nastruzzi, Mithramycin encapsulated in polymeric micelles by microfluidic technology as novel therapeutic protocol for beta-thalassemia. *International journal of Nanomedicine*. (in press).

D. Carugo, L. Capretto, S. Willis, D. Grey, M. Hill, X. Zhang, A microfluidic device for the characterisation of embolisation with polyvinyl alcohol beads through biomimetic bifurcations, *Biomedical Microdevices*, 2011 (in press).

S. Mazzitelli, L. Capretto, D. Carugo, X. Zhang, R. Piva, C. Nastruzzi, Optimised production of multifunctional microfibers by microfluidic chip technology for tissue engineering applications, *Lab On a Chip*, 11, 1776-1785, 2011.

L. Capretto, D. Carugo, W. Cheng, M. Hill, X. Zhang, Continuous-flow production of polymeric micelles in microreactors: Experimental and computational analysis, *Journal of Colloid and Interface Science*, 357, 243-251, 2011.

Book Chapters

Lorenzo Capretto, Wei Cheng, Martyn Hill and Xunli Zhang. Micromixing within Microfluidic Devices. In Bingcheng Lin (ed.), Topics in Current Chemistry, *Microfluidics: Technologies and Applications*. Vol. 304. 2011: Chap. 2, pp. 27-68, Springer, Berlin.

Wei Cheng, Lorenzo Capretto, Martyn Hill and Xunli Zhang. Organic Nanoparticles using Microfluidic Technology for Drug Delivery Applications. In Kumar, Challa S. S. R. (ed.), *Polymeric Nanomaterials*, Vol. 10. 2011: Chap. 8, pp. 221-257, Wiley-VCH, Weinheim.

References

1. Peer D., Karp J., Hong S., Farokhzad O., Margalit R., and Langer R., *Nanocarriers as an emerging platform for cancer therapy*. Nature nanotechnology, 2007. **2**(12): p. 751-760.
2. Wagner V., Dullaart A., Bock A., and Zweck A., *The emerging nanomedicine landscape*. Nature Biotechnology, 2006. **24**(10): p. 1211-1218.
3. Shi J., Votruba A., Farokhzad O., and Langer R., *Nanotechnology in Drug Delivery and Tissue Engineering: From Discovery to Applications*. 2010.
4. Jain K.K., *The handbook of nanomedicine*. 2008: Humana Pr Inc.
5. 2015. O.H.S.R.N.m.t.s.b.b. <http://ohsonline.com/articles/2009/06/29/report-on-nanomedicine-market.aspx>.
6. Davis M.E., *Nanoparticle therapeutics: an emerging treatment modality for cancer*. Nature Reviews Drug Discovery, 2008. **7**(9): p. 771-782.
7. Kwon G., *Polymeric micelles for delivery of poorly water-soluble compounds*. Critical reviews in therapeutic drug carrier systems, 2003. **20**(5): p. 357-403.
8. Ratner B. and Bryant S., *Biomaterials: where we have been and where we are going*. Annual Review of Biomedical Engineering, 2004. **6**: p. 41-75.
9. Yokoyama M., *Polymeric micelles as a new drug carrier system and their required considerations for clinical trials*. Expert Opinion on Drug Delivery, 2010. **7**(2): p. 145-158.
10. Rapoport N., *Physical stimuli-responsive polymeric micelles for anti-cancer drug delivery*. Progress in Polymer Science, 2007. **32**(8-9): p. 962-990.
11. Peng X., Manna L., Yang W., Wickham J., Scher E., Kadavanich A., and Alivisatos A., *Shape control of CdSe nanocrystals*. Nature, 2000. **404**(6773): p. 59-61.
12. Song Y., Hormes J., and Kumar C., *Microfluidic synthesis of nanomaterials*. Small, 2008. **4**(6): p. 698-711.
13. Song Y., Modrow H., Henry L., Saw C., Doomes E., Palshin V., Hormes J., and Kumar C., *Microfluidic synthesis of cobalt nanoparticles*. Chem. Mater., 2006. **18**(12): p. 2817-2827.
14. Whitesides G., *The origins and the future of microfluidics*. Nature, 2006. **442**(7101): p. 368-373.
15. Fletcher P., Haswell S., and Zhang X., *Electrokinetic control of a chemical reaction in a lab-on-a-chip micro-reactor: measurement and quantitative modelling*. Lab on a Chip, 2002. **2**(2): p. 102-112.
16. Dreher S., Kronsbein M., and Woias P. *Heat and Mass Transfer and Wall Contact for Laminar Vortices in Microreactors*. 2008: ASME.
17. Cottam B., Krishnadasan S., demello A., demello J., and Shaffer M., *Accelerated synthesis of titanium oxide nanostructures using microfluidic chips*. Lab on a Chip, 2007. **7**(2): p. 167-169.
18. Edel J., Fortt R., demello J., and demello A., *Microfluidic routes to the controlled production of nanoparticles*. Chemical Communications, 2002. **2002**(10): p. 1136-1137.

19. Krishnadasan S., Brown R., demello A., and demello J., *Intelligent routes to the controlled synthesis of nanoparticles*. Lab on a Chip, 2007. 7(11): p. 1434-1441.
20. Song H., Chen D., and Ismagilov R., *Reactions in droplets in microfluidic channels*. Angewandte Chemie (International ed. in English), 2006. 45(44): p. 7336-7356.
21. Sounart T., Safier P., Voigt J., Hoyt J., Tallant D., Matzke C., and Michalske T., *Spatially-resolved analysis of nanoparticle nucleation and growth in a microfluidic reactor*. Lab on a Chip, 2007. 7(7): p. 908-915.
22. Wagner J. and Köhler J., *Continuous synthesis of gold nanoparticles in a microreactor*. Nano Letters, 2005. 5(4): p. 685.
23. Barrow D., Bouris K., Harries N., and Jones T., *Novel microfluidic geometries and processing methodologies enabling the precision formation of micro-and nanoparticles*. 2004.
24. Kim J., Utada A., Fernández Nieves A., Hu Z., and Weitz D., *Fabrication of monodisperse gel shells and functional microgels in microfluidic devices*. Angewandte Chemie International Edition, 2007. 46(11): p. 1819-1822.
25. Ali H., York P., and Blagden N., *Preparation of hydrocortisone nanosuspension through a bottom-up nanoprecipitation technique using microfluidic reactors*. International Journal of Pharmaceutics, 2009. 375: p. 107-113.
26. Zhang S., Yun J., Shen S., Chen Z., Yao K., Chen J., and Chen B., *Formation of solid lipid nanoparticles in a microchannel system with a cross-shaped junction*. Chemical Engineering Science, 2008. 63(23): p. 5600-5605.
27. Jasch K., Barth N., Fehr S., Bunjes H., Augustin W., and Scholl S., *A Microfluidic Approach for a Continuous Crystallization of Drug Carrier Nanoparticles*. Chemical Engineering & Technology, 2009. 32(11): p. 1806-1814.
28. Chastek T., Iida K., Amis E., Fasolka M., and Beers K., *A microfluidic platform for integrated synthesis and dynamic light scattering measurement of block copolymer micelles*. Lab on a Chip, 2008. 8(6): p. 950-957.
29. Karnik R., Gu F., Basto P., Cannizzaro C., Dean L., Kyei-Manu W., Langer R., and Farokhzad O., *Microfluidic platform for controlled synthesis of polymeric nanoparticles*. Nano Letters, 2008. 8(9): p. 2906-2912.
30. Fibach E., Bianchi N., Borgatti M., Prus E., and Gambari R., *Mithramycin induces fetal hemoglobin production in normal and thalassemic human erythroid precursor cells*. Blood, 2003. 102(4): p. 1276.
31. Incropera F.P. and De Witt D.P., *Fundamentals of heat and mass transfer*. 1985.
32. Batchelor G.K., *An introduction to fluid dynamics*. 2000: Cambridge Univ Pr.
33. Beebe D.J., Mensing, G.A., Walker, G.M. , *Physics and application of microfluidic in biology*. Annu. Rev. Biomed. Eng, 2002. 4: p. 261-286.
34. Drese K., *Optimization of interdigital micromixers via analytical modeling--exemplified with the SuperFocus mixer*. Chemical Engineering Journal, 2004. 101(1-3): p. 403-407.
35. Ehlers S., Elgeti J., Menzel T., and Wießmeier G., *Mixing in the offstream of a microchannel system** 1. Chemical Engineering and Processing, 2000. 39(4): p. 291-298.
36. Aulton M.E. and Cooper J.W., *Pharmaceutics: the science of dosage form design*. 2002.

37. Edward J.T., *Molecular volumes and the Stokes-Einstein equation*. J Chem Educ, 1970.
38. Einstein A. and Fürth R., *Investigations on the Theory of the Brownian Movement*. 1956: Dover Pubns.
39. Zhang Z., Zhao P., Xiao G., Lin M., and Cao X., *Focusing-enhanced mixing in microfluidic channels*. Biomicrofluidics, 2008. 2: p. 014101.
40. Kumar V., Paraschivoiu M., and Nigam K., *Single-phase fluid flow and mixing in microchannels*. Chemical Engineering Science, 2010.
41. Yaralioglu G., Wygant I., Marentis T., and Khuri-Yakub B., *Ultrasonic mixing in microfluidic channels using integrated transducers*. Anal. Chem, 2004. 76(13): p. 3694-3698.
42. Glasgow I. and Aubry N., *Enhancement of microfluidic mixing using time pulsing*. Lab on a Chip, 2003. 3(2): p. 114-120.
43. Yang Z., Matsumoto S., Goto H., Matsumoto M., and Maeda R., *Ultrasonic micromixer for microfluidic systems*. Sensors and Actuators A: Physical, 2001. 93(3): p. 266-272.
44. Tsai Jr H. and Lin L., *Active microfluidic mixer and gas bubble filter driven by thermal bubble micropump** 1. Sensors and Actuators A: Physical, 2002. 97: p. 665-671.
45. Bau H., Zhong J., and Yi M., *A minute magneto hydro dynamic (MHD) mixer*. Sensors and Actuators B: Chemical, 2001. 79(2-3): p. 207-215.
46. Wu Z. and Nguyen N., *Convective-diffusive transport in parallel lamination micromixers*. Microfluidics and Nanofluidics, 2005. 1(3): p. 208-217.
47. Hardt S. and Schönfeld F., *Laminar mixing in different interdigital micromixers: II. Numerical simulations*. AIChE Journal, 2003. 49(3): p. 578-584.
48. Kamholz A. and Yager P., *Molecular diffusive scaling laws in pressure-driven microfluidic channels: deviation from one-dimensional Einstein approximations*. Sensors and Actuators B: Chemical, 2002. 82(1): p. 117-121.
49. Schwesinger N., Frank T., and Wurmus H., *A modular microfluid system with an integrated micromixer*. Journal of Micromechanics and Microengineering, 1996. 6: p. 99.
50. Knight J., Vishwanath A., Brody J., and Austin R., *Hydrodynamic focusing on a silicon chip: mixing nanoliters in microseconds*. Physical review letters, 1998. 80(17): p. 3863-3866.
51. Günther A., Jhunjhunwala M., Thalmann M., Schmidt M., and Jensen K., *Micromixing of miscible liquids in segmented gas- liquid flow*. Langmuir, 2005. 21(4): p. 1547-1555.
52. Song H., Tice J., and Ismagilov R., *A microfluidic system for controlling reaction networks in time*. Angewandte Chemie, 2003. 115(7): p. 792-796.
53. Johnson T., Ross D., and Locascio L., *Rapid microfluidic mixing*. Anal. Chem, 2002. 74(1): p. 45-51.
54. Stroock A., Dertinger S., Ajdari A., Mezic I., Stone H., and Whitesides G., *Chaotic mixer for microchannels*. Science, 2002. 295(5555): p. 647.
55. Kumar S. and Nann T., *Shape control of II-VI semiconductor nanomaterials*. Small, 2006. 2(3): p. 316-329.
56. Talapin D., Rogach A., Kornowski A., Haase M., and Weller H., *Highly Luminescent Monodisperse CdSe and CdSe/ZnS Nanocrystals Synthesized in a*

- Hexadecylamine- Trioctylphosphine Oxide- Trioctylphosphine Mixture.* Nano Letters, 2001. 1(4): p. 207-211.
57. Chang C., Paul B., Remcho V., Atre S., and Hutchison J., *Synthesis and post-processing of nanomaterials using microreaction technology.* Journal of Nanoparticle Research, 2008. 10(6): p. 965-980.
58. Madou M., *Fundamentals of microfabrication.* 1997. CRC Press LLC. Capítulo. 1: p. 1-50.
59. Janasek D., Franzke J., and Manz A., *Scaling and the design of miniaturized chemical-analysis systems.* Nature, 2006. 442(7101): p. 374-380.
60. Demello A., *Control and detection of chemical reactions in microfluidic systems.* Nature, 2006. 442(7101): p. 394-402.
61. Chen Q., Li G., Jin Q., Zhao J., Ren Q., and Xu Y., *A rapid and low-cost procedure for fabrication of glass microfluidic devices.* Microelectromechanical Systems, Journal of, 2007. 16(5): p. 1193-1200.
62. Becker H. and Gärtner C., *Polymer microfabrication methods for microfluidic analytical applications.* Electrophoresis, 2000. 21(1): p. 12-26.
63. Lee J., Park C., and Whitesides G., *Solvent compatibility of poly (dimethylsiloxane)-based microfluidic devices.* Anal. Chem, 2003. 75(23): p. 6544-6554.
64. Kim B., Hong L., Chung Y., Kim D., and Lee C., *Solvent Resistant PDMS Microfluidic Devices with Hybrid Inorganic/Organic Polymer Coatings.* Advanced Functional Materials, 2009. 19(23): p. 3796-3803.
65. Delille R., Urdaneta M., Moseley S., and Smela E., *Benchtop polymer MEMS.* Microelectromechanical Systems, Journal of, 2006. 15(5): p. 1108-1120.
66. Greener J., Li W., Ren J., Voicu D., Pakharenko V., Tang T., and Kumacheva E., *Rapid, cost-efficient fabrication of microfluidic reactors in thermoplastic polymers by combining photolithography and hot embossing.* Lab Chip, 2009. 10(4): p. 522-524.
67. Mack C., *Fundamental principles of optical lithography: the science of microfabrication.* 2007: Wiley-Interscience.
68. Madou M., *Fundamentals of Microfabrication,*. 1997, CRC Press LLC, Boca Raton, FL.
69. Jo S., Lee M., Lee S., and Park S., *Characterization of a modified Bosch-type process for silicon mold fabrication.* Journal of Vacuum Science & Technology A: Vacuum, Surfaces, and Films, 2005. 23: p. 905.
70. Duffy D., McDonald J., Schueller O., and Whitesides G., *Rapid prototyping of microfluidic systems in poly (dimethylsiloxane).* Anal. Chem, 1998. 70(23): p. 4974-4984.
71. Martynova L., Locascio L.E., Gaitan M., Kramer G.W., Christensen R.G., and MacCrahan W.A., *Fabrication of plastic microfluid channels by imprinting methods.* Analytical chemistry, 1997. 69(23): p. 4783-4789.
72. Peng B.Y., Wu C.W., Shen Y.K., and Lin Y., *Microfluidic chip fabrication using hot embossing and thermal bonding of COP.* Polymers for Advanced Technologies, 2010. 21(7): p. 457-466.
73. Tsao C.W. and DeVoe D.L., *Bonding of thermoplastic polymer microfluidics.* Microfluidics and Nanofluidics, 2009. 6(1): p. 1-16.
74. Ogilvie I., Sieben V., Floquet C., Zmijan R., Mowlem M., and Morgan H., *Reduction of surface roughness for optical quality microfluidic devices in PMMA*

- and COC. *Journal of Micromechanics and Microengineering*, 2010. **20**: p. 065016.
75. Morales A.M., Simmons B.A., Hunter M.C., Krafcik K.L., Domeier L.A., Sickafoose S.M., Patel K.D., and Gardea A., *Low-distortion, high-strength bonding of thermoplastic microfluidic devices employing case-II diffusion-mediated permeant activation*. *Lab on a Chip*, 2007. **7**(12): p. 1825-1831.
76. Hsu Y.C. and Chen T.Y., *Applying Taguchi methods for solvent-assisted PMMA bonding technique for static and dynamic -TAS devices*. *Biomedical microdevices*, 2007. **9**(4): p. 513-522.
77. Brown L., Koerner T., Horton J., and Oleschuk R., *Fabrication and characterization of poly (methylmethacrylate) microfluidic devices bonded using surface modifications and solvents*. *Lab on a Chip*, 2006. **6**(1): p. 66-73.
78. LaMer V. and Dinegar R., *Theory, production and mechanism of formation of monodispersed hydrosols*. *Journal of the American Chemical Society*, 1950. **72**(11): p. 4847-4854.
79. Horn D. and Rieger J., *Organic nanoparticles in the aqueous phase—theory, experiment, and use*. *Angewandte Chemie International Edition*, 2001. **40**(23): p. 4330-4361.
80. Brick M.C., Palmer H.J., and Whitesides T.H., *Formation of colloidal dispersions of organic materials in aqueous media by solvent shifting*. *Langmuir*, 2003. **19**(16): p. 6367-6380.
81. DeMello J. and DeMello A., *Microscale reactors: nanoscale products*. *Lab on a Chip*, 2004. **4**(2): p. 11N.
82. Zhao C.X., He L., Qiao S., and Middelberg A.P.J., *Nanoparticle synthesis in microreactors*. *Chemical Engineering Science*, 2010.
83. Marre S. and Jensen K.F., *Synthesis of micro and nanostructures in microfluidic systems*. *Chem. Soc. Rev.*, 2010. **39**(3): p. 1183-1202.
84. Lee C.Y., Chang C.L., Wang Y.N., and Fu L.M., *Microfluidic Mixing: A Review*. *International journal of molecular sciences*, 2011. **12**(5): p. 3263-3287.
85. Zhao C.X., He L., Qiao S., and Middelberg A.P.J., *Nanoparticle synthesis in microreactors*. *Chemical Engineering Science*, 2010. **66**(1): p. 1463-1479.
86. Sahoo H.R., Kralj J.G., and Jensen K.F., *Multistep Continuous Flow Microchemical Synthesis Involving Multiple Reactions and Separations*. *Angewandte Chemie*, 2007. **119**(30): p. 5806-5810.
87. Abou Hassan A., Bazzi R., and Cabuil V., *Multistep Continuous Flow Microsynthesis of Magnetic and Fluorescent Fe₂O₃@ SiO₂ Core/Shell Nanoparticles*. *Angewandte Chemie International Edition*, 2009. **48**(39): p. 7180-7183.
88. Ying Y., Chen G., Zhao Y., Li S., and Yuan Q., *A high throughput methodology for continuous preparation of monodispersed nanocrystals in microfluidic reactors*. *Chemical Engineering Journal*, 2008. **135**(3): p. 209-215.
89. Nakamura H., Yamaguchi Y., Miyazaki M., Maeda H., Uehara M., and Mulvaney P., *Preparation of CdSe nanocrystals in a micro-flow-reactor*. *Chem. Commun.*, 2002(23): p. 2844-2845.
90. Ju J., Zeng C., Zhang L., and Xu N., *Continuous synthesis of zeolite NaA in a microchannel reactor*. *Chemical Engineering Journal*, 2006. **116**(2): p. 115-121.
91. Boleininger J., Kurz A., Reuss V., and Sonnichsen C., *Microfluidic continuous flow synthesis of rod-shaped gold and silver nanocrystals*. *Physical Chemistry Chemical Physics*, 2006. **8**(33): p. 3824-3827.

92. Takagi M., Maki T., Miyahara M., and Mae K., *Production of titania nanoparticles by using a new microreactor assembled with same axle dual pipe*. Chemical Engineering Journal, 2004. **101**(1-3): p. 269-276.
93. Abou Hassan A., Sandre O., Neveu S., and Cabuil V., *Synthesis of goethite by separation of the nucleation and growth processes of ferrihydrite nanoparticles using microfluidics*. Angewandte Chemie International Edition, 2009. **48**(13): p. 2342-2345.
94. Hassan A.A., Sandre O., Cabuil V., and Tabeling P., *Synthesis of iron oxide nanoparticles in a microfluidic device: preliminary results in a coaxial flow millichannel*. Chem. Commun., 2008(15): p. 1783-1785.
95. Ali H.S.M., Blagden N., York P., Amani A., and Brook T., *Artificial neural networks modelling the prednisolone nanoprecipitation in microfluidic reactors*. European Journal of Pharmaceutical Sciences, 2009. **37**(3-4): p. 514-522.
96. Shalom D., Wootton R., Winkle R., Cottam B., Vilar R., demello A., and Wilde C., *Synthesis of thiol functionalized gold nanoparticles using a continuous flow microfluidic reactor*. Materials Letters, 2007. **61**(4-5): p. 1146-1150.
97. Bessoth F., deMello A., and Manz A., *Microstructure for efficient continuous flow mixing*. Analytical communications, 1999. **36**(6): p. 213-215.
98. Wagner J., Tshikhudo T., and Koehler J., *Microfluidic generation of metal nanoparticles by borohydride reduction*. Chemical Engineering Journal, 2008. **135**: p. S104-S109.
99. Köhler J.M., Romanus H., Hübner U., and Wagner J., *Formation of star-like and core-shell AuAg nanoparticles during two-and three-step preparation in batch and in microfluidic systems*. Journal of Nanomaterials, 2007. **2007**(1): p. 2-2.
100. Jahn A., Vreeland W., Gaitan M., and Locascio L., *Controlled vesicle self-assembly in microfluidic channels with hydrodynamic focusing*. J. Am. Chem. Soc, 2004. **126**(9): p. 2674-2675.
101. Rhee M., Valencia P.M., Rodriguez M.I., Langer R., Farokhzad O.C., and Karnik R., *Synthesis of Size Tunable Polymeric Nanoparticles Enabled by 3D Hydrodynamic Flow Focusing in Single Layer Microchannels*. Advanced Materials, 2011. **23**(12): p. H79-H83.
102. Weng C.H., Huang C.C., Yeh C.S., Lei H.Y., and Lee G.B., *Synthesis of hexagonal gold nanoparticles using a microfluidic reaction system*. Journal of Micromechanics and Microengineering, 2008. **18**: p. 035019.
103. Chan E., Alivisatos A., and Mathies R., *High-temperature microfluidic synthesis of CdSe nanocrystals in nanoliter droplets*. J. Am. Chem. Soc, 2005. **127**(40): p. 13854-13861.
104. Shestopalov I., Tice J., and Ismagilov R., *Multi-step synthesis of nanoparticles performed on millisecond time scale in a microfluidic droplet-based system*. Lab on a Chip, 2004. **4**(4): p. 316-321.
105. Khan S., Gunther A., Schmidt M., and Jensen K., *Microfluidic synthesis of colloidal silica*. Langmuir, 2004. **20**(20): p. 8604-8611.
106. Wang H., Nakamura H., Uehara M., Miyazaki M., and Maeda H., *Preparation of titania particles utilizing the insoluble phase interface in a microchannel reactor*. Chemical Communications, 2002. **2002**(14): p. 1462-1463.
107. Wilms D., Klos J., and Frey H., *Microstructured Reactors for Polymer Synthesis: A Renaissance of Continuous Flow Processes for Tailor-Made Macromolecules?* Macromolecular chemistry and physics, 2008. **209**(4): p. 343-356.

108. Chow A., *Lab on a chip: Opportunities for chemical engineering*. AIChE Journal, 2002. **48**(8): p. 1590-1595.
109. Kawaguchi T., Miyata H., Ataka K., Mae K., and Yoshida J., *Room Temperature Swern Oxidations by Using a Microscale Flow System*. Angewandte Chemie International Edition, 2005. **44**(16): p. 2413-2416.
110. Nakamura H., Yamaguchi Y., Miyazaki M., Maeda H., Uehara M., and Mulvaney P., *Preparation of CdSe nanocrystals in a micro-flow-reactor*. Chemical Communications, 2002. **2002**(23): p. 2844-2845.
111. Nakamura H., Tashiro A., Yamaguchi Y., Miyazaki M., Watari T., Shimizu H., and Maeda H., *Application of a microfluidic reaction system for CdSe nanocrystal preparation: their growth kinetics and photoluminescence analysis*. Lab on a Chip, 2004. **4**(3): p. 237-240.
112. Wang H., Li X., Uehara M., Yamaguchi Y., Nakamura H., Miyazaki M., Shimizu H., and Maeda H., *Continuous synthesis of CdSe-ZnS composite nanoparticles in a microfluidic reactor*. Chemical Communications, 2004. **2004**(1): p. 48-49.
113. Zinoveva S., De Silva R., D Louis R., Datta P., and SSR K., *The wet chemical synthesis of Co nanoparticles in a microreactor system: A time-resolved investigation by X-ray absorption spectroscopy*. Nuclear Instruments and Methods in Physics Research Section A: Accelerators, Spectrometers, Detectors and Associated Equipment, 2007. **582**(1): p. 239-241.
114. Polte J., Erler R., Thunemann A.F., Sokolov S., Ahner T.T., Rademann K., Emmerling F., and Krahnert R., *Nucleation and growth of gold nanoparticles studied via in situ small angle x-ray scattering at millisecond time resolution*. ACS nano, 2010. **4**(2): p. 1076-1082.
115. Khan S. and Jensen K., *Microfluidic synthesis of titania shells on colloidal silica*. Advanced Materials, 2007. **19**(18): p. 2556-2560.
116. Song Y., Zhang T., Yang W., Albin S., and Henry L., *Fine crystal structure transition of cobalt nanoparticles formed in a microfluidic reactor*. Crystal Growth and Design, 2008. **8**(10): p. 3766-3772.
117. Chastek T., Beers K., and Amis E., *Miniaturized dynamic light scattering instrumentation for use in microfluidic applications*. Review of Scientific Instruments, 2007. **78**: p. 072201.
118. Kuyper C., Budzinski K., Lorenz R., and Chiu D., *Real-time sizing of nanoparticles in microfluidic channels using confocal correlation spectroscopy*. J. Am. Chem. Soc, 2006. **128**(3): p. 730-731.
119. Kuyper C., Fujimoto B., Zhao Y., Schiro P., and Chiu D., *Accurate sizing of nanoparticles using confocal correlation Spectroscopy*. J. Phys. Chem. B, 2006. **110**(48): p. 24433-24441.
120. Amador C., Gavriilidis A., and Angeli P., *Flow distribution in different microreactor scale-out geometries and the effect of manufacturing tolerances and channel blockage*. Chemical Engineering Journal, 2004. **101**(1-3): p. 379-390.
121. Commenge J., Falk L., Corriou J., and Matlosz M., *Optimal design for flow uniformity in microchannel reactors*. AIChE Journal, 2002. **48**(2): p. 345-358.
122. Su Y., Kim H., Kovenklioglu S., and Lee W., *Continuous nanoparticle production by microfluidic-based emulsion, mixing and crystallization*. Journal of Solid State Chemistry, 2007. **180**(9): p. 2625-2629.
123. Jahn A., Vreeland W., DeVoe D., Locascio L., and Gaitan M., *Microfluidic directed formation of liposomes of controlled size*. Langmuir, 2007. **23**(11): p. 6289-6293.

124. Yun J., Zhang S., Chen Z., Yao K., and Chen J., *Continuous production of solid lipid nanoparticles by liquid flow-focusing and gas displacing method in microchannels*. Chemical Engineering Science, 2009.
125. Rondeau E. and Cooper-White J., *Biopolymer microparticle and nanoparticle formation within a microfluidic device*. Langmuir, 2008. **24**(13): p. 6937-6945.
126. Jahn A., Stavis S., Hong J., Vreeland W., DeVoe D., and Gaitan M., *Microfluidic Mixing and the Formation of Nanoscale Lipid Vesicles*. ACS nano, 2010. **4**(4): p. 2077-2087.
127. Thiele J., Steinhauser D., Pfohl T., and Fo rster S., *Preparation of Monodisperse Block Copolymer Vesicles via Flow Focusing in Microfluidics*. 2010.
128. Lo C., Jahn A., Locascio L., and Vreeland W., *Controlled Self-Assembly of Monodisperse Niosomes by Microfluidic Hydrodynamic Focusing*. Langmuir, 2010. **26**(11): p. 8559-8566.
129. Valencia P.M., Basto P.A., Zhang L., Rhee M., Langer R., Farokhzad O.C., and Karnik R., *Single-Step Assembly of Homogenous Lipid- Polymeric and Lipid-Quantum Dot Nanoparticles Enabled by Microfluidic Rapid Mixing*. ACS nano, 2010. **4**(3): p. 1671-1679.
130. Kolishetti N., Dhar S., Valencia P.M., Lin L.Q., Karnik R., Lippard S.J., Langer R., and Farokhzad O.C., *Engineering of self-assembled nanoparticle platform for precisely controlled combination drug therapy*. Proceedings of the National Academy of Sciences, 2010. **107**(42): p. 17939.
131. Almeida A. and Souto E., *Solid lipid nanoparticles as a drug delivery system for peptides and proteins*. Advanced drug delivery reviews, 2007. **59**(6): p. 478-490.
132. Johnson B. and Prud'homme R., *Mechanism for rapid self-assembly of block copolymer nanoparticles*. Physical review letters, 2003. **91**(11): p. 118302.
133. Cui H., Chen Z., Zhong S., Wooley K., and Pochan D., *Block copolymer assembly via kinetic control*. Science, 2007. **317**(5838): p. 647.
134. Johnson B. and Prud'homme R., *Flash NanoPrecipitation of organic actives and block copolymers using a confined impinging jets mixer*. Australian Journal of Chemistry, 2003. **56**(10): p. 1021-1024.
135. Matsumura Y., *Preclinical and clinical studies of anticancer drug-incorporated polymeric micelles*. Journal of drug targeting, 2007. **15**(7-8): p. 507-517.
136. Duncan R., *The dawning era of polymer therapeutics*. Nature Reviews Drug Discovery, 2003. **2**(5): p. 347-360.
137. Nishiyama N. and Kataoka K., *Current state, achievements, and future prospects of polymeric micelles as nanocarriers for drug and gene delivery*. Pharmacology and Therapeutics, 2006. **112**(3): p. 630-648.
138. Bae Y., Nishiyama N., Fukushima S., Koyama H., Yasuhiro M., and Kataoka K., *Preparation and biological characterization of polymeric micelle drug carriers with intracellular pH-triggered drug release property: tumor permeability, controlled subcellular drug distribution, and enhanced in vivo antitumor efficacy*. Bioconjugate Chem, 2005. **16**(1): p. 122-130.
139. Adams M., Lavasanifar A., and Kwon G., *Amphiphilic block copolymers for drug delivery*. Journal of pharmaceutical sciences, 2003. **92**(7): p. 1343-1355.
140. Kabanov A. and Alakhov V., *Pluronic® block copolymers in drug delivery: From micellar nanocontainers to biological response modifiers*. Critical reviews in therapeutic drug carrier systems, 2002. **19**(1): p. 1-73.

141. Bromberg L., *Polymeric micelles in oral chemotherapy*. Journal of Controlled Release, 2008. **128**(2): p. 99-112.
142. Gaucher G., Dufresne M., Sant V., Kang N., Maysinger D., and Leroux J., *Block copolymer micelles: preparation, characterization and application in drug delivery*. Journal of Controlled Release, 2005. **109**(1-3): p. 169-188.
143. Smart T., Lomas H., Massignani M., Flores-Merino M., Perez L., and Battaglia G., *Block copolymer nanostructures*. Nano Today, 2008. **3**(3-4): p. 38-46.
144. Moghimi S., Hunter A., and Murray J., *Long-circulating and target-specific nanoparticles: theory to practice*. Pharmacological reviews, 2001. **53**(2): p. 283.
145. Kabanov A., Batrakova E., and Alakhov V., *Pluronic® block copolymers as novel polymer therapeutics for drug and gene delivery*. Journal of Controlled Release, 2002. **82**(2-3): p. 189-212.
146. Kakizawa Y. and Kataoka K., *Block copolymer micelles for delivery of gene and related compounds*. Advanced drug delivery reviews, 2002. **54**(2): p. 203-222.
147. Lavasanifar A., Samuel J., and Kwon G., *Poly (ethylene oxide)-block-poly (-amino acid) micelles for drug delivery*. Advanced drug delivery reviews, 2002. **54**(2): p. 169-190.
148. Savic R., Eisenberg A., and Maysinger D., *Block copolymer micelles as delivery vehicles of hydrophobic drugs: micelle-cell interactions*. Journal of drug targeting, 2006. **14**(6): p. 343-355.
149. Lavasanifar A., Samuel J., and Kwon G., *The effect of fatty acid substitution on the in vitro release of amphotericin B from micelles composed of poly (ethylene oxide)-block-poly (N-hexyl stearate--aspartamide)*. Journal of Controlled Release, 2002. **79**(1-3): p. 165-172.
150. Allen C., Maysinger D., and Eisenberg A., *Nano-engineering block copolymer aggregates for drug delivery*. Colloids and surfaces B: Biointerfaces, 1999. **16**(1-4): p. 3-27.
151. Kwon G. and Okano T., *Soluble self-assembled block copolymers for drug delivery*. Pharmaceutical research, 1999. **16**(5): p. 597-600.
152. Lee J., Cho E., and Cho K., *Incorporation and release behavior of hydrophobic drug in functionalized poly (l-lactide)-block-poly (ethylene oxide) micelles*. Journal of Controlled Release, 2004. **94**(2-3): p. 323-335.
153. Bae K., Choi S., Park S., Lee Y., and Park T., *Thermosensitive pluronic micelles stabilized by shell cross-linking with gold nanoparticles*. Langmuir, 2006. **22**(14): p. 6380-6384.
154. Shuai X., Merdan T., Schaper A., Xi F., and Kissel T., *Core-cross-linked polymeric micelles as paclitaxel carriers*. Bioconjugate Chem, 2004. **15**(3): p. 441-448.
155. Sezgin Z., Yüksel N., and Baykara T., *Preparation and characterization of polymeric micelles for solubilization of poorly soluble anticancer drugs*. European journal of pharmaceuticals and biopharmaceutics, 2006. **64**(3): p. 261-268.
156. Kwon G., Naito M., Yokoyama M., Okano T., Sakurai Y., and Kataoka K., *Block copolymer micelles for drug delivery: loading and release of doxorubicin*. Journal of Controlled Release, 1997. **48**(2-3): p. 195-201.
157. Fournier E., Dufresne M., Smith D., Ranger M., and Leroux J., *A novel one-step drug-loading procedure for water-soluble amphiphilic nanocarriers*. Pharmaceutical research, 2004. **21**(6): p. 962-968.

158. Lund R., Willner L., Monkenbusch M., Panine P., Narayanan T., Colmenero J., and Richter D., *Structural Observation and Kinetic Pathway in the Formation of Polymeric Micelles*. Physical review letters, 2009. **102**(18): p. 188301.
159. Gelderblom H., Verweij J., Nooter K., and Sparreboom A., *Cremophor EL:: the drawbacks and advantages of vehicle selection for drug formulation*. European Journal of Cancer, 2001. **37**(13): p. 1590-1598.
160. Allen C., Han J., Yu Y., Maysinger D., and Eisenberg A., *Polycaprolactone-*b*-poly(ethylene oxide) copolymer micelles as a delivery vehicle for dihydrotestosterone*. Journal of Controlled Release, 2000. **63**(3): p. 275-286.
161. Hamaguchi T., Matsumura Y., Suzuki M., Shimizu K., Goda R., Nakamura I., Nakatomi I., Yokoyama M., Kataoka K., and Kakizoe T., *NK105, a paclitaxel-incorporating micellar nanoparticle formulation, can extend in vivo antitumour activity and reduce the neurotoxicity of paclitaxel*. British journal of cancer, 2005. **92**(7): p. 1240-1246.
162. Kim S., Kim D., Shim Y., Bang J., Oh H., Kim S., and Seo M., *In vivo evaluation of polymeric micellar paclitaxel formulation: toxicity and efficacy*. Journal of Controlled Release, 2001. **72**(1-3): p. 191-202.
163. Zhang X., Jackson J., and Burt H., *Development of amphiphilic diblock copolymers as micellar carriers of taxol*. International Journal of Pharmaceutics, 1996. **132**(1-2): p. 195-206.
164. Kwon G., Naito M., Yokoyama M., Okano T., Sakurai Y., and Kataoka K., *Physical entrapment of adriamycin in AB block copolymer micelles*. Pharmaceutical research, 1995. **12**(2): p. 192-195.
165. Rapoport N., Herron J., Pitt W., and Pitina L., *Micellar delivery of doxorubicin and its paramagnetic analog, ruboxyl, to HL-60 cells: effect of micelle structure and ultrasound on the intracellular drug uptake*. Journal of Controlled Release, 1999. **58**(2): p. 153-162.
166. Lin W., Juang L., and Lin C., *Stability and release performance of a series of pegylated copolymeric micelles*. Pharmaceutical research, 2003. **20**(4): p. 668-673.
167. Shuai X., Ai H., Nasongkla N., Kim S., and Gao J., *Micellar carriers based on block copolymers of poly (caprolactone) and poly (ethylene glycol) for doxorubicin delivery*. Journal of Controlled Release, 2004. **98**(3): p. 415-426.
168. Liu J., Xiao Y., and Allen C., *Polymer-drug compatibility: a guide to the development of delivery systems for the anticancer agent, ellipticine*. Journal of pharmaceutical sciences, 2004. **93**(1): p. 132-143.
169. Aliabadi H. and Lavasanifar A., *Polymeric micelles for drug delivery*. Expert Opinion on Drug Delivery, 2006. **3**(1): p. 139-162.
170. La S., Okano T., and Kataoka K., *Preparation and characterization of the micelle forming polymeric drug indomethacin incorporated poly (ethylene oxide)-poly (benzyl L aspartate) block copolymer micelles*. Journal of pharmaceutical sciences, 1996. **85**(1): p. 85-90.
171. Teng Y., Morrison M., Munk P., Webber S., and Prochazka K., *Release kinetics studies of aromatic molecules into water from block polymer micelles*. Macromolecules, 1998. **31**(11): p. 3578-3587.
172. Fang J., Sawa T., and Maeda H., *Factors and mechanism of "EPR" effect and the enhanced antitumor effects of macromolecular drugs including SMANCS*. Polymer Drugs in the Clinical Stage, 2004: p. 29-49.
173. Hobbs S., Monsky W., Yuan F., Roberts W., Griffith L., Torchilin V., and Jain R., *Regulation of transport pathways in tumor vessels: role of tumor type and*

- microenvironment.* Proceedings of the National Academy of Sciences of the United States of America, 1998. **95**(8): p. 4607.
174. Allen T. and Cullis P., *Drug delivery systems: entering the mainstream.* Science, 2004. **303**(5665): p. 1818.
175. Greish K., Fang J., Inutsuka T., Nagamitsu A., and Maeda H., *Macromolecular therapeutics: advantages and prospects with special emphasis on solid tumour targeting.* Clinical pharmacokinetics, 2003. **42**(13): p. 1089-1105.
176. Kang J., Toita R., and Katayama Y., *Bio and nanotechnological strategies for tumor-targeted gene therapy.* Biotechnology advances, 2010.
177. Alexis F., Pridgen E., Molnar L., and Farokhzad O., *Factors affecting the clearance and biodistribution of polymeric nanoparticles.* Molecular pharmaceutics, 2008. **5**(4): p. 505-515.
178. Riley T., Stolnik S., Heald C., Xiong C., Garnett M., Illum L., Davis S., Purkiss S., Barlow R., and Gellert P., *Physicochemical Evaluation of Nanoparticles Assembled from Poly (lactic acid)- Poly (ethylene glycol)(PLA- PEG) Block Copolymers as Drug Delivery Vehicles.* Langmuir, 2001. **17**(11): p. 3168-3174.
179. Owens III D. and Peppas N., *Opsonization, biodistribution, and pharmacokinetics of polymeric nanoparticles.* International Journal of Pharmaceutics, 2006. **307**(1): p. 93-102.
180. Ko Y., Kale A., Hartner W., Papahadjopoulos-Sternberg B., and Torchilin V., *Self-assembling micelle-like nanoparticles based on phospholipid-polyethyleneimine conjugates for systemic gene delivery.* Journal of Controlled Release, 2009. **133**(2): p. 132-138.
181. Vlerken L., Vyas T., and Amiji M., *Poly (ethylene glycol)-modified nanocarriers for tumor-targeted and intracellular delivery.* Pharmaceutical research, 2007. **24**(8): p. 1405-1414.
182. Bae Y., Jang W., Nishiyama N., Fukushima S., and Kataoka K., *Multifunctional polymeric micelles with folate-mediated cancer cell targeting and pH-triggered drug releasing properties for active intracellular drug delivery.* Molecular BioSystems, 2005. **1**(3): p. 242-250.
183. Lee E., Na K., and Bae Y., *Polymeric micelle for tumor pH and folate-mediated targeting.* Journal of Controlled Release, 2003. **91**(1-2): p. 103-113.
184. Nagasaki Y., Yasugi K., Yamamoto Y., Harada A., and Kataoka K., *Sugar-installed block copolymer micelles: their preparation and specific interaction with lectin molecules.* Biomacromolecules, 2001. **2**(4): p. 1067-1070.
185. Lukyanov A., Gao Z., and Torchilin V., *Micelles from polyethylene glycol/phosphatidylethanolamine conjugates for tumor drug delivery.* Journal of Controlled Release, 2003. **91**(1-2): p. 97-102.
186. Nasongkla N., Shuai X., Ai H., Weinberg B., Pink J., Boothman D., and Gao J., *cRGD Functionalized Polymer Micelles for Targeted Doxorubicin Delivery.* Angewandte Chemie, 2004. **116**(46): p. 6483-6487.
187. Martin G. and Jain R., *Noninvasive measurement of interstitial pH profiles in normal and neoplastic tissue using fluorescence ratio imaging microscopy.* Cancer research, 1994. **54**(21): p. 5670.
188. Lee E., Shin H., Na K., and Bae Y., *Poly (-histidine)-PEG block copolymer micelles and pH-induced destabilization.* Journal of Controlled Release, 2003. **90**(3): p. 363-374.

189. Sethuraman V. and Bae Y., *TAT peptide-based micelle system for potential active targeting of anti-cancer agents to acidic solid tumors*. Journal of Controlled Release, 2007. **118**(2): p. 216-224.
190. Miyata K., Kakizawa Y., Nishiyama N., Harada A., Yamasaki Y., Koyama H., and Kataoka K., *Block catiomer polyplexes with regulated densities of charge and disulfide cross-linking directed to enhance gene expression*. J. Am. Chem. Soc, 2004. **126**(8): p. 2355-2361.
191. Kakizawa Y., Harada A., and Kataoka K., *Glutathione-sensitive stabilization of block copolymer micelles composed of antisense DNA and thiolated poly (ethylene glycol)-block-poly (L-lysine): a potential carrier for systemic delivery of antisense DNA*. Biomacromolecules, 2001. **2**(2): p. 491-497.
192. Katayama Y., Sonoda T., and Maeda M., *A polymer micelle responding to the protein kinase A signal*. Macromolecules, 2001. **34**(24): p. 8569-8573.
193. Chung J., Yokoyama M., and Okano T., *Inner core segment design for drug delivery control of thermo-responsive polymeric micelles*. Journal of Controlled Release, 2000. **65**(1-2): p. 93-103.
194. Chung J., Yokoyama M., Yamato M., Aoyagi T., Sakurai Y., and Okano T., *Thermo-responsive drug delivery from polymeric micelles constructed using block copolymers of poly (N-isopropylacrylamide) and poly (butylmethacrylate)*. Journal of Controlled Release, 1999. **62**(1-2): p. 115-127.
195. Rapoport N., *Combined cancer therapy by micellar-encapsulated drug and ultrasound*. International Journal of Pharmaceutics, 2004. **277**(1-2): p. 155-162.
196. Rapoport N., Christensen D., Fain H., Barrows L., and Gao Z., *Ultrasound-triggered drug targeting of tumors in vitro and in vivo*. Ultrasonics, 2004. **42**(1-9): p. 943-950.
197. He Y., Huang Y., and Cheng Y., *Structure Evolution of Curcumin Nanoprecipitation from a Micromixer*. Crystal Growth & Design, 2010. **10**(3): p. 1021-1024.
198. Farokhzad O. and Langer R., *Impact of nanotechnology on drug delivery*. ACS nano, 2009. **3**(1): p. 16-20.
199. Croy S. and Kwon G., *The effects of Pluronic block copolymers on the aggregation state of nystatin*. Journal of Controlled Release, 2004. **95**(2): p. 161-171.
200. Alexandridis P., Holzwarth J., and Hatton T., *Micellization of poly (ethylene oxide)-poly (propylene oxide)-poly (ethylene oxide) triblock copolymers in aqueous solutions: thermodynamics of copolymer association*. Macromolecules, 1994. **27**(9): p. 2414-2425.
201. Kozlov M., Melik-Nubarov N., Batrakova E., and Kabanov A., *Relationship between pluronic block copolymer structure, critical micellization concentration and partitioning coefficients of low molecular mass solutes*. Macromolecules, 2000. **33**(9): p. 3305-3313.
202. Kabanov A., Batrakova E., and Alakhov V., *Pluronic® block copolymers for overcoming drug resistance in cancer*. Advanced drug delivery reviews, 2002. **54**(5): p. 759-779.
203. Alakhov V., Klinski E., Li S., Pietrzynski G., Venne A., Batrakova E., Bronitch T., and Kabanov A., *Block copolymer-based formulation of doxorubicin. From cell screen to clinical trials*. Colloids and surfaces B: Biointerfaces, 1999. **16**(1-4): p. 113-134.

204. Batrakova E. and Kabanov A., *Pluronic block copolymers: evolution of drug delivery concept from inert nanocarriers to biological response modifiers.* Journal of Controlled Release, 2008. **130**(2): p. 98-106.
205. Wu Z. and Nguyen N., *Hydrodynamic focusing in microchannels under consideration of diffusive dispersion: theories and experiments.* Sensors and Actuators B: Chemical, 2005. **107**(2): p. 965-974.
206. Khatua D., Gupta A., and Dey J., *Characterization of micelle formation of dodecyldimethyl-N-2-phenoxyethylammonium bromide in aqueous solution.* Journal of colloid and interface science, 2006. **298**(1): p. 451-456.
207. Lukyanov A.N., Gao Z., Mazzola L., and Torchilin V.P., *Polyethylene glycol-diacyllipid micelles demonstrate increased accumulation in subcutaneous tumors in mice.* Pharmaceutical research, 2002. **19**(10): p. 1424-1429.
208. Zhang C., Qineng P., and Zhang H., *Self-assembly and characterization of paclitaxel-loaded N-octyl-O-sulfate chitosan micellar system.* Colloids and surfaces B: Biointerfaces, 2004. **39**(1-2): p. 69-75.
209. Zhang X., Jones P., and Haswell S., *Attachment and detachment of living cells on modified microchannel surfaces in a microfluidic-based lab-on-a-chip system.* Chemical Engineering Journal, 2008. **135**: p. S82-S88.
210. Nilsson M., Håkansson B., Söderman O., and Topgaard D., *Influence of polydispersity on the micellization of triblock copolymers investigated by pulsed field gradient nuclear magnetic resonance.* Macromolecules, 2007. **40**(23): p. 8250-8258.
211. Bohorquez M., Koch C., Trygstad T., and Pandit N., *A study of the temperature-dependent micellization of Pluronic F127.* Journal of colloid and interface science, 1999. **216**(1): p. 34-40.
212. Perry C.C., Sabir T.S., Livingston W.J., Milligan J.R., Chen Q., Maskiewicz V., and Boskovic D.S., *Fluorescence of Commercial Pluronic F127 Samples: Temperature Dependent Micellization.* Journal of colloid and interface science, 2010.
213. Castaño-Álvarez M., Pozo Ayuso D., García Granda M., Fernández-Abedul M., Rodríguez García J., and Costa-García A., *Critical points in the fabrication of microfluidic devices on glass substrates.* Sensors and Actuators B: Chemical, 2008. **130**(1): p. 436-448.
214. Lee G., Chang C., Huang S., and Yang R., *The hydrodynamic focusing effect inside rectangular microchannels.* Journal of Micromechanics and Microengineering, 2006. **16**: p. 1024.
215. Shiraishi Y., Inoue T., and Hirai T., *Local Viscosity Analysis of Triblock Copolymer Micelle with Cyanine Dyes as a Fluorescent Probe.* Langmuir, 2010.
216. Kremer J., Van der Esker M., Pathmamanoharan C., and Wiersema P., *Vesicles of variable diameter prepared by a modified injection method.* Biochemistry, 1977. **16**(17): p. 3932-3935.
217. Bates F. and Fredrickson G., *Block copolymer thermodynamics: theory and experiment.* Annual Review of Physical Chemistry, 1990. **41**(1): p. 525-557.
218. Zhang L. and Eisenberg A., *Thermodynamic vs kinetic aspects in the formation and morphological transitions of crew-cut aggregates produced by self-assembly of polystyrene-*b*-poly(acrylic acid) block copolymers in dilute solution.* Macromolecules, 1999. **32**(7): p. 2239-2249.
219. Holden M., Kumar S., Castellana E., Beskok A., and Cremer P., *Generating fixed concentration arrays in a microfluidic device.* Sensors and Actuators B: Chemical, 2003. **92**(1-2): p. 199-207.

220. Lin T., Hosoi A., and Ehrlich D., *Vertical hydrodynamic focusing in glass microchannels*. Biomicrofluidics, 2009. **3**: p. 014101.
221. Tsai C., Chen H., Wang Y., Lin C., and Fu L., *Capabilities and limitations of 2-dimensional and 3-dimensional numerical methods in modeling the fluid flow in sudden expansion microchannels*. Microfluidics and Nanofluidics, 2007. **3**(1): p. 13-18.
222. Cubaud T. and Mason T., *Formation of miscible fluid microstructures by hydrodynamic focusing in plane geometries*. Physical Review E, 2008. **78**(5): p. 56308.
223. Ismagilov R., Stroock A., Kenis P., Whitesides G., and Stone H., *Experimental and theoretical scaling laws for transverse diffusive broadening in two-phase laminar flows in microchannels*. Applied Physics Letters, 2000. **76**: p. 2376.
224. Kamholz A., Weigl B., Finlayson B., and Yager P., *Quantitative analysis of molecular interaction in a microfluidic channel: the T-sensor*. Anal. Chem, 1999. **71**(23): p. 5340-5347.
225. Hou H., Tsai C., Fu L., and Yang R., *Experimental and numerical investigation into micro flow cytometer with 3 D hydrodynamic focusing effect and micro weir structure*. Electrophoresis, 2009. **30**(14): p. 2507-2515.
226. Tsai C., Hou H., and Fu L., *An optimal three-dimensional focusing technique for micro-flow cytometers*. Microfluidics and Nanofluidics, 2008. **5**(6): p. 827-836.
227. Fu L.M., Tsai C.H., and Lin C.H., *A high discernment microflow cytometer with microweir structure*. Electrophoresis, 2008. **29**(9): p. 1874-1880.
228. Hertzog D., Michalet X., Jäger M., Kong X., Santiago J., Weiss S., and Bakajin O., *Femtomole mixer for microsecond kinetic studies of protein folding*. Anal. Chem, 2004. **76**(24): p. 7169-7178.
229. Matteucci M., Hotze M., Johnston K., and Williams III R., *Drug nanoparticles by antisolvent precipitation: Mixing energy versus surfactant stabilization*. Langmuir, 2006. **22**(21): p. 8951-8959.
230. Johnson B.K., *Flash nanoprecipitation of organic actives via confined micromixing and block copolymer stabilization*. Ph.D thesis (Princeton University; Princeton, NJ), 2003.
231. Petros R.A. and DeSimone J.M., *Strategies in the design of nanoparticles for therapeutic applications*. Nature Reviews Drug Discovery, 2010. **9**(8): p. 615-627.
232. Zhou J., Sun Y., Du X., Xiong L., Hu H., and Li F., *Dual-modality in vivo imaging using rare-earth nanocrystals with near-infrared to near-infrared (NIR-to-NIR) upconversion luminescence and magnetic resonance properties*. Biomaterials, 2010. **31**(12): p. 3287-3295.
233. Torchilin V.P., *Structure and design of polymeric surfactant-based drug delivery systems*. Journal of Controlled Release, 2001. **73**(2-3): p. 137-172.
234. Johnson B.K. and Prud'homme R.K., *Mechanism for rapid self-assembly of block copolymer nanoparticles*. Physical review letters, 2003. **91**(11): p. 118302.
235. Gindy M.E., Panagiotopoulos A.Z., and Prud'homme R.K., *Composite block copolymer stabilized nanoparticles: Simultaneous encapsulation of organic actives and inorganic nanostructures*. Langmuir, 2008. **24**(1): p. 83-90.
236. D'Addio S.M. and Prud'homme R.K., *Controlling drug nanoparticle formation by rapid precipitation*. Advanced drug delivery reviews, 2011. **63**(6): p. 417-426.
237. Zhang H.X., Wang J.X., Shao L., and Chen J.F., *Microfluidic fabrication of monodispersed pharmaceutical colloidal spheres of atorvastatin calcium with*

- tunable sizes.* Industrial & Engineering Chemistry Research, 2010. **49**(9): p. 4156-4161.
238. Sahu K., Ding H., Valluri P., and Matar O., *Pressure-driven miscible two-fluid channel flow with density gradients.* Physics of Fluids, 2009. **21**: p. 043603.
239. Sullivan S., Akpa B., Matthews S., Fisher A., Gladden L., and Johns M., *Simulation of miscible diffusive mixing in microchannels.* Sensors and Actuators B: Chemical, 2007. **123**(2): p. 1142-1152.
240. Laughlin R.G., Bunke G.M., Eads C.D., Laidig W.D., and Shelley J.C., *Preparation and physical characterization of pure [beta]-carotene.* Chemistry and physics of lipids, 2002. **115**(1-2): p. 63-76.
241. Luk V.N., Mo G.C.H., and Wheeler A.R., *Pluronic additives: a solution to sticky problems in digital microfluidics.* Langmuir, 2008. **24**(12): p. 6382-6389.
242. Li W., Kagan G., Hopson R., and Williard P.G., *Application of 6 Li diffusion-ordered NMR spectroscopy (DOSY) to confirming the solution structure of n-butyllithium.* ARKIVOC, 2011. **5**: p. 180-187.
243. d'Orlye F., Varenne A., and Gareil P., *Determination of nanoparticle diffusion coefficients by Taylor dispersion analysis using a capillary electrophoresis instrument.* Journal of Chromatography A, 2008. **1204**(2): p. 226-232.
244. Katayama K., Nomura H., Ogata H., and Eitoku T., *Diffusion coefficients for nanoparticles under flow and stop-flow conditions.* Phys. Chem. Chem. Phys., 2009. **11**(44): p. 10494-10499.
245. Johnson B.K. and Prud'homme R.K., *Mechanism for rapid self-assembly of block copolymer nanoparticles.* Phys Rev Lett, 2003. **91**(11): p. 118302.
246. Lo C.T., Jahn A., Locascio L.E., and Vreeland W.N., *Controlled Self-Assembly of Monodisperse Niosomes by Microfluidic Hydrodynamic Focusing.* Langmuir, 2010. **26**(11): p. 8559-8566.
247. Pepic I., Filipovic-Grcic J., and Jalsenjak I., *Bulk properties of nonionic surfactant and chitosan mixtures.* Colloids and Surfaces A: Physicochemical and Engineering Aspects, 2009. **336**(1-3): p. 135-141.
248. Horn D. and Rieger J., *Organic nanoparticles in the aqueous phase - theory, experiment, and use.* Angew. Chem.-Int. Edit., 2001. **40**(23): p. 4331-4361.
249. Zhu Z., Margulis Goshen K., Magdassi S., Talmon Y., and Macosko C.W., *Polyelectrolyte stabilized drug nanoparticles via flash nanoprecipitation: A model study with carotene.* Journal of pharmaceutical sciences, 2010. **99**(10): p. 4295-4306.
250. Mordi R.C., Walton J.C., Burton G.W., Hughes L., Keith Ingold U., and David Lindsay A., *Oxidative degradation of [beta]-carotene and [beta]-apo-8'-carotenal.* Tetrahedron, 1993. **49**(4): p. 911-928.
251. Wang J.X., Zhang Q.X., Zhou Y., Shao L., and Chen J.F., *Microfluidic synthesis of amorphous cefuroxime axetil nanoparticles with size-dependent and enhanced dissolution rate.* Chemical Engineering Journal, 2010. **162**(2): p. 844-851.
252. Karnik R., Gu F., Basto P., Cannizzaro C., Dean L., Kyei-Manu W., Langer R., and Farokhzad O.C., *Microfluidic platform for controlled synthesis of polymeric nanoparticles.* Nano Letters, 2008. **8**(9): p. 2906-2912.
253. Rahme K., Oberdisse J., Schweins R., Gaillard C., Marty J.D., Mingotaud C., and Gauffre F., *Pluronics Stabilized Gold Nanoparticles: Investigation of the Structure of the Polymer-Particle Hybrid.* ChemPhysChem, 2008. **9**(15): p. 2230-2236.

254. Niesz K., Grass M., and Somorjai G.A., *Precise control of the Pt nanoparticle size by seeded growth using EO13PO30EO13 triblock copolymers as protective agents*. Nano Letters, 2005. 5(11): p. 2238-2240.
255. von Seggern D., *CRC Standard Curves and Surfaces*. 1993, Boca Raton, FL: CRC Press.
256. Thein S., *Genetic insights into the clinical diversity of thalassaemia*. British journal of haematology, 2004. 124(3): p. 264-274.
257. Bank A., *Regulation of human fetal hemoglobin: new players, new complexities*. Blood, 2006. 107(2): p. 435.
258. Old J., *Screening and genetic diagnosis of haemoglobin disorders*. Blood reviews, 2003. 17(1): p. 43-53.
259. Gambari R. and Fibach E., *Medicinal Chemistry of Fetal Hemoglobin Inducers for Treatment of Thalassemia*. Current medicinal chemistry, 2007. 14(2): p. 199-212.
260. Rodgers G. and Rachmilewitz E., *NOVEL TREATMENT OPTIONS IN THE SEVERE GLOBIN DISORDERS*. British journal of haematology, 1995. 91(2): p. 263-268.
261. Rochette J., Craig J., and Thein S., *Fetal hemoglobin levels in adults*. Blood reviews, 1994. 8(4): p. 213-224.
262. Olivieri N. and Weatherall D., *The therapeutic reactivation of fetal haemoglobin*. Human molecular genetics, 1998. 7(10): p. 1655.
263. Bianchi N., Osti F., Rutigliano C., Corradini F., Borsetti E., Tomassetti M., Mischiati C., Feriotti G., and Gambari R., *The DNA binding drugs mithramycin and chromomycin are powerful inducers of erythroid differentiation of human K562 cells*. British journal of haematology, 1999. 104(2): p. 258-265.
264. Bianchi N., Chiarabelli C., Borgatti M., Mischiati C., Fibach E., and Gambari R., *Accumulation of globin mRNA and induction of erythroid differentiation after treatment of human leukaemic K562 cells with tallimustine*. British journal of haematology, 2001. 113(4): p. 951-961.
265. Barcel F., Ortiz-Lombardia M., Martorell M., Oliver M., M ndez C., Salas J.A., and Portugal J., *DNA-binding characteristics of mithramycin and chromomycin analogues obtained by combinatorial biosynthesis*. Biochemistry, 2010.
266. Koller C.A. and Miller D.M., *Preliminary observations on the therapy of the myeloid blast phase of chronic granulocytic leukemia with plicamycin and hydroxyurea*. The New England journal of medicine, 1986. 315(23): p. 1433.
267. Yuan P., Wang L., Wei D., Zhang J., Jia Z., Li Q., Le X., Wang H., Yao J., and Xie K., *Therapeutic inhibition of Sp1 expression in growing tumors by mithramycin a correlates directly with potent antiangiogenic effects on human pancreatic cancer*. Cancer, 2007. 110(12): p. 2682-2690.
268. Ryuto M., Ono M., Izumi H., Yoshida S., Weich H.A., Kohno K., and Kuwano M., *Induction of vascular endothelial growth factor by tumor necrosis factor in human glioma cells*. Journal of Biological Chemistry, 1996. 271(45): p. 28220.
269. CAMPBELL V.W., DAVIN D., THOMAS S., JONES D., ROESEL J., TRAN-PATTERSON R., MAYFIELD C.A., RODU B., MILLER D.M., and HIRAMOTO R.A.Y.A., *The GC specific DNA binding drug, mithramycin, selectively inhibits transcription of the C-MYC and C-HA-RAS genes in regenerating liver*. The American journal of the medical sciences, 1994. 307(3): p. 167.
270. TAGASHIRA M., KITAGAWA T., ISONISHI S., OKAMOTO A., OCHIAI K., and OHTAKE Y., *Mithramycin represses MDR1 gene expression in vitro, modulating*

- multidrug resistance.* Biological & pharmaceutical bulletin, 2000. **23**(8): p. 926-929.
271. King P.D. and Perry M.C., *Hepatotoxicity of chemotherapy.* The Oncologist, 2001. **6**(2): p. 162.
272. Nastruzzi C., Cortesi R., Esposito E., Gambari R., Borgatti M., Bianchi N., Feriotto G., and Mischiati C., *Liposomes as carriers for DNA-PNA hybrids.* Journal of Controlled Release, 2000. **68**(2): p. 237-249.
273. Kedar U., Phutane P., Shidhaye S., and Kadam V., *Advances in polymeric micelles for drug delivery and tumor targeting.* Nanomedicine: Nanotechnology, Biology and Medicine, 2010. **6**(6): p. 714-729.
274. Cohen Sela E., Teitlboim S., Chorny M., Koroukhov N., Danenberg H.D., Gao J., and Golomb G., *Single and double emulsion manufacturing techniques of an amphiphilic drug in PLGA nanoparticles: formulations of mithramycin and bioactivity.* Journal of pharmaceutical sciences, 2009. **98**(4): p. 1452-1462.
275. Vonarbourg A., Passirani C., Saulnier P., and Benoit J.P., *Parameters influencing the stealthiness of colloidal drug delivery systems.* Biomaterials, 2006. **27**(24): p. 4356-4373.
276. Letchford K. and Burt H., *A review of the formation and classification of amphiphilic block copolymer nanoparticulate structures: micelles, nanospheres, nanocapsules and polymersomes.* European journal of pharmaceutics and biopharmaceutics, 2007. **65**(3): p. 259-269.
277. Park Y.J., Lee J.Y., Chang Y.S., Jeong J.M., Chung J.K., Lee M.C., Park K.B., and Lee S.J., *Radioisotope carrying polyethylene oxide-polycaprolactone copolymer micelles for targetable bone imaging.* Biomaterials, 2002. **23**(3): p. 873-879.
278. Buxton D.B., *Nanomedicine for the management of lung and blood diseases.* Nanomedicine, 2009. **4**(3): p. 331-339.
279. Dobrovolskaia M.A., Aggarwal P., Hall J.B., and McNeil S.E., *Preclinical studies to understand nanoparticle interaction with the immune system and its potential effects on nanoparticle biodistribution.* Molecular pharmaceutics, 2008. **5**(4): p. 487-495.
280. Rothen-Rutishauser B.M., Schürch S., Haenni B., Kapp N., and Gehr P., *Interaction of fine particles and nanoparticles with red blood cells visualized with advanced microscopic techniques.* Environmental Science & Technology, 2006. **40**(14): p. 4353-4359.
281. Tosi A., Mazzitelli S., Capretto L., Guerrieri R., and Nastruzzi C., *Optimization of lipospheres production by factorial design and their performances on a dielectrophoretic lab-on-a-chip platform.* Colloids and Surfaces A: Physicochemical and Engineering Aspects, 2009. **340**(1-3): p. 77-85.
282. Gambari R., Barbieri R., Buzzoni D., Bernardi F., Marchetti G., Amelotti F., Piva R., Viola L., and del Senno L., *Human leukemic K562 cells: suppression of hemoglobin accumulation by a monoclonal antibody to human transferrin receptor.* Biochimica et Biophysica Acta (BBA)-Molecular Cell Research, 1986. **886**(2): p. 203-213.
283. Bohmer R.M., Campbell T.A., and Bianchi D.W., *Selectively increased growth of fetal hemoglobin-expressing adult erythroid progenitors after brief treatment of early progenitors with transforming growth factor beta.* Blood, 2000. **95**(9): p. 2967.
284. Chouair A. and Eisenberg A., *Interfacial solubilization of model amphiphilic molecules in block copolymer micelles.* Journal of the American Chemical Society, 2003. **125**(39): p. 11993-12000.

285. Elhasi S., Astaneh R., and Lavasanifar A., *Solubilization of an amphiphilic drug by poly (ethylene oxide)-block-poly (ester) micelles*. European journal of pharmaceutics and biopharmaceutics, 2007. **65**(3): p. 406-413.
286. Alexis F., Pridgen E., Molnar L.K., and Farokhzad O.C., *Factors affecting the clearance and biodistribution of polymeric nanoparticles*. Molecular pharmaceutics, 2008. **5**(4): p. 505-515.
287. Mikhail A.S. and Allen C., *Block copolymer micelles for delivery of cancer therapy: transport at the whole body, tissue and cellular levels*. Journal of Controlled Release, 2009. **138**(3): p. 214-223.
288. Gaucher G., Marchessault R.H., and Leroux J.C., *Polyester-based micelles and nanoparticles for the parenteral delivery of taxanes*. Journal of Controlled Release, 2010. **143**(1): p. 2-12.
289. Li S.D. and Huang L., *Pharmacokinetics and biodistribution of nanoparticles*. Molecular pharmaceutics, 2008. **5**(4): p. 496-504.
290. Bae Y., Diezi T.A., Zhao A., and Kwon G.S., *Mixed polymeric micelles for combination cancer chemotherapy through the concurrent delivery of multiple chemotherapeutic agents*. Journal of Controlled Release, 2007. **122**(3): p. 324-330.
291. Fordis C.M., Anagnou N.P., Dean A., Nienhuis A.W., and Schechter A.N., *A beta-globin gene, inactive in the K562 leukemic cell, functions normally in a heterologous expression system*. Proceedings of the National Academy of Sciences of the United States of America, 1984. **81**(14): p. 4485.
292. Farokhzad O.C. and Langer R., *Impact of nanotechnology on drug delivery*. ACS nano, 2009. **3**(1): p. 16-20.
293. Park K., *Nanotechnology: What it can do for drug delivery*. Journal of controlled release: official journal of the Controlled Release Society, 2007. **120**(1-2): p. 1.
294. Herrmann E., Lihavainen H., Hyvärinen A.P., Riipinen I., Wilck M., Stratmann F., and Kulmala M., *Nucleation simulations using the fluid dynamics software FLUENT with the fine particle model FPM*. The Journal of Physical Chemistry A, 2006. **110**(45): p. 12448-12455.